

# Active emulsion droplets driven by Marangoni flow

vorgelegt von  
Diplom-Ingenieur

**Maximilian Schmitt**

geboren in Wissen (Sieg)

Von der Fakultät II - Mathematik und Naturwissenschaften  
der Technischen Universität Berlin  
zur Erlangung des akademischen Grades  
*Doktor der Naturwissenschaften (Dr. rer. nat.)*  
genehmigte Dissertation

Promotionsausschuss:

---

Vorsitzender	Prof. Dr. Martin Schoen
Erster Gutachter	Prof. Dr. Holger Stark
Zweiter Gutachter	Prof. Dr. Uwe Thiele

---

Tag der wissenschaftlichen Aussprache: 04.05.2016

Berlin 2017



# Contents

<b>1</b>	<b>Introduction</b>	<b>7</b>
<b>2</b>	<b>Microswimmers</b>	<b>11</b>
2.1	Hydrodynamics . . . . .	11
2.1.1	Navier-Stokes equation . . . . .	11
2.1.2	Reynolds number . . . . .	12
2.1.3	Stokes equation . . . . .	13
2.1.4	The squirmer . . . . .	14
2.2	Brownian motion . . . . .	16
2.3	Active Brownian particles . . . . .	18
<b>3</b>	<b>The active emulsion droplet</b>	<b>21</b>
3.1	Definition and distinction . . . . .	21
3.2	Microfluidics . . . . .	22
3.3	The fluid-fluid interface . . . . .	23
3.3.1	Surface tension . . . . .	24
3.3.2	Surfactants . . . . .	25
3.3.3	Bromination reaction . . . . .	27
3.3.4	Light sensitive surfactants . . . . .	28
3.3.5	Interfacial equation of state . . . . .	30
3.3.6	Diffusion-Advection-Reaction equation . . . . .	32
3.4	The Marangoni effect . . . . .	38
3.4.1	Early observations of surface tension driven flow . . . . .	38
3.4.2	Causes for Marangoni flow . . . . .	39
3.4.3	Plane Marangoni flow . . . . .	40
3.4.4	Marangoni number . . . . .	41
3.4.5	Droplet Marangoni flow . . . . .	42
3.5	Experiments, models, and theories on active emulsion droplets . . . . .	47
3.5.1	Early attempts on droplet Marangoni flow . . . . .	47
3.5.2	Current state of research on active emulsion droplets . . . . .	47
<b>4</b>	<b>Publications</b>	<b>51</b>
4.1	Synopsis . . . . .	51
4.2	Swimming active droplet: A theoretical analysis . . . . .	55
4.3	Marangoni flow at droplet interfaces: Three-dimensional solution and applications . . . . .	63

4.4 Active Brownian motion of emulsion droplets: Coarsening dynamics at the interface and rotational diffusion . . . . .	95
<b>5 Conclusion and Outlook</b>	<b>112</b>
<b>6 Bibliography</b>	<b>115</b>
<b>Danksagung</b>	<b>125</b>
<b>Zusammenfassung in deutscher Sprache</b>	<b>126</b>





# 1 Introduction

An active emulsion droplet is a swimming micron-sized liquid droplet immersed in a bulk liquid. It is active in a sense that the swimming motion is not driven by external forces, but rather sustained under a force-free condition. Such a droplet is therefore a typical example of a synthetic active particle and belongs to the class of active matter [1]. Active matter systems rely on a continual supply of energy, which makes these systems inherently nonequilibrium in character. They share this property with living systems, such as *e.g.* cells [2]. In fact, the boundary between active emulsion droplets and living cells is starting to blur. By confining an active gel, which is composed of microtubules, the protein streptavidin, and kinesin, to the interior of a water-in-oil emulsion, it is possible to render the streaming used by cells to circulate their fluid content as well as the active motion of cells [3, 4, 5]. Therefore, gathering knowledge about the mechanics and locomotion of droplets can help to understand various micron-sized liquid swimming objects, especially protist cells [6].

A hallmark of active matter is the emergence of large-scale patterns in a crowd of interacting active “agents”. This can be found in schools of fish, flocks of bacteria, or the collective motion of so-called Janus colloids, which are artificial microswimmers [7]. In contrast to active droplets, Janus colloids have an inherently broken symmetry in their material properties between two faces. Note that recently swarming behavior was also observed in experiments of active emulsion droplets [8].

Droplets also play a key role in the growing field of microfluidics, which set itself to miniaturize biological, chemical, and medical processes in a fluid to the microscale [9]. For instance, one can realize chemical reactions inside emulsion droplets. Such a system is sometimes called a microreactor [10]. Other digital fluidic operations that can be combined on a so-called lab-on-a-chip are droplet generation, transport, fusion, fission, mixing, and sorting of droplets. However, most of these operations are performed with passive droplets, which move due to an external flow field. A promising next step is to extend these operations to active droplets, which could open up a plethora of new applications, *e.g.*, in drug release problems [11, 12].

Consequently, it is worthwhile to study active emulsion droplets, both from a theoretical viewpoint as well as from a technical viewpoint.

A first question, which arises naturally in the study of active emulsion droplets, is how the onset of motion is realized. In contrast to Janus colloids, active droplets are initially homogeneous in their physical and chemical properties. Therefore, the onset of motion is due to a spontaneous symmetry breaking at the droplet interface. Here, typically the surfactant concentration at the interface of the droplet evolves from being uniform to a shape which is characterized by two domains with different surfactant concentrations. Since the surfactant concentration directly influences the surface tension at the droplet

interface, a gradient in surface tension emerges. This leads to a jump in shear stress at the interface, which in turn drags adjacent fluid layers in direction of increasing surface tension. Ultimately, this leads to propulsion of the droplet. This effect is called Marangoni effect [13]. In the case of the active droplet realized by Thutupalli *et al.* in Ref. [8], the interface of the droplet is covered by two surfactant types, which differ by their surface tension due to a chemical reaction with bromine. Here, the symmetry breaking can be seen as a phase separation of the two surfactant types. Thus, the onset of motion can be studied in the framework of coarsening at a fluid-fluid interface.

Once the droplet has reached a steady swimming state, one classifies it by means of swimmer types. Typical swimmer types are pushers and pullers, which resemble the flow field around bacteria and algae, respectively. The swimmer type greatly influences the hydrodynamic interactions with other droplets, obstacles, and walls, and is therefore of great practical interest [14]. Apart from simple forward propulsion, oscillatory motion, where the active emulsion droplet moves forward and backward, is also possible [15, 16]. We confirm these findings in Ref. [17], which can be found in Sect. 4.2.

Without considering thermal noise or boundary conditions, active emulsion droplets swim forward in a straight line. This is certainly not the case in real systems, where the finite temperature at the droplet interface leads to fluctuations in the surfactant mixture, which in turn randomize the swimming direction. As a result, the active droplet performs a persistent random walk. Here, the amplitude of the fluctuations directly sets the persistence of the swimming path, and with that the effective diffusion constant of the droplet. We quantify this systematically by averaging over many trajectories of active emulsion droplets in Ref. [18], which is given in Sect. 4.4.

As is typical for active matter, swimming droplets are open systems, *i.e.*, they are subject to a steady inflow and outflow of matter or energy. Here, “matter” means surfactants: They adsorb at the front of the swimming droplet and desorb back into the bulk at the posterior end. However, above the critical micelle concentration (cmc), surfactants tend to form micelles, *i.e.*, spherical aggregates of surfactants. Thus, above the cmc surfactants adsorb in form of micelles at the front of the droplet. This could lead to an additional randomization of the droplet trajectory. In a minimal model, micelles can also explain the onset of motion of an initially surfactant-free droplet. The Marangoni induced spreading, when a micelle adsorbs at the interface, leads to a motion of the droplet in direction of the adsorption site. The corresponding outer Marangoni flow field, however, preferentially advects other micelles towards the existing adsorption site. Hence, this mechanism can spontaneously break the isotropic symmetry of the droplet and lead to directed motion. We elaborate on this effect in Sect. 4.3, where we present Ref. [19].

Another possibility to locally alter the surface tension of a droplet, is to partially illuminate a droplet, which is covered with light-switchable surfactants [20]. Depending on the wavelength of the light, the surfactant changes its structure and with that its surface tension. Hereby, one can locally generate a spot of different surface tension, which induces Marangoni flow and hence propulsion of the droplet. Here, the emulsion droplet can be pushed with UV light or pulled with blue light. Furthermore, depending on the relaxation rate towards the surfactant type in bulk, the droplet shows a plethora

of trajectories, including a damped oscillation about the beam axis, an oscillation into the beam axis, and a motion out of the beam followed by a complete stop [19].

## Structure of the thesis

This is a cumulative thesis. As such, it presents the main scientific results in three publications at the end of the thesis:

- “Swimming active droplet: A theoretical analysis,” *Europhys. Lett.*, vol. 101, p. 44008, 2013.
- “Marangoni flow at droplet interfaces: Three-dimensional solution and applications,” *Phys. Fluids*, vol. 28, p. 012106, 2016.
- “Active brownian motion of emulsion droplets: Coarsening dynamics at the interface and rotational diffusion,” *Eur. Phys. J. E*, vol. 39, p. 80, 2016.

All publications are written by Maximilian Schmitt and Holger Stark. Prior to this, we prepare the reader by introducing such concepts as the active Brownian particle, active emulsion droplets, and Marangoni flow. Furthermore, we integrate our results into the current state of research. In what follows, we give a brief outline:

Section 2 introduces the physics of microswimmers. We discuss the hydrodynamical implications of swimming on the microscale and present the squirmer, which is a classical model of a spherical microswimmer. Furthermore, we shortly address Brownian motion of passive and active particles.

In Sect. 3, we specialize the discussion to active emulsion droplets. After a clear definition of active emulsion droplets, we dwell on the theoretical description of fluid-fluid interfaces. We discuss the concept of surface tension, explain how surfactants change the surface tension, and give a thorough model for the dynamics of surfactants at interfaces. We also elaborate on Marangoni flow on flat interfaces as well as on droplet interfaces. Finally, we give an overview of the literature, starting with the discovery of the Marangoni effect, up to recent experimental and theoretical results of active emulsion droplets.

Section 4 contains the publications as well as a synopsis of the published results, where we integrate our findings into the current state of research. We discuss how the spontaneous phase separation of a surfactant mixture leads to directed motion of an active emulsion droplet. Here, we also find oscillatory trajectories. By including thermal fluctuations, we can model the active Brownian motion of swimming droplets. In addition, we propose a minimal model of symmetry breaking of a droplet due to the adsorption of micelles. Lastly, we address light-driven droplet propulsion.

Finally, in Sect. 5 we present our conclusions and give an outlook.



## 2 Microswimmers

The active emulsion droplet is a typical example of an artificial microswimmer, *i.e.*, a swimmer whose size is on the order of several  $\mu\text{m}$ . We therefore take one step back and introduce the reader to the fundamental physics of microswimmers, before we dwell on active emulsion droplets and their unique features in Sect. 3. We start with a short introduction on the hydrodynamics to the microscale in Sect. 2.1, after which we discuss the erratic motion of passive particles and microswimmers in Sect. 2.2, and 2.3, respectively.

### 2.1 Hydrodynamics

What all microswimmers, including living organisms such as bacteria or algae as well as artificial microswimmers such as Janus colloids or active droplets, have in common is that they move in the regime of Stokes flow where viscous forces dominate over inertial forces. Equivalent expressions are 'creeping flow' and 'low Reynolds number flow'. This is for instance the case when micron-sized objects move in a viscous liquid such as water or oil. A precise definition by means of the Reynolds number will be given in Sect. 2.1.2. The theory of Stokes flow is a linear theory, which eases the theoretical and numerical treatment by a great extent. This will be discussed in Sect. 2.1.3 and applied to the hydrodynamic standard model of microswimmers – the squirmer – in Sect. 2.1.4.

#### 2.1.1 Navier-Stokes equation

We start with the Navier-Stokes equation, which describes the dynamics of viscous fluids. It is given by Newton's second law,

$$\mathbf{F} = m\mathbf{a} , \quad (2.1)$$

written for a fluid parcel with density  $\rho$ . The acceleration  $\mathbf{a}$  has to be written as the material derivative  $\frac{D\mathbf{u}}{Dt}$  of the velocity field  $\mathbf{u}(\mathbf{r})$  of the fluid. The material derivative is defined as  $\frac{D}{Dt} = \partial_t + \mathbf{u} \cdot \nabla$ , *i.e.*, it measures the total temporal change of a quantity flowing with the parcel due to local change  $\partial_t$  as well as due to advection  $\mathbf{u} \cdot \nabla$  in the velocity field  $\mathbf{u}$ . In addition to body forces  $\mathbf{F} = \rho\mathbf{f}$ , a fluid parcel experiences viscous forces, which are written as the divergence of the stress tensor  $\mathbf{T}$ :

$$\rho \frac{D\mathbf{u}}{Dt} = \nabla \cdot \mathbf{T} + \rho\mathbf{f} . \quad (2.2)$$

For a Newtonian fluid,  $\mathbf{T} = 2\eta\mathbf{A} - p\mathbf{1}$ , with viscosity  $\eta$  and strain rate tensor  $\mathbf{A} = \frac{1}{2}[\nabla \otimes \mathbf{u} + (\nabla \otimes \mathbf{u})^T]$  of the fluid, and pressure field  $p$ . Together with the material

derivative  $\frac{D\mathbf{u}}{Dt} = \frac{\partial\mathbf{u}}{\partial t} + (\mathbf{u} \cdot \nabla)\mathbf{u}$ , one finds the Navier-Stokes equation:

$$\rho \frac{\partial\mathbf{u}}{\partial t} + \rho(\mathbf{u} \cdot \nabla)\mathbf{u} = \eta \nabla^2 \mathbf{u} - \nabla p + \rho \mathbf{f}. \quad (2.3)$$

The way we wrote down Newton's second law in Eq. (2.1), we assumed the mass  $m$  to be constant. Similarly, we also assume a constant density  $\rho$  in Eq. (2.3). However, by writing out the continuity equation  $0 = \frac{\partial\rho}{\partial t} + \nabla \cdot (\rho\mathbf{u}) = \frac{D\rho}{Dt} + \rho \nabla \cdot \mathbf{u}$  for the density  $\rho$ , one notices that constant  $\rho$  translates into the constraint

$$\nabla \cdot \mathbf{u} = 0, \quad (2.4)$$

for the velocity field  $\mathbf{u}$ . This is the incompressibility condition. Hence, a velocity field  $\mathbf{u}$  is only a correct solution of the Navier-Stokes equation (2.3), if it also satisfies condition (2.4).

The most striking property of the Navier-Stokes equation is the nonlinearity  $(\mathbf{u} \cdot \nabla)\mathbf{u}$ , which made it impossible to write down a general solution to this day. Therefore one has to resort to numerical approaches to find an approximative solution for the flow field  $\mathbf{u}$ . In what follows we discuss a regime where the nonlinearity can be omitted, which opens up several possibilities to solve for  $\mathbf{u}$  exactly.

### 2.1.2 Reynolds number

To gain some insight into the physics of the Navier-Stokes equation (2.3), we introduce a typical length scale  $L$ , velocity  $u_0$ , and pressure  $p_0$  of the physical problem under consideration. Furthermore, we omit external forces at this point and set  $\mathbf{f} = \mathbf{0}$ . The Navier-Stokes equation reads in dimensionless quantities (denoted by the tilde):

$$\frac{\rho u_0^2}{L} \left[ \frac{\partial \tilde{\mathbf{u}}}{\partial \tilde{t}} + (\tilde{\mathbf{u}} \cdot \tilde{\nabla}) \tilde{\mathbf{u}} \right] = \frac{\eta u_0}{L^2} \tilde{\nabla}^2 \tilde{\mathbf{u}} - \frac{p_0}{L} \tilde{\nabla} \tilde{p}, \quad (2.5)$$

where we used  $t = \frac{L}{u_0} \tilde{t}$ . This can also be written as

$$\text{Re} \left[ \frac{\partial \tilde{\mathbf{u}}}{\partial \tilde{t}} + (\tilde{\mathbf{u}} \cdot \tilde{\nabla}) \tilde{\mathbf{u}} \right] = \tilde{\nabla}^2 \tilde{\mathbf{u}} - \frac{1}{2} \text{Eu} \text{Re} \tilde{\nabla} \tilde{p}, \quad (2.6)$$

with the Reynolds number  $\text{Re}$  and Euler number  $\text{Eu}$ :

$$\text{Re} = \frac{\rho u_0 L}{\eta}, \quad \text{Eu} = \frac{2p_0}{u_0^2 \rho}. \quad (2.7)$$

The Reynolds number compares inertial forces with viscous forces, while  $\text{Eu}$  is the ratio of pressure forces to inertial forces. For a microswimmer of size  $L = 10\mu\text{m}$  flowing in water ( $\rho = 1\text{kg}/\text{dm}^3$ ,  $\eta = 1\text{mPa} \cdot \text{s}$ ) with velocity  $u_0 = 10\mu\text{m}/\text{s}$ , one finds  $\text{Re} = 10^{-4} \ll 1$ . Thus, the dynamics of a microswimmer in water is mainly governed by viscous forces and not inertia.

Note that the flow fields of two systems that have the same geometry are said to be similar, when they have equal Reynolds and Euler numbers. This allows to save on costs and lab time by performing experiments on similar flows in water channels or wind tunnels, and relate the data to the far field of the actual systems.

### 2.1.3 Stokes equation

The flow of microswimmers, such as bacteria, Janus colloids, or active emulsion droplets, is in the regime of low Reynolds numbers. We can therefore omit the l.h.s of Eq. (2.3) and find:

$$\eta \nabla^2 \mathbf{u} - \nabla p + \mathbf{f} = \mathbf{0} , \quad (2.8)$$

which is called Stokes equation. Here, the constraint of incompressibility  $\nabla \cdot \mathbf{u} = 0$  still holds.

In contrast to the full Navier-Stokes equation, Eq. (2.8) is linear in  $\mathbf{u}$ . This allows to find Green's functions for a given point force  $\mathbf{f} = \mathbf{f}_0 \delta(\mathbf{r} - \mathbf{r}_0)$  for both the velocity field  $\mathbf{u}$  as well as for the pressure  $p$ . The corresponding flow singularity is called Stokeslet, and the Green's function for  $\mathbf{u}$  is a second-rank tensor called Oseen tensor:

$$\mathbf{O}(\mathbf{r}) = \frac{1}{8\pi\eta r} \left( \mathbf{1} - \frac{\mathbf{r} \otimes \mathbf{r}}{r^2} \right) , \quad (2.9)$$

with  $r = |\mathbf{r}|$  and flow field  $\mathbf{u}(\mathbf{r}) = \mathbf{f}_0 \cdot \mathbf{O}(\mathbf{r})$ . Note that this flow field decays as  $\mathbf{u} \propto 1/r$ . For instance, the far field around a spherical colloid, which is pulled through a viscous liquid, is given by the Stokeslet. By integrating the resulting stress of the flow field over the interface of the pulled colloid, one finds the Stokes drag force

$$\mathbf{f} = -6\pi\eta R \mathbf{v} , \quad (2.10)$$

of a spherical colloid with radius  $R$ , which moves with velocity  $\mathbf{v}$  through a liquid of viscosity  $\eta$ . For more complex objects, force and velocity are connected via  $\mathbf{f} = \boldsymbol{\gamma} \mathbf{v}$  with the drag tensor  $\boldsymbol{\gamma}$ .

Stokes flow is always laminar, which means that there is no disruption between parallel fluid layers, and hence no turbulence. It is therefore difficult to mix fluids in the low Reynolds number regime. Note that even though the flow field around a microswimmer is laminar, a suspension of microswimmers can still show turbulence [21].

Upon comparing the Navier-Stokes (2.3) with the Stokes equation (2.8), one notices that the latter is lacking a time derivative. Therefore, reversing an applied force, which acts on a microswimmer, leads to a perfectly reversed fluid motion. This has striking consequences for the swimming mechanisms of microswimmers. For instance the algae *Chlamydomonas*, which propels itself forward by two beating flagella, which are attached at the front of the cell, can only swim if forward and backward stroke of the flagella are not time-reversible. Otherwise, the displacement during forward and backward stroke would simply cancel each other. This circumstance is also known as Scallop theorem [22]. Swimming in the low Reynolds number regime is discussed extensively in the Reviews [14, 23, 24].

In any real physical system, the Stokes equation (2.8) is subject to boundary conditions, such as the a no-slip boundary condition  $\mathbf{u} = \mathbf{0}$  on the solid interface of a colloid or a given pressure difference  $\Delta p$  in a fluid channel. In Sect. 3.4, we dwell on the hydrodynamic conditions at a fluid-fluid interfaces of an emulsion droplet. Another possible boundary condition is a prescribed flow  $\mathbf{u}$  at an interface. In the following section, we discuss a spherical microswimmer with such a prescribed surface velocity.

### 2.1.4 The squirmer

The squirmer is a classic model of an axisymmetric spherical microswimmer [25, 26], which has been introduced to model the locomotion of microorganisms. Originally the squirmer was a model for microorganisms that propel themselves by a carpet of beating cilia on their surfaces. Instead of modeling each cilium separately, one coarse-grains into a prescribed fluid flow at the surface. Today, the squirmer model is used as a standard model for microswimmers, especially in simulations of suspensions of microswimmers [27, 28, 29]. Note that the squirmer has recently been generalized to also model non-axisymmetric swimmers [30].

The prescribed flow at the interface of an axisymmetric squirmer with radius  $R$  is written as an expansion  $\mathbf{u}(R, \theta) = \sum_{l=1}^{\infty} B_l V_l \mathbf{e}_\theta$  in the polynomials  $V_l(\cos \theta) = \frac{-2}{l(l+1)} \partial_\theta P_l(\cos \theta)$ , where  $P_l(\cos \theta)$  are Legendre polynomials of order  $l$ . The resulting flow field around the squirmer is given by [25, 26]:

$$u_r(r, \theta) = \frac{2}{3} \left[ \frac{R^3}{r^3} - 1 \right] B_1 P_1 + \sum_{l=2}^{\infty} \left[ \frac{R^{l+2}}{r^{l+2}} - \frac{R^l}{r^l} \right] B_l P_l, \quad (2.11a)$$

$$u_\theta(r, \theta) = \frac{2}{3} \left[ \frac{R^3}{2r^3} + 1 \right] B_1 V_1 + \sum_{l=2}^{\infty} \frac{1}{2} \left[ l \frac{R^{l+2}}{r^{l+2}} + (2-l) \frac{R^l}{r^l} \right] B_l V_l. \quad (2.11b)$$

These expressions are given in spherical coordinates and in the frame of the moving particle. The squirmer moves in  $z$ -direction with velocity vector  $\mathbf{v} = v \mathbf{e}_z$  and swimming speed  $v = \frac{2}{3} B_1$ . The two leading terms of the surface velocity field can also be written as

$$u_\theta|_R(\theta) = B_1 \sin \theta + \frac{B_2}{2} \sin 2\theta, \quad (2.12)$$

where one defines the squirmer parameter as  $\beta = \frac{B_2}{B_1}$ . In the following we dwell on the squirmer parameter, see also Table 2.1.

From Eq. (2.12), one finds that for  $\beta < 0$  ( $\beta > 0$ ), the flow  $u_\theta|_R$  dominates at the back (front) of the squirmer. Thus, the case  $\beta < 0$  models a microswimmer, where the swimming apparatus is located at the back of the swimmer. Since such a swimmer pushes itself through the liquid, it is called a pusher. Correspondingly a squirmer with  $\beta > 0$  is called a puller. A squirmer with  $B_2 = 0$ , hence  $\beta = 0$ , is called a neutral swimmer and a squirmer with  $B_1 = 0$ , hence  $\beta = \pm\infty$ , is called a shaker. Note that the leading flow singularity of pusher and pullers is a stresslet, which is a force-free combination of two Stokeslets [31, 32]. Here, the sign of  $\beta$  expresses the direction of the two Stokeslets, see red arrows in Table 2.1. The singularities that account for the neutral swimmer are the source dipole and the Stokes quadrupole, which is combination of two stresslets. Finally, one finds from Eq. (2.11), that for  $\beta = 0$  the velocity field decays as  $\mathbf{u} \propto 1/r^3$ , while for  $\beta \neq 0$  the flow is more long-range with  $\mathbf{u} \propto 1/r^2$ .

In Table 2.1, we also show three real life examples of microswimmers, whose velocity field can be modeled by the squirmer model. For instance, the dinoflagellate *Gonyaulax* has two flagella. One lies in a groove that runs from the center to the posterior end of the cell and propels the dinoflagellate at the back of the cell. The other flagella is in

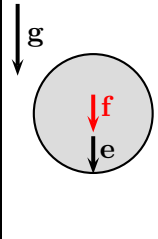
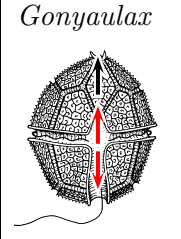
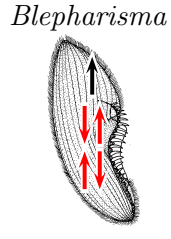
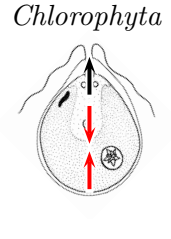
Swimmer type	passive colloid	pusher	neutral swimmer	puller	shaker
Squirmer parameter		$\beta < 0$	$\beta = 0$	$\beta > 0$	$\beta = \pm\infty$
Far field decay	$\mathbf{u} \propto 1/r$	$\mathbf{u} \propto 1/r^2$	$\mathbf{u} \propto 1/r^3$	$\mathbf{u} \propto 1/r^2$	$\mathbf{u} \propto 1/r^2$
Example					

Table 2.1: Comparison of the squirmer parameter  $\beta$  and the far field decay of the velocity field  $\mathbf{u}$  for different swimmers. For reference we also include a passive colloid that is subject to Stokes drag due to gravity, see Eq. (2.10). The illustrations of the biological examples are taken from Ref. [33]. Red arrows indicate forces and black arrows indicate direction vectors  $\mathbf{e} = \mathbf{v}/|\mathbf{v}|$ .

a groove that runs around the equator of the cell and causes the cell to rotate about its swimming axis. The cell can change the direction of this rotation and thus tune its helical swimming path and perform chemotaxis [34]. Since the flagellum, which is responsible for propulsion, is at the back of the cell, *Gonyaulax* is a pusher. The protist cell *Blepharisma*, on the other hand, is completely covered with a carpet of beating cilia. Thus, in a coarse-grained picture there is no symmetry breaking between the front and the back of the cell, and  $\beta \approx 0$ . Finally, a typical example for a puller is the algae *Chlorophyta*, which propels itself with two beating flagella at the front. Here, the forward and backward strokes have to differ due to the scallop theorem, as discussed in Sect. 2.1.3.

Note that the squirmer parameter  $\beta$  does not only differentiate between pushers and pullers, but also influences the hydrodynamic interactions between swimmers or a swimmer and a bounding wall [32, 14, 35]. The interaction between two swimmers that swim next to each other is attractive if they are pushers and repulsive if they are pullers, see Fig. 2.1. Accordingly, pushers tend to orient parallel to a wall and pullers perpendicular. The viscosity of a dilute suspension of self-propelled particles also depends on  $\beta$  [36, 37, 38]. Pushers reduce the viscosity, while pullers increase it.

The squirmer model can also be employed to model artificial microswimmers. Particularly, the flow field of spherical Janus colloids can be matched to the squirmer flow field [39]. In general, Janus colloids are colloids with two distinct faces that differ in their physical or chemical properties [7]. There are various means to construct Janus colloids, which propel themselves through viscous liquids.

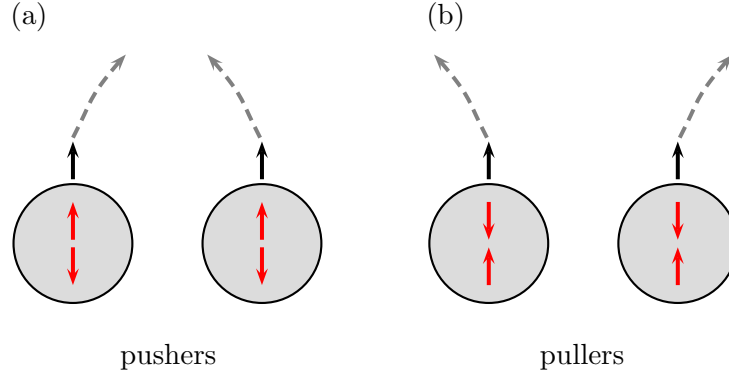


Figure 2.1: Interaction between sides of microswimmers. (a) Pushers experience an attractive interaction. Red arrows indicate forces, black arrows direction vectors, and dashed lines trajectories. (b) Pullers experience repulsive interaction.

For instance, one can construct a Janus colloid where one of the two faces catalyzes a chemical reaction and the reactants set up a self-diffusiophoretic flow, which propels the colloid [40]. Janus particles, where the thermal conductivity of both faces differs, can be heated, which generates a temperature gradient, in which the colloids move. This effect is called thermophoresis [39]. Also thinkable is the use of electrophoresis in combination with self-diffusiophoresis. Close to a bimetallic Janus particle in a peroxide solution, a electrochemical gradient is generated, which propels the colloid [41, 42]. Finally, in a binary solvent close to its critical point, the liquid around Janus colloids can demix locally, which induces a self-diffusiophoretic flow [43].

Alternatively, one can realize a squirmer by an active emulsion droplet. In contrast to a Janus colloid, active emulsion droplets are initially homogeneous in their physical and chemical properties. The symmetry between the two halves of the droplet breaks spontaneously. We will come back to this in Sect. 3.

## 2.2 Brownian motion

Having an understanding of how spherical active particles swim forward in a viscous environment, we now want to focus on their swimming trajectories. The squirmer, as we presented it in Sect. 2.1.4, can only swim along the  $z$ -direction. A straightforward way to let the squirmer change its swimming direction is to add forces  $\mathbf{f}$  to the Stokes equation (2.8). For instance a buoyancy force in  $x$ -direction would add a Stokeslet in  $x$ -direction to the presented solution (2.11). Note that the squirmer model can be generalized to account for an arbitrary surface velocity field  $\mathbf{u}|_R(\theta, \varphi)$ , [30]. Thus, by introducing a time-dependent  $\mathbf{u}|_R(\theta, \varphi, t)$ , which could represent the carpet of beating cilia, the squirmer swims in a time-dependent direction  $\mathbf{v}(t)$ . Alternatively one can explicitly model microswimmers and their swimming mechanism, *e.g.*, the rotating flagella of an

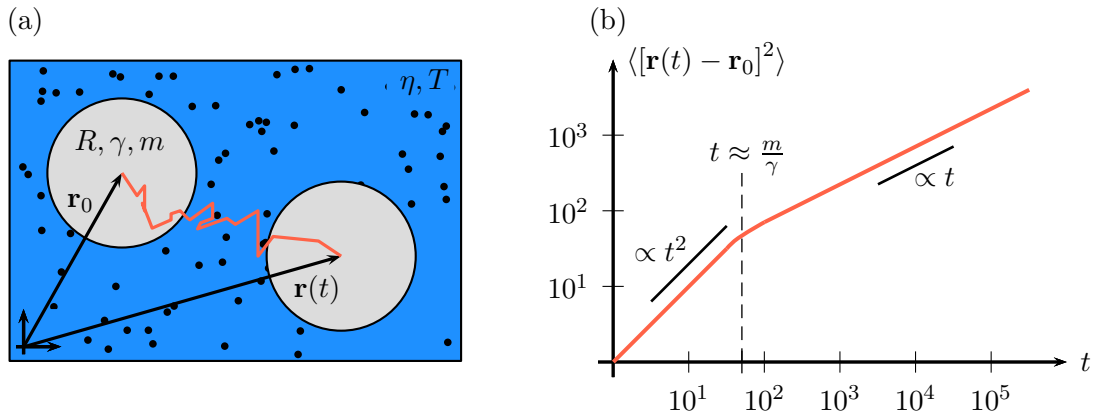


Figure 2.2: (a) Trajectory of a passive colloid from initial position  $\mathbf{r}_0 = \mathbf{r}(0)$  to position  $\mathbf{r}(t)$ . The colloid has radius  $R$ , drag coefficient  $\gamma$ , and mass  $m$ , and is immersed in a fluid with viscosity  $\eta$  and temperature  $T$ . Black dots indicate fluid particles which randomly kick the colloid. (b) Time-dependence of the mean squared displacement  $\langle [\mathbf{r}(t) - \mathbf{r}_0]^2 \rangle$  of the colloid in a log-log plot. The colloid moves ballistically until  $t \approx \frac{m}{\gamma}$  and diffusive afterwards.

*E. coli* bacterium [44], or the attached flagellum of an *African trypanosome* parasite [45, 46].

Another effect, which changes the orientation of microswimmers, is due to internal or external fluctuations. Here, we focus on the latter and discuss internal fluctuations in Sect. 2.3. External fluctuations, *i.e.*, thermal fluctuations of the surrounding fluid do not depend on the forward propulsion of the microswimmer. Therefore we first discuss it by means of a simple spherical colloid, which is immersed in a viscous fluid and subject to collisions with the fluid molecules, see Fig. 2.2 (a).

In what follows, we want to sketch the erratic motion of a spherical colloid in a fluid with temperature  $T$ . Such a motion is called Brownian motion [47]. Here, we assume that the motion is in 1D, a generalization to 2D or 3D is straightforward. We start by writing down Newton's second law for the velocity  $v(t) = \dot{r}(t)$  of a colloid with mass  $m$ :

$$m\dot{v}(t) = -\gamma v(t) + \zeta(t), \quad (2.13)$$

where  $\gamma v(t)$  is the drag force of the particle in the fluid. For a spherical colloid with radius  $R$  in a fluid with viscosity  $\eta$  the drag coefficient is given by  $\gamma = 6\pi\eta R$ , see Eq. (2.10). The second term,  $\zeta(t)$ , on the r.h.s. of Eq. (2.13) is the stochastic force due to collisions with fluid particles. These collisions vanish on average and are correlated on a short time scale:

$$\langle \zeta(t) \rangle = 0, \quad (2.14a)$$

$$\langle \zeta(t)\zeta(t') \rangle = 2\gamma k_B T \delta(t - t'). \quad (2.14b)$$

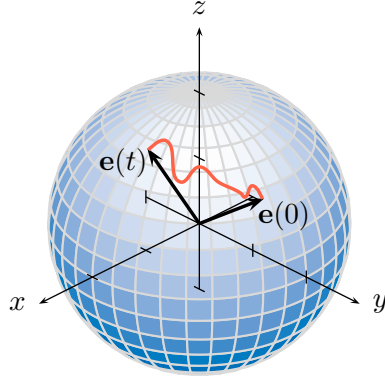


Figure 2.3: Rotational diffusion of the direction of an active Brownian particle from  $\mathbf{e}(0)$  to  $\mathbf{e}(t)$ .

The second relation is called fluctuation-dissipation theorem, as it connects the second moment of the fluctuations  $\langle \zeta^2 \rangle$  with the drag coefficient  $\gamma$ , *i.e.*, with the dissipation of the particle. Thus, apart from the material parameter  $\gamma$ , the strength of the fluctuations is set by the temperature  $T$  of the liquid.

Equation (2.13) can formally be integrated to find velocity  $v(t)$  and position  $r(t)$  of the particle, for initial speed  $v_0 = v(0)$  and position  $r_0 = r(0)$ . Of more interest is the mean squared displacement (MSD) w.r.t. the initial position  $r_0$ . It is given by [48]

$$\langle [r(t) - r_0]^2 \rangle = \left[ \frac{v_0 m}{\gamma} \left( 1 - e^{-\frac{\gamma}{m} t} \right) \right]^2 + \frac{2k_B T}{\gamma} \left[ t - \frac{2m}{\gamma} \left( 1 - e^{-\frac{\gamma}{m} t} \right) + \frac{m}{2\gamma} \left( 1 - e^{-\frac{2\gamma}{m} t} \right) \right]. \quad (2.15)$$

The MSD is ballistic with  $\langle [r(t) - r_0]^2 \rangle = v_0^2 t^2$  for  $t \ll \frac{m}{\gamma}$ . For  $t \gg \frac{m}{\gamma}$ , on the other hand, the MSD is diffusive with  $\langle [r(t) - r_0]^2 \rangle = c + 2dDt$ , where  $D = k_B T / \gamma$  is called diffusion constant and  $d$  the dimension, in which the motion takes place. Furthermore,  $c$  is constant in time. The MSD is also plotted in Fig. 2.2 (b). The interpretation is as follows. The colloid starts to move ballistically with velocity  $v_0$  and is not significantly disturbed by the individual fluid molecules. When  $t \approx \frac{m}{\gamma}$ , the ballistic motion has relaxed and the motion at later times is solely governed by the individual kicks of the fluid molecules.

Note that Brownian motion occurs in equilibrium. There is no external driving of the system. The motion of the colloid is only due to the finite temperature of the fluid.

## 2.3 Active Brownian particles

In contrast to a passive colloid, an active particle possesses an inherent velocity vector  $\mathbf{v}(t) = v(t)\mathbf{e}(t)$  with velocity  $v(t)$  and direction of motion  $\mathbf{e}(t)$  with  $|\mathbf{e}(t)| = 1$ . Thus, the trajectory of the swimmer is given by the integral  $\mathbf{r}(t) = \mathbf{r}_0 + \int_0^t dt' v(t') \mathbf{e}(t')$  with initial position  $\mathbf{r}_0$ .

Under the assumption of a constant velocity  $v$  one finds for the mean squared displacement

$$\langle [\mathbf{r}(t) - \mathbf{r}_0]^2 \rangle = v^2 \int_0^t dt' \int_0^{t'} dt'' \langle \mathbf{e}(t') \cdot \mathbf{e}(t'') \rangle . \quad (2.16)$$

Thus, to calculate the MSD of an active particle, one needs to know the auto-correlation function  $\langle \mathbf{e}(t') \cdot \mathbf{e}(t'') \rangle$  of the swimmer's direction. In the active Brownian particle model, the swimming direction  $\mathbf{e}(t)$  diffuses freely on the unit sphere [49, 50, 51], see Fig. 2.3. This can be described by the rotational diffusion equation

$$\partial_t p(\mathbf{e}, t) = D_r \nabla_s^2 p(\mathbf{e}, t) , \quad (2.17)$$

for the probability distribution  $p(\mathbf{e}, t)$ . Here  $\nabla_s = (\mathbf{1} - \mathbf{e}_r \otimes \mathbf{e}_r) \nabla$  is the surface gradient on the unit sphere and  $D_r$  the rotational diffusion constant. In this simple model, one finds for the orientational auto-correlation function [52, 53]

$$\langle \mathbf{e}(0) \cdot \mathbf{e}(t) \rangle = e^{-t/\tau_r} , \quad (2.18)$$

where the rotational correlation time  $\tau_r = 1/[(d-1)D_r]$  with dimension  $d \geq 2$  is the characteristic time it takes the swimmer to “forget” about the initial orientation  $\mathbf{e}(0)$ . Hence, for short times  $t < \tau_r$  the particle moves approximately in the direction of  $\mathbf{e}(0)$ , while at later times  $t > \tau_r$  the orientation becomes erratic. Together with Eq. (2.16) one finds for the MSD

$$\langle [\mathbf{r}(t) - \mathbf{r}_0]^2 \rangle = 2(v\tau_r)^2 \left( \frac{t}{\tau_r} - 1 + e^{-t/\tau_r} \right) . \quad (2.19)$$

By comparing this with the MSD of the passive particle, one notices the similar shape. For  $t \ll \tau_r$ , the active Brownian particle moves ballistic with velocity  $v$ , while for  $t \gg \tau_r$ , the motion becomes diffusive with  $\langle [\mathbf{r}(t) - \mathbf{r}_0]^2 \rangle = 2dDt$  and diffusion constant  $D = v^2\tau_r/3$ .

An alternative description to the rotational diffusion equation (2.17) is given by the Langevin equation

$$\partial_t \mathbf{e} = \sqrt{2D_r} \boldsymbol{\omega} \times \mathbf{e} , \quad (2.20)$$

for the direction vector  $\mathbf{e}$ . The random torque  $\boldsymbol{\omega}$  leads to a random rotation of  $\mathbf{e}$ . It fulfills

$$\langle \boldsymbol{\omega}(t) \rangle = 0 , \quad (2.21a)$$

$$\langle \boldsymbol{\omega}(t) \otimes \boldsymbol{\omega}(t') \rangle = \mathbf{1} \delta(t - t') , \quad (2.21b)$$

*i.e.*, it vanishes on average and is correlated on a short time scale. Furthermore, the components of  $\boldsymbol{\omega}$  are not cross-correlated.

We want to note that the origin of the random motion of an active Brownian particle can be manifold. As discussed in Sect. 2.2, the thermal fluctuations, which induce small translational kicks against the passive colloid, are only due to the temperature of the fluid. This is a pure equilibrium effect. The random torque  $\boldsymbol{\omega}$ , which induces a rotation

of the direction vector  $\mathbf{e}$  of an active particle, on the other hand, can also be connected with its internal swimming mechanism [54].

One should also keep in mind that the presented model of an active Brownian particle is highly idealized. In real systems, the rotational diffusion of  $\mathbf{e}$  is usually not perfectly isotropic due to interactions with obstacles, such as other particles, or walls. Furthermore, if the density of the particle does not match the fluid density, gravity has to be taken into account [55]. In general, the motion of an active swimmer is also subject to thermal translational fluctuations, as described for the passive particle in Sect. 2.2. However, for a sufficiently large velocity  $v$  of the swimmer, these become negligible. Finally, we assumed a constant velocity  $v$  of the swimmer. One can show that this is only a good approximation, if the (indeed always present) velocity fluctuations decay on a time scale  $\tau$  similar to  $\tau_r$  of Eq. (2.18) [56]. Otherwise, the MSD can have several regimes with different power laws.

## 3 The active emulsion droplet

In this section we want to narrow the focus down from microswimmers to active emulsion droplets. We begin with a definition of active emulsion droplets in Sect. 3.1 and discuss various applications in the growing field of microfluidics in Sect. 3.2. From a theoretical physicist's viewpoint, an active emulsion droplet is a closed fluid-fluid interface which moves w.r.t. to a lab frame due to the Marangoni effect. We therefore discuss fluid-fluid interfaces in detail in Sect. 3.3 and introduce the Marangoni effect in Sect. 3.4. Finally, in Sect. 3.5 we update the reader to the current state of research on active emulsion droplets.

### 3.1 Definition and distinction

We start with a definition of the central object of this work, the active emulsion droplet:

#### 'active'

As already pointed out in Sect. 2.3, active particles differ from passive particles by having an inherent velocity vector  $\mathbf{v}$ . Here, 'inherent' means that they have the ability to move on their own and do not require external or stochastic forces to do so. This also applies to active versus passive droplets. Here, the activity or the motion of active droplets arises from an inhomogeneous surface tension  $\sigma$  along the interface of the droplet. The resulting shear stress at the interface drags adjacent fluid layers in direction of increasing surface tension. This effect is called Marangoni effect and will be treated in Sect. 3.4. Active droplets rely on a supply of energy, such as a solvent which changes the surface tension of the fluid-fluid interface. They are therefore not in equilibrium, in contrast to *e.g.* the passive colloid, which we discussed in Sect. 2.2. Active droplets are also referred to as 'self-propelled droplets', 'self-driven droplets', or simply 'swimming droplets'.

#### 'emulsion'

An emulsion droplet is a liquid droplet immersed in a second liquid. In general, one distinguishes between droplets on interfaces and droplets immersed in a fluid. Droplets on interfaces sit either on a solid or a liquid interface. The top phase can be a gas or a liquid. Droplets immersed in a fluid are also either in gas or in liquid. In the latter case, the droplets are called emulsion droplets. A collection of many emulsion droplets is usually called emulsion. As a side note, gas droplets are called bubbles and a collection of many bubbles is usually called foam.

	passive	active
droplet on interface	<ul style="list-style-type: none"> <li>• friction <i>i.e.</i> lateral adhesion of sliding droplets [57]</li> <li>• spreading dynamics [58]</li> <li>• wettability of surfaces and polymers [59, 60]</li> </ul>	<ul style="list-style-type: none"> <li>• light-induced Marangoni propulsion [61, 20]</li> <li>• Marangoni driven spreading [62, 63]</li> </ul>
emulsion droplet	<ul style="list-style-type: none"> <li>• droplet formation, breakup, and coalescence</li> <li>• lab-on-a-chip operations [9]</li> <li>• effect of surfactants on velocity of sinking droplets [64]</li> <li>• shape of raindrops in flow [65]</li> <li>• drop deformation in flow [66]</li> <li>• mixing within droplets [67]</li> </ul>	<ul style="list-style-type: none"> <li>• swimming bifurcation</li> <li>• swimming trajectories</li> <li>• pattern formation on droplet interface</li> <li>• light-induced Marangoni propulsion</li> </ul>

Table 3.1: Common classification of liquid droplets and some exemplary research topics. This work focuses on active emulsion droplets (blue part in the table).

### ‘droplet’

The term droplet is a diminutive of ‘drop’. It is usually used for drops with diameters up to  $500\mu\text{m}$ . Sometimes the term ‘liquid colloid’ is used instead.

In Table 3.1, we list a few common research topics of liquid droplets. An in-depth discussion of the current state of research of active emulsion droplets (blue part in Table 3.1) is given in Sect. 3.5.

## 3.2 Microfluidics

Similar to the advancements in the 1950s in microelectronics, in the 1980s the multidisciplinary field of microfluidics emerged. Here, the goal is to miniaturize biological, chemical, and medical processes in fluids to the microscale. The implications of miniaturization to the physics of fluids have already been discussed in Sect. 2.1: Fluid motion on the microscale takes usually place in the low Reynolds number regime, where the linear and time-reversible Stokes equation (2.8) holds. A certain analogy to microelectronics can not be denied. However, while a microchip combines independent electronic components through conducting paths on a single plate of a semiconductor, a lab-on-a-chip in microfluidics combines several microfluidic devices through microchannels on a single piece of a moldable elastomeric polymer.

Emulsion droplets play a key role in microfluidics. Ref. [9] summarizes various digital fluidic operations and applications of droplet-based microfluidics. Basic operations are droplet generation, transport, fusion, fission, mixing, and sorting of droplets. A key

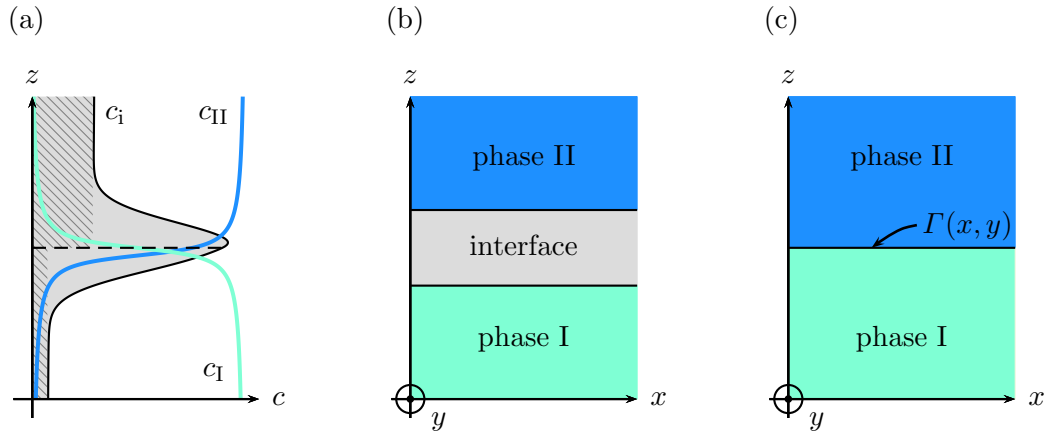


Figure 3.1: Coarse-graining of a fluid-fluid interface from (a) a full 3D description of the interface with volume concentration  $c_i(\mathbf{r})$  of surfactants to, (b) an interface with finite thickness to, (c) an idealized interface with zero thickness and excess concentration of surfactants per area  $\Gamma(x, y)$ .

application of droplet microfluidics is the realization of chemical reactions inside emulsion droplets. Reactants are either dissolved in the droplet fluid or again encapsulated in smaller emulsion droplets inside the droplet. By carefully timing the droplet breakup of the sub-droplets, it is possible to exactly trigger the reaction. Such a system is sometimes called a microreactor [10]. These “matryoshka droplets”, *i.e.*, hierarchically encapsulated emulsion droplets are also widely used in the synthesis of biomolecules [9]. Some day this might lead the way to an old dream of scientist: the self-assembly of artificial living cells.

In the future, digital fluidic operations might lead to computers, which consist of moving droplets. As a matter of fact, it was recently possible to couple magnetic and hydrodynamic interaction forces between droplets to develop logic gates such as AND, OR, XOR, as well as a flip-flop [68]. Usually these digital fluidic operations are carried out by passive emulsion droplets. A possible next step is to extend these tools to active emulsion droplets. This could also be of interest in drug release applications [11, 12].

### 3.3 The fluid-fluid interface

An understanding of the fluid-fluid interface is crucial in the study of emulsion droplets, which is why we discuss such interfaces in detail in this section. Albeit we have a liquid-liquid interface in mind, the theory of this section holds for fluid-fluid interfaces in general. Figure 3.1 (a) shows a cut through a typical fluid-fluid interface. The interface is characterized by sigmoidal concentration profiles  $c_I$  and  $c_{II}$  of the two components that make up the two phases, *e.g.*, water and oil. Additionally, interfaces are often stabilized by surface active molecules, co-called surfactants. These have the concentration  $c_i$  in Fig. 3.1 (a). Here we assume, without loss of generality, that the surfactants are hardly soluble

in phase I, highly soluble in phase II, but above all favor the interface. The tendency to favor interfaces is typical for amphiphilic surfactants, which possess a hydrophilic and a hydrophobic side. In Sect. 3.3.2 we discuss surfactants in detail.

In the following sections we ignore the finite width of the fluid-fluid interface and instead idealize it as a sharp interface. This concept of an interface with zero thickness is called Gibbs diving surface. Figure 3.1 (b)-(c) shows the coarse-graining of the fluid-fluid interface of Fig. 3.1 (a). This approach is very convenient in studies of the surfactant dynamics at the interface as it allows to reduce the volume concentration of surfactants  $c_1(\mathbf{r})$  to an excess concentration per area  $\Gamma(x, y)$ . This is the excess over what would be present if the bulk concentration continued all the way to the interface, *i.e.* the excess over the shaded area in Fig. 3.1 (a). In the following, we call the excess concentration  $\Gamma$  of surfactants at the interface simply the “surfactant concentration”.

Note that the coarse-graining to a Gibbs diving surface, which we depicted in Fig. 3.1, can also be done for curved interfaces.

### 3.3.1 Surface tension

A central physical quantity of a fluid-fluid interface is its surface tension. It plays a key role in understanding many related fundamental effects. In general, the surface tension is a property of liquids caused by intermolecular attraction, which makes them minimize their surface area. In the following we use the term surface tension also for interfaces between liquids.

Let us assume a film of water in an open container. The individual water molecules are held together by an attractive potential, *e.g.*, a Lennard-Jones potential  $U(r)$  as depicted in the lower panel of Fig. 3.2 (a). This phenomenon is known as cohesion. At the interface, however, water molecules have fewer neighboring molecules, which puts them in a higher energy state. The top panel of Fig. 3.2 (a) shows a simplistic sketch of the situation. Thus, by increasing the interface of the liquid film, the number of molecules in the higher energy state increases, which leads to a higher total energy of the film. The surface tension  $\sigma$  is then defined as the ratio of the change in the energy of the liquid, and the change in the surface area of the liquid. It is measured in energy per area or force per length:  $[\sigma] = \text{N/m}$ .

In equilibrium thermodynamics surface tension is usually formulated in the grand canonical ensemble. Its thermodynamic variables are temperature  $T$ , volume  $V$ , and chemical potential  $\mu$ . The corresponding energy potential is called grand potential  $\Omega = \Omega(T, V, \mu)$ . However, since the system under consideration is an interface, the variable  $V$  is replaced by area  $A$ . The total differential of the grand potential for a surface is given by:

$$d\Omega = -SdT + \sigma dA - Nd\mu, \quad (3.1)$$

with surface tension

$$\sigma = \left. \frac{\partial \Omega}{\partial A} \right|_{T, \mu}. \quad (3.2)$$

Thus, surface tension measures the increase of energy  $\Omega$  with increasing area  $A$ , while temperature  $T$  and chemical potential  $\mu$  are held constant. In the simple case of a clean

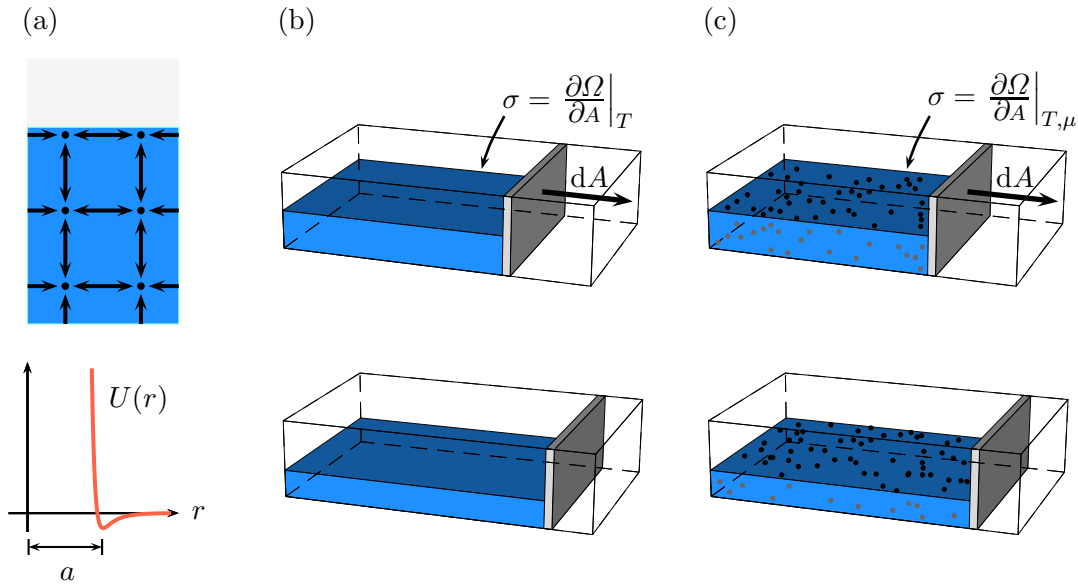


Figure 3.2: (a) Top: sketch of water molecules at a water-air interface. Bottom: Lennard-Jones interaction potential  $U(r)$  between water molecules. (b) Illustration of a water film with variable interface area  $A$ . (c) Illustration of a surfactant-laden water film with variable interface area  $A$ .

interface without surfactants, *i.e.*  $N = 0$ , one finds  $\sigma = \frac{\partial \Omega}{\partial A} \Big|_T$ , which is illustrated in Fig. 3.2 (b). However, the reason for using  $\Omega$  to define  $\sigma$  in the first place, instead of *e.g.* the Helmholtz free energy  $F$ , is that  $\Omega$  allows particle exchange, *i.e.*, adsorption and desorption of surfactants. It is therefore the natural choice for fluid-fluid interfaces, which are in contact with surfactant enriched phases.

### 3.3.2 Surfactants

Surfactants (**surface active agents**) are molecules which accumulate at fluid-fluid interfaces and lower the surface tension. They are amphiphilic, *i.e.*, they consist of a hydrophilic (water-soluble) head and a hydrophobic (water-insoluble) tail. Therefore, when a surfactant diffuses to the proximity of a fluid-fluid interface, such as water-air or water-oil, it will readily adsorb and then stay at the interface. The lowering of surface tension  $\sigma$  can be understood as follows.

Due to their amphiphilic nature, surfactants are in a lower energy state when adsorbed at an interface compared to the bulk. This leads to the following thought experiment. A liquid film is enriched with surfactants and kept at a constant temperature  $T$ . Thus, the interface of the film is coupled to a reservoir of surfactants with chemical potential  $\mu$ . Figure 3.2 (c) illustrates the situation. Upon increasing the interface area, more surfactants can migrate to the interface and thus reach a state of lower energy. This

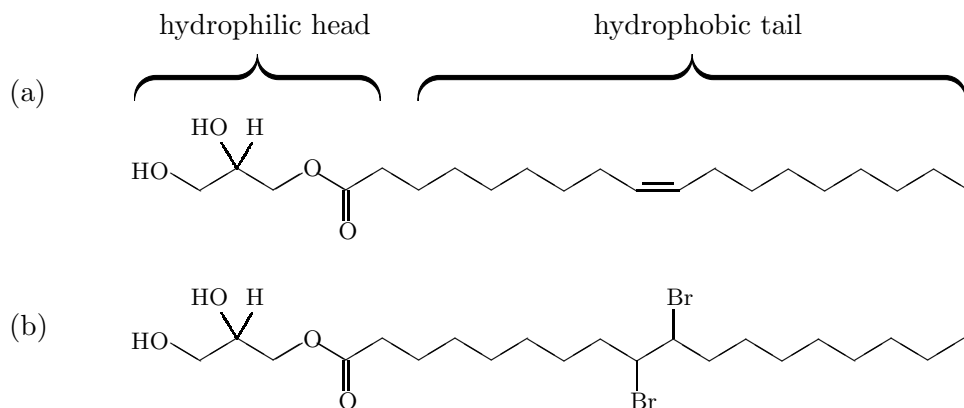


Figure 3.3: (a) Surfactant molecule monoolein with hydrophilic head and a hydrophobic tail. (b) Monoolein molecule after halogen addition reaction with bromine.

effect counteracts the general mechanism of energy cost to establish the interface. Thus, compared to the case without surfactants in Fig. 3.2 (b), increasing the interface has a less pronounced effect on the energy of the interface. Thus, the surface tension  $\sigma$ , which measures the effect of increasing area  $A$  on energy  $\Omega$  [compare Eq. (3.2)] is lower when surfactants are present:

$$\frac{\partial \sigma}{\partial \Gamma} < 0, \quad (3.3)$$

with surface concentration  $\Gamma$  of surfactants. In Sect. 3.3.5 we use the definition (3.2) of the surface tension  $\sigma$  to derive this relation. Note that  $\sigma$  remains always positive, regardless of the bulk concentration of surfactants, or else the interface would be destroyed by small fluctuations.

There is a plethora of different surfactants which mainly differ by their hydrophilic head. Most head groups are either anionic, cationic, or nonionic. Fig. 3.3 (a) shows a typical nonionic surfactant called monoolein. It is one of the most important surfactants in many applications such as emulsion stabilization, drug delivery, and protein crystallization [69]. The hydrophilic head consists of glycerol with two hydroxyl groups. Thus, the head of the surfactant is polar and can form hydrogen bonds with water. The C18 alkyl tail features a double bond in the middle and is strongly hydrophobic [70]. In Sect. 3.3.3 we discuss a chemical reaction that changes the structure of the hydrophobic tail and with that the surface tension of monoolein. Note that monoolein is soluble in oil but insoluble in water.

In general, surfactants play a crucial role in living cells as well as in industrial applications such as cosmetics, foam, and in the food industry [71]. Surfactants also act as oil dispersants in the fracking industry or after an oil spillage to break the oil layer into small droplets. Apart from these applications, surfactants are interesting objects from a physicist's viewpoint since they have the tendency to form self-organized aggregates at high densities. Figure 3.4 (a) shows the simplest structure: a micelle with hydrophobic

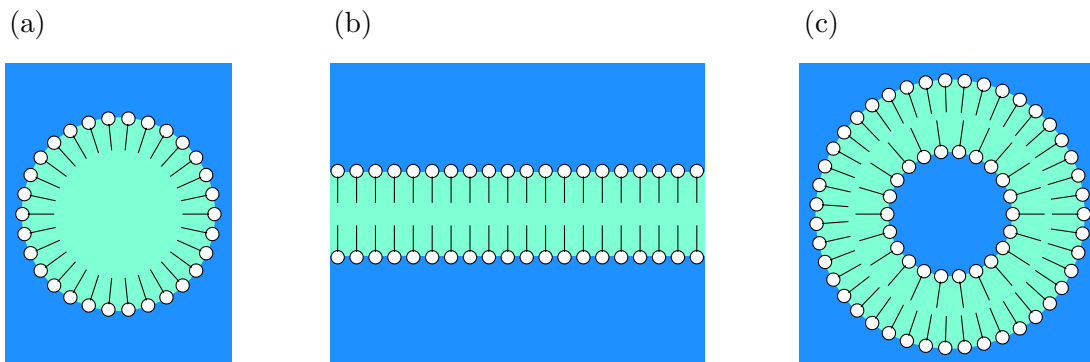


Figure 3.4: Example structures formed by surfactants: (a) micelle, (b) bilayer, and (c) spherical liposome.

tails inside. Micelles, where the tails point outwards, are called inverse micelles. Micelles are formed above the critical micelle concentration  $c_{CMC}$ . For instance, monoolein molecules form micelles at  $c \geq c_{CMC} = 1\text{mM/l}$ . Other possible structures are bilayers or liposomes as shown in Fig. 3.4 (b), and (c), respectively. Surfactants have very rich phase diagrams which include, in addition to the mentioned structures above, cylindrical micelles, lamellar, hexagonal, and cubic phases [69].

There are various possibilities to change the “surface tension of surfactants”. Here and in the following, when we speak of the “surface tension of a surfactant”, we mean the surface tension of an oil-water interface, which is completely covered by the surfactant. By increasing the temperature of a surfactant layer, the surface tension decreases approximately linearly [72]. Furthermore, many surfactants react with reactants that are dissolved in the adjacent fluid layers. This can also change the surface tension. This will be discussed in the following section. Other surfactants are light sensitive, *i.e.*, they change their surface tension when illuminated with light of a specific wavelength. In Sect. 3.3.4 we dwell on these so-called photosurfactants.

### 3.3.3 Bromination reaction

The effect of surfactants on the surface tension of a fluid-fluid interface is due to their amphiphilic structure. Thus, by changing the structure of head or tail of a surfactant, it should be possible to increase or decrease its surface tension. In the case of monoolein this is possible by adding the halogen bromine to one of the adjacent fluid layers [8]. Figure 3.3 (b) shows the structure of a monoolein molecule after it has reacted with a bromine molecule. By comparing with the pristine monoolein surfactant in Fig. 3.3 (a), one notices that the bromine molecule reacted with the carbon-carbon double bond in the hydrophobic tail. Such a reaction is called halogen addition reaction and the corresponding chemical formula reads:



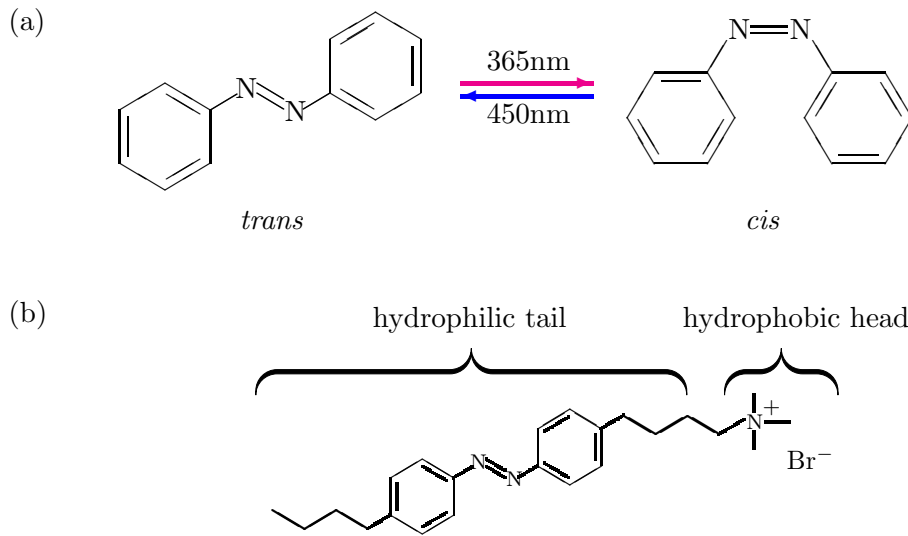


Figure 3.5: (a) Photo-isomerization of azobenzene. The *trans* state can be converted to the *cis* state by using ultraviolet light with wavelength 365nm. Blue light (450nm) can be used to convert the molecule back to the *trans* state. (b) AzoTAB surfactant in the *trans* state.

The actual reaction mechanism of the “bromination” reaction is rather complex [73]. The result is a saturated C–C bond, which weakens the hydrophobic nature of the alkyl chain of the surfactant. Experiments showed that the surface tension of a droplet interface covered with monoolein increases from 1.3 to 2.7mN/m [8].

As we will discuss in detail in Sect. 3.4, an inhomogeneous surface tension  $\sigma$  at a fluid-fluid interface causes the adjacent fluid layers to be pulled in direction of  $\nabla_s \sigma$ . This effect is known as Marangoni effect. Thus, a monoolein covered interface which is locally in contact with a supply of bromine, will experience Marangoni flow. Ref. [8] uses the Marangoni effect to create active emulsion droplets. We will elaborate on this in detail in Sect. 4.2.

### 3.3.4 Light sensitive surfactants

Changing the surface tension of a surfactant by means of a chemical reaction with a reactant relies on diffusion or advection of the reactant to the interface. It is therefore difficult to change the surface tension in a spatially controlled manner with *e.g.* bromine. However, there are other surfactants which change their structure and thereby their surface tension, when illuminated with light. For instance, the photosurfactant AzoTAB uses the *trans-cis* isomorphism of azobenzene to change its surface tension under illumination [74, 75, 61, 76, 77].

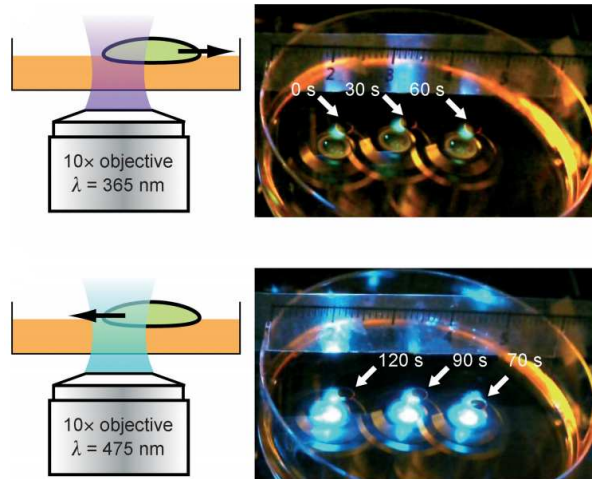


Figure 3.6: A droplet on an interface is first pushed with UV light (top panel) and then pulled back with blue light (bottom panel). Taken from Ref. [20].

Figure 3.5 (a) depicts the azobenzene molecule and its *trans-cis* isomorphism. Azobenzene is a molecule composed of two phenyl rings which are connected by a N=N double bond. When illuminated with UV light, the N=N double bond changes its orientation from *trans* to *cis* state. Note that the two states have exactly the same atoms but in a different arrangement. The *trans* state is the thermodynamically stable state of the molecule and the *cis* molecule falls back into it within about an hour. Alternatively, the *cis* molecule can be transformed back by using blue light. Photoisomerizable molecules or so-called smart molecules play an important role in rewritable optical data storage, such as CDs or DVDs [78].

The surfactant AzoTAB is synthesized by adding alkyl chains to both sides of the azobenzene molecule and a trimethylammonium hydrophobic head group to one end [79], see Fig. 3.5 (b). Thus, the *trans-cis* isomorphism modifies the hydrophobic tail of the surfactant as in the case of the bromination reaction of monoolein, discussed in the previous section. The tail of the *cis* molecule is more polar, *i.e.*, more water-like or less hydrophobic than the *trans* molecule. Thus, the surface tension  $\sigma$  is higher in the *cis* state of AzoTAB. The surface tension is around 7mN/m in the *trans* state, and around 8mN/m in the *cis* state, respectively [20].

The photoisomorphism of AzoTAB can be utilized to generate light-driven Marangoni flow. This effect was first used by Diguët *et al.* in the group of D. Baigl in Paris to induce the motion of droplets [20]. Here, the oil droplets are placed on an aqueous interface. Figure 3.6 shows the reversible motion of a droplet due to partial illumination with UV light and blue light, respectively. Note that the motion of the droplet is only due to the local illumination and not due to local heating of the interface.

Photosensitive surfactants have also been used to fragment a continuous liquid stream into droplets [80], to design an optofluidic mixer [81], and to fuse droplets [82]. Ref. [83] reviews light-driven microfluidics.

Ichikawa *et al.* also studied light-induced droplet motion [84]. They, however, used a slightly different setup, where an oil droplet on water is pushed or pulled with green laser light. Here the direction of motion depends on the presence of surfactants in the aqueous solution. In contrast to the Baigl system, heat plays a crucial role in the driving of the droplet.

### 3.3.5 Interfacial equation of state

In the previous sections, we discussed how the surface tension of a fluid-fluid interface is modulated by surfactants. In general, the presence of surfactants lowers the surface tension, but by using either bromine in the case of monoolein or UV light in the case of AzoTAB the surface tension can be increased again. In order to simulate surfactant laden interfaces properly it is crucial to have a qualitative understanding of their surface tension. Thus, we seek an expression for the surface tension as a function of surfactant concentrations, a so-called interfacial equation of state. Usually an equation of state  $\sigma(\Gamma)$  is achieved from an adsorption isotherm, *i.e.* an equation that relates surface concentration  $\Gamma$  to bulk concentration  $c$ . We want to follow a different approach by first setting up a microscopic model for the surfactants at the interface. This allows us to model surfactant diffusion in a thermodynamically consistent way in Sect. 3.3.6, [85].

In the following we derive the equation of state for a single surfactant type. A generalization to a mixture of surfactants (*e.g.* pristine and brominated surfactants) can be found in Sect. 4.2. Note that the equation of state is defined in thermal equilibrium. We start by writing down the Helmholtz free energy  $F = E - TS$  for a surfactant-laden fluid-fluid interface of area  $A$ . Here,  $T$  is the temperature,  $E$  is the surfactant internal energy including interaction energy, and  $S$  the mixing entropy of the surfactants at the interface. In the following model, we consider an ideal mixture of surfactants and therefore set  $E = 0$ . A more elaborate system, which takes surfactant interactions into account, can be found in Sect. 4.2. The mixing entropy is calculated from the multiplicity  $\Omega_M$ ,

$$S = k_B \ln \Omega_M = -N_{\text{tot}} k_B [\Gamma \ln \Gamma + (1 - \Gamma) \ln(1 - \Gamma)] ,$$

with surface excess concentration  $\Gamma = N/N_{\text{tot}}$ , which relates the actual number of surfactants  $N$  to the maximum number of surfactants  $N_{\text{tot}} = A/\ell^2$  at the interface. Here,  $\ell^2$  is the area of a surfactant molecule at the interface. The free energy takes the form

$$F = N_{\text{tot}} k_B T [\Gamma \ln \Gamma + (1 - \Gamma) \ln(1 - \Gamma)] .$$

For non-ideal, *i.e.*, dense systems, a surfactant interaction term  $E = \epsilon \Gamma^2$  has to be added. We define the free energy density as  $f = F/A$  or:

$$f = \frac{k_B T}{\ell^2} [\Gamma \ln \Gamma + (1 - \Gamma) \ln(1 - \Gamma)] . \quad (3.5)$$

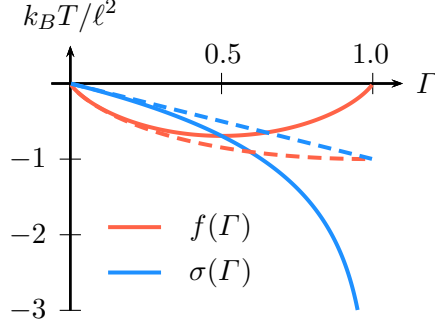


Figure 3.7: Free energy density  $f(\Gamma)$  and interfacial equation of state  $\sigma(\Gamma)$  from Eq. (3.5) and Eq. (3.8), respectively. Here we set  $\sigma_0 = 0$ . The dashed lines show the dilute limit  $\Gamma \ll 1$ , *i.e.*, Eqs. (3.10) and (3.11). Note that the diffusive and advective dynamics of the surfactant laden interface, which we discuss in Sect. 3.3.6, only depend on derivatives of  $f(\Gamma)$  and  $\sigma(\Gamma)$ , respectively. The absolute values of  $f(\Gamma)$  and  $\sigma(\Gamma)$  are therefore irrelevant.

We will use this expression in Sect. 3.3.6 to derive the diffusive dynamics of surfactants at the interface.

The surface tension  $\sigma$  was defined in Sect. 3.3.1 in terms of the grand potential  $\Omega(T, A, \mu)$ , which is related to  $F = F(T, A, N)$  by the Legendre transformation

$$\Omega = F - \frac{\partial F}{\partial N} N. \quad (3.6)$$

However,  $\Omega$  also follows from the Euler relation  $U = TS + \sigma A + \mu N$ ,

$$\Omega = \Omega_0 + \sigma A, \quad (3.7)$$

where we used the fact that the interface is in thermal equilibrium, *i.e.*, the surface tension  $\sigma$  is homogeneous, and that  $T$  and  $\mu$  are intensive. Thus, using (3.6) in (3.7) yields:

$$\sigma = \frac{\Omega - \Omega_0}{A} = \frac{F}{A} - \frac{\partial F}{\partial N} \frac{N}{A} - \frac{\Omega_0}{A} = \sigma_0 + f - \frac{\partial f}{\partial \Gamma} \Gamma,$$

with  $\sigma_0 = -\Omega_0/A$ . For the ideal free energy density (3.5) one finds the equation of state:

$$\sigma = \sigma_0 + \frac{k_B T}{\ell^2} \ln(1 - \Gamma). \quad (3.8)$$

Figure 3.7 shows  $\sigma(\Gamma)$  together with the corresponding free energy density  $f(\Gamma)$  from Eq. (3.5). Hence, the surface tension is at its maximum for a clean, *i.e.*, surfactant-free interface  $\sigma(\Gamma = 0) = \sigma_0$  and decreases with increasing surfactant concentration  $\Gamma$ :

$$\frac{\partial \sigma}{\partial \Gamma} = \frac{k_B T}{\ell^2} \frac{1}{\Gamma - 1} < 0, \quad 0 \leq \Gamma < 1. \quad (3.9)$$

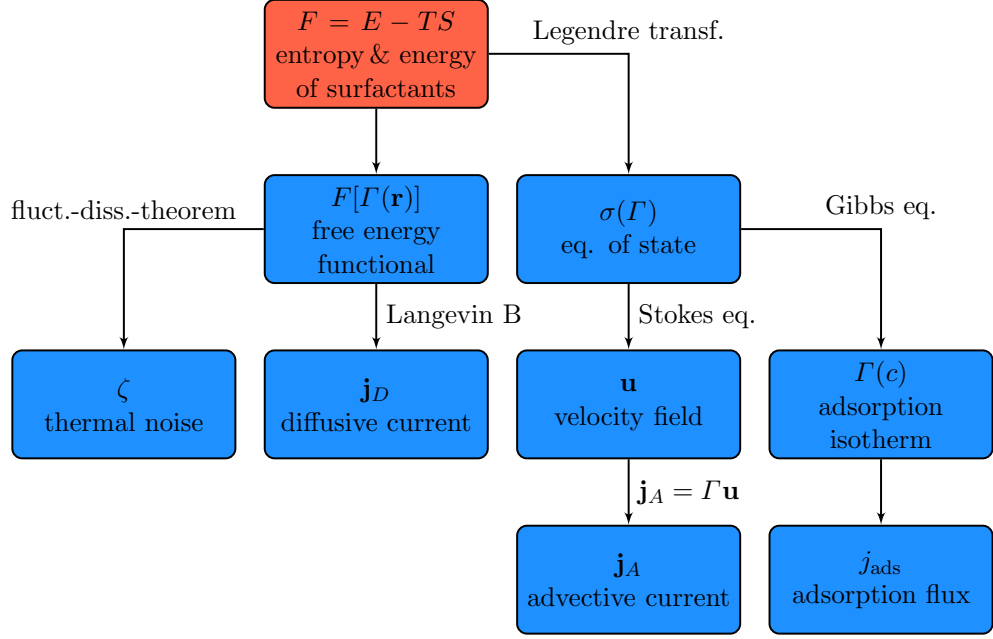


Figure 3.8: Derivation of thermal noise, diffusion, advection, and adsorption terms in the dynamic equation for the surfactant density  $\Gamma$  at a fluid-fluid interface.

Thus, as illustrated in Sect. 3.3.2, surfactants lower the surface tension of fluid-fluid interfaces. Equation (3.8) is called Szyszkowski equation [13]. It is the basis for various complex models of the surface tension of surfactant laden fluid-fluid interfaces [86]. Note that Eq. (3.8) breaks down for  $\Gamma \rightarrow 1$ .

In the dilute limit  $\Gamma \ll 1$ , the free energy density (3.5) simplifies to

$$f = \frac{k_B T}{\ell^2} \Gamma (\ln \Gamma - 1), \quad (3.10)$$

and the surface tension becomes

$$\sigma = \sigma_0 - \frac{k_B T}{\ell^2} \Gamma, \quad (3.11)$$

or  $\sigma A \sim -N k_B T$  which is reminiscent of the ideal gas law  $pV = N k_B T$ . In Fig. 3.7, we plot the dilute limit of  $f(\Gamma)$  and  $\sigma(\Gamma)$  as dashed lines.

### 3.3.6 Diffusion-Advection-Reaction equation

In this section we formulate a dynamic equation for the surfactant density  $\Gamma$  at a fluid-fluid interface. The physical processes that we take into account are (i) diffusion, (ii) advection within the interface, (iii) adsorption/desorption from/to the bulk, (iv) chemical reactions, and (v) thermal noise. The evolution of the interfacial surfactant concen-

tration is governed by the following equation [87, 13]:

$$\frac{\partial \Gamma}{\partial t} = \nabla_s \cdot (\mathbf{j}_D + \mathbf{j}_A) + j_{\text{ads}} + j_{\text{react}} + \zeta . \quad (3.12)$$

Here  $\nabla_s = (\mathbf{1} - \mathbf{n} \otimes \mathbf{n})\nabla$  is the surface gradient and  $\mathbf{n}$  the surface normal. The terms in the bracket are interfacial diffusion current  $\mathbf{j}_D$  and interfacial advection current  $\mathbf{j}_A$ , while  $j_{\text{ads}}$  and  $j_{\text{react}}$  are the flux of adsorption (desorption) from (to) the bulk and the change of  $\Gamma$  due to a chemical reaction, respectively. The last term  $\zeta$  incorporates thermal noise. The groundwork for defining  $\zeta$ ,  $\mathbf{j}_D$ ,  $\mathbf{j}_A$ , and  $j_{\text{ads}}$  has been laid in the previous section in form of the free energy  $F$ . The flow chart in Fig. 3.8 gives a preview of the procedure. In the following we discuss the individual terms.

## Diffusion

In the previous sections we considered a fluid-fluid interface in thermal equilibrium. This implies that the surface tension  $\sigma$  is homogeneous. However, the various physical models that we want to lay the groundwork for all deal with inhomogeneous concentrations  $\Gamma$  of surfactants, and hence with inhomogeneous surface tensions  $\sigma$ . Therefore, these models are inherently in non-equilibrium. As a result, Marangoni flow, *i.e.*, fluid flow due to an inhomogeneous surface tension will emerge at the interface. This will be covered in Sect. 3.4 in detail. Another consequence of surfactant concentration gradients is interfacial diffusion. It can be quantified as follows.

In non-equilibrium, the surface excess concentration  $\Gamma$  depends both on position and time [88]. Hence, the free energy  $F$  becomes a functional of  $\Gamma(\mathbf{r}, t)$ :

$$F[\Gamma(\mathbf{r}, t)] = \int f(\Gamma) \, dA , \quad (3.13)$$

with free energy density  $f(\Gamma)$  from Eq. (3.5). Note that for more complicated forms of  $f(\Gamma)$ , *e.g.*, a double well potential, a term which penalizes boundaries between regions of different  $\Gamma$  within the interface has to be added. Such a term usually has the form  $(\nabla_s \Gamma)^2$  [88].

The diffusion equation for surfactants at the interface can be written as a continuum equation

$$\frac{\partial \Gamma}{\partial t} - \nabla_s \cdot \mathbf{j}_D = 0 . \quad (3.14)$$

The diffusive current is connected to the free energy functional (3.13) via

$$\mathbf{j}_D = -\lambda \nabla_s \mu , \quad (3.15)$$

with chemical potential  $\mu = \frac{\delta F}{\delta \Gamma}$  and mobility  $\lambda$ , which, in general, is a function of concentration  $\Gamma$ . Such a dynamics for a conserved quantity is called Langevin model B. It is widely used to model separating phases of binary mixtures [88]. For the free energy functional (3.13), we find

$$\mathbf{j}_D = -\lambda \nabla_s \frac{\delta F}{\delta \Gamma} = -\lambda \nabla_s f'(\Gamma) = -\lambda f''(\Gamma) \nabla_s \Gamma . \quad (3.16)$$

The resulting diffusion equation is then

$$\frac{\partial \Gamma}{\partial t} = \nabla_s \cdot [\lambda f''(\Gamma) \nabla_s \Gamma] = \nabla_s \cdot \left[ \frac{\lambda}{\Gamma(1-\Gamma)} \nabla_s \Gamma \right].$$

Here, we used the free energy density  $f(\Gamma)$  of the ideal mixture from (3.5) in the second step. Note that the prefactor  $(\Gamma - \Gamma^2)^{-1}$  diverges for  $\Gamma \rightarrow 0$  and  $\Gamma \rightarrow 1$ . However, in the dilute limit  $\Gamma \rightarrow 0$ , one expects linear, or ‘‘Fickian’’, diffusion with  $\partial_t \Gamma \propto \nabla_s^2 \Gamma$ . To account for this one sets  $\lambda = D_i \Gamma$  and finds for  $\Gamma \ll 1$  linear diffusion with

$$\frac{\partial \Gamma}{\partial t} = D_i \nabla_s^2 \Gamma,$$

and interfacial diffusion constant  $D_i$ .

In Ref. [17], which is given in Sect. 4.2, we extend the presented procedure to mixtures of brominated and non-brominated surfactants. Since we assume the interface to be fully covered with surfactants, we have to include energetic interactions between surfactants in the free energy density.

### Advection

Another interfacial transport process is advection, *i.e.*, transport of surfactant density  $\Gamma$  due to tangential fluid flow at the interface. The origin of the interfacial flow  $\mathbf{u}_i$  can be the bulk flow  $\mathbf{u}$  of an adjacent liquid layer or flow that is generated by the interface itself. The latter is the case if the surface tension is inhomogeneous, *i.e.*,  $\sigma = \sigma(\mathbf{r})$ , which induces Marangoni flow. For the time being we assume that the flow field  $\mathbf{u}_i$  is known. The resulting surfactant advection current is given by

$$\mathbf{j}_A = \Gamma \mathbf{u}_i.$$

Thus, the dynamics due to diffusion and advection is governed by the continuum equation (3.14) with the diffusive current replaced by  $\mathbf{j}_D + \mathbf{j}_A$ .

When surfactants are present at the interface, they are also present in one or both of the surrounding bulk phases. The corresponding continuum equation for the bulk concentration  $c$  of surfactants is given by

$$0 = \frac{\partial c}{\partial t} + \nabla \cdot (c \mathbf{u}) = \underbrace{\frac{\partial c}{\partial t} + \nabla c \cdot \mathbf{u}}_{\frac{Dc}{Dt}} + c \nabla \cdot \mathbf{u}, \quad (3.17)$$

where we omit diffusion for the time being. Thus, Eq. (3.17) illustrates that in incompressible fluids with  $\nabla \cdot \mathbf{u} = 0$  the material derivative vanishes,  $\frac{Dc}{Dt} = 0$ , and the concentration stays constant within a flowing fluid parcel. Throughout this thesis we assume that all fluids are incompressible, see also the derivation of the Navier-Stokes equation in Sect. 2.1. Therefore, for advection equations in bulk, the term  $\nabla \cdot (c \mathbf{u})$  can be written as  $\nabla c \cdot \mathbf{u}$ .

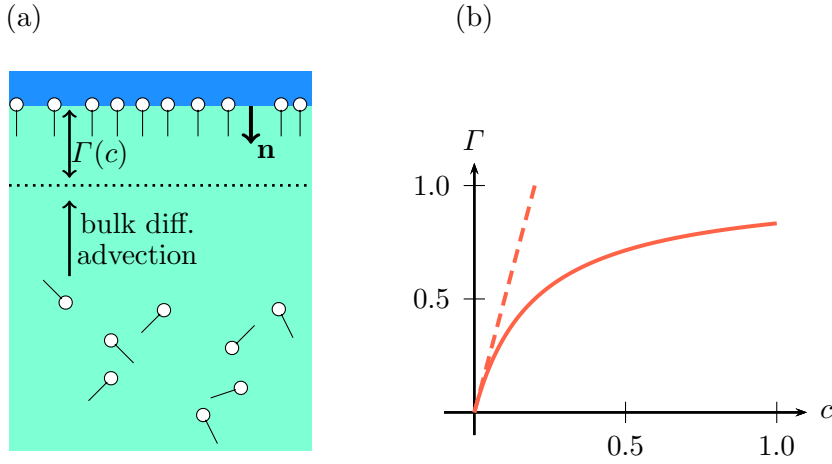


Figure 3.9: (a) Illustration of the two-step adsorption process. In a first step surfactants are transported via diffusion and/or advection to the adsorption layer. At the adsorption layer, surfactants aggregate at the interface. The surface concentration  $\Gamma$  is connected to the concentration  $c$  in the adsorption layer via an adsorption isotherm  $\Gamma = \Gamma(c)$ . (b) Adsorption isotherms. Solid line shows Langmuir adsorption, *i.e.*, Eq. (3.22), dashed line shows Henry adsorption, *i.e.*, Eq. (3.23). Parameters are  $b = 1/a = 5$ .

However, in the diffusion-advection-reaction equation (3.12), the surface divergence  $\nabla_s \cdot$  acts on  $\mathbf{j}_A$ . While, the incompressibility condition  $\nabla \cdot \mathbf{u} = 0$  also holds at the interface, it does not hold for the surface divergence. It is therefore not possible to rewrite the term  $\nabla_s \cdot (\Gamma \mathbf{u}_i)$  as  $\nabla_s \Gamma \cdot \mathbf{u}_i$ . This is owed to the fact that fluid can flow away and towards the interface from the bulk. In other words, the surfactant density  $\Gamma$  at the interface is not conserved, since surfactants can adsorb and desorb from and into the bulk. This is expressed by the flux  $j_{\text{ads}}$  in Eq. (3.12). In Ref. [19], which is given in Sect. 4.3, we show that one can directly relate the surface divergence  $\nabla_s \cdot \mathbf{u}_i$  to the radial flow toward or from the droplet interface.

### Adsorption

In all surfactant systems, adsorption plays a key role, since the tendency of surfactants to adsorb at fluid-fluid interfaces is their major property. The adsorption of surfactants is a process that occurs in two sequential steps, see Fig. 3.9 (a). In a first step surfactants are transported through diffusion and/or advection to the interface. The corresponding flux to the interface is given by:

$$j_{\text{ads}} = \mathbf{n} \cdot (D\nabla c - c\mathbf{u}), \quad (3.18)$$

with bulk diffusion constant  $D$ , surfactant concentration  $c$ , and velocity field  $\mathbf{u}$ . Here, the surface normal  $\mathbf{n}$  points into the surfactant laden bulk fluid. The second step is the adsorption as such, *i.e.*, aggregation of surfactant molecules at the interface by means

of interfacial kinetics. Thus, there is a second relation for the adsorption flux at the interface [13]:

$$j_{\text{ads}} = k_a c - k_d \Gamma, \quad (3.19)$$

with adsorption and desorption constants  $k_a$  and  $k_d$ .

Here we assume a adsorption layer with a given concentration  $c$  of surfactants close to the interface and focus on the second step of the adsorption process. This process is typically described via an adsorption isotherm, which relates the surface excess concentration  $\Gamma$  to the concentration  $c$  in the adjacent adsorption layer [13]. Knowledge of the adsorption isotherm  $\Gamma(c)$  allows to express  $j_{\text{ads}}$  in Eq. (3.19) in terms of  $\Gamma$ . In the following we describe how the adsorption isotherm can be derived from the surfactant equation of state  $\sigma(\Gamma)$ .

From the relation  $\Omega = \Omega_0 + \sigma A$  from Eq. (3.7) for the grand potential  $\Omega$  one finds  $d\Omega = A d\sigma + \sigma dA$  which can be compared with the total differential in Eq. (3.1). For constant temperature  $T$ , we find

$$d\sigma = -\frac{N}{A} d\mu = -\frac{\Gamma}{\ell^2} d\mu, \quad (3.20)$$

which is called Gibbs adsorption isotherm or simply Gibbs equation [13]. A generalization to multicomponent systems is straightforward. Equation (3.20) can be rewritten as

$$-\frac{\Gamma}{\ell^2} = \frac{\partial \sigma}{\partial \mu} = \frac{\partial \sigma}{\partial c} \frac{\partial c}{\partial \mu}.$$

Using the chemical potential of the bulk fluid,  $\mu = \mu_0 + k_B T \ln \frac{c}{c_0}$ , one finds  $\frac{\partial c}{\partial \mu} = \frac{c}{k_B T}$  and thus

$$\frac{\partial \sigma}{\partial c} = -\frac{k_B T}{\ell^2} \frac{\Gamma}{c}.$$

By using the chain rule to split up  $\frac{\partial \sigma}{\partial c} = \frac{\partial \sigma}{\partial \Gamma} \frac{\partial \Gamma}{\partial c}$  we find:

$$\frac{\partial \sigma}{\partial \Gamma} \frac{1}{\Gamma} d\Gamma = -\frac{k_B T}{\ell^2} \frac{1}{c} dc. \quad (3.21)$$

This equation can be integrated for a given equation of state  $\sigma(\Gamma)$ . For the ideal mixture we find with Eq. (3.9):

$$\Gamma = \frac{c}{c + a}, \quad (3.22)$$

where  $a$  is an integration constant. This widely used relation is called Langmuir adsorption isotherm. It can also be derived by setting up an equilibrium reaction equation between molecules, empty sites, and occupied sites at the interface while neglecting any site interaction [72]. In the dilute case  $\Gamma \ll 1$ , one finds:

$$\Gamma = b \cdot c, \quad (3.23)$$

where  $b$  is an integration constant. This relation is called Henry adsorption isotherm and is the simplest possible adsorption isotherm [72]. In Fig. 3.9 (b), we plot the Langmuir isotherm (3.22) as well as the Henry adsorption isotherm (3.23) for  $b = 1/a = 5$ .

Apparently, the latter lacks any saturation of the surface concentration  $\Gamma$  for large bulk concentration  $c$ , which is certainly unphysical beyond the dilute regime. By comparing the linear Henry adsorption isotherm (3.23) with the adsorption flux  $j_{\text{ads}}$  of Eq. (3.19), one notices that linear adsorption corresponds to  $j_{\text{ads}} = 0$  and  $b = k_a/k_d$ . In that case the interface is in local equilibrium with the adjacent adsorption layer.

When the concentration  $c$  of surfactants in the bulk fluid is above the critical micelle concentration, the adsorption process is more complicated. Micelles have to attach to the interface, break open, and then aggregate at the interface. In that case it can be appropriate to rather model the micelles and their adsorption explicitly. In Ref. [19], which can be found in Sect. 4.3, we present a possible implementation.

## Reaction

Certain surfactants can react with a reactant and reach a state with a lower or higher surface tension, compare Sect. 3.3.3. In these systems, two surfactant states (pristine and reacted state) coexist at the interface. If  $\Gamma$  denotes the concentration of the pristine surfactants, a reaction term can be written as  $j_{\text{react}} = -k\Gamma$ , where infinite supply of the reactant is assumed. Here  $k > 0$  denotes the reaction constant. The concentration  $\Gamma'$  of reacted surfactants, on the other hand, increases with  $j_{\text{react}} = k\Gamma'$ .

In cases where adsorption and a reaction take place, both effects can be combined into one term in the dynamic equation for  $\Gamma$ , Eq. (3.12) [8]. In Sect. 4.2 we use this approach to model monoolein surfactants that react with bromine.

## Thermal noise

The thermal noise term in Eq. (3.12) represents the effect of thermally induced collisions between surfactant molecules at the interface. It has the following properties: [88]

$$\langle \zeta \rangle = 0, \quad (3.24a)$$

$$\langle \zeta(\mathbf{r}, t) \zeta(\mathbf{r}', t') \rangle = -2k_B T \lambda \nabla_s^2 \delta(\mathbf{r} - \mathbf{r}') \delta(t - t'). \quad (3.24b)$$

Here, the strength of the noise correlations is connected to the mobility  $\lambda$  of the diffusive current in Eq. (3.16) via the fluctuation-dissipation theorem. The first property (3.24a) ensures that – on average – the noise vanishes, while Eq. (3.24b) expresses that the noise is delta correlated in time and short-range correlated in space. This is due to the fact that the thermal noise is connected to the dynamics of the Langevin model B, which we discussed around Eq. (3.16), and as such it is a conserved quantity. Thus, one obtains the usual white noise auto-correlation for the noise current  $\mathbf{j}_\zeta$  which is defined via  $\zeta = \nabla_s \cdot \mathbf{j}_\zeta$ :

$$\langle \mathbf{j}_\zeta(\mathbf{r}, t) \otimes \mathbf{j}_\zeta(\mathbf{r}', t') \rangle = 2k_B T \lambda \mathbf{1} \delta(\mathbf{r} - \mathbf{r}') \delta(t - t').$$

This is equivalent to the expression (3.24b). Hence, the  $\nabla_s^2$ -operator in Eq. (3.24b) accounts for the conservation law of the noise. A random noise addition to the surfactant concentration  $\Gamma$  added at one site at the interface must be balanced by noise contributions in the neighborhood of the site [89].

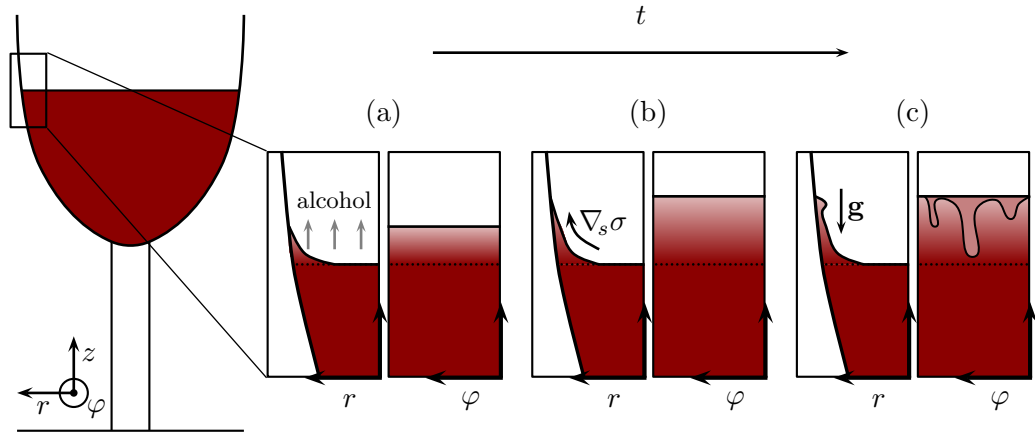


Figure 3.10: Marangoni flow in a glass of wine. Shown are three sequential snapshots, each with side view and frontal view of the side of a wine glass. (a) Capillary action makes the wine climb up at the glass’ wall. Both alcohol and water evaporate from the rising film, but the alcohol evaporates faster, due to its higher vapor pressure. Hence, at the side of the glass the alcohol concentration is decreased. (b) Since the surface tension  $\sigma$  of alcohol is lower than that of water, a gradient  $\nabla_s\sigma$  is initiated. The resulting Marangoni flow causes more wine to be pulled upwards. (c) The wine forms droplets – so-called “tears of wine” – which fall back under their own weight.

### 3.4 The Marangoni effect

The surface tension  $\sigma$  is a quantity, which originates in the intermolecular attraction at a fluid-fluid interface. Molecules in regions with a high surface tension experience a higher attraction towards each other than molecules in regions with a low surface tension. This leads to a flow of surfactant molecules and thereby to fluid flow  $\mathbf{u}$  of the adjacent liquid in direction of the gradient:

$$\mathbf{u} \sim \nabla_s\sigma . \tag{3.25}$$

This effect is called Marangoni effect. In this section, we show how Marangoni flow can be created, derive the flow field for a simple planar geometry, and discuss Marangoni flow around emulsion droplets. We start with a short introduction to the history of the Marangoni effect.

#### 3.4.1 Early observations of surface tension driven flow

The Marangoni effect was likely discovered over a glass of wine. James Thomson, who was the older brother of William Thomson (Lord Kelvin), first mentioned so-called “tears of wine” in 1855, [90]. Tears of wine describes a phenomenon, where wine climbs up on the inside of a wineglass and droplets fall back under their own weight. It is illustrated in Fig. 3.10. The wine is pulled upwards since the alcohol evaporates faster than water at the side of the glass, but water has a higher surface tension than alcohol. Hence,

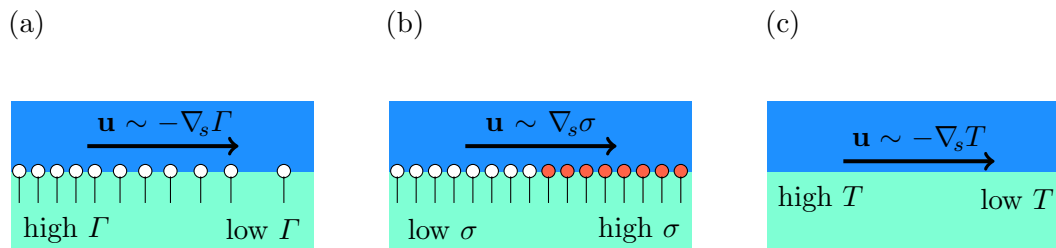


Figure 3.11: Marangoni effect induced by (a) a gradient in surfactant concentration  $\Gamma$  at the interface, (b) a gradient in surface tension  $\sigma$  of the surfactants, and (c) a gradient in temperature  $T$  along the interface.

tears of wine are the result of Marangoni flow. A quantitative study of the tears of wine phenomenon can be found in Ref. [91].

Although Thomson discovered that fluids flow in direction of increasing surface tension, the effect was named after Marangoni, who wrote his Ph.D thesis about the topic in 1865 [92]. A first rigorous theoretical treatment of the subject was conducted by Gibbs in 1876 [93].

### 3.4.2 Causes for Marangoni flow

Figure 3.11 depicts three examples of Marangoni flow. A simple scenario that leads to so-called solutocapillary Marangoni flow, is an inhomogeneous concentration  $\Gamma$  of surfactants at the interface, see Fig. 3.11 (a). As elaborated in Sect. 3.3.5, the surface tension  $\sigma$  of a surfactant-laden interface is in first order proportional to  $-\Gamma$ , see Eq. (3.11). Therefore, Marangoni flow  $\mathbf{u}$  is directed away from regions of high surfactant concentration. The flow  $\mathbf{u}$ , however, transports the surfactants by means of advection. Hence, surfactants generally spread at interfaces until the surface tension is homogeneous [94].

Alternatively one can generate solutocapillary Marangoni flow by directly tuning the surface tension of surfactants in a fully covered interface, see Fig. 3.11 (b). In Sect. 3.3.3 and 3.3.4 we introduced the bromination reaction of monoolein and the photoisomerization of AzoTAB. Both can lead to an inhomogeneous mixture of surfactants with different surface tensions and thus to Marangoni flow.

The surface tension of a liquid-liquid interface can also be altered without the aid of surfactants – by changing the temperature. At most interfaces, the surface tension decreases with increasing temperature [95], as shown in Fig. 3.11 (c). This also holds, when surfactants are present [96]. Flow, which is generated by gradients in temperature  $T$ , is called thermocapillary Marangoni flow.

In general, several of the above effects occur simultaneously. For instance, an interfacial layer of AzoTAB surfactants, which is partially illuminated with UV light, experiences flow away from the illuminated, *i.e.*, *cis* surfactant covered region. The resulting

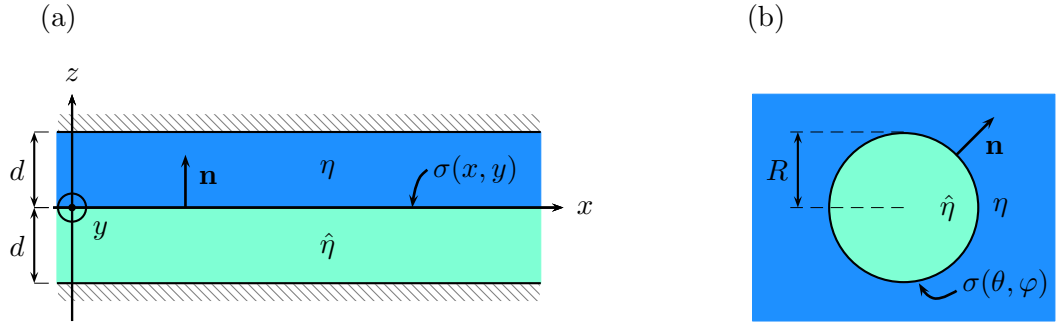


Figure 3.12: (a) Two immiscible fluid layers with viscosities  $\eta$  and  $\hat{\eta}$  and thickness  $d$  confined between plates. The interface in between has a surface tension  $\sigma(x, y)$ . (b) Spherical emulsion droplet of radius  $R$  with viscosity  $\hat{\eta}$  immersed in unbounded bulk fluid with viscosity  $\eta$ . The interface in between the two immiscible fluids has a surface tension  $\sigma(\theta, \varphi)$ .

advection leads to a thinning of surfactants in the illuminated region. This counteracts the light induced Marangoni flow. Furthermore, the light beam possibly heats the surfactants which also counteracts the light induced Marangoni flow. Thus the physics of Marangoni flow at fluid-fluid interfaces becomes quite complex for seemingly primitive systems.

In what follows, we want to define Eq. (3.25) more precisely.

### 3.4.3 Plane Marangoni flow

Here, we discuss immiscible fluid-fluid stratified flow confined between two infinitely extended plates. The fluid layers are of height  $d$  and have the respective viscosities  $\eta$  and  $\hat{\eta}$ , while the interface between the two liquids is subject to a given surface tension  $\sigma(x, y)$ . Figure 3.12 (a) depicts the setup. Only this plane geometry yields the simple relation  $\mathbf{u} \propto \nabla_s \sigma$ , *i.e.*, flow in the direction of increasing surface tension, exactly. It is therefore paradigmatic for the Marangoni effect and serves for several studies of the stability of stratified flow [97, 98, 99].

At low Reynolds number we have to solve the Stokes equation (2.8) to determine both the velocity field  $\mathbf{u}(\mathbf{r})$  above the interface ( $z > 0$ ) and the field  $\hat{\mathbf{u}}(\mathbf{r})$  below the interface ( $z < 0$ ). We start by collecting the boundary and interface conditions:

$$\mathbf{u} = \mathbf{0}, \quad z = \pm d, \quad (3.26a)$$

$$u_z = \hat{u}_z = 0, \quad z = 0, \quad (3.26b)$$

$$\mathbf{u} = \hat{\mathbf{u}}, \quad z = 0, \quad (3.26c)$$

$$\nabla_s \sigma = \mathbf{P}_s(\hat{\mathbf{T}} - \mathbf{T})\mathbf{e}_z, \quad z = 0. \quad (3.26d)$$

The first condition (3.26a) takes into account the two confining plates. Furthermore, we assume an impenetrable interface, see Eq. (3.26b), with continuous tangential velocity, see Eq. (3.26c). Condition (3.26d) is the essential condition regarding the Marangoni effect. It states that  $\nabla_s \sigma$ , *i.e.*, the gradient in surface tension along the interface, is balanced by a jump in the fluid shear stresses [13]. Here we introduce the surface projector  $\mathbf{P}_s = \mathbf{1} - \mathbf{n} \otimes \mathbf{n}$  with surface normal  $\mathbf{n} = \mathbf{e}_z$  and use the notation  $\nabla_s = \mathbf{P}_s \nabla$  for the surface gradient. Finally, the viscous part of the Cauchy stress tensor of an incompressible Newtonian fluid with viscosity  $\eta$  is given by  $\mathbf{T} = \eta [\nabla \otimes \mathbf{u} + (\nabla \otimes \mathbf{u})^T]$ . Writing out condition (3.26d) in Cartesian coordinates yields the two equations:

$$\partial_x \sigma = \hat{\eta} \partial_z \hat{u}_x - \eta \partial_z u_x, \quad (3.27a)$$

$$\partial_y \sigma = \hat{\eta} \partial_z \hat{u}_y - \eta \partial_z u_y. \quad (3.27b)$$

Next, we employ the ansatz

$$u_x(x, z) = f(x) + zg(x), \quad (3.28a)$$

$$u_y(y, z) = h(y) + zw(y), \quad (3.28b)$$

$$u_z = 0, \quad (3.28c)$$

where  $f, g, h, w$  are functions to be determined. An analogous ansatz is made for  $\hat{\mathbf{u}}$  with functions  $\hat{f}, \hat{g}, \hat{h}, \hat{w}$ . This ansatz resembles the ansatz for Couette flow. As such it is laminar, *i.e.*, there is no interference between layers that are parallel to the  $x$ - $y$ -plane. Note that ansatz (3.28) does already incorporate condition (3.26b). By successively evaluating the remaining conditions, one finds for the flow field:

$$\mathbf{u} = \frac{d-z}{\eta + \hat{\eta}} \nabla_s \sigma, \quad \hat{\mathbf{u}} = \frac{d+z}{\eta + \hat{\eta}} \nabla_s \sigma, \quad (3.29)$$

and at the interface

$$\mathbf{u}(z=0) = \frac{d}{\eta + \hat{\eta}} \nabla_s \sigma, \quad (3.30)$$

which is the hallmark of the Marangoni effect: fluid flow in the direction of increasing surface tension  $\sigma$ .

### 3.4.4 Marangoni number

The dimensionless Marangoni number  $M$  compares the diffusion time scale to the advection time scale at a fluid-fluid interface. It is an important parameter in all systems that include Marangoni flow, as it determines its stability [13]. It can be derived from Eq. (3.30) as follows. We first consider the case of solutocapillary Marangoni flow, *i.e.*, flow due a gradient in concentration  $\Gamma$  of surfactants, see Fig. 3.11 (a). Hence, one can write  $\nabla_s \sigma = \frac{\partial \sigma}{\partial \Gamma} \nabla_s \Gamma$ . A natural rescaling of the surface gradient is  $\tilde{\nabla}_s \equiv d \nabla_s$ , *i.e.*, by the only length scale in the system. The flow field is rescaled by  $\tilde{\mathbf{u}} \equiv \frac{\tau_D}{d} \mathbf{u}$ . Here  $\tau_D$  is the

diffusion time scale of the system, with  $\tau_D = d^2/D$  and diffusion constant  $D$ . Thus, one finds for concentration driven Marangoni flow at the interface:

$$\tilde{\mathbf{u}} = \underbrace{\frac{d}{D(\eta + \hat{\eta})}}_{M_{\text{sol}}} \frac{\partial \sigma}{\partial \Gamma} \tilde{\nabla}_s \Gamma. \quad (3.31)$$

Note that the concentration  $\Gamma$  is assumed to be dimensionless. The dimensionless parameter  $M_{\text{sol}}$  is called solutocapillary Marangoni number [13]. It can also be written as the ratio  $M_{\text{sol}} = \tau_D/\tau_A$  where we introduce the advection time scale  $\tau_A = d(\eta + \hat{\eta}) \left(\frac{\partial \sigma}{\partial \Gamma}\right)^{-1}$ . The quantity  $\frac{\partial \sigma}{\partial \Gamma}$  is given in Eq. (3.9) for an ideal interface. In Ref. [17], which is given in Sect. 4.2, we will derive the solutocapillary Marangoni number for a more elaborate system, where two species of surfactants are present at the interface.

In the case of thermocapillary flow, *i.e.*, flow due to a gradient in temperature  $T$  one can write  $\nabla_s \sigma = \frac{\partial \sigma}{\partial T} \nabla_s T$ . This case is depicted in Fig. 3.11 (c). Again, one rescales  $\tilde{\nabla}_s \equiv d \nabla_s$  and  $\tilde{\mathbf{u}} \equiv \frac{\tau_D}{d} \mathbf{u}$  with  $\tau_D = d^2/\alpha$  and thermal diffusivity  $\alpha$ . Thus, one finds

$$\tilde{\mathbf{u}} = \underbrace{\frac{d \Delta T}{\alpha(\eta + \hat{\eta})}}_{M_{\text{th}}} \frac{\partial \sigma}{\partial T} \tilde{\nabla}_s \tilde{T}, \quad (3.32)$$

with thermocapillary Marangoni number  $M_{\text{th}}$ . Here, we also rescaled temperature  $\tilde{T} \equiv T/\Delta T$ .

Finally, we want to note that these Marangoni numbers are quite general. Albeit the expression for the flow field  $\mathbf{u}$  can become more complex, *e.g.* around an emulsion droplet, the prefactor  $d/(\eta + \hat{\eta})$  and with that the advection time scale  $\tau_A$  remain the same.

### 3.4.5 Droplet Marangoni flow

Including any boundary conditions in  $x$  or  $y$  direction in the plane system of Fig. 3.12 (a), makes the ansatz (3.28) insufficient. Instead, one has to resort to techniques such as an expansion in orthonormal basis functions in order to fulfill the additional boundary conditions. For the surface tension  $\sigma(\theta, \varphi)$  of the spherical emulsion droplet in Fig. 3.12 (b), spherical harmonics are the natural choice for a basis. We use this approach in Ref. [19], which is given in Sect. 4.3, to solve for the flow field around a droplet. In contrast to the plane system, Marangoni flow around a droplet leads to motion of the droplet w.r.t. a fixed lab frame of reference. Therefore one also has to consider the resulting hydrodynamic drag of the moving droplet. This is done by superimposing the Marangoni flow with the drag flow. This approach ensures that the droplet is a force-free swimmer [14].

First calculations of droplet hydrodynamics date back to the beginning of the 20th century. In 1911, the famous Stokes drag formula (2.10) was generalized to liquid droplets

by Hadamard and Rybczynski [100, 101]. The drag force of a droplet with viscosity  $\hat{\eta}$  and radius  $R$ , which moves with velocity  $\mathbf{v}$  through a liquid of viscosity  $\eta$  is

$$\mathbf{f} = -6\pi\eta R \frac{2\eta + 3\hat{\eta}}{3\eta + 3\hat{\eta}} \mathbf{v} . \quad (3.33)$$

This reduces to Stokes drag, *i.e.*, Eq. (2.10) for  $\hat{\eta} \gg \eta$ , whereas it predicts a reduced drag for droplets, due to a finite slip velocity at the droplet interface. This formula, however, overestimated the velocity, which was found in experiments of sinking emulsion droplets. The explanation was found by Levich in 1962: While the droplet sinks, the flow field at the interface advects surface active agents to the posterior end of the droplet and the induced Marangoni effect reduces the sinking velocity [102]. In other words, the Hadamard-Rybczynski formula is only correct for perfectly clean droplets.

The first rigorous calculation of the velocity reduction of a sinking surfactant-laden droplet was presented by Levan and Newman in 1976 in Ref. [64]. Their derivation uses the Stokes stream function  $\psi(r, \theta)$  to find the velocity field  $u_r = (r^2 \sin \theta)^{-1} \partial_\theta \psi$ ,  $u_\theta = -(r \sin \theta)^{-1} \partial_r \psi$ . Note that the stream function can only be used in two dimensions or in three dimensions with axisymmetry. The authors found for the interfacial flow field  $u_\theta|_R = u_\theta(R, \theta)$  of a droplet, which is axisymmetric about  $\mathbf{e}_z$  [64]:

$$u_\theta|_R = \frac{\eta \sin \theta v}{2(\eta + \hat{\eta})} + \frac{1}{2(\eta + \hat{\eta})} \sum_{l=1}^{\infty} \left( \int_{-1}^1 \sigma(\theta) P_l \, d\cos \theta \right) \partial_\theta P_l , \quad (3.34)$$

and  $u_r|_R = 0$ . Here,  $P_l(\cos \theta)$  are Legendre polynomials of degree  $l$ , with  $P_1 = \cos \theta$ . The front of the droplet is at  $\theta = 0$ . This flow field incorporates the set of boundary conditions in Eqs. (3.26b)-(3.26d), albeit modified to suit spherical coordinates. Note that  $\mathbf{u}|_R = u_r|_R \mathbf{e}_r + u_\theta|_R \mathbf{e}_\theta$  is given in the frame of reference of the moving droplet. The droplet velocity in  $z$ -direction is calculated from [64]:

$$v = \frac{-1}{2\eta + 3\hat{\eta}} \int_{-1}^1 \sigma(\theta) \cos \theta \, d\cos \theta . \quad (3.35)$$

Here, we omitted any external forces such as gravity. Note that the first term of Eq. (3.34) is the drag flow, while the second term is the pumping Marangoni flow. The latter can be related to the pumping part of the squirmer flow field (2.11) of Sect. 2.1.4 by substituting

$$\int_{-1}^1 \sigma(\theta) P_l \, d\cos \theta = \frac{-8(\eta + \hat{\eta})}{l(l+1)} B_l .$$

The drag flow of the squirmer (Stokes flow around a colloid) is given by the droplet drag flow in the limit of infinite internal viscosity  $\hat{\eta} \rightarrow \infty$  [19].

Albeit Ref. [64], and the subsequent Ref. [103] by Levan, discuss a droplet which moves due to gravity, the flow field (3.34) also holds for a self-propelled active droplet.

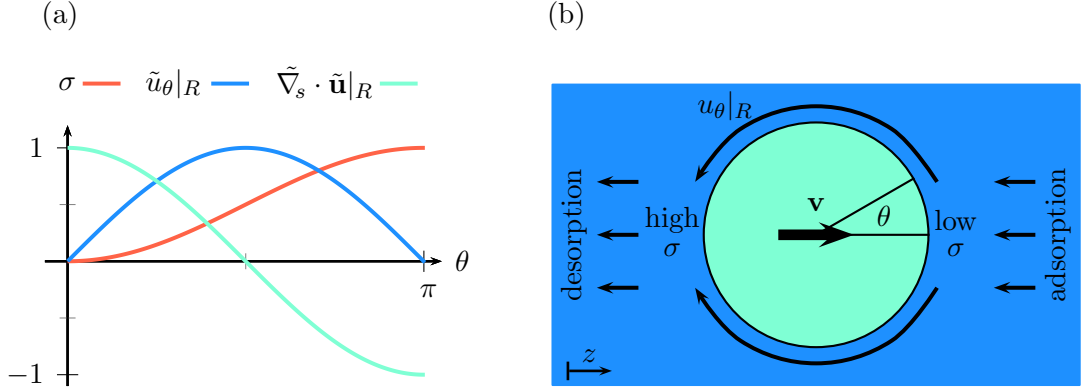


Figure 3.13: (a) Surface tension  $\sigma(\theta) = \sigma_0(1 - \cos\theta)$  and the resulting surface flow field  $\tilde{u}_\theta|_R$  and surface divergence  $\tilde{\nabla}_s \cdot \tilde{\mathbf{u}}|_R$ . Here, we made  $\mathbf{u}|_R$  and  $\nabla_s$  dimensionless. (b) Illustration of a swimming emulsion droplet. Marangoni induced droplet propulsion is always accompanied by an inflow of matter at the front and outflow of matter at the back of the droplet.

In 2000, the velocity field around an emulsion droplet with arbitrary surface tension  $\sigma(\theta, \varphi)$  was found by Bławdziewicz *et al.* by using a set of fundamental solutions of the Stokes equation [104]. They used the formulas to study the rheology of a dilute emulsion of surfactant laden spherical droplets. In Sect. 4.3 we derive and discuss Marangoni flow around a spherical emulsion droplet in detail. The full three-dimensional velocity field was later used to calculate the migration of spherical droplets in Poiseuille flow [105, 106].

The lowest mode of Eq. (3.34), *i.e.*  $l = 1$ , corresponds to  $\sigma(\theta) \propto \cos\theta$ . Note that this is the only mode that gives  $v \neq 0$  in Eq. (3.35), and it is therefore responsible for propulsion of the droplet. We therefore set  $\sigma(\theta) = \sigma_0(1 - \cos\theta)$  for the time being to discuss the basic features of droplet Marangoni flow. We find

$$v = \frac{2}{3} \frac{\sigma_0}{2\eta + 3\hat{\eta}} \quad \text{and} \quad u_\theta|_R = \frac{\sigma_0 \sin\theta}{2\eta + 3\hat{\eta}}, \quad (3.36)$$

which we plot in Fig. 3.13 (a), together with  $\sigma(\theta)$ . The tangential surface flow  $u_\theta|_R$  is directed along  $\mathbf{e}_\theta$ , which leads to swimming in  $z$ -direction with droplet velocity vector  $\mathbf{v} = v\mathbf{e}_z$ , see Fig. 3.13 (b).

Note that the surface flow field in the simple case  $\sigma = \sigma_0(1 - \cos\theta)$  can also be written as

$$\mathbf{u}|_R = \frac{R}{2\eta + 3\hat{\eta}} \nabla_s \sigma, \quad (3.37)$$

where  $\nabla_s = R^{-1}\partial_\theta$ . This relation resembles Eq. (3.30). Here, however, the characteristic length scale is given by the droplet radius  $R$ . Indeed, this simple relation is an approximation, which is only valid for the  $l = 1$  mode of Eq. (3.34). It is therefore only applicable if variations in  $\sigma$  are on the order of the droplet radius  $R$ . For finer variations

in  $\sigma$ , one has to resort to the full expression (3.34). In contrast to the simple relation (3.36), the full expression prevents the flow field  $\mathbf{u}|_R$  from diverging for sharp steps in  $\sigma$ . In Fig. 3.14 (b), we compare both expressions for the case when  $\sigma$  is given by a smoothed step function.

The surface divergence  $\nabla_s \cdot \mathbf{u}|_R$ , which we introduced in Sect. 3.3.6, is given by  $(R \sin \theta)^{-1} \partial_\theta (\sin \theta u_\theta|_R)$  in the case of an axisymmetric flow field. For the simple flow field given in Eq. (3.36), one finds

$$\nabla_s \cdot \mathbf{u}|_R = \frac{2\sigma_0 \cos \theta}{(2\eta + 3\hat{\eta})R} \quad \text{or} \quad \nabla_s \cdot \mathbf{u}|_R \propto -\sigma(\theta), \quad (3.38)$$

see Fig. 3.13 (a). This illustrates an important property of droplet Marangoni flow. Since it is the lowest mode in  $\sigma$  that leads to propulsion of the droplet and the lowest mode leads to  $\nabla_s \cdot \mathbf{u}|_R \neq 0$ , we conclude that droplet propulsion is always accompanied by a non-vanishing surface divergence. This is a general property of active particles [107]. Furthermore, at the front of the droplet, the surface divergence  $\nabla_s \cdot \mathbf{u}|_R > 0$ , *i.e.*, there is a source of matter. This is realized by a radial flow of matter (usually surfactants) towards the interface, as depicted in Fig. 3.13 (b) and derived in Ref. [19], which is given in Sect. 4.3.

Surfactants then adsorb at the interface and move along the streamlines of  $\mathbf{u}|_R$  towards the posterior end of the droplet, where they desorb back into the bulk. Accordingly, the surface divergence is negative, *i.e.*  $\nabla_s \cdot \mathbf{u}|_R < 0$ , at the back of the droplet. This exchange of matter with the bulk by adsorption and desorption is a necessary condition for droplet flow driven by the Marangoni effect.

Three slightly more elaborate surface tension profiles are shown together with  $u_\theta|_R$  as well as streamlines of the interior and the surrounding flow in Fig. 3.14. The surface tension is given by the smoothed step function

$$\sigma(\theta) = \frac{1}{\pi} \left[ \arctan \left( \frac{\theta - \theta_0}{\epsilon} \right) + \frac{2}{\pi} \right], \quad (3.39)$$

for  $\epsilon = 0.1$  and (a)  $\theta_0 = \frac{\pi}{4}$ , (b)  $\theta_0 = \frac{\pi}{2}$ , and (c)  $\theta_0 = \frac{3\pi}{2}$ . The streamlines are depicted in the droplet frame as well as in the lab frame, which is given by  $\mathbf{u}^L = \mathbf{u} + \mathbf{v}$ . The lab frame is characterized by  $\mathbf{u}^L|_{r \rightarrow \infty} = 0$ , while in the droplet frame  $\mathbf{u}|_{r \rightarrow \infty} = -\mathbf{v}$ . Furthermore, note that the normal velocity at the interface  $u_r^L|_R$  does not vanish in the lab frame. The resulting internal flow in the droplet frame develops into two vortices. Indeed, any surface tension  $\sigma$ , which is not a monotonic function of  $\theta$ , leads to more than two vortices. Note that depending on  $\theta_0$ , hence the position of the step in  $\sigma(\theta)$ , the droplet is either (a) a puller, (b) a neutral swimmer, or (c) a pusher; compare the discussion in Sect. 2.1.3.

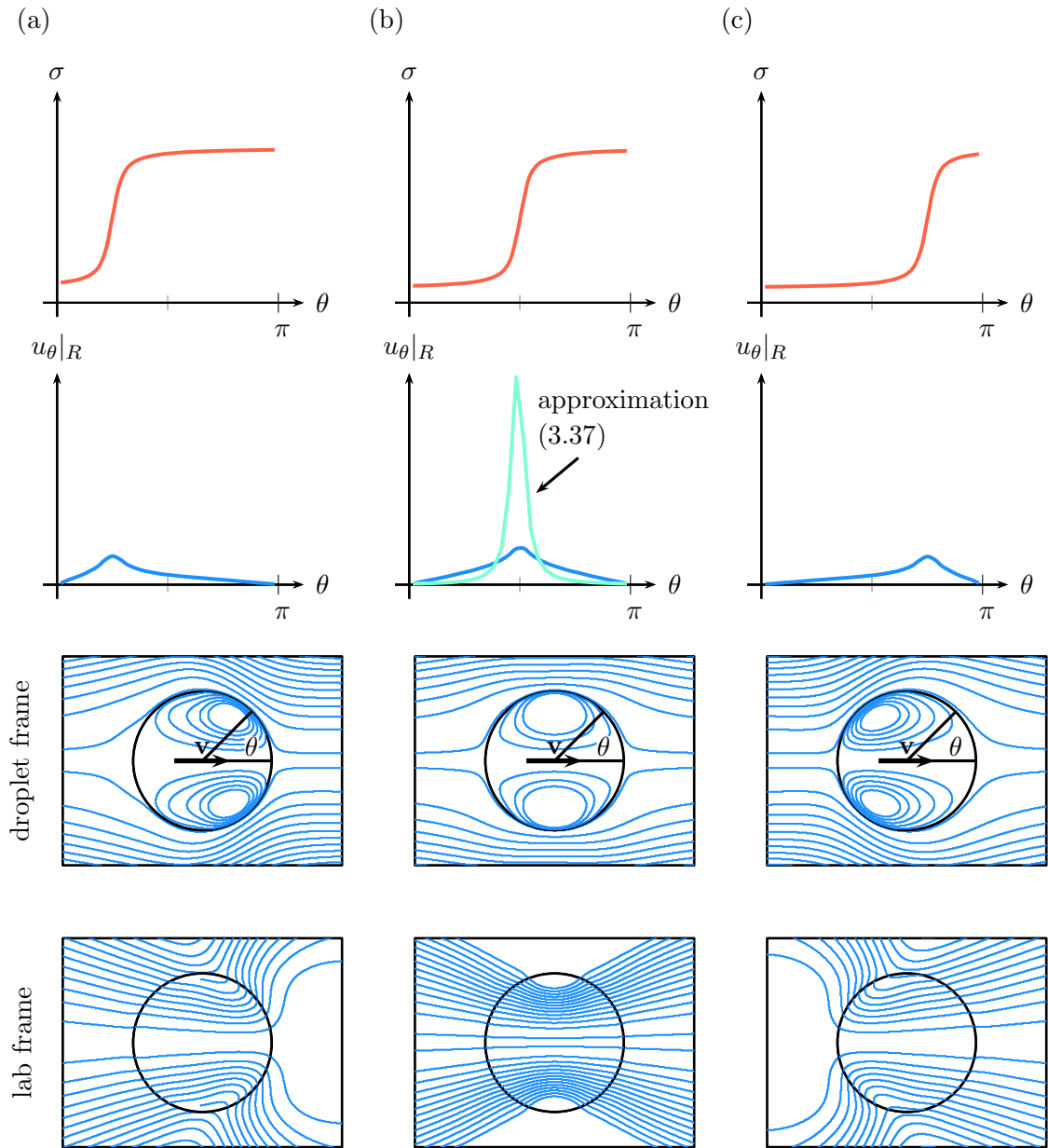


Figure 3.14: Surface tension  $\sigma(\theta)$ , surface velocity flow field  $u_{\theta}|_R$ , and stream lines of the flow fields in and around the droplet for three different shapes of  $\sigma(\theta)$ . (a) The step in  $\sigma(\theta)$  is located at the front of the droplet. The droplet is a puller. (b) The step is located at the equator and the droplet is a neutral swimmer. (c) The step is located at the back and the droplet is a pusher.

## 3.5 Experiments, models, and theories on active emulsion droplets

Before discussing several models of active emulsion droplets in Sect. 4, we want to give the reader an overview of experiments, models, and theories on active emulsion droplets in the literature.

### 3.5.1 Early attempts on droplet Marangoni flow

Prior to experimental realizations of active emulsion droplets, researchers started to study the stability of flat and spherical interfaces. In 1959, Sternling and Scriven showed that convection cells can be generated in a thin horizontal liquid layer, which is heated from below [108]. In resemblance to Rayleigh-Bénard cells, these cells are called Bénard-Marangoni cells. However, the instability, which leads to Bénard-Marangoni cells, is only due to the Marangoni effect and not due to buoyancy. This hydrodynamic instability of an interface was then also studied on a spherical interface in 1976 [109] and in 1979 [110].

The first model of a self-propelled emulsion droplet was presented by Ryazantsev in 1985 [111] and refined in a subsequent publication a year later [112]. He studied droplet motion due to thermocapillary Marangoni flow, where the temperature gradient on the droplet interface is a consequence of the motion of the droplet itself and not externally generated, as assumed in former systems, *e.g.*, in Ref. [113]. The model of Refs. [111, 112] was extended to solutocapillary Marangoni flow in 1990 [114].

In 1993-1995 several articles were published by Ryazantsev, Rednikov, *et al.*, which refined the model above by including gravity [115, 116] and discussing several instability thresholds for different swimming modes [117, 118, 119, 120]. Ref. [121] gives an overview of these publications.

### 3.5.2 Current state of research on active emulsion droplets

In the following, we classify the publications by denoting citations with superscripts. E stands for experimental, T for theoretical, S for simulations, and R for review.

Inspired by the growing interest in the physics of active particles, Sumino *et al.* and Nagai *et al.* studied self-running droplets on interfaces in 2005 [122, 123]<sup>E</sup>. These studies also initiated a comeback of the active emulsion droplet.

In 2007, the first experimental results of active emulsion droplets since the mid 1990s were published by Hanczyc *et al.* [124]<sup>E</sup>. Oil droplets loaded with a fatty acid precursor, which are placed into an aqueous fatty acid micelle solution, showed autonomous movement. They also found directional motion of the droplets within chemical gradients and exhibited a type of chemotaxis. In a follow-up study, Toyota *et al.* shortly report on similar experiments of active oil emulsion droplets, which consume hydrolyzable surfactants as a “fuel”, which is supported from the bulk phase [125]<sup>E</sup>.

In what follows, we present recent advancements about swimming emulsion droplets in chronological order.

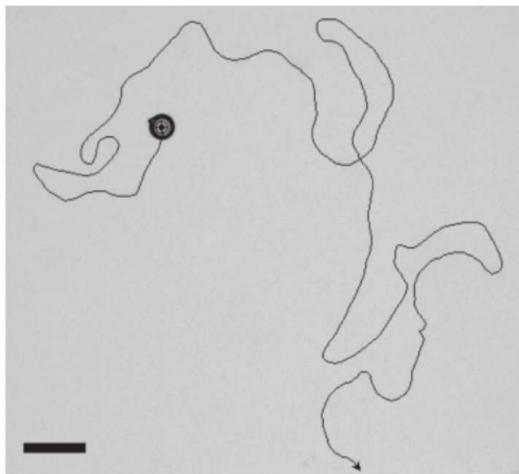


Figure 3.15: Trajectory of an active emulsion droplet over a duration of 400s, from Ref. [8]. The scale bar represents  $300\mu\text{m}$ .

## 2011

Kitahata *et al.* studied the spontaneous oscillatory droplet motion due to a Belousov-Zhabotinsky (BZ) reaction medium inside a droplet [15]<sup>E,S</sup>. They were able to reproduce their experimental results, which were obtained with a BZ droplet in an oil phase in a petri dish, with numerical simulations of scroll waves inside the droplet.

At the same time Thutupalli *et al.* performed experiments on bromine enriched water emulsion droplets in oil [8]<sup>E</sup>. The droplets swim due to the bromination reaction of monoolein, discussed in Sect. 3.3.3. Figure 3.15 shows a path of a bromine water droplet in oil. Apart from a description of the propulsion mechanism, Ref. [8]<sup>E</sup> contains results of the collective motion of the droplets. The results of Ref. [8]<sup>E</sup> have been extended by Thutupalli and Herminghaus to the self-propulsion of oscillating droplets [16]<sup>E</sup>.

## 2012

Yoshinaga *et al.* derived an amplitude equation, which explains the drift instability in the motion of an active emulsion droplet [126]<sup>T,S</sup>. Numerical simulations support the obtained critical point at the onset of motion, as well as the characteristic velocity of the droplet.

Furthermore, Tjhung *et al.* simulated a droplet filled with actomyosin (“an active gel whose polarity describes the mean sense of alignment of actin fibres”) to model the spontaneous symmetry breaking of contractile active cells [5]<sup>S</sup>. The droplet is found to be elongated perpendicular to the swimming direction. Stationary swimming as well as oscillatory motion, and spiral motion is observed.

Yabunaka *et al.* introduced a model of an active emulsion droplet by means of a phase-field model that does not consider the interface explicitly [127]<sup>T,S</sup>. Here, the droplet

motion arises due to a reaction of the interface with a chemical product in the bulk phase. They found a drift bifurcation between a resting and a swimming droplet.

Finally, Sanchez *et al.* presented experiments of active water-in-oil emulsion droplets, which contain extensile microtubule bundles [4]<sup>E</sup>. The flow inside the droplet resembles the cytoplasmic streaming in fruit fly egg cells. A short note by Marchetti discusses how the results of Ref. [4]<sup>E</sup> can shed light on the physics of dynamic reorganization, which occurs inside living cells [3].

## 2013

Ban *et al.* presented experimental results of active oil emulsion droplets in an aqueous phase of NaOH solution [128]<sup>E</sup>. Here, the swimming of the droplet is due to the deprotonation of DEHPA surfactants at the interface. They found that the swimming of the droplets depends critically on the pH condition of the aqueous bulk phase as well as on the radius of the droplets.

Albeit Ref. [129]<sup>T, S</sup> considers a droplet on a surface, we still want to mention it here. Nagai *et al.* studied experimentally and theoretically the rotational motion of a flat droplet induced by Marangoni flow. Here, the droplet rotation is only possible since a small particle is attached at the interface, which breaks the mirror symmetry about the anterior-posterior axis.

Finally, Michelin *et al.* showed that the onset of motion of initially isotropic particles is a quite general mechanism [130]<sup>T, S</sup>. The requirements are (i) surface flow and (ii) advection of a solute to the front of the particle and away from the back of the particle. Their calculations also show that such a swimmer is a pusher.

## 2014

Yoshinaga introduced a model of a swimming emulsion droplet, whose shape can deform from a sphere [131]<sup>T, S</sup>. He found that the swimming droplet is elongated perpendicular to the swimming direction and that it is a pusher.

Izri *et al.* showed that self-propulsion of active droplets is also possible for pure monoolein covered water droplets (*i.e.* without bromine) in an oil phase [132]<sup>E</sup>. Their droplets shrink while they swim. Furthermore, Izri *et al.* noticed that inverse micelles in the oil phase are necessary for propulsion. They, therefore, proposed that water is solubilized by the inverse micelles, and hence produces a gradient of water outside the droplet.

A similar approach is taken in Ref. [133]<sup>T, E</sup>, which was published by Herminghaus *et al.*. It explains the locomotion of liquid crystal filled emulsion droplets by means of a molecular pathway of solubilizing the liquid crystal in micelles surrounding the droplet. In contrast, a micellar pathway, where micelles are filled directly at the droplet interface does not lead to locomotion.

Banno and Toyota reported on novel reactive surfactants, which lengthen the locomotion time of self-propelled n-heptyloxybenzaldehyde droplets in a cationic reactive surfactant solution [134]<sup>E</sup>.

Finally, Whitfield *et al.* presented a continuum level analytical model of a contractile droplet of active polar fluid consisting of filaments and motors [135]<sup>T,S</sup>.

## 2015

Shklyaev studied theoretically the self-propulsion of a so-called Janus droplet, where only half of the interface is active [136]<sup>T,S</sup>. Here, the swimming does not depend on a symmetry breaking instability, which allows to scale down the droplet to micrometers.

## 2016

Zwicker *et al.* studied shape instabilities of growing active emulsion droplets that trigger the division into two smaller droplets [137]<sup>S</sup>. Such droplets resemble the proliferation of living cells and could serve as a model for protocells.

A comprehensive review on swimming droplets by Maass *et al.* is published [6]<sup>R</sup>.

## 4 Publications

This section is the centerpiece of the thesis. It puts together knowledge about microswimmers in general and droplets in particular from Sects. 2 and 3 to study several applications of active emulsion droplets. Before we proceed with the corresponding publications, we give a short synopsis where we position our findings within the current state of research on active emulsion droplets, discussed in Sect. 3.5.

### 4.1 Synopsis

In the first publication “Swimming active droplet: A theoretical analysis”, which we present in Sect. 4.2, we develop a model for the active emulsion droplet of Thutupalli *et al.* [8]. We start from the mixing free energy of pristine and brominated monoolein surfactants, along the lines of Secs. 3.3.5-3.3.6, and derive a diffusion-advection-reaction equation for the surfactant mixture at the droplet interface. For the Marangoni flow around the droplet and at the interface, we employ the axisymmetric formulas (3.34) and (3.35) by Levan *et al.* [64].

Numerical solutions obtained by a Finite difference scheme reveal a stable swimming regime above a critical Marangoni number  $M$ . The bifurcation at the onset of motion is found to be subcritical, in agreement with the findings in a different model by Yoshinaga *et al.* [126]. The swimming emulsion droplet is a pusher, which confirms the experimental findings in Ref. [8], as well as the general results for swimming particles, which are initially isotropic, by Michelin *et al.* [130]. When  $M$  is increased further, the droplet stops again and becomes a shaker. The flow field in that case corresponds to the flow field found in early studies on the stability of spherical liquid interfaces [109, 110]. Finally, for even larger  $M$  the droplet reaches an oscillating state similar to the experimental findings in Refs. [15] and [16]. In our simulations, the swimmer type also oscillates between pusher and puller, see Fig. 4.1 (a). Note that these results are for a droplet, which is axisymmetric about the swimming axis. Thus, the swimming trajectory is always one-dimensional.

From Fig. 3.15, which shows the path of a swimming emulsion droplet, it is clear that these droplets do not swim along straight lines but rather with an erratically changing direction. A simple model for the random walk of a self-propelled particle is the active Brownian particle, discussed in Sect. 2.3. However, this raises the question, where the random torque  $\omega(t)$  in the corresponding Langevin equation (2.20) originates from. To tackle this question, we generalize the model of Sect. 4.2. We omit the axisymmetric constraint and include thermal noise into the diffusion-advection-reaction equation for the surfactant mixture, akin to Eq. (3.12) in Sect. 3.3.6. To omit the axisymmetric constraint, we need to use the full three-dimensional Marangoni flow of a spherical

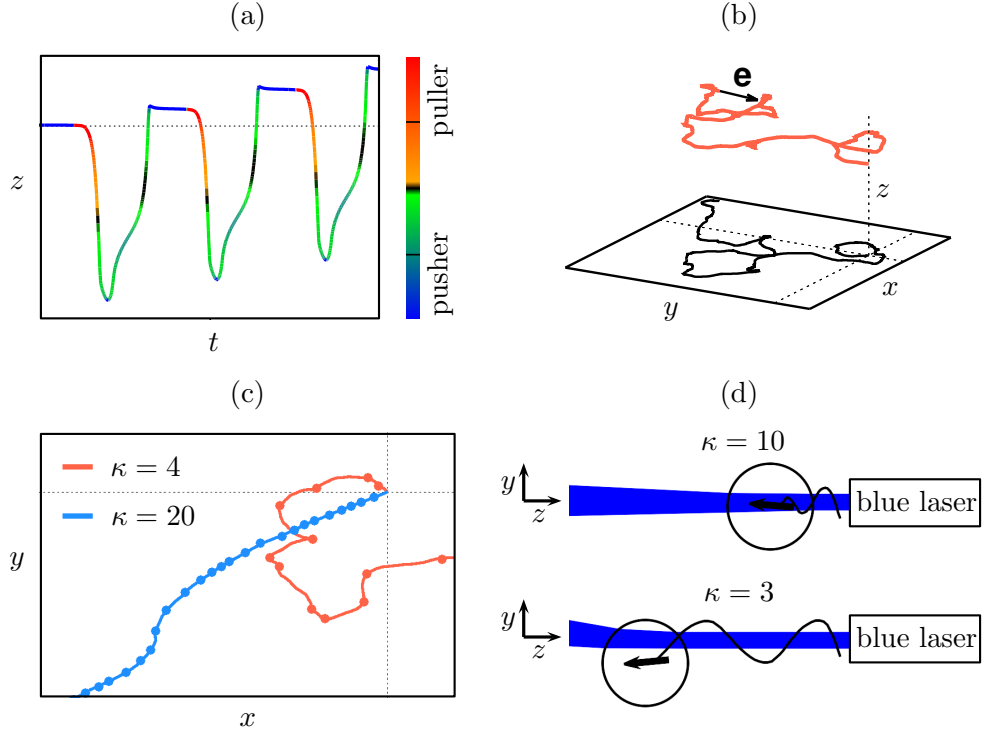


Figure 4.1: Samples of droplet trajectories, which are discussed in Secs. 4.2-4.4. (a) Oscillating axisymmetric droplet. (b) Thermal fluctuations lead to persistent random walk. (c) Micelles can induce directed motion of an initially surfactant free droplet. (d) Transparent droplet pushed by blue light.

droplet. The solution for the flow field was available in the literature, see Sect. 3.4.5. However, the derivation is very compact and the results are written in a manner which is not well suited for our applications. We therefore present an alternative derivation step by step in the publication “Marangoni flow at droplet interfaces: Three-dimensional solution and applications”, presented in Sect. 4.3. There, we specifically focus on active droplets and their swimming kinematics, *i.e.*, the velocity vector  $\mathbf{v}$  and the squirmer parameter  $\beta$ . We also discuss two applications, which do not directly concern our model of the bromine water-in-oil droplet. We will come back to these at the end of this section.

Having at hand the three-dimensional Marangoni flow, we can generalize the dynamic equation of the surfactant mixture to account for surfactant mixtures with arbitrary profile on the spherical emulsion droplet. Furthermore, we add thermal noise. This allows us to focus on two new aspects of droplet dynamics that we could not address before. They are presented in the third publication “Active Brownian motion of emulsion droplets: Coarsening dynamics at the interface and rotational diffusion” in Sect. 4.4.

First, we study in detail the dynamics of a droplet with an initially uniform surfactant mixture towards a stationary uniaxial swimming state, where the surfactant mixture is phase-separated into the two surfactant types. We quantify the coarsening dynamics by means of the growth rate of domains. Two steps exist: An initially slow growth

of domain size is followed by a nearly ballistic regime, which is reminiscent of coarsening in the dynamic model H [138]. Second, we address the random changes in the swimming direction, which were observed in experiments [8]. The thermally fluctuating surfactant mixture induces random changes in the swimming direction, and thereby the emulsion droplet behaves like an active Brownian particle. Figure 4.1 (b) shows a sample trajectory from a simulation. We characterize trajectories by means of the rotational correlation time  $\tau_r$ , introduced in Sect. 2.3, and discuss how the noise strength of the thermal fluctuations affects  $\tau_r$ .

As noted above, the publication in Sect. 4.3 also contains two other applications of the three-dimensional droplet Marangoni flow. The simplest way to generate Marangoni flow is a non-uniform distribution of a single surfactant type at an interface, as noted in Sect. 3.4 and depicted in Fig. 3.11 (a). In our first application we consider an initially surfactant free emulsion droplet immersed in a micelle enriched fluid. When a micelle adsorbs at the droplet interface, the surfactants are spread by Marangoni flow and thereby the droplet is propelled in direction of the adsorption site. The corresponding outer Marangoni flow field, however, preferentially advects other micelles towards the existing adsorption site. Hence, when the concentration of micelles is sufficiently large, this mechanism can spontaneously break the isotropic symmetry of the droplet and lead to directed motion. Figure 4.1 (c) shows the projection onto the  $x$ - $y$ -plane of two sample trajectories for high and low concentration of micelles with parameter  $\kappa = 20$  and  $\kappa = 4$ , respectively. The dots indicate the micelle adsorption events. Our explicit hydrodynamical treatment of the spontaneous symmetry breaking due to micelle adsorption could help to understand other systems, in which micelles have been shown to be crucial [132, 133].

In the second example of Sect. 4.3 we propose light-driven droplet propulsion. By partially illuminating an emulsion droplet covered by light-switchable surfactants, one locally generates a spot of different surface tension, which induces Marangoni flow and hence propulsion of the droplet. So far, light-driven droplet propulsion was only studied on interfaces. The Baigl group found that droplets on an interface can be pushed with UV light or pulled with blue light, see Sect. 3.3.4 and Ref. [20]. We find a similar behavior of the emulsion droplet. Furthermore, depending on the relaxation rate  $\kappa$  towards the surfactant in bulk, the UV illuminated droplet shows a plethora of trajectories. It can perform a damped oscillation about the beam axis, oscillate in the beam axis, or leave the beam and stop. Figure 4.1 (d) shows two sample trajectories. We explore these cases for strongly absorbing and for transparent droplets and also discuss, how the results depend on the type of emulsion (water-in-oil *vs.* oil-in-water).

Table 4.1 summarizes the content of the publications.

Sect. 4.2	<p><b>Swimming active droplet: A theoretical analysis</b></p> <ul style="list-style-type: none"> <li>• Model for Thutupalli <i>et al.</i> droplet from Ref. [8] based on Diffusion-Advection-Reaction equation for surfactant mixture</li> <li>• Axisymmetric simulations reveal stable swimming, stopping, and oscillating states</li> <li>• Study of droplet dynamics in reduced phase space</li> </ul>
Sect. 4.3	<p><b>Marangoni flow at droplet interfaces:</b></p> <p><b>Three-dimensional solution and applications</b></p> <ul style="list-style-type: none"> <li>• Derivation of flow field, velocity vector, stresslet tensor, and squirmer parameter of droplet with arbitrary surface tension <math>\sigma(\theta, \varphi)</math></li> <li>• Spontaneous symmetry breaking and persistent motion of droplet due to micelle adsorption</li> <li>• Light-induced Marangoni flow: Pushing/pulling an absorbing or transparent droplet with UV/blue light</li> </ul>
Sect. 4.4	<p><b>Active Brownian motion of emulsion droplets:</b></p> <p><b>Coarsening dynamics at the interface and rotational diffusion</b></p> <ul style="list-style-type: none"> <li>• Refined model for Thutupalli <i>et al.</i> droplet without axisymmetry and with thermal noise</li> <li>• Coarsening dynamics of surfactant mixture towards swimming state studied by means of power spectrum of <math>\sigma</math> and average domain size</li> <li>• Rotational diffusion of active droplet due to thermal noise</li> <li>• Perturbation theory confirms scaling law <math>\tau_r \propto \xi^{-2}</math> for rotational correlation time <math>\tau_r</math> and noise strength <math>\xi</math></li> </ul>

Table 4.1: Overview of the publications in Sects. 4.2-4.4.

## **4.2 Swimming active droplet: A theoretical analysis**

*Europhysics Letters*, vol. **101**, p. 44008, 2013, DOI: 10.1209/0295-5075/101/44008

The final publication is available at IOP Science via:

<http://dx.doi.org/10.1209/0295-5075/101/44008>



---

# Swimming active droplet: A theoretical analysis

M. SCHMITT and H. STARK

*Institut für Theoretische Physik, Technische Universität Berlin - Hardenbergstraße 36, 10623 Berlin, Germany, EU*

PACS 47.20.Dr – Surface-tension-driven instability

PACS 47.55.D– Drops and bubbles

PACS 47.55.pf – Marangoni convection

**Abstract** – Recently, an active microswimmer was constructed where a micron-sized droplet of bromine water was placed into a surfactant-laden oil phase. Due to a bromination reaction of the surfactant at the interface, the surface tension locally increases and becomes non-uniform. This drives a Marangoni flow which propels the squirming droplet forward. We develop a diffusion-advection-reaction equation for the order parameter of the surfactant mixture at the droplet interface using a mixing free energy. Numerical solutions reveal a stable swimming regime above a critical Marangoni number  $M$  but also stopping and oscillating states when  $M$  is increased further. The swimming droplet is identified as a pusher whereas in the oscillating state it oscillates between being a puller and a pusher.

---

**Introduction.** – A rigorous understanding of swimming on the micron scale is crucial for developing microfluidic devices such as a lab-on-a-chip [1]. This understanding comes from watching nature, i.e., by studying the locomotion of living organisms such as bacteria or algae [2] but also from designing artificial microswimmers, used for example as medical microrobots [3]. Both, real live cells and man-made microswimmers, have thoroughly been used to study interaction between swimmers [4], interaction with walls [5–8], or swarming [9]. One possible design of an artificial swimmer is an active droplet. Here, we think of a droplet with a surface where a chemical reaction occurs. Alternatively, droplets or bubbles can be made active by having an internal heat source [10]. Droplets are particularly interesting systems to study since they are used extensively in microfluidic devices as microreactors in which chemical or biological reactions take place [11, 12]. In the following we give an example of an active droplet and investigate in detail its propulsion mechanism. Self-propelled active droplets have been studied in various experiments, including droplets on interfaces [13, 14], droplets coupled to a chemical wave [15], and droplets in a bulk fluid [16–19]. Theoretical treatments include a model of droplet motion in a chemically reacting fluid [20], studies of the stability of a resting droplet [21–25], and simulations of contractile droplets [26] and of droplets driven by nonlinear chemical kinetics [27].

The swimming active droplet we consider in the following is a solution of water and bromine which is placed in a

surfactant-rich oil phase [18]. The resulting water droplet has a typical radius of  $80\mu\text{m}$ . In order to lower the surface tension and thus the total energy of the system, the surfactants in the oil phase form a dense monolayer at the droplet interface, giving the droplet the structure of an inverse micelle. The observed directed swimming motion of the droplet with a typical swimming speed of  $15\mu\text{m/s}$  can be understood as follows [18].

The bromine within the droplet chemically reacts with the surfactants in the interface which results in a weaker surfactant. Hence, the 'bromination' reaction locally leads to a higher surface tension in the interface. As a consequence local gradients in surface tension will lead to a fluid flow at the interface and in the adjacent fluid inside and outside of the droplet in the direction of increasing surface tension. This effect is called Marangoni effect. The fluid flow then leads in turn to advection of surfactants at the interface. As a result gradients in surface tension are enhanced. Thus, the resting state becomes unstable and the droplet starts to move. Additionally, brominated surfactants are constantly replaced by non-brominated surfactants from the oil phase by means of desorption and adsorption. The droplet stops to swim when either the bromine or the non-brominated surfactants in the oil phase are exhausted. This was also observed in the experiments [18].

The active droplet is an interesting realization of the 'squirmers' [28, 29] which has been introduced to model the locomotion of microorganisms. Often they propel them-

selves by a carpet of beating short filaments called cilia on their surfaces. Instead of modeling each cilium separately, one prescribes the fluid flow at the surface initiated by the beating cilia which then drags the squirmer through the fluid. Here, for the active droplet the surface flow is generated by the Marangoni effect.

The swimming active droplet crucially depends on the dynamics of the mixture of non-brominated and brominated surfactants at the interface. In this article we model it by means of a diffusion-advection-reaction equation based on a free energy functional for the surfactant mixture. Numerical solutions then show that in a certain parameter range the resting state of the droplet becomes unstable and the droplet starts to move. The solutions reach a stationary state corresponding to a swimming motion and confirm that the droplet is a pusher [2], as found in the experiments [18]. In addition, we identify further patterns of motion. We find that the droplet stops after an initial motion or that it oscillates back and forth.

**Model.** – In order to model the droplet propulsion we set up a dynamic equation for the surfactant mixture at the droplet interface that includes all processes mentioned before. We assume that the surfactant completely covers the droplet interface without any intervening solvent. We also assume that the area of both types of surfactant molecules (brominated and non-brominated) is the same. Denoting the brominated surfactant density by  $c_1$  and the non-brominated density by  $c_2$ , we can therefore set  $c_1 + c_2 = 1$ . We then take the concentration difference between brominated and non-brominated surfactants as an order parameter  $\phi = c_1 - c_2$ . In other words  $\phi = 1$  corresponds to fully brominated and  $\phi = -1$  to fully non-brominated and  $c_1 = (1+\phi)/2$  and  $c_2 = (1-\phi)/2$ . Finally, we choose a constant droplet radius  $R$ .

*Diffusion-Advection-Reaction equation.* The dynamics of  $\phi$  is governed by a diffusion-advection-reaction equation:

$$\dot{\phi} = -\nabla \cdot (\mathbf{j}_D + \mathbf{j}_A) - \tau_R^{-1}(\phi - \phi_{eq}), \quad (1)$$

with diffusive current  $\mathbf{j}_D$  and advective current  $\mathbf{j}_A$  due to the Marangoni effect. The third term on the right-hand side of Eq. (1) is the reaction term and describes the bromination reaction as well as desorption of brominated and adsorption of non-brominated surfactants to and from the outer fluid.  $\tau_R$  is the timescale on which these processes happen and  $\phi_{eq}$  sets the equilibrium coverage of  $\phi$ . In other words, ad- and desorption dominates for  $\phi_{eq} < 0$ , while bromination dominates for  $\phi_{eq} > 0$ . Imagine for instance the case  $\phi_{eq} = 1$ , i.e., a droplet with bromination but without ad- and desorption of surfactants. The reaction term would then always be positive, therefore driving the droplet to a completely brominated state  $\phi = 1$ .

The general mechanism of Eq. (1) is as follows. The diffusive current always points 'downhill',  $\mathbf{j}_D \propto -\nabla\phi$ . However, we will show below that the opposite is true for  $\mathbf{j}_A$  since approximately  $\mathbf{j}_A \propto \nabla\phi$ . Thus, apart from the reaction term,  $\mathbf{j}_D$  and  $\mathbf{j}_A$  are competing and as soon as  $\mathbf{j}_A$

dominates over  $\mathbf{j}_D$ ,  $\phi$  experiences 'uphill' diffusion, i.e. phase separation. As a result the resting state will become unstable and the droplet will start to move. We will now present a careful derivation of  $\mathbf{j}_D$  and  $\mathbf{j}_A$  from a free energy approach. This shows that the diffusive and advective currents in Eq. (1) are in general non-linear functions of  $\phi$ .

*Diffusive current.* The basis for the following is a free energy density  $f$  for the droplet interface, which we write down as a function of concentrations  $c_1$  and  $c_2$ . In formulating the free energy density  $f$ , we follow the Flory-Huggins approach [30]. Accordingly,  $f$  is composed of the mixing entropy plus terms mimicking lateral attractive interaction between surfactants:

$$f = \frac{k_B T}{A} [c_1 \ln c_1 + c_2 \ln c_2 - b_1 c_1^2 - b_2 c_2^2 - b_{12} c_1 c_2], \quad (2)$$

where  $A$  denotes the area of a surfactant in the interface and  $b_1$  ( $b_2$ ) is a dimensionless parameter characterizing the interaction between brominated (non-brominated) surfactants and  $b_{12}$  the interaction between different kind of surfactants. In the following we assume for simplicity  $b_{12} = (b_1 + b_2)/2$ . In terms of the order parameter  $\phi$  we obtain:

$$f(\phi) = \frac{k_B T}{A} \left[ \frac{1+\phi}{2} \ln \frac{1+\phi}{2} + \frac{1-\phi}{2} \ln \frac{1-\phi}{2} - \frac{3}{8}(b_1 + b_2) - \frac{\phi}{2}(b_1 - b_2) - \frac{\phi^2}{8}(b_1 + b_2) \right]. \quad (3)$$

The total free energy is then given by the functional

$$F[\phi] = \int f(\phi) dA. \quad (4)$$

For a conserved order parameter field the diffusive current is proportional to the gradient of the variation in  $F$  with respect to  $\phi$  [31]:

$$\mathbf{j}_D = -\lambda \nabla \frac{\delta F}{\delta \phi} = -\lambda f''(\phi) \nabla \phi \quad (5)$$

$$= -\frac{\lambda k_B T}{A} \left[ \frac{1}{1-\phi^2} - \frac{1}{4}(b_1 + b_2) \right] \nabla \phi, \quad (6)$$

with positive mobility  $\lambda$ . Substituting  $\mathbf{j}_D$  into Eq. (1) yields a Cahn-Hilliard type equation [32]. Note that the diffusion constant in Eq. (6) decreases with increasing interaction energy. In fact, the condition  $\mathbf{j}_D \propto -\nabla\phi$  is only fulfilled for a convex free energy with  $f''(\phi) > 0$ , i.e. if  $b_1 + b_2 < 4$ . In addition, the diffusion coefficient in  $\mathbf{j}_D$  is smallest for  $\phi = 0$ . It increases with  $|\phi|$  and diverges at  $|\phi| = 1$ . An alternative approach of deriving diffusion currents in mixtures is presented in [33, 34].

*Advective current.* The advective current for the order parameter  $\phi$  is given by

$$\mathbf{j}_A = \phi \mathbf{u}, \quad (7)$$

where  $\mathbf{u}$  is the velocity of the surfactants at the interface.<sup>1</sup> Since we are studying the active droplet in an axisymmetric geometry, we assume  $\phi = \phi(\theta)$  and  $\mathbf{u} = u_\theta(\theta)\mathbf{e}_\theta$ , where the front of the droplet is at  $\theta = 0$ , see inset of Fig. 1 (b). For this geometry there exists a solution of the Stokes equation for the fluid flow field inside and outside of the droplet as well as the fluid velocity at the interface [35, 36]. The solution at the interface is given in terms of the surface tension gradient:

$$u_\theta|_{r=R} = \sum_{n=2}^{\infty} \frac{n(n-1)}{2\eta} \left[ \int_0^\pi C_n^{-1/2}(z') \frac{d\sigma}{d\theta'} d\theta' \right] \frac{C_n^{-1/2}(z)}{\sin\theta}, \quad (8)$$

where  $z = \cos(\theta)$ .  $\eta = \eta_i + \eta_o$  is the sum of the viscosities inside and outside of the droplet and  $C_n^{-1/2}$  are Gegenbauer polynomials. They are related to Legendre polynomials by  $P_n(z) = -\frac{d}{dz} C_{n+1}^{-1/2}(z)$ . Equation (8) is nothing but a representation of the Marangoni effect. It essentially states  $\mathbf{u} \propto \nabla\sigma$ , i.e., a fluid flow in the direction of  $\nabla\sigma$ .

Thus, in order to calculate  $u_\theta$ , we need an expression for  $d\sigma/d\theta$ , which can be found by deriving an equation of state for the surface tension  $\sigma$ . The surface tension  $\sigma$  is the thermodynamic force conjugate to the surface area. This gives:

$$\sigma = f - \frac{\partial f}{\partial c_1} c_1 - \frac{\partial f}{\partial c_2} c_2, \quad (9)$$

which we identify as the Legendre transform of the free energy (2) to the chemical potentials  $\mu_i = \frac{\partial f}{\partial c_i}$ . Hence,  $\sigma = \frac{k_B T}{A} [b_1 c_1^2 + b_2 c_2^2 + b_{12} c_1 c_2]$ , or in terms of  $\phi$  and again with  $b_{12} = (b_1 + b_2)/2$ :

$$\sigma(\phi) = \frac{k_B T}{4A} \left[ \frac{9}{8}(b_1 + b_2) + 2(b_1 - b_2)\phi + \frac{7}{8}(b_1 + b_2)\phi^2 \right]. \quad (10)$$

In order to obtain the proper behavior of the equation of state, i.e. an increasing surface tension with increasing  $\phi$ , we need to assure that  $\sigma'(\phi) > 0$ . This holds if  $b_1 > b_2$ , meaning that the interaction energy between brominated surfactants has to be higher than between the non-brominated ones. Note that in the limit of  $\phi \rightarrow 0$  the equation of state becomes linear in  $\phi$ . The gradient of  $\sigma$  is given by

$$\frac{d\sigma}{d\theta} = \sigma'(\phi) \frac{d\phi}{d\theta} = \frac{k_B T}{2A} (b_1 - b_2) \left[ 1 + \frac{7}{8} \frac{b_1 + b_2}{b_1 - b_2} \phi \right] \frac{d\phi}{d\theta}. \quad (11)$$

By substituting this into Eq. (8), one can calculate the advective current (7) for a given  $\phi(\theta)$ .

Eqs. (8) and (11) essentially state that  $\mathbf{u} \propto \nabla\phi$ . Therefore, when  $\phi > 0$ , the advective current  $\mathbf{j}_A = \phi\mathbf{u}$  apparently always points 'uphill', i.e., in the opposite direction compared to  $\mathbf{j}_D$ . On the other hand, when  $\phi < 0$ , the

<sup>1</sup>Let the advective currents of the two types of surfactants be  $\mathbf{j}_A^1 = c_1 \mathbf{u}_1$  and  $\mathbf{j}_A^2 = c_2 \mathbf{u}_2$ . Under the assumption that the individual velocities are identical  $\mathbf{u}_1 = \mathbf{u}_2 = \mathbf{u}$ , one obtains  $\mathbf{j}_A = \mathbf{j}_A^1 + \mathbf{j}_A^2 = \phi \mathbf{u}$ .

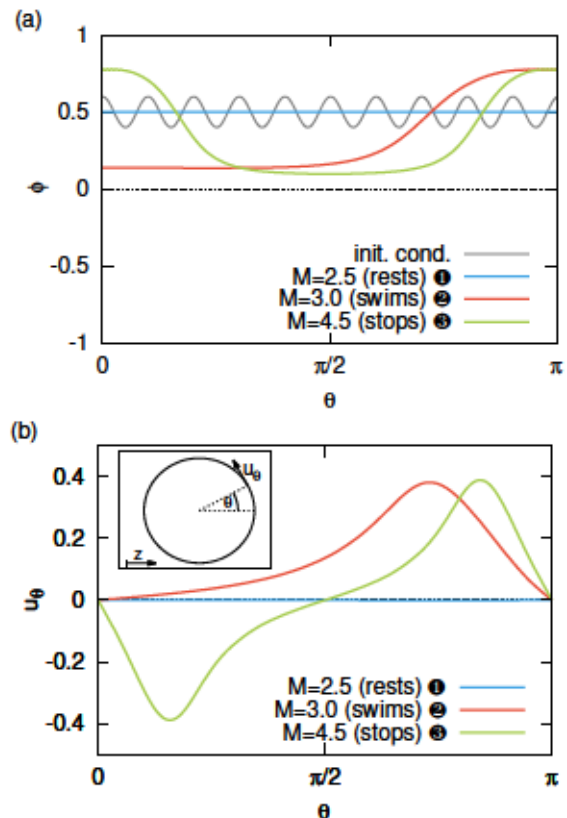


Fig. 1: (a) Stationary order parameter profiles after  $10^6$  time steps for  $\phi_{eq} = 0.5$  and several Marangoni numbers  $M$ . Gray solid line: Initial condition. (b) Corresponding interface velocity profiles. Inset: Droplet geometry.

advective current acts 'downhill', i.e., in the same direction as  $\mathbf{j}_D$ . As a consequence, the Marangoni flow will only drive the droplet when  $\phi > 0$ . This is the case when there are more brominated surfactants than non-brominated ones.

Together with (6) and (7), Eq. (1) becomes a closed equation for  $\phi$ . Writing gradients in units of  $R^{-1}$  and time in units of the diffusion time scale  $\tau_D = R^2 A (\lambda k_B T)^{-1}$  yields

$$\dot{\phi} = -\nabla \cdot (\mathbf{j}_D + M\phi\mathbf{u}) - \kappa(\phi - \phi_{eq}), \quad (12)$$

where the currents  $\mathbf{j}_D$  and  $\mathbf{j}_A = M\phi\mathbf{u}$  are now dimensionless and

$$M = \frac{(b_1 - b_2)R}{\lambda\eta}, \quad (13)$$

is called Marangoni number. This number compares the advective current due to the Marangoni effect, which scales as  $k_B T (b_1 - b_2) (RA\eta)^{-1}$ , to the diffusive current. Accordingly,  $\kappa = \tau_D \tau_R^{-1}$  is the ratio between diffusion and reaction time scale.

**Results.** – We numerically solve the diffusion-advection-reaction equation for  $\phi$  with the initial condition  $\phi(\theta) = \phi_{eq} + \delta\phi(\theta)$ , where  $\delta\phi(\theta)$  is a small perturbation [solid line in Fig. 1(a)]. The boundary conditions at  $\theta = 0, \pi$  are given by a vanishing current,  $\mathbf{j}_D + M\phi\mathbf{u} = 0$ .

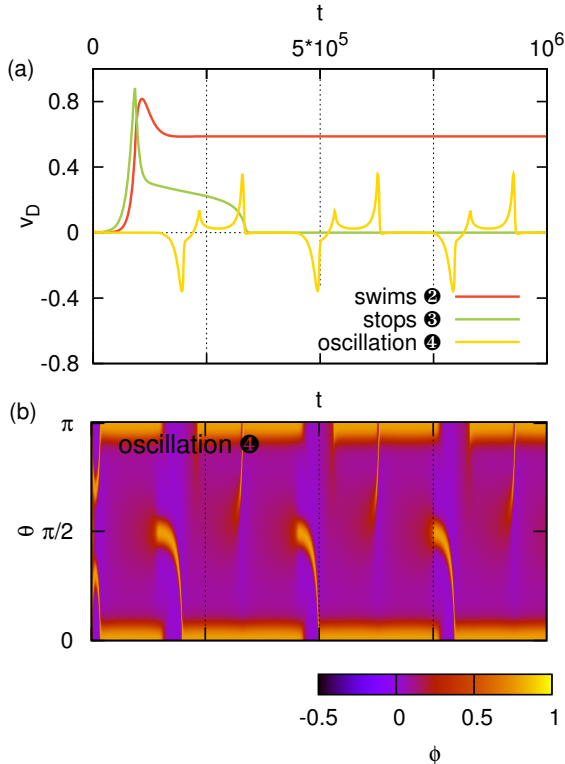


Fig. 2: (a) Droplet swimming velocity  $v_D$  for swimming, stopping, and oscillating droplets. Parameters are the same as in Fig. 1 and case 4 belongs to  $M = 10.5$ . (b) Depiction of the chemical wave of case 4 in a  $\phi(\theta, t)$  plot. Same timescale as in (a).

We keep  $\kappa$  fixed to a value of 0.1 for all numerical solutions and comment later on the impact of  $\kappa$  on the results. Therefore, we are left with the Marangoni number  $M$  and  $\phi_{eq}$  as the crucial parameters. To assure a convex free energy, we set  $b_1 + b_2 = 3$ .

*Order parameter and velocity profiles.* Figure 1(a) shows examples of the stationary order parameter profile for  $\phi_{eq} = 0.5$  and different values of  $M$  together with the corresponding interface velocity profiles in Fig. 1(b). Starting with a small Marangoni number of  $M = 2.5$ , the order parameter relaxes into the homogeneous trivial solution  $\phi = \phi_{eq}$  of Eq. (1), thus the droplet rests. Above a critical Marangoni number, the order parameter evolves to a stationary inhomogeneous profile, as Fig. 1 shows for  $M = 3$ . In parallel, the droplet velocity  $v_D$  depicted in Fig. 2(a) saturates on a non-zero value. The droplet swimming speed is given by  $v_D = (6\eta_i + 4\eta_o)^{-1} \int_0^\pi \sin^2 \theta \frac{d\sigma}{d\theta} d\theta$  [35]. Since  $C_2^{-1/2}(\cos(\theta)) = \sin^2(\theta)/2$ ,  $v_D$  is determined by the first coefficient of the sum in (8) and thus  $v_D = \frac{8}{\pi} \frac{\eta_i + \eta_o}{6\eta_i + 4\eta_o} \int_0^\pi \sin \theta u_\theta d\theta$ . Note that in our approach  $v_D$  reaches a stationary value without having to introduce a 'backward' Marangoni stress, as suggested in [18]. Further increasing the Marangoni number to  $M = 4.5$ , the droplet starts to swim but then stops rapidly. The stationary order parameter profile becomes symmetric around  $\theta = \pi/2$  and swimming is not possible. Finally, the droplet reaches

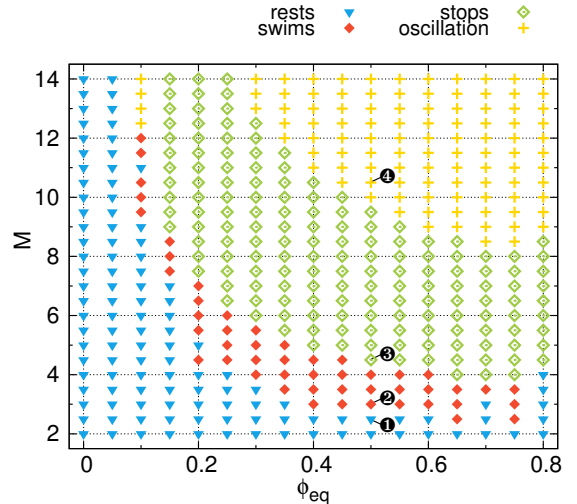


Fig. 3: Phase diagram of the active droplet in  $(\phi_{eq}, M)$  parameter space. Examples for the order parameter profiles at the positions marked with numbers are given in Fig. 1(a) (regime 1-3) and Fig. 2(b) (regime 4).

an oscillating state for even higher Marangoni numbers where it oscillates back and forth as the droplet swimming speed in Fig. 2(a) demonstrates. In this case the order parameter  $\phi(\theta, t)$  resembles a chemical wave that travels back and forth between  $\theta = 0$  and  $\theta = \pi$ . The wave is depicted in Fig. 2(b). Note that the frequency of the oscillation increases with  $M$ . Finally, we remark that from comparing Figs. 1 (a) and (b), it is now apparent that indeed Eq. (8) essentially gives  $\mathbf{u} \propto \nabla \phi$ .

*Phase diagram.* Figure 3 shows the phase diagram in  $(\phi_{eq}, M)$  parameter space with the four regimes of the droplet dynamics: resting, swimming, stopping, and oscillating. Since there is no swimming motion possible for negative  $\phi_{eq}$ , as discussed before, we only show the phase diagram in the range  $0 \leq \phi_{eq} \leq 0.8$ .<sup>2</sup> We find similar phase diagrams for smaller values of  $\kappa$ . For  $\kappa = 0.01$  the swimming region increases in size and then shrinks again for  $\kappa = 0.001$  until for  $\kappa = 0$  swimming solutions are no longer possible. The critical Marangoni number at the onset of the swimming regime stays, however, roughly constant. On the other hand, for  $\kappa = 1$  and 10, i.e., in the limit of fast bromination reaction and exchange of surfactants, only resting, stopping and oscillating solutions but no stable swimming solutions were found.

*Reduced phase space.* Due to the axisymmetric geometry we decompose the order parameter  $\phi$  into Legendre modes

$$\phi(\theta, t) = \sum_{n=0}^{\infty} P_n(\cos(\theta)) \phi_n(t). \quad (14)$$

<sup>2</sup>Due to the  $\phi$  dependent diffusion coefficient in Eq. (6), numerics requires a much finer grid above  $\phi_{eq} = 0.8$ . However, in several tests for different values of  $M$  no swimming solutions were found above  $\phi_{eq} = 0.8$ .

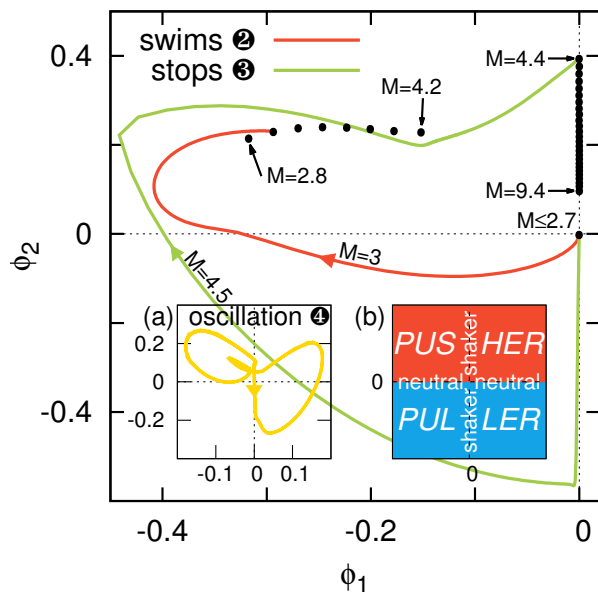


Fig. 4: Droplet dynamics in the reduced phase space  $(\phi_1, \phi_2)$ . Black dots show the fixed points for different values of  $M$ ; from dot to dot  $M$  increases by 0.2. The red and the green line show, respectively, trajectories in the swimming ( $M = 3$ ) and stopping ( $M = 4.5$ ) state. Inset (a): limit cycle in the oscillating state ( $M = 10.5$ ). Inset (b): map for the swimmer type in  $(\phi_1, \phi_2)$  space classified by the stirring parameter  $\beta = -\phi_2/|\phi_1|$  (see main text).

Together with Eqs. (11) and (8) one obtains an expression for  $u_\theta$  as a function of the mode amplitudes  $\phi_n$ .  $\phi_1$  determines the swimming speed and  $\phi_{n>1}$  corresponds to the higher modes of  $u_\theta$ . In the following, we use the initial condition  $\phi_0(t=0) = \phi_{eq}$ . In order to investigate the four regimes of the droplet dynamics, we plot in Fig. 4 the fixed points in  $(\phi_1, \phi_2)$  space for increasing Marangoni number  $M$  at  $\phi_{eq} = 0.5$ . For the cases  $M = 3$  and  $M = 4.5$  the full trajectories are shown. Note that this illustration is a projection onto only two modes of infinitely many modes that make up the full phase space of  $\phi$ . Starting with the resting state, one has a stable fixed point at  $\phi_1 = 0, \phi_2 = 0$  for  $M \leq 2.7$ . Via a subcritical bifurcation the droplet enters the swimming state at the critical Marangoni number  $M = 2.8$ . Figure 4 demonstrates that for the chosen initial condition  $(\phi_1, \phi_2) \approx (0, 0)$  both modes  $\phi_1$  and  $\phi_2$  develop non-zero amplitudes at the same critical Marangoni number. The trajectory in the swimming state does increase its size with increasing  $M$ , whereas the swimming speed decreases until the droplet reaches the stopping state at  $M = 4.3$ . As already observed in Fig. 1, the second mode  $\phi_2$ , which is symmetric around  $\theta = \pi/2$ , clearly dominates in the stopping state. In the oscillating regime above  $M = 9.5$  a stationary solution does not exist. Instead, the dynamics follows a stable limit cycle as the inset (a) in Fig. 4 demonstrates for  $M = 10.5$ . Finally we remark, since the bifurcation is subcritical, the critical Marangoni number for the onset of the swimming state depends on

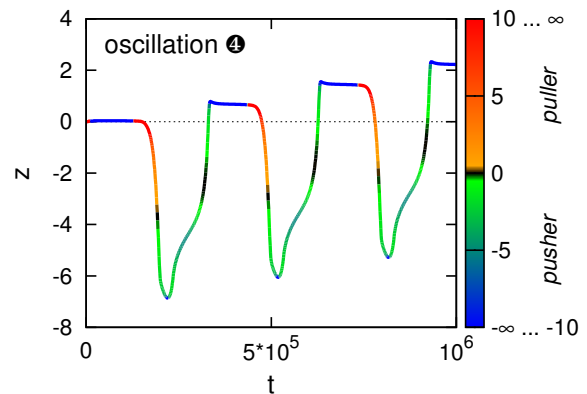


Fig. 5: Displacement of oscillating droplet plotted versus time. Color of line shows the value of stirring parameter  $\beta$ .

the chosen initial condition. For example, starting the numerical solution at  $\phi_1 = \phi_2 = -0.1$  the critical Marangoni number is  $M = 1.7$ .

*The active droplet as pusher.* To describe the basic features of a squirming swimmer, it is sufficient to only study the first two modes of its surface velocity field [2, 28, 29, 37, 38]. While the first mode  $\phi_1$  determines the swimming velocity, the dimensionless 'stirring' parameter  $\beta = -\phi_2/|\phi_1|$  characterizes the swimmer type. When  $\beta$  is negative, the flow around the droplet is similar to the flow around a swimming bacterium such as *E. coli*. Such a swimmer is called a 'pusher' since it pushes fluid away from itself at the front and at the back. Accordingly, a swimmer with  $\beta > 0$  is called a 'puller'. The algae *Chlamydomonas* is an example for a puller since it swims by pulling liquid towards itself at the front and at the back [9]. For  $\beta \rightarrow \pm\infty$  the droplet becomes a 'shaker', i.e., a droplet that shakes the adjacent fluid but does not swim. If  $\beta = 0$ , the first mode dominates and propels the droplet, as is the case for *Volvox* algae [9]. The classification of the swimmers according to the 'stirring' parameter  $\beta$  is illustrated in the inset (b) of Fig. 4. Hydrodynamic interactions between swimmers and with bounding walls depend on their type ('stirring' parameter  $\beta$ ) and strongly influence their (collective) dynamics [7, 39]. For instance, adjacent pushers generally tend to align and swim parallel to each other, i.e., show a polar velocity correlation [40, 41]. In fact this kind of behavior was observed in experiments of our active droplets [18]. It is therefore of great interest to determine  $\beta$ . The swimming droplet with  $\phi_{eq} = 0.5$  is a pusher with  $\beta$  ranging from  $-0.7$  for  $M = 2.8$  to  $-1.5$  for  $M = 4.2$ . Similar values from  $\beta = -0.5$  up to  $-7$  were observed throughout the whole swimming regime of the droplet. The stopping droplet is always a shaker with  $\beta = -\infty$ . Since the limit cycle of the oscillating droplet perambulates all four quadrants of the reduced phase space, it oscillates in the swimming direction as well as in  $\beta$ , i.e., between being a pusher and a puller. This is demonstrated by the droplet displacement plotted versus time in Fig. 5.

**Conclusions.** – We have presented a model for an active squirmer droplet with a surfactant mixture at its interface that drives a Marangoni flow and thereby drags the droplet forward. Based on a free energy functional for the mixture, we derived a diffusion-advection-reaction equation for the mixture order parameter at the droplet interface. Relevant parameters are the Marangoni number  $M$  and the reduced relaxation time  $\kappa^{-1}$  with which the mixture approaches its equilibrium value  $\phi_{eq}$  by bromination or de- and absorption of the surfactants from the surrounding.

As predicted from linear stability analysis in [18], numerical solutions of the diffusion-advection-reaction equation show that above a critical Marangoni number the resting state of the droplet becomes unstable. The order parameter develops a non-uniform profile and the droplet moves with a constant swimming velocity. This only occurs when the relaxation time  $\kappa^{-1}$  (relative to the diffusion time) is sufficiently large. The negative stirring parameter  $\beta$  identifies the droplet as a pusher in agreement with polar velocity correlations found in experiments [18]. A full parameter study in  $(\phi_{eq}, M)$  space also reveals a stopping droplet, which is a shaker ( $\beta = -\infty$ ), and an oscillating droplet that oscillates between being a puller and a pusher. We hope that our work initiates further research on the active droplet which constitutes an attractive realization of the model swimmer called squirmer.

\*\*\*

We thank S. Herminghaus, U. Thiele, S. Thutupalli and A. Zöttl for helpful discussions and the Deutsche Forschungsgemeinschaft for financial support through the Research Training Group GRK 1558.

## REFERENCES

- [1] ABGRALL P. and GU A.-M., *J. Micromech. Microeng.* , **17** (2007) R15.
- [2] LAUGA E. and POWERS T. R., *Rep. Prog. Phys.* , **72** (2009) 096601.
- [3] NELSON B. J., KALIAKATSOS I. K. and ABBOTT J. J., *Annu. Rev. Biomed. Eng.* , **12** (2010) 55.
- [4] ISHIKAWA T., SEKIYA G., IMAI Y. and YAMAGUCHI T., *Biophys. J.* , **93** (2007) 2217 .
- [5] BERKE A. P., TURNER L., BERG H. C. and LAUGA E., *Phys. Rev. Lett.* , **101** (2008) 038102.
- [6] DRESCHER K., DUNKEL J., CISNEROS L. H., GANGULY S. and GOLDSTEIN R. E., *Proc. Natl. Acad. Sci. U. S. A.* , **108** (2011) 10940.
- [7] ZÖTTL A. and STARK H., *Phys. Rev. Lett.* , **108** (2012) 218104.
- [8] REDDIG S. and STARK H., *J. Chem. Phys.* , **135** (2011) 165101.
- [9] LAUGA E. and GOLDSTEIN R. E., *Phys. Today* , **65** (2012) 30.
- [10] REDNIKOV A. Y., RYAZANTSEV Y. S. and VELARDE M. G., *J. Colloid Interface Sci.* , **164** (1994) 168 .
- [11] TEH S.-Y., LIN R., HUNG L.-H. and LEE A. P., *Lab Chip* , **8** (2008) 198.
- [12] SEEMANN R., BRINKMANN M., PFOHL T. and HERMINGHAUS S., *Rep. Prog. Phys.* , **75** (2012) 016601.
- [13] CHEN Y.-J., NAGAMINE Y. and YOSHIKAWA K., *Phys. Rev. E* , **80** (2009) 016303.
- [14] BLIZNYUK O., JANSEN H. P., KOOLJ E. S., ZANDVLIET H. J. W. and POELSEMA B., *Langmuir* , **27** (2011) 11238.
- [15] KITAHATA H., YOSHINAGA N., NAGAI K. H. and SUMINO Y., *Phys. Rev. E* , **84** (2011) 015101.
- [16] TOYOTA T., MARU N., HANCZYC M. M., IKEGAMI T. and SUGAWARA T., *J. Am. Chem. Soc.* , **131** (2009) 5012.
- [17] HANCZYC M. M., TOYOTA T., IKEGAMI T., PACKARD N. and SUGAWARA T., *J Am Chem Soc* , **129** (2007) 9386.
- [18] THUTUPALLI S., SEEMANN R. and HERMINGHAUS S., *New J. Phys.* , **13** (2011) 073021.
- [19] BANNO T., KUROHA R. and TOYOTA T., *Langmuir* , **28** (2012) 1190.
- [20] YABUNAKA S., OHTA T. and YOSHINAGA N., *J. Chem. Phys.* , **136** (2012) 074904.
- [21] REDNIKOV A. Y., RYAZANTSEV Y. S. and VELARDE M. G., *Phys. Fluids* , **6** (1994) 451.
- [22] REDNIKOV A. Y., RYAZANTSEV Y. S. and VELARDE M. G., *J. Non-Equil. Thermody.* , **19** (1994) 95.
- [23] VELARDE M. G., REDNIKOV A. Y. and RYAZANTSEV Y. S., *J. Phys.: Condens. Matter* , **8** (1996) 9233.
- [24] VELARDE M. G., *Phil. Trans. R. Soc. Lond. A* , **356** (1998) 829.
- [25] YOSHINAGA N., NAGAI K. H., SUMINO Y. and KITAHATA H., *Phys. Rev. E* , **86** (2012) 016108.
- [26] TJHUNG E., MARENDUZZO D. and CATES M. E., *Proc. Natl. Acad. Sci. U. S. A.* , **109** (2012) 12381.
- [27] FURTADO K., POOLEY C. M. and YEOMANS J. M., *Phys. Rev. E* , **78** (2008) 046308.
- [28] LIGHTHILL M. J., *Commun. Pur. Appl. Math.* , **5** (1952) 109.
- [29] BLAKE J. R., *J. Fluid. Mech.* , **46** (1971) 199.
- [30] FLORY P. J., *J. Chem. Phys.* , **10** (1942) 51.
- [31] BRAY A. J., *Adv. Phys.* , **51** (2002) 481.
- [32] DESAI R. C. and KAPRAL R., *Dynamics of Self-Organized and Self-Assembled Structures* (Cambridge University Press) 2009.
- [33] NAUMAN E. and HE D. Q., *Chem. Eng. Sci.* , **56** (2001) 1999 .
- [34] THIELE U., ARCHER A. J. and PLAPP M., *Phys. Fluids* , (2012) (submitted).
- [35] LEVAN M. D. and NEWMAN J., *AIChE Journal* , **22** (1976) 695.
- [36] MASON D. P. and MOREMEDI G. M., *Pramana* , **77** (2011) 493.
- [37] DOWNTON M. T. and STARK H., *J. Phys.: Condens. Matter* , **21** (2009) 204101.
- [38] ZHU L., LAUGA E. and BRANDT L., *Phys. Fluids* , **24** (2012) 051902.
- [39] EVANS A. A., ISHIKAWA T., YAMAGUCHI T. and LAUGA E., *Phys. Fluids* , **23** (2011) 111702.
- [40] ISHIKAWA T., SIMMONDS M. P. and PEDLEY T. J., *J. Fluid. Mech.* , **568** (2006) 119.
- [41] ISHIKAWA T. and PEDLEY T. J., *Phys. Rev. Lett.* , **100** (2008) 088103.

### **4.3 Marangoni flow at droplet interfaces: Three-dimensional solution and applications**

*Physics of Fluids*, vol. **28**, p. 012106, 2016, DOI: 10.1063/1.4939212

The publication is available at AIP via:  
<http://dx.doi.org/10.1063/1.4939212>



# Marangoni flow at droplet interfaces: Three-dimensional solution and applications

M. Schmitt and H. Stark

*Institute of Theoretical Physics, Technical University Berlin, Hardenbergstraße 36,  
10623 Berlin, Germany*

(Received 15 June 2015; accepted 15 December 2015; published online 11 January 2016)

The Marangoni effect refers to fluid flow induced by a gradient in surface tension at a fluid-fluid interface. We determine the full three-dimensional Marangoni flow generated by a non-uniform surface tension profile at the interface of a self-propelled spherical emulsion droplet. For all flow fields inside, outside, and at the interface of the droplet, we give analytical formulas. We also calculate the droplet velocity vector  $\mathbf{v}^D$ , which describes the swimming kinematics of the droplet, and generalize the squirmer parameter  $\beta$ , which distinguishes between different swimmer types called neutral, pusher, or puller. In the second part of this paper, we present two illustrative examples, where the Marangoni effect is used in active emulsion droplets. First, we demonstrate how micelle adsorption can spontaneously break the isotropic symmetry of an initially surfactant-free emulsion droplet, which then performs directed motion. Second, we think about light-switchable surfactants and laser light to create a patch with a different surfactant type at the droplet interface. Depending on the setup such as the wavelength of the laser light and the surfactant type in the outer bulk fluid, one can either push droplets along unstable trajectories or pull them along straight or oscillatory trajectories regulated by specific parameters. We explore these cases for strongly absorbing and for transparent droplets. © 2016 AIP Publishing LLC. [<http://dx.doi.org/10.1063/1.4939212>]

## I. INTRODUCTION

Self-propelled particles swimming in fluids at low Reynolds number have recently gained a lot of attention.<sup>1-4</sup> Different methods to construct microswimmers exist. One idea is to generate a slip velocity field close to the swimmer's surface by different phoretic mechanisms that drag the particle forward. A typical example of an artificial swimmer is a nano- or micron-sized Janus colloid. It has two distinct faces that differ in their physical or chemical properties.<sup>5</sup> In the simplest realization, one face catalyzes a chemical reaction and the reactants set up a self-diffusiophoretic flow.<sup>6</sup> A combination of self-diffusio- and electrophoresis close to bimetallic Janus particles in a peroxide solution generates an electrochemical gradient to propel the swimmer.<sup>7,8</sup> Heating a Janus particle, where the thermal conductivity of both faces differs, generates a temperature gradient, in which the colloid moves. This effect is called thermophoresis.<sup>9</sup> Finally, in a binary solvent close to the critical point, the liquid around Janus colloids demixes locally, which also induces a self-diffusiophoretic flow.<sup>10</sup>

Both the individual swimming mechanisms of these Janus particles and other microswimmers as well as their collective motion have evolved into very attractive research topics.<sup>4,11</sup> In fact, the study of collective motion in non-equilibrium systems has opened up a new field in statistical physics. Recent studies of collective motion also concentrate on the role of hydrodynamic flow fields.<sup>12-17</sup>

An alternative realization of a self-propelled particle is an active emulsion droplet. Motivated by the experimental realization of such a swimming droplet<sup>18</sup> and our own work,<sup>19</sup> we construct here first the full three-dimensional solution for the flow field inside and outside of the droplet. It is driven by a non-uniform surface tension profile at the droplet interface. Then, we present two illustrative examples, where it is necessary to use this full solution.

When two immiscible liquid phases are mixed, they form emulsion droplets, which are often stabilized by surfactants. Emulsion droplets can be prepared with a well-defined size. Since they

can enclose very small quantities of matter down to single molecules, they are predestined as microreactors in which chemical or biological reactions take place. Therefore, they are an important building block in microfluidic devices.<sup>20,21</sup> Droplets are commonly divided into two classes: passive droplets, which move due to external forces, and active droplets, which swim autonomously without any external forces. This force-free swimming is a general signature of self-propelled particles.<sup>4</sup>

Self-propelled active droplets in a bulk fluid have been studied in various experiments<sup>18,22–26</sup> including droplets coupled to a chemical wave.<sup>27</sup> Theoretical as well as numerical treatments include deformable and contractile droplets,<sup>28,29</sup> droplets in a chemically reacting fluid,<sup>30</sup> studies of the drift bifurcation of translational motion,<sup>31–35</sup> droplets driven by nonlinear chemical kinetics,<sup>36</sup> and a diffusion-advection-reaction equation for surfactant mixtures at the droplet interface.<sup>19</sup>

In the first part of this paper, we derive the flow field around an emulsion droplet initiated by a non-uniform surface tension at the droplet interface. This phenomenon is known as Marangoni effect.<sup>37</sup> In the proximity of the droplet interface, Marangoni flow is directed towards increasing surface tension. So far, there have been detailed studies of the flow field around active droplets, where the surface tension is axisymmetric  $\sigma = \sigma(\theta)$ .<sup>38,39</sup> Formulas of the non-axisymmetric case have been mentioned in an extensive study of the rheology of emulsion drops and have been used to explain cross-streamline migration of emulsion droplets in Poiseuille flow.<sup>40–42</sup> Here, we present a detailed derivation and illustration of the full flow field for an arbitrary surface tension profile  $\sigma(\theta, \varphi)$  at the droplet interface. We provide formulas for the flow fields inside and outside of the droplet, the droplet velocity vector  $\mathbf{v}^D$ , as well as for the squirmer parameter  $\beta$ , which determines whether a droplet is a pusher or a puller.

In the second part of this paper, we apply the presented formulas to two illustrative examples. There are various causes for a non-uniform surface tension field  $\sigma(\theta, \varphi)$ . A surfactant lowers the surface tension by accumulating at an interface. Thus, the simplest way to generate Marangoni flow is a non-uniform distribution of a surfactant within an interface. In our first, simple example, we consider an initially “clean” or surfactant free droplet<sup>43</sup> immersed in a fluid, which is enriched by micelles, i.e., aggregates of surfactant molecules. When a micelle adsorbs somewhere at the droplet interface, Marangoni flow is induced and propels the droplet in the direction of the adsorption site. Now, the resulting outer fluid flow preferentially advects other micelles towards the existing adsorption site. This mechanism can spontaneously break the isotropic symmetry of the droplet, which then moves persistently in one direction, if the mean adsorption rate of the micelles is sufficiently large. Micelles have been shown to be crucial in the dynamics of active water as well as liquid crystal droplets.<sup>25,26</sup> While we do not attempt to unravel the detailed mechanism for activity in these examples, we present here a simple idea how micelle adsorption generates directed motion.

In the second example, we use a non-uniform mixture of two surfactant types to induce Marangoni flow. Such a mixture can be created by a chemical reaction.<sup>18</sup> Here, we illustrate a different mechanism. Light-switchable surfactants exist which change their conformation under illumination with light.<sup>44</sup> So, by shining laser light onto a droplet covered by light-switchable surfactants,<sup>44</sup> one locally generates a spot of different surfactant molecules. Depending on the surfactant type in the bulk fluid and the wavelength of the laser light, the emulsion droplet is either pushed by the laser beam or pulled towards it. The first situation is unstable and the droplet moves away from the beam and then stops. In the second situation, the droplet moves on a straight trajectory along the beam. With decreasing relaxation rate towards the surfactant in bulk, a Hopf bifurcation occurs and the droplet also oscillates about the beam axis. We explore these cases for strongly absorbing and for transparent droplets.

The article is organized as follows. In Sec. II, we derive the flow fields inside and outside an emulsion droplet induced by a non-uniform surface tension profile. The flow fields depend on the droplet velocity vector  $\mathbf{v}^D$ , which we evaluate and discuss in Sec. III. Section IV discusses characteristics of the flow field and introduces the squirmer parameter in order to classify active droplets as pushers or pullers. The Secs. V and VI contain the illustrative examples. Section V demonstrates how micelle adsorption spontaneously breaks the isotropic droplet symmetry and induces directed propulsion. Finally, in Sec. VI, we introduce and discuss the emulsion droplet covered by a light-switchable surfactant. The article concludes in Sec. VII.

## II. VELOCITY FIELD OF A FORCE-FREE ACTIVE EMULSION DROPLET

In the following, we consider a droplet of radius  $R$  with viscosity  $\hat{\eta}$  of the inside liquid immersed in an unbounded bulk fluid with viscosity  $\eta$ . At low Reynolds number, we have to solve the creeping flow or Stokes equation to determine both the velocity field  $\mathbf{u}(\mathbf{r})$  outside the droplet ( $r > R$ ) and the field  $\hat{\mathbf{u}}(\mathbf{r})$  inside the droplet ( $r < R$ ). Solving the problem needs two steps.<sup>45</sup>

At first, we solve the Stokes equation for a droplet, which is fixed in space, with a given inhomogeneous surface tension  $\sigma$  at the interface. The resulting flow field of this ‘‘pumping problem’’ will be called  $\mathbf{w}$ . Second, we derive the flow field  $\mathbf{v}$  of a passive droplet swimming with a prescribed velocity  $\mathbf{v}^D$ , the so-called Hadamard Rybczynski solution.<sup>46</sup> The complete flow field of the swimming droplet is then given by the superposition of both flow fields:  $\mathbf{u} = \mathbf{v} + \mathbf{w}$ . This approach ensures that the swimming droplet is a force-free swimmer.<sup>4</sup> The droplet velocity vector  $\mathbf{v}^D$  is calculated by means of the Lorentz reciprocal theorem for Stokes flow in Sec. III.

### A. Pumping active droplet

In this section, we fix the active emulsion droplet in space and analyze the velocity fields outside ( $\mathbf{w}$ ) and inside ( $\hat{\mathbf{w}}$ ) of the droplet generated by the inhomogeneous surface tension at the fluid interface. We start with the boundary conditions formulated in spherical coordinates in the droplet frame of reference,

$$\mathbf{w} = \mathbf{0}, \quad r \rightarrow \infty, \quad (1)$$

$$w_r = \hat{w}_r = 0, \quad r = R, \quad (2)$$

$$\mathbf{w} = \hat{\mathbf{w}}, \quad r = R, \quad (3)$$

$$\nabla_s \sigma = \mathbf{P}_s (\hat{\mathbf{T}} - \mathbf{T}) \mathbf{e}_r, \quad r = R, \quad (4)$$

where  $r$  is the distance from the droplet center and  $R$  the droplet radius. These conditions assure that the droplet is fixed in space (1), has an impenetrable interface (2), and the tangential velocity at the interface is continuous (3). Condition (4) states that a gradient in surface tension  $\sigma$  at the interface has to be balanced by a jump in the fluid shear stresses. This gradient in surface tension induces the Marangoni flow close to the interface. Here, we introduce the surface projector  $\mathbf{P}_s = \mathbf{1} - \mathbf{n} \otimes \mathbf{n}$  with surface normal  $\mathbf{n} = \mathbf{e}_r$ . Correspondingly, we use the notation  $\nabla_s = \mathbf{P}_s \nabla$  for the surface gradient, where  $\nabla$  is the nabla operator. In addition, we assume the droplet to be undeformable, i.e., of constant curvature  $\nabla \cdot \mathbf{n} = 2/R$ , and thus do not need to consider the normal stress balance at the interface. Hence, we are in the regime of small capillary number  $Ca = R|\nabla_s \sigma|/|\sigma| \ll 1$ .<sup>33</sup> Finally, the viscous part of the Cauchy stress tensor of an incompressible Newtonian fluid with viscosity  $\eta$  is given by  $\mathbf{T} = \eta [\nabla \otimes \mathbf{w} + (\nabla \otimes \mathbf{w})^T]$ . In spherical coordinates, we find following two equations from condition (4) for the polar and azimuthal components of  $\nabla_s \sigma$ :

$$(\nabla_s \sigma)_\theta = \hat{\eta}(\partial_r \hat{w}_\theta - R^{-1} \hat{w}_\theta) - \eta(\partial_r w_\theta - R^{-1} w_\theta), \quad (5a)$$

$$(\nabla_s \sigma)_\varphi = \hat{\eta}(\partial_r \hat{w}_\varphi - R^{-1} \hat{w}_\varphi) - \eta(\partial_r w_\varphi - R^{-1} w_\varphi). \quad (5b)$$

Fluid flow at the liquid-liquid interface is always driven by a gradient in  $\sigma$ , whereas pressure only acts in normal direction.

We now use the set of boundary conditions (1)-(3) and (5) to solve the Stokes equation  $\eta \nabla^2 \mathbf{w} - \nabla p = \mathbf{0}$  outside and inside the droplet. Due to the spherical symmetry of our problem and since pressure  $p$  satisfies the Laplace equation, the following *ansatz* for the velocity and pressure fields outside the droplet are feasible according to Refs. 47 and 48:

$$\begin{aligned} \mathbf{w} &= \sum_{l=0}^{\infty} \left[ \frac{2-l}{\eta l(4l-2)} r^2 \nabla p_l + \frac{1+l}{\eta l(2l-1)} p_l \mathbf{r} + \nabla \Phi_l + \nabla \times (\chi_l \mathbf{r}) \right], \\ p &= \sum_{l=0}^{\infty} p_l. \end{aligned} \quad (6)$$

Here,  $\chi_l$ ,  $\Phi_l$ , and  $p_l$  are irregular solid harmonics to assure  $\mathbf{w} = 0$  as  $r \rightarrow \infty$  according to Eq. (1),<sup>48</sup>

$$p_l = r^{-(l+1)} \sum_{m=-l}^l \alpha_l^m Y_l^m(\theta, \varphi),$$

$$\Phi_l = r^{-(l+1)} \sum_{m=-l}^l \beta_l^m Y_l^m(\theta, \varphi),$$

where we give the spherical harmonics  $Y_l^m(\theta, \varphi)$  in Appendix A. We already set the pseudoscalar  $\chi_l$  in Eq. (6) to zero. We will express the flow field as a linear function in the surface tension, which is a scalar quantity. Due to the isotropic symmetry of the spherical droplet, a preferred direction does not exist and one cannot construct a term which contains the pseudoscalar  $\chi_l$ . Using the solid harmonics in Eq. (6) results in the following spherical components of the flow field  $\mathbf{w}$  in Eq. (6):

$$w_r = \sum_{l=1}^{\infty} \sum_{m=-l}^l \left[ \frac{l+1}{(4l-2)\eta} \frac{\alpha_l^m}{r^l} Y_l^m - (l+1) \frac{\beta_l^m}{r^{l+2}} Y_l^m \right],$$

$$w_\theta = \sum_{l=1}^{\infty} \sum_{m=-l}^l \left[ \frac{2-l}{l(4l-2)\eta} \frac{\alpha_l^m}{r^l} \partial_\theta Y_l^m + \frac{\beta_l^m}{r^{l+2}} \partial_\theta Y_l^m \right],$$

$$w_\varphi = \sum_{l=1}^{\infty} \sum_{m=-l}^l \left[ \frac{im(2-l)}{l(4l-2)\eta} \frac{\alpha_l^m}{r^l} \frac{Y_l^m}{\sin \theta} + im \frac{\beta_l^m}{r^{l+2}} \frac{Y_l^m}{\sin \theta} \right].$$

The coefficients  $\alpha_l^m$  and  $\beta_l^m$  will be determined in the following. Terms with  $l = 0$  do not appear since the coefficients either vanish due to boundary conditions (1) and (2) ( $\alpha_0^0 = \beta_0^0 = 0$ ).

The *ansatz* for the interior flow inside the droplet is obtained from Eq. (6) by replacing  $l$  by  $-(l+1)$  in the prefactor of each term.<sup>47,48</sup>

$$\hat{\mathbf{w}} = \sum_{l=0}^{\infty} \left[ \frac{(l+3)}{\hat{\eta}(l+1)(4l+6)} r^2 \nabla \hat{p}_l - \frac{l}{\hat{\eta}(l+1)(2l+3)} \hat{p}_l \mathbf{r} + \nabla \hat{\Phi}_l + \nabla \times (\hat{\chi}_l \mathbf{r}) \right],$$

$$\hat{p} = \sum_{l=0}^{\infty} \hat{p}_l,$$
(7)

with regular solid harmonics, which do not diverge at  $r = 0$ ,

$$\hat{p}_l = r^l \sum_{m=-l}^l \hat{\alpha}_l^m Y_l^m(\theta, \varphi),$$

$$\hat{\Phi}_l = r^l \sum_{m=-l}^l \hat{\beta}_l^m Y_l^m(\theta, \varphi).$$

Again, we can set  $\hat{\chi}_l = 0$ . This results in the following spherical components of the flow field  $\hat{\mathbf{w}}$  in Eq. (7):

$$\hat{w}_r = \sum_{l=1}^{\infty} \sum_{m=-l}^l \left[ \frac{l}{(4l+6)\hat{\eta}} r^{l+1} \hat{\alpha}_l^m Y_l^m + l r^{l-1} \hat{\beta}_l^m Y_l^m \right],$$

$$\hat{w}_\theta = \sum_{l=1}^{\infty} \sum_{m=-l}^l \left[ \frac{l+3}{(l+1)(4l+6)\hat{\eta}} r^{l+1} \hat{\alpha}_l^m \partial_\theta Y_l^m + r^{l-1} \hat{\beta}_l^m \partial_\theta Y_l^m \right],$$

$$\hat{w}_\varphi = \sum_{l=1}^{\infty} \sum_{m=-l}^l \left[ \frac{im(l+3)}{(l+1)(4l+6)\hat{\eta}} r^{l+1} \hat{\alpha}_l^m \frac{Y_l^m}{\sin \theta} + im r^{l-1} \hat{\beta}_l^m \frac{Y_l^m}{\sin \theta} \right].$$

Terms with  $l = 0$  are not relevant.

In the following, we successively evaluate conditions (2), (3), and (5) to determine all the coefficients  $\alpha_l^m$ ,  $\hat{\alpha}_l^m$  and  $\beta_l^m$ ,  $\hat{\beta}_l^m$ . The condition of impenetrable interface (2) connects  $\alpha_l^m$  ( $\hat{\alpha}_l^m$ ) with

$\beta_l^m$  ( $\hat{\beta}_l^m$ ),

$$\hat{\alpha}_l^m = \frac{-2\hat{\eta}(2l+3)}{R^2} \hat{\beta}_l^m, \alpha_l^m = \frac{-2\eta(1-2l)}{R^2} \beta_l^m.$$

We eliminate  $\alpha_l^m$  and  $\hat{\alpha}_l^m$  and use the condition  $\hat{w}_\theta|_R = w_\theta|_R$  from Eq. (3) to relate the interior to the exterior coefficients:

$$\hat{\beta}_l^m = -\frac{l+1}{l} R^{-2l-1} \beta_l^m.$$

Evaluating  $\hat{w}_\varphi|_R = w_\varphi|_R$  yields the same relations. In the next step, we use final condition (5) to match the jump in the shear stress to a given profile of the surface tension  $\sigma$ . From Eq. (5) and the coefficients determined above, we find

$$(\nabla_s \sigma)_\theta = \sum_{l=1}^{\infty} \sum_{m=-l}^l \left[ (\eta + \hat{\eta}) \frac{4l+2}{l} \frac{\beta_l^m}{R^{l+3}} \partial_\theta Y_l^m \right], \quad (8a)$$

$$(\nabla_s \sigma)_\varphi = \sum_{l=1}^{\infty} \sum_{m=-l}^l \left[ (\eta + \hat{\eta}) \frac{4l+2}{l} \frac{im\beta_l^m}{R^{l+3}} \frac{Y_l^m}{\sin \theta} \right]. \quad (8b)$$

We also expand the surface tension into spherical harmonics,

$$\sigma(\theta, \varphi) = \sum_{l=1}^{\infty} \sum_{m=-l}^l s_l^m Y_l^m(\theta, \varphi), \quad (9)$$

with coefficients

$$s_l^m = \int_0^{2\pi} \int_0^\pi \sigma(\theta, \varphi) \bar{Y}_l^m(\theta, \varphi) \sin \theta d\theta d\varphi, \quad (10)$$

where  $\bar{Y}_l^m$  is the complex conjugate of  $Y_l^m$  (see Appendix A). Thus, the l.h.s. of Eqs. (8) are given by

$$(\nabla_s \sigma)_\theta = \frac{1}{R} \sum_{l=1}^{\infty} \sum_{m=-l}^l s_l^m \partial_\theta Y_l^m, \quad (11a)$$

$$(\nabla_s \sigma)_\varphi = \frac{1}{R} \sum_{l=1}^{\infty} \sum_{m=-l}^l im s_l^m \frac{Y_l^m}{\sin \theta}. \quad (11b)$$

Comparing Eqs. (8a) and (11a) or alternatively (8b) and (11b), we finally find

$$\beta_l^m = \frac{R^{l+2}}{\eta + \hat{\eta}} \frac{l}{4l+2} s_l^m.$$

This completes the derivation of the velocity field of an active droplet with a given surface tension profile  $\sigma$ , which is fixed in space.

The fluid flow at the interface is now easily calculated by inserting the coefficients  $\beta_l^m$  into the *ansatz* for  $\mathbf{w}$  and setting  $r = R$ ,

$$w_\theta|_R = \frac{1}{\eta + \hat{\eta}} \sum_{l=1}^{\infty} \sum_{m=-l}^l \frac{s_l^m}{2l+1} \partial_\theta Y_l^m, \quad (12a)$$

$$w_\varphi|_R = \frac{1}{\eta + \hat{\eta}} \sum_{l=1}^{\infty} \sum_{m=-l}^l \frac{ims_l^m}{2l+1} \frac{Y_l^m}{\sin \theta}, \quad (12b)$$

with  $s_l^m$  from Eq. (10).

Comparing the components of Eqs. (11) and (12) with each other, we realize that the expansion coefficients only differ by a factor  $1/(2l+1)$ . Thus, the fluid flow at the interface  $\mathbf{w}|_R$  is basically equivalent to a smoothed gradient of the surface tension  $\nabla_s \sigma$ .

## B. Passive droplet

In this section, we will calculate the velocity field  $\mathbf{v}$  of the viscous flow around a passive sphere moving with a velocity  $\mathbf{v}^D$ . In the rest frame of the moving sphere, boundary conditions (2) and (3) from the analysis of the fixed active droplet remain unchanged, while Eqs. (1) and (5) are replaced by

$$\mathbf{v} = -\mathbf{v}^D, \quad r \rightarrow \infty, \quad (13)$$

$$\mathbf{0} = \mathbf{P}_s(\hat{\mathbf{T}} - \mathbf{T})\mathbf{e}_r, \quad r = R. \quad (14)$$

The second condition is equivalent to  $\nabla_s \sigma = 0$ . It means that the fluid shear stress is continuous across the droplet interface and hence the droplet is passive. The procedure of calculating the flow field  $\mathbf{v}$  is very similar to the case of the active droplet in Sec. II A. We outline it in the following.

We employ the same *ansatz* for the external ( $\mathbf{v}$ ) and internal ( $\hat{\mathbf{v}}$ ) droplet field, as we did for  $\mathbf{w}$  and  $\hat{\mathbf{w}}$  for the pumping active droplet in Eqs. (6) and (7). However, in order to satisfy boundary condition (13), we have to add the three spherical components of  $-\mathbf{v}^D$ ,

$$\begin{aligned} -\mathbf{e}_r \cdot \mathbf{v}^D &= -v_1^{-1} Y_1^{-1} - v_1^0 Y_1^0 - v_1^1 Y_1^1, \\ -\mathbf{e}_\theta \cdot \mathbf{v}^D &= -v_1^{-1} \partial_\theta Y_1^{-1} - v_1^0 \partial_\theta Y_1^0 - v_1^1 \partial_\theta Y_1^1, \\ -\mathbf{e}_\varphi \cdot \mathbf{v}^D &= -i v_1^1 \frac{Y_1^1}{\sin \theta} + i v_1^{-1} \frac{Y_1^{-1}}{\sin \theta}, \end{aligned}$$

to the *ansatz* for  $\mathbf{v}$ , where we have introduced the coefficients  $v_l^m$  for  $\mathbf{v}^D$ . This is equivalent to  $\mathbf{v}^D$  in Cartesian representation,

$$\mathbf{v}^D = -\sqrt{\frac{3}{8\pi}} \begin{pmatrix} v_1^1 - v_1^{-1} \\ i(v_1^1 + v_1^{-1}) \\ -\sqrt{2}v_1^0 \end{pmatrix}. \quad (15)$$

From condition (2), we find

$$\begin{aligned} \hat{\alpha}_l^m &= \frac{-2\hat{\eta}(2l+3)}{R^2} \hat{\beta}_l^m, \\ \alpha_l^m &= \frac{-2\eta(1-2l)}{R^2} \left( \beta_l^m + \delta_{l,1} \frac{R^3}{2} v_l^m \right), \end{aligned}$$

just as in the active case of Sec. II A. Boundary condition (3) relates  $\hat{\beta}_l^m$  to  $\beta_l^m$ ,

$$\hat{\beta}_l^m = -\frac{l+1}{l} R^{-2l-1} \beta_l^m + \frac{\delta_{l,1}}{2} v_l^m.$$

Finally, we use boundary condition (14) to derive

$$\hat{\beta}_1^m = \frac{\eta}{2(\eta + \hat{\eta})} v_1^m,$$

while all other coefficients with  $l \geq 2$  vanish. So, we have related all coefficients to the components  $v_1^m$  of  $\mathbf{v}^D$ .

We obtain the axially symmetric velocity field  $\mathbf{v}$  of a passive droplet, the so called Hadamard-Rybczynski solution of a creeping droplet,<sup>46</sup> which moves with velocity  $\mathbf{v}_D$ . In Appendix B, where we give the complete velocity field  $\mathbf{u}$  of the active droplet, one can read off the flow field  $\mathbf{v}$  as the terms that contain  $\mathbf{v}_D$ . These terms either decay as  $1/r$  or  $1/r^3$ . In particular, the velocity field at the interface is

$$v_\theta|_R = \frac{-\eta}{2(\eta + \hat{\eta})} \mathbf{e}_\theta \cdot \mathbf{v}^D, \quad (16a)$$

$$v_\varphi|_R = \frac{-\eta}{2(\eta + \hat{\eta})} \mathbf{e}_\varphi \cdot \mathbf{v}^D. \quad (16b)$$

We will calculate the droplet velocity  $\mathbf{v}^D$  in Sec. III.

Note that, as  $\hat{\eta} \rightarrow \infty$ , one recovers the usual no-slip boundary condition of a rigid sphere.

### C. Complete solution

The complete flow field of the force-free swimming active droplet is the sum of both contributions, from the fixed active and the passive droplet. The velocity fields inside ( $\hat{\mathbf{u}} = \hat{\mathbf{v}} + \hat{\mathbf{w}}$ ) and outside ( $\mathbf{u} = \mathbf{v} + \mathbf{w}$ ) of the droplet are summarized in [Appendix B](#). The formulas are equivalent to the ones in Refs. [40–42](#). The outside flow field is also presented in the lab frame. Here, we mention the velocity field  $\mathbf{u}|_R = \mathbf{w}|_R + \mathbf{v}|_R$  at the interface with  $\mathbf{w}|_R$  taken from Eq. (12) and  $\mathbf{v}|_R$  from Eq. (16),

$$u_{\theta}|_R = \frac{-\eta}{2(\eta + \hat{\eta})} \mathbf{e}_{\theta} \cdot \mathbf{v}^D + \frac{1}{\eta + \hat{\eta}} \sum_{l=1}^{\infty} \sum_{m=-l}^l \frac{s_l^m}{2l+1} \partial_{\theta} Y_l^m, \quad (17a)$$

$$u_{\varphi}|_R = \frac{-\eta}{2(\eta + \hat{\eta})} \mathbf{e}_{\varphi} \cdot \mathbf{v}^D + \frac{1}{\eta + \hat{\eta}} \sum_{l=1}^{\infty} \sum_{m=-l}^l \frac{ims_l^m}{2l+1} \frac{Y_l^m}{\sin \theta}. \quad (17b)$$

Before studying the axisymmetric limit, we investigate the role of viscosity. The most commonly studied droplet emulsions are either oil droplets in water or vice versa, where typical viscosities are  $\eta_{\text{water}} = 1$  mPa s and  $\eta_{\text{oil}} = 36$  mPa s.<sup>18,25</sup> We will show in Sec. III that  $\mathbf{v}^D \propto (2\eta + 3\hat{\eta})^{-1}$ . Using this result in Eqs. (17), we find that in the case  $\eta \geq \hat{\eta}$ , both  $\mathbf{w}$  and  $\mathbf{v}$  scale as  $1/\eta$ . In the opposite case,  $\eta \ll \hat{\eta}$ , the pumping solution scales as  $\mathbf{w} \propto 1/\hat{\eta}$  while  $\mathbf{v} \propto \eta/\hat{\eta}^2$ . Hence, for an oil drop in water, one can neglect  $\mathbf{v}$ , when calculating the velocity field (17) at the interface.

An axisymmetric surface tension  $\sigma = \sigma(\theta)$ , where only spherical harmonics with  $m = 0$  contribute in Eqs. (9) and (17a), yields

$$u_{\theta}|_R = \frac{\eta \sin \theta v_z^D}{2(\eta + \hat{\eta})} + \frac{1}{2(\eta + \hat{\eta})} \sum_{l=1}^{\infty} \left( \int_0^{\pi} \sigma P_l \sin \theta d\theta \right) P_l^1. \quad (18)$$

Here,  $P_l(\cos \theta)$  are Legendre polynomials of degree  $l$  and  $P_l^1(\cos \theta) = \partial_{\theta} P_l(\cos \theta)$ .

Levan and Newman already solved the case of an axisymmetric swimming droplet,<sup>38</sup> where the Stokes equation can be rephrased to a simpler fourth-order partial differential equation for a scalar stream function.<sup>48</sup> They found the flow field at the interface,

$$u_{\theta}|_R = \frac{\eta \sin \theta v_z^D}{2(\eta + \hat{\eta})} + \frac{1}{2(\eta + \hat{\eta})} \sum_{l=2}^{\infty} l(l-1) \left( \int_0^{\pi} C_l^{-1/2} \partial_{\theta} \sigma d\theta \right) \frac{C_l^{-1/2}}{\sin \theta}, \quad (19)$$

where  $C_l^{-1/2}(\cos \theta)$  are Gegenbauer polynomials of order  $l$  and degree  $-1/2$ . These are connected to Legendre polynomials by  $\frac{d}{d \cos \theta} C_l^{-1/2} = -P_{l-1}$ . A standard calculation, which uses the properties of Legendre and Gegenbauer polynomials, shows indeed that Eqs. (19) and (18) are equivalent.

The general solution for the surface flow, Eqs. (17), still contains the unknown droplet velocity vector  $\mathbf{v}^D$ . We will calculate  $\mathbf{v}^D$  in Sec. III, by relating it to the non-uniform surface tension.

### III. DROPLET VELOCITY VECTOR

A central quantity in all studies of swimming droplets is the swimming speed  $v^D$ . Furthermore, for droplets without an axial symmetry, the swimming direction  $\mathbf{e}$  is not obvious. Both together define the droplet velocity vector  $\mathbf{v}^D = v^D \mathbf{e}$ . Once this quantity is known, the flow field  $\mathbf{u}|_R$  in (17) is completely determined.

In order to derive an expression for  $\mathbf{v}^D$ , we stress that an active particle is force-free.<sup>4</sup> Accordingly, the total hydrodynamic drag force  $\mathbf{F} = \mathbf{F}_a + \mathbf{F}_p$ , acting on the particle, has to vanish. Here,  $\mathbf{F}_a$  and  $\mathbf{F}_p$  are the drag forces of the active pumping droplet and the passive droplet, treated in Secs. II A and II B, respectively. The drag forces are given by  $\mathbf{F}_a = -4\pi \nabla(r^3 p_{1|a})$  and  $\mathbf{F}_p = -4\pi \nabla(r^3 p_{1|p})$ , respectively, with solid harmonics  $p_{1|a}$  and  $p_{1|p}$  of the corresponding flow fields.<sup>48</sup> For the passive droplet, one finds

$$\mathbf{F}_p = -6\pi\eta R \frac{2\eta + 3\hat{\eta}}{3\eta + 3\hat{\eta}} \mathbf{v}^D, \quad (20)$$

also known as the Hadamard and Rybczynski drag force of a droplet.<sup>46,49,50</sup> It reduces to the well known Stokes drag of a solid sphere for  $\hat{\eta} \gg \eta$ , whereas it predicts a reduced drag for droplets and bubbles, due to a finite slip velocity at the interface. The condition  $\mathbf{F}_a + \mathbf{F}_p = 0$  gives the simple relation  $\alpha_1^m|_a + \alpha_1^m|_p = 0$  between the coefficients determined in Secs. II A and II B and ultimately yields  $v_1^m = -2s_1^m/(9\hat{\eta} + 6\eta)$ . Here,  $v_1^m$  are the coefficients of the velocity vector  $\mathbf{v}^D$  introduced in Eq. (15). Thus, one finds<sup>41,51</sup>

$$\mathbf{v}^D = \sqrt{\frac{1}{6\pi} \frac{1}{2\eta + 3\hat{\eta}}} \begin{pmatrix} s_1^1 - s_1^{-1} \\ i(s_1^1 + s_1^{-1}) \\ -\sqrt{2}s_1^0 \end{pmatrix}. \quad (21)$$

An equivalent relation writes  $\mathbf{v}^D$  as the average of flow field  $\mathbf{w}$  over the droplet surface, see Appendix C. The droplet velocity vector is solely determined by the dipolar coefficients ( $l = 1$ ) in the multipole expansion of the surface tension  $\sigma$ . It can be written as  $\mathbf{v}^D = v^D \mathbf{e}$  with

$$v^D = \frac{\sqrt{2(s_1^0)^2 - 4s_1^1 s_1^{-1}}}{\sqrt{6\pi(2\eta + 3\hat{\eta})}}, \quad (22a)$$

$$\mathbf{e} = \frac{1}{\sqrt{2(s_1^0)^2 - 4s_1^1 s_1^{-1}}} \begin{pmatrix} s_1^1 - s_1^{-1} \\ i(s_1^1 + s_1^{-1}) \\ -\sqrt{2}s_1^0 \end{pmatrix}. \quad (22b)$$

Next, we derive an alternative formula for  $\mathbf{v}^D$ . Using the explicit expressions for the  $s_1^m$  from Eq. (10) and the Cartesian components of the radial unit vector  $\mathbf{e}_r$ , we rewrite Eq. (21) as  $\mathbf{v}^D = -[2\pi R^2(2\eta + 3\hat{\eta})]^{-1} \iint \sigma \mathbf{e}_r dA$ . Finally, extending  $\sigma$  into the droplet with  $\partial\sigma/\partial r = 0$  and applying Gauss's theorem, we obtain

$$\mathbf{v}^D = \frac{-1}{4\pi R(2\eta + 3\hat{\eta})} \iint \nabla_s \sigma dA.$$

Thus, the droplet velocity vector  $\mathbf{v}^D$  is simply given by the integral of the surface-tension gradient  $\nabla_s \sigma$  over the whole droplet surface. By comparing this with the alternative formula for  $\mathbf{v}^D$  in Eq. (C1), we realize that for calculating the droplet speed, the following equivalence holds:

$$\mathbf{w}|_R \hat{=} \frac{R}{3(\eta + \hat{\eta})} \nabla_s \sigma. \quad (23)$$

By using the  $\hat{=}$  symbol, we stress that this equivalence is only valid in Eq. (C1) and not for the flow field  $\mathbf{w}|_R$  in general. However, Eq. (23) illustrates that the surface flow is initiated by a gradient in the surface tension.

In the axisymmetric case ( $m = 0$ ),  $\mathbf{v}^D = -v^D \mathbf{e}_z$  points against the  $z$  direction with

$$v^D = \frac{1}{2\eta + 3\hat{\eta}} \int_0^\pi \sigma \cos \theta \sin \theta d\theta,$$

which is equivalent to the swimming speed calculated by Levan and Newman.<sup>38</sup> Note that the swimming velocity is independent of the droplet radius  $R$ .

*Ansätze* (6) and (7) for flow and pressure fields can also be used to treat droplets of non-spherical shape.<sup>48</sup> For the torque, which a droplet experiences from the surrounding fluid, one finds  $\mathbf{M} = -8\pi\eta \nabla(r^3 \chi_1)$ .<sup>48</sup> However, as explained in Sec. II A, the solid harmonic  $\chi_1$  vanishes and thus  $\mathbf{M} = 0$ . Therefore, for a spherical droplet, the angular velocity is zero,  $\mathbf{\Omega} = \mathbf{0}$ , and the swimming kinematics is completely determined by  $\mathbf{v}^D$ . Hence, there is no generalization of the Stokes drag torque  $\mathbf{M} = -8\pi\eta R^3 \mathbf{\Omega}$  of a rigid particle to an emulsion droplet.

#### IV. CHARACTERISTICS OF FLOW FIELD

In this section, we discuss some characteristics of the outside flow field  $\mathbf{u}(\mathbf{r})$  fully presented in [Appendix B](#). Flow fields around an active particle can be written as a superposition of flow singularities.<sup>52,53</sup> The lowest singularity, the Stokeslet, is the flow field due to a point force  $f\delta(\mathbf{r})\mathbf{a}$  pointing in direction  $\mathbf{a}$ . It decays as  $\mathbf{u} \propto r^{-1}$  and is only present if external forces act on the particle. In our analysis, we do not consider external forces.

The leading singularity of a force-free active droplet is the stresslet. An example is the force dipole constructed from two Stokeslets, which one obtains by taking the derivative of the Stokeslet along a given direction  $\mathbf{b}$ . The resulting flow field decays as  $\mathbf{u} \propto r^{-2}$ . In general, the stresslet corresponds to the symmetrized first moment of the force distribution on the particle surface. Thus, it is characterized by the symmetric tensor  $\mathbf{S} = -\frac{2\pi}{3}\nabla \otimes \nabla(r^5 p_2)$  with solid harmonic  $p_2$ , which here comes from the pumping active droplet.<sup>54</sup> One obtains

$$\mathbf{S} = \sqrt{\frac{6\pi}{5}} \frac{R^2\eta}{\eta + \hat{\eta}} \begin{pmatrix} s_2^{-2} - \sqrt{\frac{2}{3}}s_2^0 + s_2^2 & i(s_2^2 + s_2^{-2}) & s_2^{-1} - s_2^1 \\ i(s_2^2 + s_2^{-2}) & -s_2^{-2} - \sqrt{\frac{2}{3}}s_2^0 - s_2^2 & -i(s_2^{-1} + s_2^1) \\ s_2^{-1} - s_2^1 & -i(s_2^{-1} + s_2^1) & 2\sqrt{\frac{2}{3}}s_2^0 \end{pmatrix}. \quad (24)$$

For instance, the flow field of two Stokeslets in direction  $\mathbf{a} = \pm\mathbf{e}_x$ , which are connected along  $\mathbf{b} = \mathbf{e}_y$ , is given by component  $S_{xy}$ . Clearly, only the coefficients  $s_2^m$  account for the stresslet.

The singularities that account for a decay of the velocity field as  $\mathbf{u} \propto r^{-3}$  are both the source dipole and the Stokes quadrupole. The source dipole is responsible for droplet propulsion and thus related to the droplet velocity vector  $\mathbf{v}^D$  with the coefficients  $s_1^m$  [see Eq. (21)]. Hence, these coefficients are always non-zero when the droplet is swimming. The Stokes quadrupole is, for example, a combination of two stresslets. It is related to the second moment of the force distribution, a tensor of rank three. As can be observed from [Appendix B](#), the coefficients  $s_3^m$  account for the Stokes quadrupole. To summarize, the lowest-order decay of the flow field around a swimming active droplet is therefore either  $\mathbf{u} \propto r^{-3}$  in the case of  $\mathbf{S} = 0$  or  $\mathbf{u} \propto r^{-2}$  if  $\mathbf{S} \neq 0$ .

#### A. Generalized squirmer parameter

A useful parameter to quantify the type of a microswimmer driven by surface flow is the squirmer parameter  $\beta$ . It compares the stresslet strength to the source dipole. The squirmer is a classic model of an axisymmetric spherical microswimmer.<sup>55,56</sup> It has recently been generalized to the non-axisymmetric case.<sup>45</sup> The essential boundary condition of a squirmer is a prescribed flow field  $\mathbf{w}|_R$  at the surface of a sphere. In contrast, the flow field  $\mathbf{w}|_R$  of an active droplet is the result of a non-uniform surface tension at the fluid interface.

In the following, we calculate the squirmer parameter  $\beta$  for an active droplet with arbitrary swimming direction as a function of the angular expansion coefficients  $s_2^m$  of the surface tension. For an axisymmetric squirmer with surface flow velocity

$$u_\theta|_R = B_1 \sin \theta + \frac{B_2}{2} \sin 2\theta, \quad (25)$$

one defines the squirmer parameter  $\beta$  as<sup>4,55-58</sup>

$$\beta = B_2/|B_1|, \quad (26)$$

where  $2/3 |B_1|$  is the swimming speed. When  $\beta$  is positive, the surface flow is stronger in the front on the northern hemisphere and the flow around the squirmer is similar to the flow field initiated by a swimming algae such as *Chlamydomonas*. The swimmer is called a ‘‘puller’’ since it pulls itself through the fluid. Accordingly, a swimmer with  $\beta < 0$  is called a ‘‘pusher.’’ For example, the bacterium *E. coli* swims by pushing fluid away from itself at the back by a rotating flagellum.<sup>4</sup> For  $\beta \neq 0$ , the flow field far away from the swimmer is dominated by the hydrodynamic stresslet or force dipole

with  $\mathbf{u} \propto r^{-2}$ . However, in the case  $\beta = 0$  (“neutral swimmer”), the source dipole with  $\mathbf{u} \propto r^{-3}$  dominates. One example for a neutral swimmer is the *Volvox* algae.<sup>4</sup> For  $\beta \rightarrow \pm\infty$ , the swimmer becomes a “shaker” that shakes the adjacent fluid but does not swim. Note that hydrodynamic interactions between swimmers as well as between swimmers and walls strongly depend on their type, i.e., on the squirmer parameter  $\beta$ . Thus,  $\beta$  is a key parameter in the study of individual swimmers as well as their collective dynamics.<sup>13,15,16,19</sup>

For squirmers without axisymmetry but still swimming along the  $z$ -axis, Eq. (25) also contains terms depending on the azimuthal angle  $\varphi$ . In addition, a multipole expansion for the azimuthal velocity component  $u_\varphi|_R$  has to be added. Still, the coefficient  $B_1$  determines the swimming speed and  $\beta$  the swimmer type since contributions from multipole terms with  $m \neq 0$  vanish when averaging over  $\varphi$ .

So, we first determine the squirmer parameter for an axisymmetric droplet that swims in  $z$  direction. Since  $\beta$  is related to flow fields decaying like  $1/r^2$ , we only have to consider the velocity field  $\mathbf{w}$  of the pumping active droplet. For the surface tension profile

$$\begin{aligned}\sigma &= s_1^0 Y_1^0 + s_2^0 Y_2^0 \\ &= \sqrt{\frac{3}{4\pi}} s_1^0 \cos\theta + \sqrt{\frac{5}{4\pi}} s_2^0 \left( \frac{3}{2} \cos^2\theta - \frac{1}{2} \right),\end{aligned}$$

where we have only included the relevant two leading modes, we find from Eq. (12a) the following:

$$w_\theta|_R = \frac{-1}{\eta + \hat{\eta}} \left( \frac{s_1^0}{\sqrt{12\pi}} \sin\theta + \frac{1}{2} \frac{3s_2^0}{\sqrt{20\pi}} \sin 2\theta \right).$$

Comparing with Eq. (25), we identify the squirmer parameter of the swimming axisymmetric droplet as the ratio

$$\beta = -\sqrt{\frac{27}{5}} \frac{s_2^0}{|s_1^0|}. \quad (27)$$

In Eq. (D1) in Appendix D, we relate all the angular coefficients  $s_l^0$  to the squirmer coefficients  $B_l$ , which yields the same expression for  $\beta$ .

The ratio of stresslet tensor component  $S_{zz} = \mathbf{e}_z \cdot \mathbf{S} \mathbf{e}_z$  and velocity  $v^D$  is proportional to  $\beta$  from Eq. (27). Similarly, when projecting the stresslet tensor  $\mathbf{S}$  onto an arbitrary swimming direction  $\mathbf{e}$ , one averages over the azimuthal angle about  $\mathbf{e}$ . So, the generalized squirmer parameter to characterize pushers and pullers becomes

$$\beta = -\frac{3}{4\pi R^2} \frac{\eta + \hat{\eta}}{(2\eta + 3\hat{\eta})\eta} \frac{\mathbf{e} \cdot \mathbf{S} \mathbf{e}}{v^D}. \quad (28)$$

Here, we have set the prefactor such that  $\beta$  agrees with Eq. (27) for  $\mathbf{e} = \mathbf{e}_z$ . In Eq. (E1) in Appendix E, we give the concrete expression for  $\beta$  in terms of  $s_1^m$  and  $s_2^m$ . Note that in the non-axisymmetric case,  $\beta = 0$  does not mean that the stresslet is zero. For this, all components of the stresslet tensor have to vanish. Only then one can conclude that a flow field with  $\mathbf{u} \propto r^{-2}$  does not exist.

## B. Surface divergence

The solution of the Stokes equation for the flow field  $\mathbf{u}$ , which we presented in Sec. II C, fulfills the incompressibility condition  $\nabla \cdot \mathbf{u} = 0$  everywhere, i.e., also at the interface. However, this does not necessarily hold for the surface divergence  $\nabla_s \cdot \mathbf{u}|_R$ . Using  $\nabla_s^2 Y_l^m = -l(l+1)R^{-2}Y_l^m$ , one finds from Eqs. (17) the following:

$$\nabla_s \cdot \mathbf{u}|_R = \frac{R^{-1}}{\eta + \hat{\eta}} \left[ \eta \mathbf{e}_r \cdot \mathbf{v}^D - \sum_{l=1}^{\infty} \sum_{m=-l}^l \frac{l(l+1)s_l^m}{2l+1} Y_l^m \right]. \quad (29)$$

Thus, any surface actuation  $s_l^m \neq 0$  results in  $\nabla_s \cdot \mathbf{u}|_R \neq 0$ . In other words, surface divergence is a necessary condition for propulsion.<sup>25,59</sup> In fact, the surface divergence of the pumping field  $\nabla_s \cdot \mathbf{w}|_R$ , i.e., the second term on the r.h.s. of Eq. (29), contains the expansion coefficients of  $\sigma$  amplified

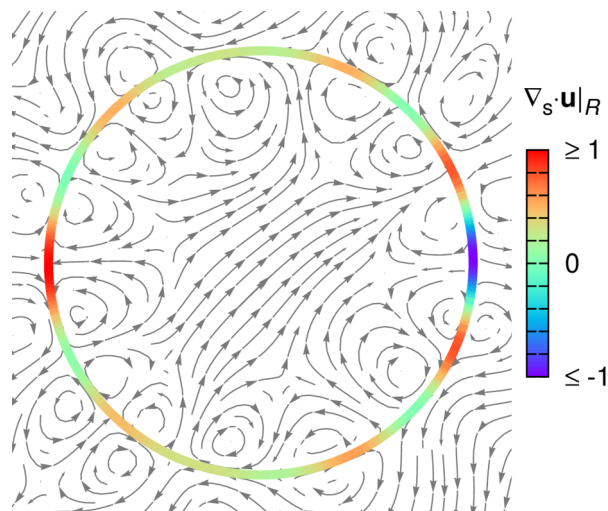


FIG. 1. Inside ( $\hat{\mathbf{u}}$ ) and outside ( $\mathbf{u}$ ) velocity field streamlines at a cross section through an emulsion droplet for a given surface tension  $\sigma(\theta, \varphi)$ . To draw the streamlines, the velocity vectors at the cross section are projected onto the cross section. Moreover, the surface divergence  $\nabla_s \cdot \mathbf{u}|_R$  at the droplet interface is shown.

by a prefactor  $O(l)$ . Furthermore, comparing Eq. (29) with the radial components of the inside and outside velocity fields  $\hat{u}_r$  and  $u_r$  from (B1a) and (B1d), respectively, one finds the following. Regions at the interface with positive divergence,  $\nabla_s \cdot \mathbf{u}|_R > 0$ , are accompanied by radial flows  $\hat{u}_r > 0$  and  $u_r < 0$  towards the interface. On the other hand, regions with convergence, i.e., negative divergence,  $\nabla_s \cdot \mathbf{u}|_R < 0$ , induce radial flows  $\hat{u}_r < 0$  and  $u_r > 0$  away from the interface. Figure 1 illustrates this. Depicted is the surface divergence  $\nabla_s \cdot \mathbf{u}|_R$  along with the streamlines of  $\hat{\mathbf{u}}$  and  $\mathbf{u}$  at a cross section through an emulsion droplet with given surface tension field  $\sigma(\theta, \varphi)$ . In Section V, we will build on this finding and demonstrate how micelle adsorption spontaneously breaks the isotropic symmetry of the droplet interface and thereby induces propulsion.

## V. SPONTANEOUS SYMMETRY BREAKING BY MICELLE ADSORPTION

For the remainder of this paper, we will discuss possible applications for Marangoni flow initiated at the interface of an emulsion droplet. In this section, we present a model of a droplet which performs directed motion by adsorbing micelles, i.e., spherical aggregates of surfactant molecules. We consider a spherical oil droplet in water, the surface of which, initially, is hardly covered by surfactant molecules. Due to the small ratio of viscosities outside and inside the droplet,  $\eta \ll \hat{\eta}$ , we neglect the passive part  $\mathbf{v}$  of the velocity field and set  $\mathbf{u} = \mathbf{w}$ , as pointed out in Sec. II C. The surrounding water phase is homogeneously enriched with micelles formed by surfactant molecules. In the following, we explain how this setup can lead to a persistent swimming motion of the droplet. Once one of the micelles with radius  $R_M$  hits the droplet interface, the surfactants will adsorb at the droplet interface with a probability  $p$  and cover a circular region of area  $4\pi R_M^2$ , as illustrated in Fig. 2. Thus, at the adsorption site, surface tension is lower compared to the surrounding surfactant-free interface. The resulting Marangoni flow is directed away from the adsorption site and therefore spreads the surfactants over the droplet interface. The interfacial Marangoni flow  $\mathbf{u}|_R = \mathbf{w}|_R$  induces a displacement of the droplet in the direction of the adsorption site with a velocity given in Eq. (C1). Furthermore, the flow is accompanied by a positive surface divergence  $\nabla_s \cdot \mathbf{u}|_R > 0$  and inward radial flow  $u_r < 0$  at the front of the droplet, as discussed in Sec. IV B. The flow field initiated by an adsorbed micelle is illustrated in the inset of Fig. 2. Now, the radial flow towards the interface advects additional micelles and thereby increases the rate with which surfactants adsorb at the front of the droplet. Following this train of thought, we expect the droplet to eventually develop a spot with increased surfactant coverage thereby breaking the isotropic symmetry of the interface. As a result, the droplet performs directed motion that comes to an end when the interface is fully covered by surfactants.

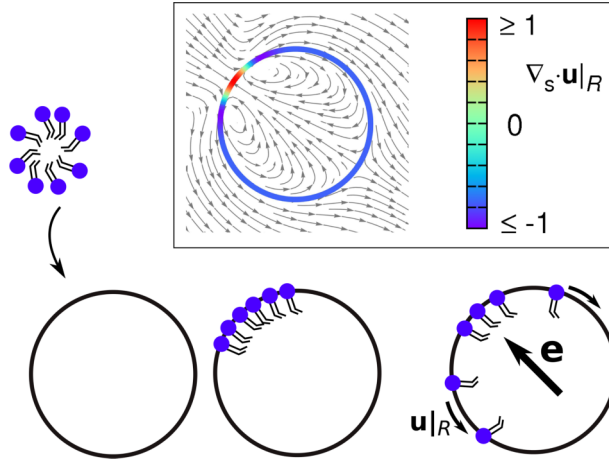


FIG. 2. Cartoon of a micelle adsorbing at the interface of an emulsion droplet. Marangoni flow  $\mathbf{u}|_R$  spreads the surfactants over the interface and propels the droplet in direction  $\mathbf{e}$  towards the adsorption site. Inset: Flow field and color-coded surface divergence  $\nabla_s \cdot \mathbf{u}|_R$  shortly after a micelle has adsorbed at the droplet interface. Same representation as in Fig. 1.

Note that this model starts with the assumption that the interface of the emulsion droplet initially is almost surfactant free. Such systems exist and Ref. 43 summarizes recent advances on realizing surfactant-free emulsion droplets. Furthermore, we do not take into account the detailed kinetics of the micelle adsorption.<sup>60</sup> We rather assume that when micelles adsorb at the interface, they simply spread their surfactant molecules.

### A. Diffusion-advection equation

We propose a simple model for the surfactant dynamics at the droplet interface. The surfactant concentration  $\Gamma$  obeys a diffusion-advection equation with additional source term,

$$\partial_t \Gamma = -\nabla_s \cdot (-D_s \nabla_s \Gamma + \Gamma \mathbf{u}|_R) + q. \quad (30)$$

The two terms in brackets describe transport of surfactants due to diffusion and advection induced by Marangoni flow, respectively, and  $D_s$  is the diffusion constant within the interface. The third term on the r.h.s. of Eq. (30) represents the bulk current of micelles hitting the droplet interface, where they are ultimately adsorbed with a mean rate  $1/\tau_{\text{ads}}$  and  $\tau_{\text{ads}}$  is mean adsorption time.

The Marangoni flow  $\mathbf{u}|_R$  at the droplet interface is generated by a concentration dependent surface tension, which we assume to be linear in  $\Gamma$ , for simplicity,

$$\sigma(\Gamma) = \sigma_0 - \sigma_s \Gamma, \quad (31)$$

where  $\sigma_0 > \sigma_s > 0$ . Here,  $\sigma_0$  is the surface tension of the clean or surfactant free droplet ( $\Gamma \ll 1$ ) and  $\sigma_0 - \sigma_s$  the surface tension of a droplet, which is fully covered by surfactants ( $\Gamma = 1$ ). Thus, for a given surfactant density  $\Gamma(\theta, \varphi)$ , Eq. (31) yields the field of surface tension, which is expanded into spherical harmonics with coefficients  $s_l^m$  according to Eq. (10). Note that equation of state (31) typically breaks down at large surface coverage. Here, we mainly focus on the early droplet dynamics, when the interface is only lightly covered with surfactants.

The micellar source term  $q$  has two contributions. Micelles perform a random walk through the outer fluid and ultimately hit the droplet interface which acts as a sink for the micelles. This sets up a diffusive current towards the interface. More importantly, as soon as Marangoni flow is initiated, micelles are also advected towards the interface as quantified by the radial flow component  $u_r$ , which is connected to the surface divergence  $\nabla_s \cdot \mathbf{u}|_R$  at the droplet interface, as outlined in Sec. IV B and discussed in Ref. 61 in more detail. A rigorous study of the full 3D bulk diffusion-advection equation for the bulk concentration of micelles  $c$  is beyond the scope of this paper. Instead, we proceed as follows. Comparing the time scale of micellar bulk diffusion  $t_D = R^2/(6D) = \pi\eta R^2 R_M/(k_B T)$  to the time scale of bulk advection  $t_A = R(\eta + \hat{\eta})/\sigma_s$ , we find a Peclet number  $\text{Pe} = t_D/t_A$  on the order of  $10^3$ . For the

estimate, we took  $R_M = R/20 = 50$  nm,  $\eta = 1$  mPa s,  $\hat{\eta} = 36$  mPa s,  $\sigma_s = 1$  mN/m, and room temperature. Due to the large Peclet number, we neglect bulk diffusion completely and consider advection only in the following. We view micelle adsorption to occur anywhere at the interface as a Poissonian process. Adsorption events are independent of each other and the mean adsorption time between the events is  $\tau_{\text{ads}}$  as already mentioned. Micelles preferentially adsorb at positions on the interface with large  $\nabla_s \cdot \mathbf{u}|_R > 0$ , while they do not adsorb at locations with  $\nabla_s \cdot \mathbf{u}|_R < 0$ , where the radial flow is directed away from the droplet. We will explain the detailed implementation of the adsorption event in Sec. V B.

We introduce a dimensionless form of the diffusion-advection equation (30) for the droplet interface rescaling lengths by droplet radius  $R$  and times by diffusion time  $\tau = R^2/D_s$ ,

$$\partial_t \Gamma = -\nabla_s \cdot (-\nabla_s \Gamma + M \Gamma \mathbf{u}|_R) + q. \quad (32)$$

As one relevant parameter, the so-called Marangoni number  $M = \tau/\tau_A$  compares the typical advection time  $\tau_A = R(\eta + \hat{\eta})/\sigma_s$  to  $\tau$ , where we used  $\mathbf{u}|_R = \sigma_s/(\eta + \hat{\eta})$  to estimate the Marangoni flow. Furthermore, the reduced adsorption rate becomes  $\kappa = \tau/\tau_{\text{ads}}$ , which is the most important parameter in this problem. Although we kept the same symbols, all quantities in Eq. (32), including  $\Gamma$ ,  $t$ ,  $\nabla_s$ ,  $\mathbf{u}|_R$ , and  $q$ , are from now on dimensionless.

## B. Numerical solution

To solve Eq. (32) numerically, we used a finite-volume scheme on a spherical mesh.<sup>62</sup> Initially, at time  $t = 0$ , the droplet is free of surfactants,  $\Gamma = 0$ , and at rest. While diffusive and advective currents are implemented within the standard finite-volume algorithm, we model the micelle adsorption by a Poissonian process.<sup>63</sup> At each time step  $\Delta t$  in the numerical scheme, we allow an adsorption event with probability  $\kappa \Delta t$ . If it is successful, the micelle is adsorbed with larger probability at positions where  $\nabla_s \cdot \mathbf{u}|_R > 0$  is large. To implement this, we introduce the weight function,

$$f(\theta, \varphi) = \frac{\nabla_s \cdot \mathbf{u}|_R}{\int \nabla_s \cdot \mathbf{u}|_R d\Omega} \quad \text{for } \nabla_s \cdot \mathbf{u}|_R > 0. \quad (33)$$

Then, the probability for micelle adsorption during time  $\Delta t$  and within the solid angle element  $d\Omega$  at an angular position  $(\theta, \varphi)$  becomes

$$p(\theta, \varphi, \Delta t) d\Omega = \begin{cases} \kappa \Delta t f(\theta, \varphi) d\Omega & \text{for } \nabla_s \cdot \mathbf{u}|_R > 0, \\ 0 & \text{for } \nabla_s \cdot \mathbf{u}|_R \leq 0. \end{cases}$$

After a micelle adsorption event at site  $(\theta, \varphi)$  is determined, we set  $\Gamma$  to one in a circular patch with radius  $2R_M$  centered around  $(\theta, \varphi)$ . In addition, we assume that surfactants stay at the droplet interface once adsorbed.

In this setup, Marangoni flow and diffusion current act in the same direction along  $-\nabla_s \Gamma$ . So, the Marangoni number is not the relevant parameter to initiate directed motion and we always set  $M = 1$ . However, by tuning the adsorption rate  $\kappa$ , the droplet starts to swim.

Figure 3(a) shows the swimming speed  $v^D$  of an emulsion droplet for three values of the reduced adsorption rate  $\kappa = \tau/\tau_{\text{ads}}$ . For  $\kappa = 4$ , the mean adsorption time is too large. The surfactant patch from a first micellar impact has already spread over the whole interface by diffusion and advection when a second micelle hits the droplet interface at a different location. As a result, the droplet follows a random trajectory. Figure 3(b) shows the corresponding swimming trajectory determined from  $\mathbf{r}(t) = \mathbf{r}(0) + \int_0^t dt' v^D(t') \mathbf{e}(t')$ . Increasing  $\kappa$  to 11, increases the number of micelles, which adsorb per unit time, and the swimming speed becomes larger. The swimming trajectory is still irregular albeit with an increased persistence.

Finally, for  $\kappa = 20$ , mean adsorption time is significantly shorter than the characteristic diffusion time. Thus, when a second micelle is about to hit the droplet interface, surfactant concentration  $\Gamma$  and surface divergence  $\nabla_s \cdot \mathbf{u}|_R$  are still peaked at the impact of the previous micelle. Therefore, the probability of the following micelle to adsorb at the front of the droplet is increased compared to the back. This spontaneously breaks spherical symmetry. A defined swimming direction evolves and the droplet shows directed motion with swimming velocity  $v^D$ . This is confirmed by the swimming

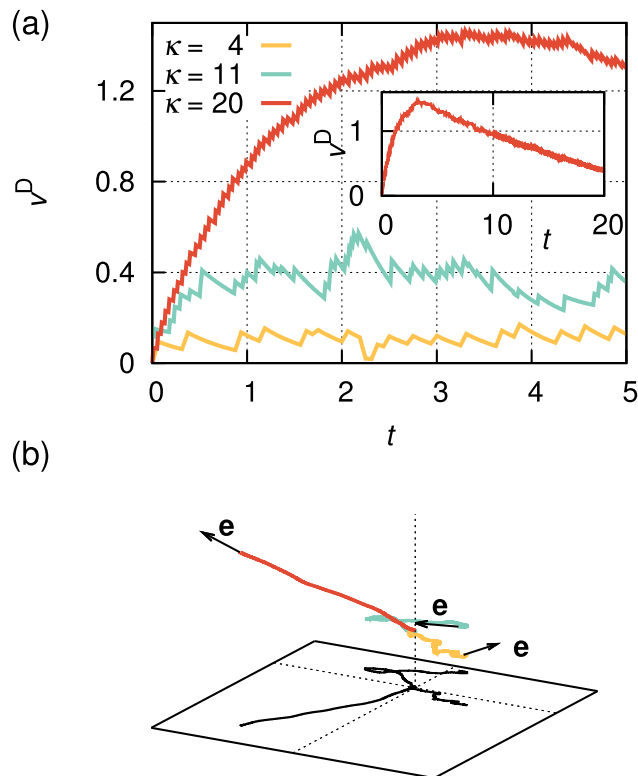


FIG. 3. (a) Swimming velocity  $v^D$  plotted versus time  $t$  for an emulsion droplet adsorbing surfactant micelles. The reduced adsorption rates are  $\kappa = 4, 11$ , and  $20$ . Other parameters are  $M = 1$  and  $R/R_M = 20$ . The inset shows the long-time limit for  $\kappa = 20$ . (b) Swimming trajectories from the same simulations as in (a) starting from  $t = 0$  until the droplets stop when they are fully covered with surfactants.

trajectory in Fig. 3(b). As the droplet continues to swim, the difference in surfactant concentration at the adsorption site and the mean concentration at the interface decreases. As a consequence, the Marangoni flow extenuates and  $v^D$  decreases in time [see inset of Fig. 3(a)]. Finally, when the interface is fully covered, i.e.,  $\Gamma = 1$  on the whole interface, the droplet stops.

Figure 4 shows the onset of directed swimming by plotting swimming speed versus reduced adsorption rate  $\kappa$ . Due to amplification of micellar adsorption at a specific spot, the droplet switches

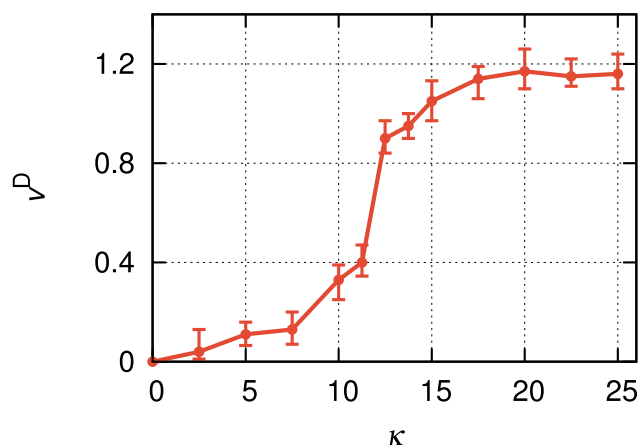


FIG. 4. Swimming speed  $v^D$  plotted versus reduced adsorption rate  $\kappa$ . For each  $\kappa$ , speed  $v^D$  is taken at time  $t = 5$  and averaged over 60 simulation runs.

at  $\kappa \approx 12$  from slow, random motion with  $v^D \approx 0.1 \dots 0.4$  to fast and persistent motion with  $v^D \approx 0.9 \dots 1.2$ .

In experiments,  $\kappa = \tau/\tau_{\text{ads}}$  can be tuned by adjusting the surfactant concentration  $c_S$ . We equate the micellar adsorption rate  $\tau_{\text{ads}}^{-1}$  with the flux  $j \cdot 4\pi R^2$  of micelles from the bulk to the droplet interface. The current is advective,  $j = c_M v_A$ , with micelle concentration  $c_M$  and velocity  $v_A = R/t_A$ . Using also  $\tau = R^2/D_s$ , one finds  $\kappa = c_M \cdot 4\pi R^4/(D_s t_A)$ . We assume that a micelle consists of  $10^4$  surfactants and introduce the degree of micellization as the ratio  $\gamma$  between micellized surfactants and all surfactants in the system, and this yields  $c_M = \gamma 10^{-4} c_S$ . The ratio  $\gamma$  changes strongly around the critical micelle concentration  $c_{\text{CMC}}$ . For example, for  $c_S = 0.9 \cdot c_{\text{CMC}}$ , i.e., slightly below  $c_{\text{CMC}}$ , one finds  $\gamma \approx 5 \cdot 10^{-4}$ .<sup>64</sup> Together with estimates  $D_s = 10^{-5} \text{ cm}^2/\text{s}$ ,<sup>65</sup>  $c_{\text{CMC}} = 1.5 \text{ mmol/l}$ , and values for  $R$  and  $t_A$  from Sec. V A, we obtain  $\kappa \approx 15$ , thus around the onset of motion in Fig. 4. However,  $\gamma \approx 10^{-4}$  means that micelle adsorption strongly competes with monomer adsorption, which is not contained in our model to keep it simple. Thus, to observe the onset of droplet motion in experiments, one has to increase  $c_M$  by tuning the system closer to  $c_{\text{CMC}}$  or even above.

Finally, we note that for increasing Marangoni number  $M$ , the patch of surfactants spreads faster due to advection and the crossover in Fig. 4 simply shifts towards larger  $\kappa$ .

## VI. LIGHT-INDUCED MARANGONI FLOW

Certain surfactants are known to be photosensitive.<sup>66–69</sup> For instance, surfactants based on azobenzene can undergo photoisomerization, where UV light (365 nm) transforms a *trans* to a *cis* configuration and blue light (450 nm) causes a transformation from *cis* to *trans*. During the *trans-cis* isomerization, subunits within the molecule change their relative orientation. Naturally, a different molecular structure also affects the surface tension of a surfactant-covered interface. Experiments showed that surfactants in the *cis* state cause a higher surface tension compared to the ones in the *trans* state.<sup>67</sup> This effect has recently been used to generate Marangoni flow.<sup>44</sup> Therefore, we suggest two possible applications of the formulas presented in Sec. II. We first treat light-driven motion of a strongly absorbing, i.e., “dark,” emulsion droplet and then discuss how the results alter in the case of a transparent droplet.

### A. Pushing an absorbing droplet with UV light

We think of an experiment where a spherical oil droplet of constant radius  $R$  is placed in a water phase laden with *trans* surfactants. Initially, the emulsion droplet is in equilibrium with the exterior phase and thus completely covered with *trans* surfactants. This corresponds to times  $t \gg \kappa^{-1}$  in Sec. V. An UV laser beam with cross-sectional radius  $\rho < R$  is focused on the center of the droplet. It locally transforms surfactants at the interface into the *cis* state and thereby increases surface tension, see Fig. 5(a).

Here, we assume that the droplet oil phase completely absorbs the incident light beam. Accordingly, the laser beam does not reach the interface opposite to the illuminated side. A thinkable droplet phase is crude oil, which has a penetration depth of  $\alpha \approx 100 \mu\text{m}$  at wavelength 400 nm.<sup>70</sup> On this length scale, the droplet is still in the low Reynolds number regime and all findings of Secs. II–IV are valid. Alternatively, one may fabricate a “dark” droplet by enriching the oil phase with soot or black pigment. In Sec. VI C, we study a transparent droplet.

The initiated Marangoni flow is oriented towards the laser beam and thus the droplet is propelled away from the laser beam, see Fig. 5(a). Due to the advective current of surfactants towards the laser beam, the *cis* surfactants converge at the laser spot on the droplet interface and ultimately leave the interface. Fresh *trans* surfactants are adsorbed at the leading front of the droplet, i.e., at the side opposite to the laser beam.

#### 1. Diffusion-advection-reaction equation

In the following, we review our theoretical approach to describe how the mixture of *trans* and *cis* molecules evolves in time, which then determines the dynamics of the flow field. More details

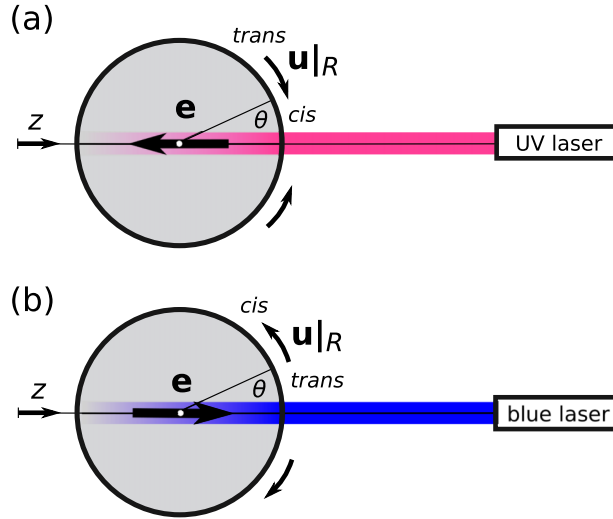


FIG. 5. (a) UV laser light is aimed at a strongly absorbing oil droplet in water. This increases the surface tension  $\sigma$  locally at the droplet interface by transforming *trans* to *cis* surfactants. The resulting Marangoni flow  $\mathbf{u}|_R$  is directed towards increasing surface tension and leads to propulsion in direction  $\mathbf{e}$  away from the laser beam. (b) Blue laser light locally decreases the surface tension  $\sigma$  at a droplet interface by transforming *cis* to *trans* surfactants. The resulting Marangoni flow  $\mathbf{u}|_R$  leads to propulsion in direction  $\mathbf{e}$  towards the laser beam.

can be found in Ref. 19. We introduce the order parameter field  $\phi(\theta, \varphi)$  with respective values  $\phi = +1$  or  $-1$  in regions where all surfactants are either in the *cis* or *trans* state, while in mixtures of both surfactants  $\phi$  is in the range  $-1 < \phi < 1$ .

The dynamics of the order parameter  $\phi$  at the droplet interface can be expressed by the diffusion-advection-reaction equation,

$$\partial_t \phi = -\nabla_s \cdot (\mathbf{j}_D + \phi \mathbf{u}|_R) - \tau_{\text{eq}}^{-1} (\phi - \phi_{\text{eq}}), \quad (34)$$

with diffusive current  $\mathbf{j}_D$  and advective Marangoni current  $\phi \mathbf{u}|_R$ . The source term couples the order parameter to the outer fluid laden with *trans* surfactants, i.e.,  $\phi_{\text{eq}} = -1$ , by introducing a relaxation dynamics with time scale  $\tau_{\text{eq}}$ .

To derive the diffusive current  $\mathbf{j}_D$ , we use a Flory-Huggins free energy density,<sup>19</sup>

$$f(\phi) = \frac{k_B T}{\ell^2} \left[ \frac{1+\phi}{2} \ln \frac{1+\phi}{2} + \frac{1-\phi}{2} \ln \frac{1-\phi}{2} - \frac{1}{4}(b_1 + b_2 + b_{12}) - \frac{\phi}{2}(b_1 - b_2) - \frac{\phi^2}{4}(b_1 + b_2 - b_{12}) \right], \quad (35)$$

where  $\ell^2$  is the head area of a surfactant at the interface. We introduce dimensionless parameters  $b_1$  and  $b_2$  to characterize the respective interactions between either *cis* or *trans* surfactants and  $b_{12}$  describes the interaction between the two types of surfactants. With the total free energy  $F[\phi] = \int f(\phi) dA$  the diffusive current becomes

$$\mathbf{j}_D = -\lambda \nabla_s \frac{\delta F}{\delta \phi} = -D_s \left[ \frac{1}{1-\phi^2} - \frac{1}{2}(b_1 + b_2 - b_{12}) \right] \nabla_s \phi, \quad (36)$$

where the Einstein relation  $D_s = \lambda k_B T / \ell^2$  relates mobility  $\lambda$  to the interfacial diffusion constant  $D_s$ . Note that the condition  $\mathbf{j}_D \propto -\nabla_s \phi$  is only fulfilled for a convex free energy with  $f''(\phi) > 0$ , i.e., if  $b_1 + b_2 - b_{12} < 2$ . In the following, we assume for simplicity  $b_{12} = (b_1 + b_2)/2$ .

In order to determine the Marangoni flow at the interface, we need an expression for the surface tension  $\sigma$ . From free energy (35), we obtain the equation of state for the surface tension,<sup>19</sup>

$$\sigma(\phi) = \frac{k_B T}{\ell^2} (b_1 - b_2) \left[ \frac{3}{8} \frac{b_1 + b_2}{b_1 - b_2} + \frac{1}{2} \phi + \frac{1}{8} \frac{b_1 + b_2}{b_1 - b_2} \phi^2 \right]. \quad (37)$$

Hence, for a given order parameter profile  $\phi(\theta, \varphi)$ , Eq. (37) yields the field of surface tension, which is expanded into spherical harmonics with coefficients  $s_l^m$  according to Eq. (10). Note that in contrast to equation of state (31) of the single-surfactant model in Sec. V, expression (37) is nonlinear.

In order to make Eq. (34) dimensionless, we rescale lengths by droplet radius  $R$  and time by the diffusion time scale  $\tau = R^2/D_s$  and obtain

$$\partial_t \phi = -\nabla_s \cdot (\mathbf{j}_D + M \phi \mathbf{u}|_R) - \kappa(\phi - \phi_{\text{eq}}). \quad (38)$$

Here, we introduced the Marangoni number  $M = \tau/\tau_A$ , where  $\tau_A = \ell^2 R(\eta + \hat{\eta})[(b_1 - b_2)k_B T]^{-1}$  is the advection time scale, and  $\kappa = \tau/\tau_{\text{eq}}$ . All quantities of Eq. (38) are dimensionless. We numerically solve Eq. (38) on a spherical domain by the method of finite volumes as explained in detail in Ref. 71. In all what follows, we set  $b_1 = 2$  and  $b_2 = 1$  as well as  $M = 1$ , i.e.,  $\tau = \tau_A$ . Furthermore, we choose  $\kappa = 1$  to illustrate the main behavior but also discuss the system's dynamics for different values of  $\kappa$ .

## 2. Stationary solution of pushed droplet

Initially, we set the order parameter  $\phi$  to  $-1$  on the whole interface. We then turn on the UV laser beam hitting the interface on a circular patch with radius  $\rho = 0.2R$ . In our numerical scheme, this is implemented by setting  $\phi = 1$  in the area of exposure. Furthermore, to couple the droplet to the outer fluid laden by *trans* surfactants, we set  $\phi_{\text{eq}} = -1$ . Figure 6, case (a) shows a typical stationary order parameter profile  $\phi$ , which results from the dynamics of Eq. (38). While  $\phi$  exhibits a step-like function, the interfacial Marangoni flow  $u_{\theta}|_R$ , also illustrated in Fig. 6, case (a), spreads over the whole droplet interface. However, since the flow field is concentrated on the northern hemisphere and directed towards  $\theta = 0$ , the droplet is a pusher. This is confirmed by the formulas for the squirmer parameter from Sec. IV A, which yield  $\beta = -2.8$ . Increasing  $\kappa$  enhances the coupling to  $\phi_{\text{eq}} = -1$  at the droplet front and the step in the order parameter profile  $\phi$  becomes steeper, whereas the profile  $\phi$  does not significantly depend on the Marangoni number  $M$ .

## 3. Pushing the droplet off-center

So far, the pushed droplet swims with a constant velocity  $\mathbf{v}^D = -v^D \mathbf{e}_z$ . Now, we introduce an offset  $\Delta y$  of the UV laser beam from the center of the droplet, and study the impact on the droplet trajectory. Figure 7(a) illustrates the situation. Due to the offset  $\Delta y$ , the Marangoni flow  $\mathbf{u}|_R$  pushes the droplet out of the laser beam. This increases the offset further and the orientation vector  $\mathbf{e}$  tilts further away from the laser beam.

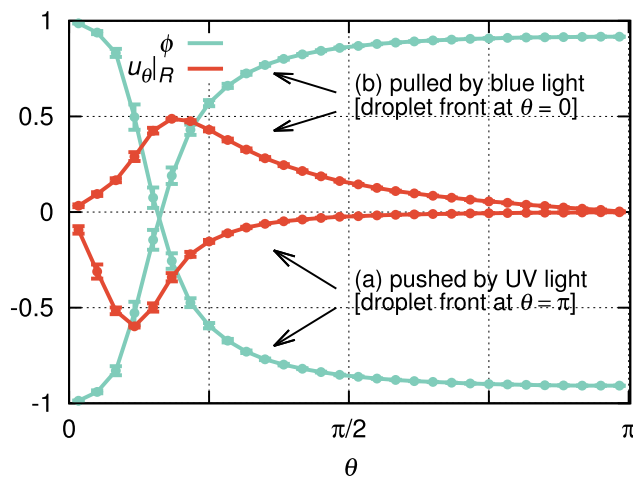


FIG. 6. Stationary solutions of the order parameter field  $\phi$  and the flow field  $u_{\theta}|_R$  for (a) the droplet which is pushed by UV light and (b) the droplet which is pulled by blue light. In both cases, the laser light hits the droplet interface at  $\theta = 0$ , compare Fig. 5. Order parameter  $\phi = 1$  and  $-1$  corresponds to pure *cis* and *trans* surfactants, respectively. Further parameters are  $M = \kappa = 1$ .

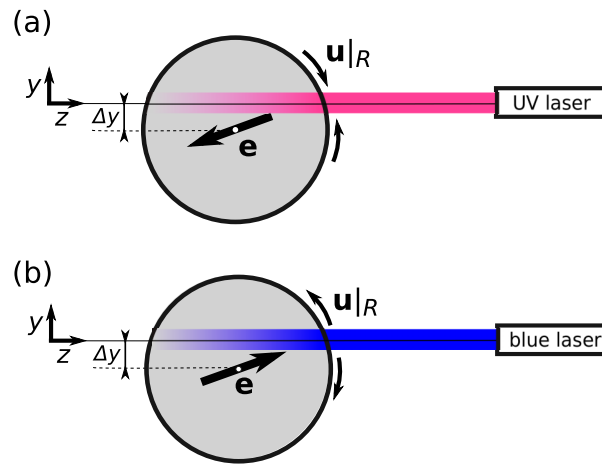


FIG. 7. (a) UV laser light is aimed at a spot which is offset by  $\Delta y$  from the droplet center. The resulting Marangoni flow drives the droplet out of the laser beam. (b) Blue laser light is aimed at a spot which is offset by  $\Delta y$  from the droplet center. The resulting Marangoni flow pulls the droplet back into the laser beam.

Figure 8(a) shows the trajectory of the droplet center for several values of the initial offset  $\Delta y$ . For vanishing initial offset,  $\Delta y = 0$ , the droplet swims in a straight line to the left, while in the case  $\Delta y \neq 0$ , the droplet clearly moves away from the laser beam. As the droplet leaves the laser beam at  $y/R = -1$ , it continues to swim in a straight line until the surface is completely covered with *trans* surfactants and the droplet halts. Thus, the swimming of pushed droplets is unstable with respect to an offset  $\Delta y$  of the pushing laser beam.

Finally, we discuss how the trajectories are influenced by the reduced relaxation rate  $\kappa$ , with which the surfactant mixture relaxes towards the equilibrium value  $\phi_{\text{eq}}$ . In Fig. 8(a), we also plot trajectories for  $\kappa = 2$  and 10 in addition to the default case  $\kappa = 1$  for the same initial offset  $\Delta y = -0.2R$ . In all three cases, the trajectories lie on top of each other, but for increasing  $\kappa$ , the droplet stops earlier. This is clear since the surfactant mixture relaxes faster to its equilibrium value, after the droplet has left the laser beam. Again, changing Marangoni number  $M$  does not alter the results significantly.

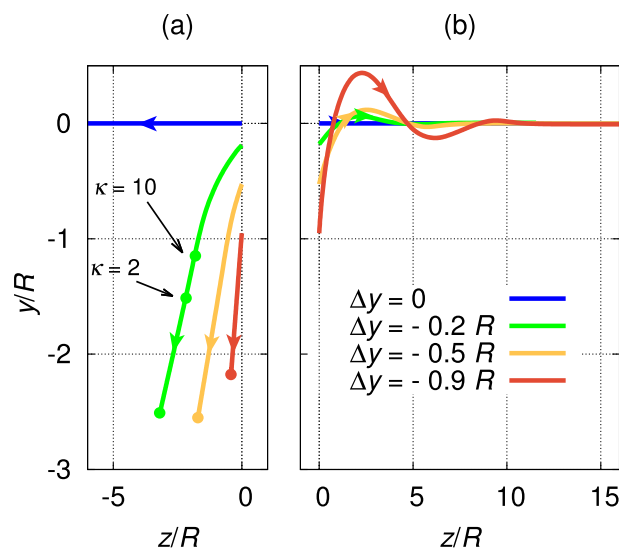


FIG. 8. (a) Trajectories of a droplet which is pushed by UV light. The droplet initially starts at  $z = 0$  and  $y = \Delta y$  and stops at the positions marked by dots. The laser is positioned at  $y = 0$  and shines from right to left [compare Fig. 7(a)]. Parameters are set to  $M = 1$  and  $\kappa = 1$ , unless otherwise noted. The trajectories are symmetric with respect to changing the sign of  $\Delta y$ . (b) Trajectories of a droplet which is pulled by blue light. The droplet initially starts at  $z = 0$  and  $y = \Delta y$ . The laser is positioned at  $y = 0$  and shines from right to left [compare Fig. 7(b)]. Again  $M = \kappa = 1$ .

## B. Pulling an absorbing droplet with blue light

In the following, we present an alternative mechanism to drive an oil droplet by light. Here, the droplet of constant radius  $R$  initially is in equilibrium with a water phase laden by *cis* surfactant. A blue laser beam with cross-sectional radius  $\rho < R$  is focused on the center of the droplet and locally transforms the surfactant into the *trans* state [see Fig. 5(b)], thereby lowering the surface tension of this region. The resulting Marangoni flow at the interface points away from the laser beam and thus pulls the droplet towards the laser beam. The advective current moves surfactants away from the laser beam, which are replenished by *cis* surfactants from the water phase. Again, the droplet oil phase completely absorbs the incident light beam. In Sec. VI D, we consider a transparent droplet, which is pulled by blue light.

### 1. Stationary solution of pulled droplet

For the numerical solution of Eq. (38), the order parameter  $\phi$  is initially set to  $\phi = \phi_{\text{eq}} = 1$ . The blue laser beam with its circular patch of radius  $\rho = 0.2R$  is implemented by setting  $\phi = -1$  in the area of exposure. Figure 6, case (b) shows the stationary order parameter profile  $\phi$  as well as the interfacial Marangoni flow  $u_{\theta}|_R$ . Since the maximum of  $u_{\theta}|_R$  is at the front of the droplet, the droplet is a puller with  $\beta = 1.4$ . Note the different shape of  $u_{\theta}|_R$  compared to the pushed droplet. The difference is due to positive curvature  $\sigma''(\phi) > 0$  of the nonlinear equation of state (37). Again, for increasing  $\kappa$ , the step in the order parameter profile  $\phi$  becomes steeper.

### 2. Pulling the droplet back to center

In Sec. VI A 3, we demonstrated the unstable swimming of the pushed droplet. The droplet pulled by the blue laser beam shows the opposite behavior. As sketched in Fig. 7(b), the droplet with offset  $\Delta y$  is pulled into the laser beam. This decreases the offset and the orientation vector  $\mathbf{e}$  tilts towards and finally aligns along the laser beam. Figure 8(a) shows droplet trajectories for several initial offsets  $\Delta y$ . For  $\Delta y = 0$ , the droplet swims in a straight line to the right, while in the case  $\Delta y \neq 0$ , the droplet position relaxes towards  $y = 0$  while performing damped oscillations about the stable swimming direction. Thus, the straight swimming trajectory along the laser beam is stable with respect to lateral excursions.

Now, we discuss how the pulled droplet trajectories depend on  $\kappa$ . Figure 9 depicts them for an initial offset of  $\Delta y = -0.9R$ . For large relaxation rates such as  $\kappa = 10$  (yellow curve in Fig. 9), the surfactants relax back to the *cis* conformation as soon as the illuminated region moves out of the laser beam. Hence, the swimming direction  $\mathbf{e}$  is always directed towards the illuminated spot [see

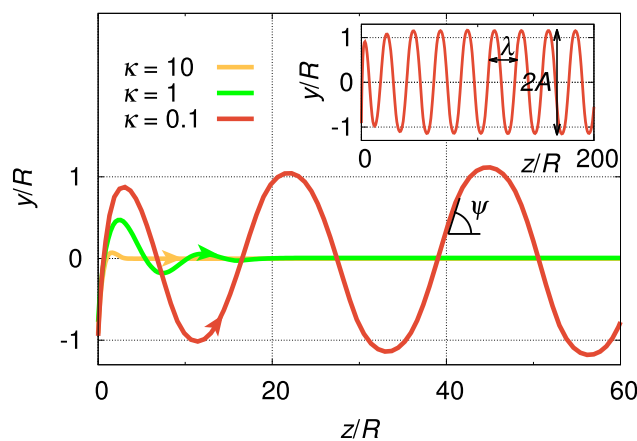


FIG. 9. Trajectories of a droplet, which is pulled by blue light for different relaxation rates  $\kappa$ . Initially, the droplet is placed at  $z = 0$  and  $y = -0.9R$ . The laser is positioned at  $y = 0$  and shines from right to left [compare Fig. 7(b)]. Inset: For  $\kappa = 0.1$ , a stable oscillation with wavelength  $\lambda$  and amplitude  $A$  develops.

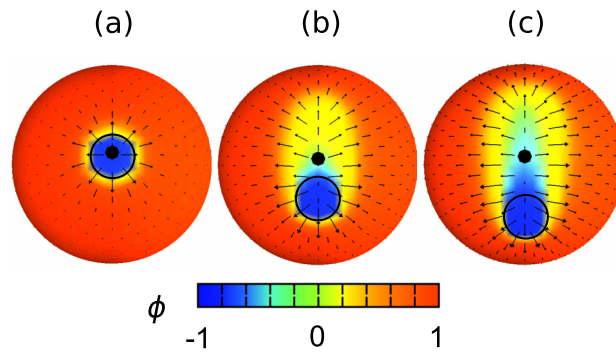


FIG. 10. Snapshots of the order parameter profile  $\phi$  and the flow field  $\mathbf{u}|_R$  at the interface of the pulled droplet for (a)  $\kappa = 10$ , (b)  $\kappa = 1$ , and (c)  $\kappa = 0.1$ . The area illuminated by the laser beam is shown by a circle and the bold dot indicates the swimming direction  $\mathbf{e}$ . The snapshots are taken from a supplemental movie. (Multimedia view) [URL: <http://dx.doi.org/10.1063/1.4939212.1>]

snapshot (a) in Fig. 10 (Multimedia view)] and relaxes towards the beam direction as illustrated in the supplemental movie (see Multimedia view associated with Fig. 10). However, a closer inspection of the yellow curve in Fig. 9 shows that the droplet crosses the  $z$  axis before relaxing towards  $y = 0$ . This happens since the surfactant relaxation is not infinitely fast. The effect becomes even clearer for  $\kappa = 1$  green curve in Fig. 9, where the lateral droplet position performs a damped oscillatory motion about the laser beam axis. Since the surfactant relaxation ( $\kappa = 1$ ) is sufficiently slow compared to the droplet speed  $M = 1$ , the swimming direction  $\mathbf{e}$  does not point towards the illuminated spot at early times [see snapshot (b) in Fig. 10 (Multimedia view)]. The droplet crosses several times the  $z$  axis before its direction aligns along the laser beam, as the supplemental movie shows. The movie also demonstrates how the step in the order parameter profile  $\phi$  becomes steeper with increasing  $\kappa$  when the stationary state is reached. This was already mentioned before. Interestingly, at very slow surfactant relaxation ( $\kappa = 0.1$ ), the droplet performs a stable oscillatory motion about the beam axis, which is nicely illustrated by the supplemental movie. Increasing the Marangoni number  $M$  increases swimming velocity and the oscillations occur at lower  $\kappa^{-1}$ .

Figure 11 plots the amplitude  $A$  of the stable oscillations versus  $\kappa^{-1}$  and reveals a subcritical Hopf bifurcation. In the parameter range  $\kappa^{-1} = 7.5\text{--}14$ , both straight swimming (amplitude  $A = 0$ ) and oscillatory motion ( $A \neq 0$ ) occur depending on the initial lateral displacement  $\Delta y$ . Indeed, if  $\Delta y$  is above the unstable branch of the Hopf bifurcation, plotted as dashed line in Fig. 11, the droplet assumes the oscillating state. The two swimming regimes are illustrated by phase portraits in

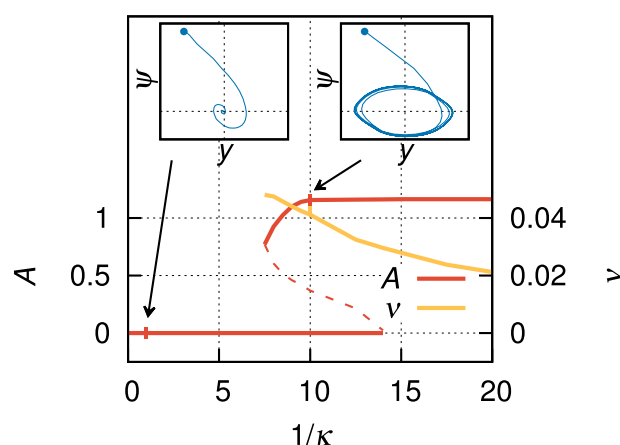


FIG. 11. Amplitude  $A$  and wave number  $\nu = 1/\lambda$  of the oscillating droplet trajectory (see inset of Fig. 9) plotted versus  $\kappa^{-1}$ . The two insets depict trajectories in  $(y, \psi)$  phase space, where  $\psi$  is the angle between droplet orientation and laser beam axis (see Fig. 9). Phase trajectories for  $\kappa^{-1} = 1$  and 10 are shown and dots indicate the initial positions.

orientation angle  $\psi = \cos^{-1}(\mathbf{e} \cdot \mathbf{e}_z)$  versus  $y$ . They either reveal a stable fixpoint (inset for  $\kappa^{-1} = 1$ ) or a stable limit cycle (inset for  $\kappa^{-1} = 10$ ). Finally, we also plot the wave number  $\nu = 1/\lambda$  of the oscillatory swimming motion along the  $z$  axis. It decreases with  $\kappa^{-1}$  since the droplet moves more persistently and thereby performs longer excursions from the beam axis.

In experiments,  $\kappa = \tau/\tau_{\text{eq}}$  can again be tuned by adjusting the surfactant concentration  $c_S$  in the bulk phase. We estimate the equilibration rate by  $\tau_{\text{eq}}^{-1} = j \cdot 4\pi R^2$ , where  $j = k_a \cdot c_S$  is the flux of surfactants from the bulk to the droplet interface and  $k_a$  is a typical adsorption rate constant. Using also  $\tau = R^2/D_s$ , one obtains  $\kappa = k_a \cdot c_S \cdot 4\pi R^4/D_s$ . With typical values  $R = 50 \mu\text{m}$ ,  $D_s = 10^{-5} \text{cm}^2/\text{s}$ , and  $k_a = 10^9 \text{m}/(\text{mol s})$ , one then finds  $\kappa \approx 10^5 \text{l}/\text{mol} \cdot c_S$ .<sup>72</sup> Thus, in order to observe the Hopf bifurcation at  $\kappa \approx 0.1$ , one has to set up an emulsion with surfactant density  $c_S \approx 10^{-3} \text{mmol/l}$ . For smaller  $c_S$ , we expect oscillations and for larger  $c_S$  damped motion.

Finally, we note that we observed the same qualitative behavior as in Figs. 8-11 for a linear diffusive current  $\mathbf{j}_D = D\nabla_s\phi$  and a linear equation of state for the surface tension  $\sigma$ . Hence, the origin of the Hopf bifurcation lies clearly in the nonlinear advection term  $M\phi\mathbf{u}|_R$  of Eq. (38).

### C. Pushing a transparent droplet with UV light

In the following, we discuss the case of an emulsion droplet with negligible light absorbance. The laser beam crosses the droplet and also actuates it at a second spot as illustrated in Fig. 12(a). Here, we focus on a water droplet immersed in a transparent oil phase laden with *trans* surfactants. But we will also comment on the inverse case of an oil droplet in water. Due to the different refractive indices of oil and water, the transmitted beam is refracted at each interface according to the refraction law  $n \sin \alpha = \hat{n} \sin \hat{\alpha}$ . Here,  $\alpha$  and  $\hat{\alpha}$  are the respective angles of the beam with respect to the surface normal in the oil and water phase while  $n$  and  $\hat{n}$  are the respective refraction indices. We apply the refraction law to partial beams of the incident light so that it widens while crossing and leaving the droplet. In what follows, we use  $n = 1.45$  and  $\hat{n} = 1.35$ . Note that we neglect any reflection except for total reflection above the critical angle  $\alpha_{\text{max}} = \arcsin(\hat{n}/n)$ . For the emulsion droplet, this implies that laser light is completely reflected if it hits the interface with a lateral distance to droplet center above  $\Delta y_{\text{max}}/R = \hat{n}/n \approx 0.93$ . The general mechanism for the light-induced Marangoni flow is the same as in Sec. VI A. It is directed away from each illuminated spot. Since the spots are well separated from each other, the droplet velocity vector is a superposition of the vectors induced by each spot.

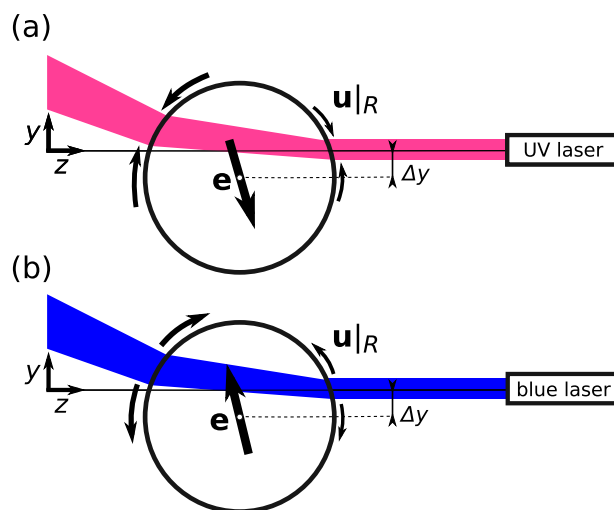


FIG. 12. (a) UV laser light is aimed at a transparent water droplet in oil, which is offset by  $\Delta y$  from the laser beam. The resulting Marangoni flow at the two spots drives the droplet out of the beam. (b) Blue laser light is aimed at a water droplet in oil, which is offset by  $\Delta y$  from the laser beam. The resulting Marangoni flow at the two spots pulls the droplet back into the laser beam.

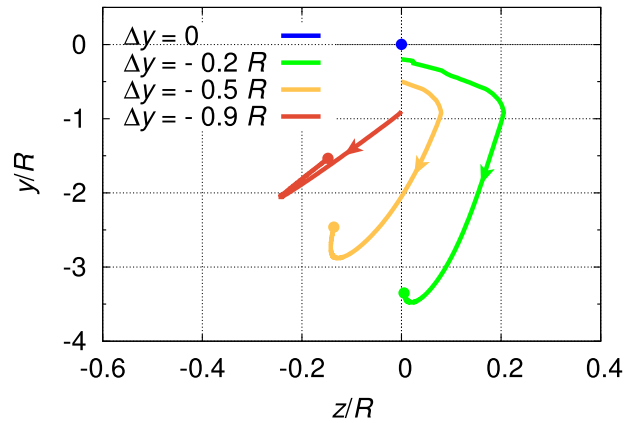


FIG. 13. Trajectories of a transparent droplet which is pushed by UV light. The droplet initially starts at  $z=0$  and  $y=\Delta y$  and stops at the positions marked by dots. The laser is positioned at  $y=0$  and shines from right to left [compare Fig. 12(a)]. Parameters are set to  $M=1$  and  $\kappa=1$ . The trajectories are symmetric with respect to changing the sign of  $\Delta y$ .

Again, we start with a laser beam which is aimed at the center of the droplet. Due to refraction, the transmitted beam widens and the second illuminated spot is slightly larger than the first one. Thus, the velocity vector induced by the second spot is also slightly larger and slowly pushes the droplet towards the laser beam. This effect is hardly visible in our simulations. However, as soon as we introduce an offset  $\Delta y$ , the widening of the laser beam becomes stronger. The resulting velocity vector with orientation  $\mathbf{e}$  pushes the droplet further away from the laser beam and also against the beam direction, as illustrated in Fig. 12(a). Ultimately, the droplet leaves the beam completely. Figure 13 shows trajectories for various initial offsets. In the cases  $\Delta y = -0.2R$  and  $-0.5R$ , the droplet initially moves in negative  $y$  and positive  $z$  direction [see also Fig. 12(a)]. Once the second laser spot has sufficiently decreased in size, since part of the beam is totally reflected, the droplet moves in negative  $z$  direction. It leaves the beam and finally stops. Thus, in analogy to the findings of Sec. VI A, the droplet is pushed out of the beam.

For an oil droplet immersed in water, the transmitted beam becomes more narrower. The droplet is still pushed out of the beam but the motion along  $z$  direction is reversed. The corresponding trajectories are similar to the ones in Fig. 13, albeit reflected about the  $y$ -axis. If droplet and surrounding phase have equal refractive indices, the motion out of the beam is exactly along the  $y$ -axis. In all cases, the interfacial flow field is concentrated at the back of the droplet and the droplet is a pusher.

#### D. Pulling a transparent droplet with blue light

Now, we study the effect of a blue light beam aimed at a water droplet, which is suspended in an oil phase laden with *cis* surfactants [see Fig. 12(b)]. In this case, the Marangoni flow is directed away from the illuminated spots. At zero offset,  $\Delta y = 0$ , the droplet slowly moves along the negative  $z$  direction. Any offset  $\Delta y \neq 0$  pulls the droplet back into the beam with the velocity vector slightly tilted towards  $-\mathbf{e}_z$  [see Fig. 12(b)]. As in Sec. VI B, we use coupling strength  $\kappa$  to distinguish between different regimes of motion.

Figure 14 (Multimedia view) shows trajectories from a supplemental movie (see Multimedia view A associated with Fig. 14). In the case of strong coupling to the bulk phase,  $\kappa = 10$ , the droplet performs a damped oscillation about  $y = 0$ . The spatial resolution of our numerical method is not large enough to resolve the size difference between the two illuminated spots. Therefore, in the supplemental movie, the droplet stops and does not move into the negative  $z$  direction. Upon decreasing the relaxation rate to values below  $\kappa = 4.5$ , the droplet undergoes a subcritical Hopf bifurcation and the droplet starts to oscillate about the laser beam. Figure 14 (Multimedia view) shows the trajectory from the supplemental movie; the droplet has already left the scene to the left. Figure 15 shows the subcritical bifurcation in the bottom graph, where amplitude  $A$  and wave number  $\nu$  are plotted versus  $\kappa^{-1}$ , or in the top phase portraits, where the limit cycle in case 2 is visible. Below  $\kappa = 2.2$ , the droplet

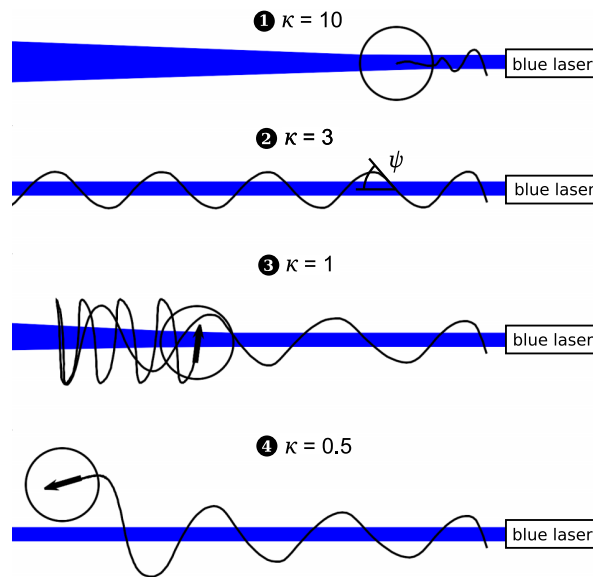


FIG. 14. Trajectories of a transparent water droplet suspended in oil, which is actuated by blue light for  $\kappa = 10, 3, 1, 0.5$ . The snapshots are taken from a supplemental movie. Trajectories of a transparent oil droplet suspended in water, which is actuated by blue light, are shown in a second supplemental movie. In all cases, we set  $M = 1$  and used an initial offset  $\Delta y = -0.5$  [compare Fig. 12(b)]. (Multimedia view) [URL: <http://dx.doi.org/10.1063/1.4939212.2>] [URL: <http://dx.doi.org/10.1063/1.4939212.3>]

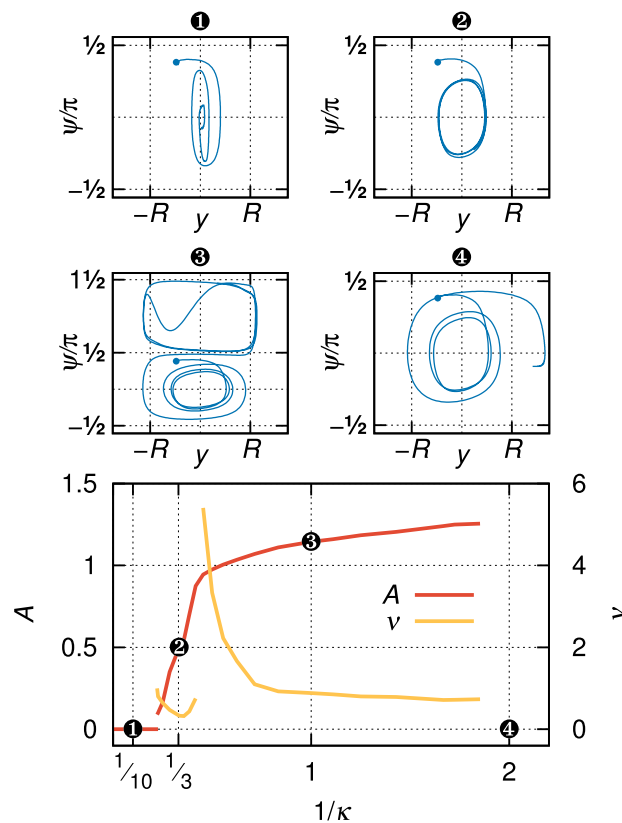


FIG. 15. Bottom: Amplitude  $A$  and wave number  $\nu = 1/\lambda$  of the oscillating droplet trajectories plotted versus  $\kappa^{-1}$ . Top: Trajectories in  $(y, \psi)$  phase space at values of  $\kappa^{-1}$  marked by numbers in the bottom plot. Here,  $\psi$  is the angle between droplet orientation and laser beam axis, as indicated in Fig. 14 (Multimedia view). Dots indicate the initial positions. Fig. 14 (Multimedia view) shows the corresponding trajectories in  $(z, y)$  space.

changes its dynamics completely. After moving along the negative  $z$  direction for a few droplet radii  $R$ , the droplet reverses its swimming direction and reaches a stationary oscillating state. The reversal occurs because the amplitude of the oscillation is so large that the size of the second spot decreases in size due to total reflection and the first spot pulls more strongly. This oscillation is characterized by larger amplitude  $A$  and wave number  $\lambda$  compared to the first oscillation state [see Fig. 15]. Finally, at relaxation rates below  $\kappa = 0.54$ , the droplet eventually leaves the beam and stops. For the experimental realization of different values of  $\kappa$ , we refer to the discussion in Sec. VI B 2.

For an oil droplet immersed in water, where total reflection does not occur, we only observe three states, in which the droplet moves against the laser beam: damped oscillations, stationary oscillations, and where the droplet ultimately leaves the laser beam. A supplemental movie illustrates the three cases (see Multimedia view B associated with Fig. 14).

## VII. CONCLUSIONS

A non-uniform surface tension profile  $\sigma$  at the interface of an emulsion droplet generates flow fields at the interface and inside as well as outside of the droplet. The flow at the interface is directed along the gradient of  $\sigma$ . Using this Marangoni effect, the emulsion droplet becomes active. We decomposed the surface tension profile into spherical harmonics,  $\sigma(\theta, \varphi) = \sum s_l^m Y_l^m$ , and for this most general form of  $\sigma$  we determined the full three-dimensional flow field inside  $[\hat{\mathbf{u}}(\mathbf{r})]$ , outside  $[\mathbf{u}(\mathbf{r})]$ , and at the interface  $[\mathbf{u}|_R(\theta, \varphi)]$  of the droplet as a function of the expansion coefficients  $s_l^m$ . The swimming kinematics of the droplet follows from the droplet velocity vector  $\mathbf{v}^D$ , which solely depends on the coefficients  $s_1^m$ . The flow field outside of the droplet decays either as  $1/r^3$  in the case of a neutral swimmer or as  $1/r^2$  in the case of a pusher or a puller. The squirmer parameter  $\beta$ , for which we derived an expression in terms of the coefficients  $s_1^m$  and  $s_2^m$  for arbitrary swimming direction, enables to distinguish between these cases.

In the second part of this paper, we presented two illustrative examples to demonstrate how gradients in the surface tension  $\sigma$  can be achieved and studied the resulting droplet motion.

In the first example, we considered an initially surfactant free droplet, which adsorbs micelles formed by surfactants. The adsorbed micelle not only induces Marangoni flow in the proximity of the droplet interface but also radial fluid flow towards the adsorption site. The radial flow enhances the probability that other micelles adsorb at the same site. This mechanism leads to directed propulsion of an initially isotropic emulsion droplet if the micellar adsorption rate is sufficiently large. Clearly, the mechanism only works when surfactants are adsorbed through micelles. Single surfactants would not produce a sufficiently strong radial flow to spontaneously break the isotropic symmetry of the droplet. Our idealized example stresses the role which micelles play in generating directed motion in active emulsions. Therefore, it might contribute to understanding the self-propulsion of water and liquid-crystal droplets, which has been demonstrated in recent publications.<sup>25,26</sup>

The second example considered a non-uniform mixture of two surfactant types in order to generate Marangoni flow. We used light-switchable surfactants based on the *trans-cis* isomerism of azobenzene to generate a non-uniform surfactant mixture. The analytic formulas for the flow field together with a diffusion-advection-reaction equation for the mixture order parameter determine the dynamics of the surfactant mixture and hence the droplet trajectory. We demonstrated that an emulsion droplet laden with *trans* surfactants, and either strongly adsorbing or transparent, can be pushed by a laser beam with UV light. However, the resulting straight trajectory is unstable with respect to displacing the droplet center relative to the laser beam axis. In contrast, a droplet laden with *cis* surfactants can be pulled into a laser beam with blue light. The straight trajectory is stable against lateral displacements. By decreasing the surfactant relaxation rate, the droplet develops an oscillatory trajectory about the laser beam via a subcritical Hopf bifurcation.

Having at hand analytic formulas for the full three-dimensional flow field, we are now able to fully discuss the recently introduced active emulsion droplet, where the surfactant mixture is generated by a bromination reaction.<sup>18,19</sup> We included thermal noise in the diffusion-advection-reaction equation of the mixture order parameter and currently study the coarsening dynamics of the surfactant mixture towards the stationary order parameter profile.<sup>71</sup> Thermal fluctuations in the composition

of the surfactant mixture are responsible for the rotational diffusion of the swimming direction and thereby generate a persistent random walk of the active emulsion droplet.

## ACKNOWLEDGMENTS

We acknowledge financial support by the Deutsche Forschungsgemeinschaft in the framework of the collaborative research center SFB 910 and the research training group GRK 1558.

## APPENDIX A: SPHERICAL HARMONICS

Throughout this paper, we use the following definition of spherical harmonics:

$$Y_l^m(\theta, \varphi) = \sqrt{\frac{2l+1}{4\pi} \frac{(l-m)!}{(l+m)!}} P_l^m(\cos \theta) e^{im\varphi},$$

with associated Legendre polynomials  $P_l^m$  of degree  $l$ , order  $m$ , and with orthonormality,

$$\int_0^\pi \int_0^{2\pi} Y_l^m \bar{Y}_{l'}^{m'} \sin \theta d\theta d\varphi = \delta_{l,l'} \delta_{m,m'},$$

where  $\bar{Y}_l^m$  denotes the complex conjugate of  $Y_l^m$ .

## APPENDIX B: FLUID FLOW IN THE BULK

Here, we give the complete velocity field inside  $\hat{\mathbf{u}} = \hat{\mathbf{v}} + \hat{\mathbf{w}}$  and outside  $\mathbf{u} = \mathbf{v} + \mathbf{w}$  of the droplet in the droplet frame,

$$\hat{u}_r = \frac{-\eta}{2(\eta + \hat{\eta})} \left[ \frac{r^2}{R^2} - 1 \right] \mathbf{e}_r \cdot \mathbf{v}^D + \frac{1}{\eta + \hat{\eta}} \sum_{l=1}^{\infty} \sum_{m=-l}^l \left[ \frac{r^{l+1}}{R^{l+1}} - \frac{r^{l-1}}{R^{l-1}} \right] \frac{l(l+1)s_l^m}{4l+2} Y_l^m, \quad (\text{B1a})$$

$$\hat{u}_\theta = \frac{-\eta}{2(\eta + \hat{\eta})} \left[ \frac{2r^2}{R^2} - 1 \right] \mathbf{e}_\theta \cdot \mathbf{v}^D + \frac{1}{\eta + \hat{\eta}} \sum_{l=1}^{\infty} \sum_{m=-l}^l \left[ (l+3) \frac{r^{l+1}}{R^{l+1}} - (l+1) \frac{r^{l-1}}{R^{l-1}} \right] \frac{s_l^m}{4l+2} \partial_\theta Y_l^m, \quad (\text{B1b})$$

$$\hat{u}_\varphi = \frac{-\eta}{2(\eta + \hat{\eta})} \left[ \frac{2r^2}{R^2} - 1 \right] \mathbf{e}_\varphi \cdot \mathbf{v}^D + \frac{1}{\eta + \hat{\eta}} \sum_{l=1}^{\infty} \sum_{m=-l}^l \left[ (l+3) \frac{r^{l+1}}{R^{l+1}} - (l+1) \frac{r^{l-1}}{R^{l-1}} \right] \frac{ims_l^m Y_l^m}{4l+2 \sin \theta}, \quad (\text{B1c})$$

$$u_r = \left( \frac{-\eta}{2(\eta + \hat{\eta})} \left[ \frac{R}{r} - \frac{R^3}{r^3} \right] - \left[ 1 - \frac{3R}{2r} + \frac{R^3}{2r^3} \right] \right) \mathbf{e}_r \cdot \mathbf{v}^D + \frac{1}{\eta + \hat{\eta}} \sum_{l=1}^{\infty} \sum_{m=-l}^l \left[ \frac{R^l}{r^l} - \frac{R^{l+2}}{r^{l+2}} \right] \frac{l(l+1)s_l^m}{4l+2} Y_l^m, \quad (\text{B1d})$$

$$u_\theta = \left( \frac{-\eta}{4(\eta + \hat{\eta})} \left[ \frac{R}{r} + \frac{R^3}{r^3} \right] - \left[ 1 - \frac{3R}{4r} - \frac{R^3}{4r^3} \right] \right) \mathbf{e}_\theta \cdot \mathbf{v}^D + \frac{1}{\eta + \hat{\eta}} \sum_{l=1}^{\infty} \sum_{m=-l}^l \left[ (2-l) \frac{R^l}{r^l} + l \frac{R^{l+2}}{r^{l+2}} \right] \frac{s_l^m}{4l+2} \partial_\theta Y_l^m, \quad (\text{B1e})$$

$$u_\varphi = \left( \frac{-\eta}{4(\eta + \hat{\eta})} \left[ \frac{R}{r} + \frac{R^3}{r^3} \right] - \left[ 1 - \frac{3R}{4r} - \frac{R^3}{4r^3} \right] \right) \mathbf{e}_\varphi \cdot \mathbf{v}^D + \frac{1}{\eta + \hat{\eta}} \sum_{l=1}^{\infty} \sum_{m=-l}^l \left[ (2-l) \frac{R^l}{r^l} + l \frac{R^{l+2}}{r^{l+2}} \right] \frac{ims_l^m Y_l^m}{4l+2 \sin \theta}. \quad (\text{B1f})$$

Note that for  $r = R$ , one recaptures Eqs. (17) and boundary condition  $u_r = \hat{u}_r = 0$ , while for  $r \rightarrow \infty$ ,  $\mathbf{u} = -\mathbf{v}^D$ .

Note, by combining the outside field of the pumping solution  $\mathbf{w}$  with the first term of the passive-droplet field  $\mathbf{v}$ , the stokeslet components, i.e., terms with  $\mathbf{u} \propto r^{-1}$ , cancel each other,

$$\begin{aligned} u_r &= -\mathbf{e}_r \cdot \mathbf{v}^D \left(1 - \frac{R^3}{r^3}\right) + \frac{1}{\eta + \hat{\eta}} \sum_{l=2}^{\infty} \sum_{m=-l}^l \left[ \frac{R^l}{r^l} - \frac{R^{l+2}}{r^{l+2}} \right] \frac{l(l+1)s_l^m}{4l+2} Y_l^m, \\ u_\theta &= -\mathbf{e}_\theta \cdot \mathbf{v}^D \left(1 + \frac{R^3}{2r^3}\right) + \frac{1}{\eta + \hat{\eta}} \sum_{l=2}^{\infty} \sum_{m=-l}^l \left[ (2-l) \frac{R^l}{r^l} + l \frac{R^{l+2}}{r^{l+2}} \right] \frac{s_l^m}{4l+2} \partial_\theta Y_l^m, \\ u_\varphi &= -\mathbf{e}_\varphi \cdot \mathbf{v}^D \left(1 + \frac{R^3}{2r^3}\right) + \frac{1}{\eta + \hat{\eta}} \sum_{l=2}^{\infty} \sum_{m=-l}^l \left[ (2-l) \frac{R^l}{r^l} + l \frac{R^{l+2}}{r^{l+2}} \right] \frac{ims_l^m}{4l+2} \frac{Y_l^m}{\sin \theta}. \end{aligned}$$

This shows that the droplet is a force-free swimmer.<sup>4</sup> Thus, in leading order, the flow field is given by a stresslet with  $\mathbf{u} \propto r^{-2}$ . The squirmer parameter  $\beta$  calculated in Sec. IV A determines the sign and the magnitude of the stresslet. In particular, if the coefficients  $s_2^m$  vanish, the squirmer parameter also becomes zero ( $\beta = 0$ ). Then, the flow field is less long-ranged and decays as  $\mathbf{u} \propto r^{-3}$ .

Finally, by adding the droplet velocity vector to our solution, one arrives at the velocity field  $\mathbf{u}^L = \mathbf{u} + \mathbf{v}^D$  in the lab frame,

$$\begin{aligned} u_r^L &= \frac{R^3}{r^3} \mathbf{e}_r \cdot \mathbf{v}^D + \frac{1}{\eta + \hat{\eta}} \sum_{l=2}^{\infty} \sum_{m=-l}^l \left[ \frac{R^l}{r^l} - \frac{R^{l+2}}{r^{l+2}} \right] \frac{l(l+1)s_l^m}{4l+2} Y_l^m, \\ u_\theta^L &= \frac{-R^3}{2r^3} \mathbf{e}_\theta \cdot \mathbf{v}^D + \frac{1}{\eta + \hat{\eta}} \sum_{l=2}^{\infty} \sum_{m=-l}^l \left[ (2-l) \frac{R^l}{r^l} + l \frac{R^{l+2}}{r^{l+2}} \right] \frac{s_l^m}{4l+2} \partial_\theta Y_l^m, \\ u_\varphi^L &= \frac{-R^3}{2r^3} \mathbf{e}_\varphi \cdot \mathbf{v}^D + \frac{1}{\eta + \hat{\eta}} \sum_{l=2}^{\infty} \sum_{m=-l}^l \left[ (2-l) \frac{R^l}{r^l} + l \frac{R^{l+2}}{r^{l+2}} \right] \frac{ims_l^m}{4l+2} \frac{Y_l^m}{\sin \theta}. \end{aligned}$$

In this frame, the velocity field satisfies the boundary condition  $\mathbf{u}^L|_{r \rightarrow \infty} = 0$ . Note that in this frame, the radial component  $u_r^L$  does not vanish at  $r = R$ .

## APPENDIX C: LORENTZ RECIPROCAL THEOREM

Applying the Lorentz reciprocal theorem to relate the flow fields of the pumping active droplet from Sec. II A and the passive droplet from Sec. II B to each other, one arrives at the alternative expression for the droplet velocity,<sup>73</sup>

$$\mathbf{v}^D = \frac{-1}{4\pi R^2} \frac{3\eta + 3\hat{\eta}}{2\eta + 3\hat{\eta}} \iint \mathbf{w}|_R dA. \quad (\text{C1})$$

Note that this generalizes the expression for rigid active spherical swimmers ( $\hat{\eta} \rightarrow \infty$ ) in Ref. 59. Using the surface flow field of the pumping droplet from Eqs. (12) in Eq. (C1), one obtains Eq. (21).

## APPENDIX D: COMPARISON WITH SQUIRMER MODEL

The presented solution  $\mathbf{u}(\mathbf{r})$  for the flow field around an active droplet can be related to the axisymmetric squirmer model introduced by Lighthill<sup>55</sup> and later by Blake<sup>56</sup> as follows. The squirmer flow field can also be decomposed into a pumping active and a passive part,  $\mathbf{u}^{sq} = \mathbf{w}^{sq} + \mathbf{v}^{sq}$ , where  $\mathbf{v}^{sq}$  is the usual Stokes flow field of a solid sphere, which we obtain in the limit of infinite internal viscosity:  $\mathbf{v}^{sq} = \lim_{\hat{\eta} \rightarrow \infty} \mathbf{v}$ . In order to match  $\mathbf{w}$  with the known squirmer field  $\mathbf{w}^{sq}$ , one has to set

$$s_l = -(\eta + \hat{\eta}) \frac{4l+2}{l(l+1)} \sqrt{\frac{4\pi}{2l+1}} B_l. \quad (\text{D1})$$

<sup>l</sup> This yields the correct flow field of a swimming squirmer with surface velocity field  $u_\theta = \sum_{l=1}^{\infty} B_l V_l(\cos \theta)$ , where  $V_l = \frac{1}{l(l+1)} P_l(\cos \theta)$ . Here, we used the notation of Blake.

## APPENDIX E: WRITTEN-OUT GENERALIZED SQUIRMER PARAMETER

The generalized squirmer parameter in Eq. (28) for a droplet swimming in an arbitrary direction can be written in terms of the coefficients  $s_1^m$  and  $s_2^m$  using Eqs. (22) and (24),

$$\beta = -\sqrt{\frac{27}{5}} \frac{\tilde{s}_2^0}{|\tilde{s}_1^0|}, \quad (\text{E1a})$$

$$\tilde{s}_1^0 = \sqrt{(s_1^0)^2 - 2s_1^1 s_1^{-1}}, \quad (\text{E1b})$$

$$\tilde{s}_2^0 = \left( \sqrt{6} [s_2^2 (s_1^{-1})^2 + s_2^{-2} (s_1^1)^2] - \sqrt{12} s_1^0 [s_2^1 s_1^{-1} + s_2^{-1} s_1^1] + 2s_2^0 [(s_1^0)^2 + s_1^1 s_1^{-1}] \right) / [2(s_1^0)^2 - 4s_1^1 s_1^{-1}]. \quad (\text{E1c})$$

- <sup>1</sup> A. Najafi and R. Golestanian, "Simple swimmer at low Reynolds number: Three linked spheres," *Phys. Rev. E* **69**, 062901 (2004).
- <sup>2</sup> R. Dreyfus, J. Baudry, M. L. Roper, M. Fermigier, H. A. Stone, and J. Bibette, "Microscopic artificial swimmers," *Nature* **437**, 862 (2005).
- <sup>3</sup> E. Gauger and H. Stark, "Numerical study of a microscopic artificial swimmer," *Phys. Rev. E* **74**, 021907 (2006).
- <sup>4</sup> E. Lauga and T. R. Powers, "The hydrodynamics of swimming microorganisms," *Rep. Prog. Phys.* **72**, 096601 (2009).
- <sup>5</sup> A. Walther and A. H. Müller, "Janus particles," *Soft Matter* **4**, 663 (2008).
- <sup>6</sup> R. Golestanian, T. B. Liverpool, and A. Ajdari, "Propulsion of a molecular machine by asymmetric distribution of reaction products," *Phys. Rev. Lett.* **94**, 220801 (2005).
- <sup>7</sup> W. F. Paxton, A. Sen, and T. E. Mallouk, "Motility of catalytic nanoparticles through self-generated forces," *Chem. - Eur. J.* **11**, 6462 (2005).
- <sup>8</sup> J. L. Moran and J. D. Posner, "Electrokinetic locomotion due to reaction-induced charge auto-electrophoresis," *J. Fluid. Mech.* **680**, 31 (2011).
- <sup>9</sup> T. Bickel, A. Majee, and A. Würger, "Flow pattern in the vicinity of self-propelling hot Janus particles," *Phys. Rev. E* **88**, 012301 (2013).
- <sup>10</sup> I. Buttinoni, G. Volpe, F. Kümmel, G. Volpe, and C. Bechinger, "Active Brownian motion tunable by light," *J. Phys.: Condens. Matter* **24**, 284129 (2012).
- <sup>11</sup> M. C. Marchetti, J. F. Joanny, S. Ramaswamy, T. B. Liverpool, J. Prost, M. Rao, and R. A. Simha, "Hydrodynamics of soft active matter," *Rev. Mod. Phys.* **85**, 1143 (2013).
- <sup>12</sup> T. Ishikawa and T. J. Pedley, "Coherent structures in monolayers of swimming particles," *Phys. Rev. Lett.* **100**, 088103 (2008).
- <sup>13</sup> A. A. Evans, T. Ishikawa, T. Yamaguchi, and E. Lauga, "Orientational order in concentrated suspensions of spherical microswimmers," *Phys. Fluids* **23**, 111702 (2011).
- <sup>14</sup> F. Alarcón and I. Pagonabarraga, "Spontaneous aggregation and global polar ordering in squirmer suspensions," *J. Mol. Liq.* **185**, 56 (2013).
- <sup>15</sup> A. Zöttl and H. Stark, "Hydrodynamics determines collective motion and phase behavior of active colloids in quasi-two-dimensional confinement," *Phys. Rev. Lett.* **112**, 118101 (2014).
- <sup>16</sup> M. Hennes, K. Wolff, and H. Stark, "Self-induced polar order of active Brownian particles in a harmonic trap," *Phys. Rev. Lett.* **112**, 238104 (2014).
- <sup>17</sup> A. Bricard, J.-B. Caussin, N. Desreumaux, O. Dauchot, and D. Bartolo, "Emergence of macroscopic directed motion in populations of motile colloids," *Nature* **503**, 95 (2013).
- <sup>18</sup> S. Thutupalli, R. Seemann, and S. Herminghaus, "Swarming behavior of simple model squirmers," *New J. Phys.* **13**, 073021 (2011).
- <sup>19</sup> M. Schmitt and H. Stark, "Swimming active droplet: A theoretical analysis," *Europhys. Lett.* **101**, 44008 (2013).
- <sup>20</sup> S.-Y. Teh, R. Lin, L.-H. Hung, and A. P. Lee, "Droplet microfluidics," *Lab Chip* **8**, 198 (2008).
- <sup>21</sup> R. Seemann, M. Brinkmann, T. Pfohl, and S. Herminghaus, "Droplet based microfluidics," *Rep. Prog. Phys.* **75**, 016601 (2012).
- <sup>22</sup> M. M. Hanczyc, T. Toyota, T. Ikegami, N. Packard, and T. Sugawara, "Fatty acid chemistry at the oil-water interface: Self-propelled oil droplets," *J. Am. Chem. Soc.* **129**, 9386 (2007).
- <sup>23</sup> T. Toyota, N. Maru, M. M. Hanczyc, T. Ikegami, and T. Sugawara, "Self-propelled oil droplets consuming 'Fuel' surfactant," *J. Am. Chem. Soc.* **131**, 5012 (2009).
- <sup>24</sup> T. Banno, R. Kuroha, and T. Toyota, "pH-sensitive self-propelled motion of oil droplets in the presence of cationic surfactants containing hydrolyzable ester linkages," *Langmuir* **28**, 1190 (2012).
- <sup>25</sup> S. Herminghaus, C. C. Maass, C. Krüger, S. Thutupalli, L. Goehring, and C. Bahr, "Interfacial mechanisms in active emulsions," *Soft Matter* **10**, 7008 (2014).
- <sup>26</sup> Z. Izri, M. N. van der Linden, S. Michelin, and O. Dauchot, "Self-propulsion of pure water droplets by spontaneous marangoni-stress-driven motion," *Phys. Rev. Lett.* **113**, 248302 (2014).
- <sup>27</sup> H. Kitahata, N. Yoshinaga, K. H. Nagai, and Y. Sumino, "Spontaneous motion of a droplet coupled with a chemical wave," *Phys. Rev. E* **84**, 015101 (2011).
- <sup>28</sup> E. Tjhung, D. Marenduzzo, and M. E. Cates, "Spontaneous symmetry breaking in active droplets provides a generic route to motility," *Proc. Natl. Acad. Sci. U. S. A.* **109**, 12381 (2012).

- <sup>29</sup> N. Yoshinaga, "Spontaneous motion and deformation of a self-propelled droplet," *Phys. Rev. E* **89**, 012913 (2014).
- <sup>30</sup> S. Yabunaka, T. Ohta, and N. Yoshinaga, "Self-propelled motion of a fluid droplet under chemical reaction," *J. Chem. Phys.* **136**, 074904 (2012).
- <sup>31</sup> A. Y. Rednikov, Y. S. Ryazantsev, and M. G. Velarde, "Drop motion with surfactant transfer in a homogeneous surrounding," *Phys. Fluids* **6**, 451 (1994).
- <sup>32</sup> A. Y. Rednikov, Y. S. Ryazantsev, and M. G. Velarde, "Active drops and drop motions due to nonequilibrium phenomena," *J. Non-Equilib. Thermodyn.* **19**, 95 (1994).
- <sup>33</sup> M. G. Velarde, A. Y. Rednikov, and Y. S. Ryazantsev, "Drop motions and interfacial instability," *J. Phys.: Condens. Matter* **8**, 9233 (1996).
- <sup>34</sup> M. G. Velarde, "Drops, liquid layers and the Marangoni effect," *Philos. Trans. R. Soc., A* **356**, 829 (1998).
- <sup>35</sup> N. Yoshinaga, K. H. Nagai, Y. Sumino, and H. Kitahata, "Drift instability in the motion of a fluid droplet with a chemically reactive surface driven by Marangoni flow," *Phys. Rev. E* **86**, 016108 (2012).
- <sup>36</sup> K. Furtado, C. M. Pooley, and J. M. Yeomans, "Lattice Boltzmann study of convective drop motion driven by nonlinear chemical kinetics," *Phys. Rev. E* **78**, 046308 (2008).
- <sup>37</sup> L. E. Scriven and C. V. Sternling, "The Marangoni effects," *Nature* **187**, 186 (1960).
- <sup>38</sup> M. D. Levan and J. Newman, "The effect of surfactant on the terminal and interfacial velocities of a bubble or drop," *AIChE J.* **22**, 695 (1976).
- <sup>39</sup> D. P. Mason and G. M. Moremedi, "Effects of non-uniform interfacial tension in small Reynolds number flow past a spherical liquid drop," *Pramana* **77**, 493 (2011).
- <sup>40</sup> J. Bławdziewicz, P. Vlahovska, and M. Loewenberg, "Rheology of a dilute emulsion of surfactant-covered spherical drops," *Physica A* **276**, 50 (2000).
- <sup>41</sup> J. A. Hanna and P. M. Vlahovska, "Surfactant-induced migration of a spherical drop in Stokes flow," *Phys. Fluids* **22**, 013102 (2010).
- <sup>42</sup> J. T. Schwalbe, F. R. Phelan, Jr., P. M. Vlahovska, and S. D. Hudson, "Interfacial effects on droplet dynamics in Poiseuille flow," *Soft Matter* **7**, 7797 (2011).
- <sup>43</sup> T. Sakai, "Surfactant-free emulsions," *Curr. Opin. Colloid Interface Sci.* **13**, 228 (2008).
- <sup>44</sup> A. Diguët, R.-M. Guillemic, N. Magome, A. Saint-Jalmes, Y. Chen, K. Yoshikawa, and D. Baigl, "Photomanipulation of a droplet by the chromocapillary effect," *Angew. Chem., Int. Ed.* **121**, 9445 (2009).
- <sup>45</sup> O. Pak and E. Lauga, "Generalized squirming motion of a sphere," *J. Eng. Math.* **88**, 1 (2014).
- <sup>46</sup> S. Sadhal, P. Ayyaswamy, and J. Chung, *Transport Phenomena with Drops and Bubbles*, Mechanical Engineering Series (Springer, 1996).
- <sup>47</sup> H. Lamb, *Hydrodynamics* (Cambridge University Press, 1932).
- <sup>48</sup> J. Happel and H. Brenner, *Low Reynolds Number Hydrodynamics: With Special Applications to Particulate Media*, Mechanics of Fluids and Transport Processes (Springer, Netherlands, 1983).
- <sup>49</sup> R. Clift, J. R. Grace, and M. E. Weber, *Bubbles, Drops, and Particles* (Academic Press, 1978).
- <sup>50</sup> V. A. Nepomniashchii, M. G. Velarde, and P. Colinet, *Interfacial Phenomena and Convection*, 1st ed. (Chapman & Hall/CRC, 2002).
- <sup>51</sup> O. S. Pak, J. Feng, and H. A. Stone, "Viscous Marangoni migration of a drop in a Poiseuille flow at low surface Péclet numbers," *J. Fluid. Mech.* **753**, 535 (2014).
- <sup>52</sup> G. Batchelor, "The stress system in a suspension of force-free particles," *J. Fluid. Mech.* **41**, 545 (1970).
- <sup>53</sup> T. Ishikawa, M. P. Simmonds, and T. J. Pedley, "Hydrodynamic interaction of two swimming model micro-organisms," *J. Fluid. Mech.* **568**, 119 (2006).
- <sup>54</sup> S. Kim and S. Karrila, *Microhydrodynamics: Principles and Selected Applications*, Butterworth—Heinemann Series in Chemical Engineering (Dover Publications, 2005).
- <sup>55</sup> M. J. Lighthill, "On the squirming motion of nearly spherical deformable bodies through liquids at very small Reynolds numbers," *Commun. Pure Appl. Math.* **5**, 109 (1952).
- <sup>56</sup> J. R. Blake, "A spherical envelope approach to ciliary propulsion," *J. Fluid. Mech.* **46**, 199 (1971).
- <sup>57</sup> M. T. Downton and H. Stark, "Simulation of a model microswimmer," *J. Phys.: Condens. Matter* **21**, 204101 (2009).
- <sup>58</sup> L. Zhu, E. Lauga, and L. Brandt, "Self-propulsion in viscoelastic fluids: Pushers vs. pullers," *Phys. Fluids* **24**, 051902 (2012).
- <sup>59</sup> H. A. Stone and A. D. Samuel, "Propulsion of microorganisms by surface distortions," *Phys. Rev. Lett.* **77**, 4102 (1996).
- <sup>60</sup> I. Griffiths, C. Bain, C. Breward, D. Colegate, P. Howell, and S. Waters, "On the predictions and limitations of the Becker-Döring model for reaction kinetics in micellar surfactant solutions," *J. Colloid Interface Sci.* **360**, 662 (2011).
- <sup>61</sup> V. G. Levich, *Physicochemical Hydrodynamics* (Prentice-Hall, 1962).
- <sup>62</sup> Here, we decompose the surface tension up to  $l_{max} = 60$ , which has proven to be sufficient to model an adsorbed micelle without leading to numerical problems such as the Gibbs phenomenon. More details about the simulation method can be found in Ref. 71.
- <sup>63</sup> N. Van Kampen, *Stochastic Processes in Physics and Chemistry* (North-Holland Personal Library, Elsevier Science, 1992).
- <sup>64</sup> W. Al-Soufi, L. Piñeiro, and M. Novo, "A model for monomer and micellar concentrations in surfactant solutions: Application to conductivity, NMR, diffusion, and surface tension data," *J. Colloid Interface Sci.* **370**, 102 (2012).
- <sup>65</sup> S. S. Dukhin, G. Kretzschmar, and R. Miller, *Dynamics of Adsorption at Liquid Interfaces: Theory, Experiment, Application* (Elsevier, 1995), Vol. 1.
- <sup>66</sup> O. Karthaus, M. Shimomura, M. Hioki, R. Tahara, and H. Nakamura, "Reversible photomorphism in surface monolayers," *J. Am. Chem. Soc.* **118**, 9174 (1996).
- <sup>67</sup> J. Y. Shin and N. L. Abbott, "Using light to control dynamic surface tensions of aqueous solutions of water soluble surfactants," *Langmuir* **15**, 4404 (1999).
- <sup>68</sup> K. Ichimura, S.-K. Oh, and M. Nakagawa, "Light-driven motion of liquids on a photoresponsive surface," *Science* **288**, 1624 (2000).

- <sup>69</sup> J. Eastoe and A. Vesperinas, "Self-assembly of light-sensitive surfactants," *Soft Matter* **1**, 338 (2005).
- <sup>70</sup> T. Krol, A. Stelmaszewski, and W. Freda, "Variability in the optical properties of a crude oil-seawater emulsion," *Oceanologia* **48**, 203 (2006), Available at: <http://www.iopan.gda.pl/oceanologia/48Skrol.pdf>.
- <sup>71</sup> M. Schmitt and H. Stark, "Marangoni phase separation of surfactants drives active Brownian motion of emulsion droplet" (unpublished).
- <sup>72</sup> B. Binks and D. Furlong, *Modern Characterization Methods of Surfactant Systems* (CRC Press, 1999), Vol. 83.
- <sup>73</sup> R. S. Subramanian, "The Stokes force on a droplet in an unbounded fluid medium due to capillary effects," *J. Fluid. Mech.* **153**, 389 (1985).



#### **4.4 Active Brownian motion of emulsion droplets: Coarsening dynamics at the interface and rotational diffusion**

*European Physics Journal E*, vol. **39**, p. 80, 2016, DOI: 10.1140/epje/i2016-16080-y

The final publication is available at Springer via:  
<http://dx.doi.org/10.1140/epje/i2016-16080-y>



# Active Brownian motion of emulsion droplets: Coarsening dynamics at the interface and rotational diffusion

M. Schmitt and H. Stark

Institut für Theoretische Physik, Technische Universität Berlin - Hardenbergstraße 36, 10623 Berlin, Germany

Received: date / Revised version: date

**Abstract.** A micron-sized droplet of bromine water immersed in a surfactant-laden oil phase can swim [1]. The bromine reacts with the surfactant at the droplet interface and generates a surfactant mixture. It can spontaneously phase-separate due to solutocapillary Marangoni flow, which propels the droplet. We model the system by a diffusion-advection-reaction equation for the mixture order parameter at the interface including thermal noise and couple it to fluid flow. Going beyond previous work, we illustrate the coarsening dynamics of the surfactant mixture towards phase separation in the axisymmetric swimming state. Coarsening proceeds in two steps: an initially slow growth of domain size followed by a nearly ballistic regime. On larger time scales thermal fluctuations in the local surfactant composition initiates random changes in the swimming direction and the droplet performs a persistent random walk, as observed in experiments. Numerical solutions show that the rotational correlation time scales with the square of the inverse noise strength. We confirm this scaling by a perturbation theory for the fluctuations in the mixture order parameter and thereby identify the active emulsion droplet as an active Brownian particle.

**PACS.** 47.20.Dr Surface-tension-driven instability – 47.55.D- Drops and bubbles – 47.55.pf Marangoni convection

## 1 Introduction

In the past decade autonomous swimming of particles at low Reynolds number has attracted a tremendous amount of attention [2–6]. Both, in the study of living organisms such as bacteria or algae or of artificial microswimmers a plethora of exciting research subjects has evolved. They include understanding the swimming mechanism [7–10] and generic properties of microswimmers [11–14], their swimming trajectories [15–18], and the study of their interaction with surfaces as well as obstacles [19–22]. The study of emergent collective motion has opened up a new field in non-equilibrium statistical physics [23–31].

There are various methods to construct a microswimmer. One idea is to generate a slip velocity field close to the swimmer's surface using a phoretic mechanism. A typical example of such an artificial swimmer is a micron-sized spherical Janus colloid, which has an inherent polar symmetry. Its two faces are made of different materials and thus differ in their physical or chemical properties [32]. For example, a Janus particle with faces of different thermal conductivity moves if exposed to heat. The conversion of thermal energy to mechanical work in a self-generated temperature gradient is called self-thermophoresis [33]. Janus colloids also employ other phoretic mechanisms to become active [34–37].

A different realization of a self-propelled particle is an active emulsion droplet. The striking difference to an active Janus particle is the missing inherent polar symmetry. Instead, the symmetry between front and back breaks spontaneously, for example, in a subcritical bifurcation [38]. The self-sustained motion of active droplets is due to a gradient in surface tension, which is usually caused by an inhomogeneous density of surfactants. The resulting stresses set up a solutocapillary Marangoni flow directed along the surface tension gradient that drags the droplet through the fluid. An active droplet generates a flow field in the surrounding fluid typical for the “squirmers” [39–43]. Originally, the squirmer was introduced to model the locomotion of microorganisms that propel themselves by a carpet of short active filaments called cilia beating in synchrony on their surfaces. The squirmer flow field at the interface is then a coarse-grained model of the cilia carpet.

Active droplets have extensively been studied in experiments, including droplets in a bulk fluid [44, 45, 1, 46–50] and droplets on interfaces [51, 52]. Theoretical and numerical studies address the drift bifurcation of translational motion [53–57], deformable and contractile droplets [58, 59], droplets in a chemically reacting fluid [60], droplets driven by nonlinear chemical kinetics [61], and the diffusion-advection-reaction equation for the dynamics of a surfactant mixture at the droplet interface [38]. A comprehensive review on active droplets is given in ref. [10].

An active droplet, which swims due to solutocapillary Marangoni flow, has recently been realized [1]. Water droplets with a diameter of  $50 - 150\mu\text{m}$  are placed into a surfactant-rich oil phase. The surfactants migrate to the droplet interface where they form a dense monolayer. Bromine dissolved in the water droplets reacts with the surfactants at the interface. It saturates the double bond in the surfactant molecule and the surfactant becomes weaker than the original one. Hence, the “bromination” reaction locally increases the interfacial surface tension. This induces Marangoni flow, which advects surfactants and thereby further enhances the gradients in surface tension. If the advective current exceeds the smoothing diffusion current, the surfactant mixture phase-separates. The droplet develops a polar symmetry and starts to move in a random direction, which fluctuates around such that the droplet performs a persistent random walk. While the droplet swims with a typical swimming speed of  $15\mu\text{m/s}$ , brominated surfactants are constantly replaced by non-brominated surfactants from the oil phase by means of desorption and adsorption. Finally, the swimming motion comes to an end when the fueling bromine is exhausted.

In ref. [38] we developed a diffusion-advection-reaction equation for the surfactant mixture at the droplet interface and coupled it to the axisymmetric flow field initiated by the Marangoni effect. In a parameter study we could then map out a state diagram including the transition from the resting to the swimming state and an oscillating droplet motion. In this paper we combine our theory with the full three-dimensional solution for the Marangoni flow, which we derived for an arbitrary surface tension field at the droplet interface in ref. [43]. Omitting the constraint of axisymmetry and adding thermal noise to the dynamic equation of the surfactant mixture, we will focus on two new aspects of droplet dynamics that we could not address in ref. [38]. First, while reaching the stationary uniaxial swimming state, the surfactant mixture phase-separates into the two surfactant types. We illustrate the coarsening dynamics and demonstrate that it proceeds in two steps. An initially slow growth of domain size is followed by a nearly ballistic regime. This is reminiscent to coarsening in the dynamic model H [62]. Second, even in the stationary swimming state the surfactant composition fluctuates thermally and thereby initiates random changes in the swimming direction, which diffuses on the unit sphere. As a result the droplet performs a persistent random walk, as observed in experiments [1], which we will characterize in detail.

The article is organized as follows. In sect. 2 we recapitulate our model of the active emulsion droplet from ref. [38] and generalize it to a droplet without the constraint of axisymmetry. While sect. 3 explains the numerical method to solve the diffusion-advection-reaction equation on the droplet surface, the following two sections contain the results of this article. Section 4 describes the coarsening dynamics of the surfactant mixture before reaching the steady swimming state and sect. 5 characterizes the persistent random walk of the droplet in the swimming state. The article concludes in sect. 6.

## 2 Model of an active droplet

In order to model the dynamics of the active droplet, we follow our earlier work [38]. We use a dynamic equation for the surfactant mixture at the droplet interface that includes all the relevant processes. We assume that the surfactant completely covers the droplet interface without any intervening solvent. We also assume that the head area of both types of surfactant molecules (brominated and non-brominated) is the same. Denoting the brominated surfactant density by  $c_1$  and the non-brominated density by  $c_2$ , we can therefore set  $c_1 + c_2 = 1$ . We then take the concentration difference between brominated and non-brominated surfactants as an order parameter  $\phi = c_1 - c_2$ . In other words  $\phi = 1$  corresponds to fully brominated and  $\phi = -1$  to fully non-brominated surfactants and  $c_1 = (1 + \phi)/2$  and  $c_2 = (1 - \phi)/2$ . Finally, we choose a constant droplet radius  $R$ .

### 2.1 Diffusion-advection-reaction equation

The dynamics of the order parameter  $\phi$  at the droplet interface can be expressed as [38]:

$$\partial_t \phi = -\nabla_s \cdot (\mathbf{j}_D + \mathbf{j}_A) - \tau_R^{-1}(\phi - \phi_{\text{eq}}) + \zeta(\mathbf{r}, t), \quad (1)$$

which we formulate in the form of a continuity equation with an additional source and thermal noise ( $\zeta$ ) term.  $\nabla_s = (\mathbf{1} - \mathbf{n} \otimes \mathbf{n})\nabla$  stands for the directional gradient on a sphere with radius  $R$ , where  $\nabla$  is the nabla operator and  $\mathbf{n}$  the surface normal. The current is split up into a diffusive part  $\mathbf{j}_D$  and an advective part  $\mathbf{j}_A$ , which arises due to the Marangoni effect. We summarize them below and in sect. 2.2. The source term describes the bromination reaction as well as desorption of brominated and adsorption of non-brominated surfactants to and from the outer fluid. Both processes tend to establish an equilibrium mixture with order parameter  $\phi_{\text{eq}}$  during the characteristic relaxation time  $\tau_R$ . Ad- and desorption dominate for  $\phi_{\text{eq}} < 0$  while bromination dominates for  $\phi_{\text{eq}} > 0$ . The source term is a simplified phenomenological description for the ad- and desorption of surfactants. A more detailed model would include fluxes from and to the bulk fluid [63]. We will explain the thermal noise term further below.

The general mechanism of eq. (1) to initiate steady Marangoni flow is as follows. The diffusive current  $\mathbf{j}_D$  smoothes out gradients in  $\phi$ , while the advective Marangoni current  $\mathbf{j}_A$  amplifies gradients in  $\phi$ . Hence,  $\mathbf{j}_D$  and  $\mathbf{j}_A$  are competing and as soon as  $\mathbf{j}_A$  dominates over  $\mathbf{j}_D$ ,  $\phi$  experiences phase separation. As a result, the resting state becomes unstable and the droplet starts to swim.

We now summarize features of the diffusive current  $\mathbf{j}_D$ , more details can be found in ref. [38]. We formulate a Flory-Huggins free energy density in terms of the order parameter of the surfactant mixture, which includes entropic terms and interactions between the different types

of surfactants:

$$f(\phi) = \frac{k_B T}{\ell^2} \left[ \frac{1+\phi}{2} \ln \frac{1+\phi}{2} + \frac{1-\phi}{2} \ln \frac{1-\phi}{2} - \frac{1}{4}(b_1 + b_2 + b_{12}) - \frac{\phi}{2}(b_1 - b_2) - \frac{\phi^2}{4}(b_1 + b_2 - b_{12}) \right],$$

Here,  $\ell^2$  is the head area of a surfactant at the interface. We introduce dimensionless parameters  $b_1$  ( $b_2$ ) to characterize the interaction between brominated (non-brominated) surfactants and  $b_{12}$  describes the interaction between the two types of surfactants. The diffusive current is now driven by a gradient in the chemical potential derived from the total free energy functional  $F[\phi] = \iint f(\phi) dA$ :

$$\mathbf{j}_D = -\lambda \nabla_s \frac{\delta F}{\delta \phi} = -D \left[ \frac{1}{1-\phi^2} - \frac{1}{2}(b_1 + b_2 - b_{12}) \right] \nabla_s \phi, \quad (2)$$

where the Einstein relation  $D = \lambda k_B T / \ell^2$  relates the interfacial diffusion constant  $D$  to the mobility  $\lambda$ . To rule out a double well form of  $f(\phi)$ , which would generate phase separation already in thermal equilibrium, we only consider  $b_1 + b_2 - b_{12} < 2$ . This also means that the diffusive current  $\mathbf{j}_D \propto -\nabla_s \phi$  is for all  $\phi$  indeed directed against  $\nabla_s \phi$ . In the following we assume  $b_{12} = (b_1 + b_2)/2$  and therefore require  $b_1 + b_2 < 4$ .

We formulate the thermal noise term in eq. (1) as Gaussian white noise with zero mean following ref. [64]:

$$\langle \zeta \rangle = 0, \quad (3a)$$

$$\langle \zeta(\mathbf{r}, t) \zeta(\mathbf{r}', t') \rangle = -2k_B T \lambda \nabla_s^2 \delta(\mathbf{r} - \mathbf{r}') \delta(t - t'). \quad (3b)$$

Here, the strength of the noise correlations is connected to the mobility  $\lambda$  of the diffusive current via the fluctuation-dissipation theorem. In order to close eq. (1), we now discuss the advective Marangoni current  $\mathbf{j}_A$ .

## 2.2 Marangoni flow

The advective current for the order parameter  $\phi$  is given by

$$\mathbf{j}_A = \phi \mathbf{u}|_R, \quad (4)$$

where  $\mathbf{u}|_R$  is the flow field at the droplet interface. It is driven by a non-uniform surface tension  $\sigma$  and therefore called Marangoni flow [65, 63]. In our case, we have a non-zero surface divergence  $\nabla_s \cdot \mathbf{u}|_R \neq 0$ . In fact, it can be shown that an incompressible surface flow cannot lead to propulsion of microswimmers [66].

In order to evaluate  $\mathbf{u}|_R$ , one has to solve the Stokes equation for the flow field  $\mathbf{u}(\mathbf{r})$  surrounding the spherical droplet ( $r > R$ ) as well as for the flow field  $\hat{\mathbf{u}}(\mathbf{r})$  inside the droplet ( $r < R$ ). Both solutions are matched at the droplet interface by the condition [63],

$$\nabla_s \sigma = \mathbf{P}_s (\mathbf{T} - \hat{\mathbf{T}}) \mathbf{e}_r \Big|_{r=R}, \quad (5)$$

where  $\mathbf{P}_s = \mathbf{1} - \mathbf{e}_r \otimes \mathbf{e}_r$  is the surface projector. Equation (5) means that a gradient in surface tension  $\sigma$  is compensated by a jump in viscous shear stress. Here,  $\mathbf{T} =$

$\eta[\nabla \otimes \mathbf{u} + (\nabla \otimes \mathbf{u})^T]$  is the viscous shear stress tensor of a Newtonian fluid with viscosity  $\eta$  outside of the droplet and the same relation holds for  $\hat{\mathbf{T}}$  of the fluid with viscosity  $\hat{\eta}$  inside the droplet. We have performed this evaluation in ref. [43] for a given surface tension field and only summarize here the results relevant for the following. Alternative derivations are found in ref. [67–70].

In spherical coordinates the Marangoni flow field  $\mathbf{u}|_R$  at the interface reads [43, 67–69]

$$\mathbf{u}|_R = \frac{-\eta}{2(\eta + \hat{\eta})} \mathbf{v}_D + \frac{1}{\eta + \hat{\eta}} \sum_{l=1}^{\infty} \sum_{m=-l}^l \frac{R s_l^m}{2l+1} \nabla_s Y_l^m, \quad (6)$$

with spherical harmonics  $Y_l^m(\theta, \varphi)$  given in appendix A. Here,

$$s_l^m = \iint \sigma(\theta, \varphi) \bar{Y}_l^m(\theta, \varphi) d\Omega \quad (7)$$

are the expansion coefficients of the surface tension, where  $\bar{Y}_l^m$  means complex conjugate of  $Y_l^m$ , and [43, 68, 70]

$$\mathbf{v}_D = v_D \mathbf{e} = \frac{1}{\sqrt{6\pi}} \frac{1}{2\eta + 3\hat{\eta}} \begin{pmatrix} s_1^1 - s_1^{-1} \\ i(s_1^1 + s_1^{-1}) \\ -\sqrt{2}s_1^0 \end{pmatrix}. \quad (8)$$

is the droplet velocity vector. It is solely given by the dipolar coefficients ( $l = 1$ ) of the surface tension and determines propulsion speed  $v_D \geq 0$  as well as the swimming direction  $\mathbf{e}$  with  $|\mathbf{e}| = 1$ . Note that by setting  $m = 0$ , eqs. (6)-(8) reduce to the case of an axisymmetric droplet swimming along the  $z$ -direction, as studied in ref. [38].

In ref. [43] we give several examples of flow fields  $\mathbf{u}|_R$ . In general, Marangoni flow is directed along gradients in surface tension, *i.e.*  $\mathbf{u}|_R \parallel \nabla_s \sigma$ . This is confirmed by eq. (6) and also clear from fig. 2 (b), which we discuss later. However, according to eq. (6) higher modes of surface tension contribute with a decreasing coefficient [43]. Note the velocity field in eq. (6) is given in a frame of reference that moves with the droplet's center of mass but the directions of its axis are fixed in space and do not rotate with the droplet. Finally, the velocity fields inside ( $\hat{\mathbf{u}}$ ) and outside ( $\mathbf{u}$ ) of the droplet in both the droplet and the lab frame can be found in the appendix of ref. [43].

The surface tension necessary to calculate  $\mathbf{v}_D$  and  $\mathbf{u}|_R$  is connected to the order parameter  $\phi$  by the equation of state,  $\sigma = f - \frac{\partial f}{\partial c_1} c_1 - \frac{\partial f}{\partial c_2} c_2$ , which gives [38]

$$\sigma(\phi) = \frac{k_B T}{\ell^2} (b_1 - b_2) \left( \frac{3}{8} \frac{b_1 + b_2}{b_1 - b_2} + \frac{1}{2} \phi + \frac{1}{8} \frac{b_1 + b_2}{b_1 - b_2} \phi^2 \right). \quad (9)$$

This implies that for  $b_1 > b_2 > 0$ ,  $\nabla_s \phi$  points along  $\nabla_s \sigma$ . Moreover, since the Marangoni flow  $\mathbf{u}|_R$  is oriented along  $\nabla_s \sigma$ , as noted above, we conclude that for  $\phi > 0$  the advective current  $\mathbf{j}_A = \phi \mathbf{u}|_R$  points “uphill”, *i.e.*, in the direction of  $\nabla_s \phi$ , in contrast to  $\mathbf{j}_D$  [38].

This completes the derivation of the surface flow field  $\mathbf{u}|_R$  as a function of the expansion coefficients  $s_l^m$  of the surface tension. Together with the equation of state  $\sigma(\phi)$  the advective current  $\mathbf{j}_A$  in eq. (4) is specified. Finally,

using the diffusion current  $\mathbf{j}_D$  from eq. (2), the diffusion-advection-reaction equation (1) becomes a closed equation in  $\phi$ .

The swimming emulsion droplet is an example of a spherical microswimmer, a so-called squirmer [39–43]. Squirmers are often classified by means of the so-called squirmer parameter  $\beta$  [5]. When  $\beta < 0$ , the surface flow dominates at the back of the squirmer, similar to the flow field of the bacterium *E. coli*. Since such a swimmer pushes fluid outward along its major axis, it is called a ‘pusher’. Accordingly, a swimmer with  $\beta > 0$  is called a ‘puller’. The algae *Chlamydomonas* is a biological example of a puller. Swimmers with  $\beta = 0$  are called ‘neutral’.

For an axisymmetric emulsion droplet swimming along the  $z$ -direction, the squirmer parameter is given by

$$\beta = -\sqrt{\frac{27}{5}} \frac{s_2^0}{|s_1^0|}, \quad (10)$$

with coefficients  $s_l^m$  from the multipole expansion (7) of the surface tension  $\sigma$  [43]. A generalization of this formula to droplets without axisymmetry and swimming in arbitrary directions is derived in ref. [43]. The relevant expressions are presented in appendix B.

### 2.3 Reduced dynamic equations and system parameters

In order to write eq. (1) in reduced units, we rescale time by the characteristic diffusion time  $\tau_D = R^2/D$  and lengths by droplet radius  $R$ , and arrive at

$$\partial_t \phi = -\nabla_s \cdot (\mathbf{j}_D + M\phi \mathbf{u}|_R) - \kappa(\phi - \phi_{\text{eq}}) + \xi \zeta(\mathbf{r}, t), \quad (11)$$

where the Gaussian noise variable fulfills

$$\langle \zeta(\mathbf{r}, t) \zeta(\mathbf{r}', t') \rangle = -2\nabla_s^2 \delta(\mathbf{r} - \mathbf{r}') \delta(t - t'). \quad (12)$$

The dimensionless velocity field at the interface and the droplet velocity vector read, respectively,

$$\mathbf{u}|_R = -\frac{\mathbf{v}_D}{2} + \sum_{l=1}^{\infty} \sum_{m=-l}^l \frac{s_l^m}{2l+1} \nabla_s Y_l^m, \quad (13a)$$

$$\mathbf{v}_D = v_D \mathbf{e} = \frac{1}{\sqrt{6\pi}(2+3\nu)} \begin{pmatrix} s_1^1 - s_1^{-1} \\ i(s_1^1 + s_1^{-1}) \\ -\sqrt{2}s_1^0 \end{pmatrix}. \quad (13b)$$

All quantities in eqs. (11) and (13), including  $\mathbf{j}_D$ ,  $\mathbf{u}|_R$ ,  $t$ ,  $\nabla_s$ ,  $\zeta$ , and  $\mathbf{v}_D$ , are from now on dimensionless, although we use the same symbols as before. Writing the dynamics equations in reduced units, introduces the relevant system parameters  $M$ ,  $\nu$ ,  $\kappa$ ,  $\phi_{\text{eq}}$ , and  $\xi$ , which we discuss now.

The Marangoni number  $M$  quantifies the strength of the advective current in eq. (11) and is given by  $M = \frac{(b_1 - b_2)R}{\lambda(\eta + \hat{\eta})}$ . It is the most important parameter of our model, as it determines whether the droplet swims. In eq. (13a) we introduced the ratio of shear viscosities,  $\nu = \hat{\eta}/\eta$ , for the fluids inside and outside of the droplet, respectively. In our study we consider a water droplet suspended in

oil and set  $\nu \approx 1/36$  [1]. The interaction parameters  $b_1$  and  $b_2$  not only appear in  $M$  but also as  $b_1 + b_2$  in the diffusive current in eq. (2) and in the equation of state  $\sigma(\phi)$  in eq. (9). Therefore, they need to be set individually. Assuming the head area of a surfactant  $\ell^2$  to be on the order of  $\text{nm}^2$ , we can fit eq. (9) to the experimental values  $\sigma(\phi = 1) \approx 2.7 \text{mN/m}$  and  $\sigma(\phi = -1) \approx 1.3 \text{mN/m}$  [1] to find  $b_1 \approx 0.6$  and  $b_2 \approx 0.3$ . We keep these values fixed throughout the article.

Parameter  $\kappa = \tau_D/\tau_R$  tunes the ratio between diffusion and relaxation time and the equilibrium order parameter  $\phi_{\text{eq}}$  measures whether ad- and desorption of surfactants ( $\phi_{\text{eq}} < 0$ ) or bromination ( $\phi_{\text{eq}} > 0$ ) dominates. In this study we set  $\kappa = 0.1$  and  $\phi_{\text{eq}} = 0.5$ . A parameter study for these parameters can be found in [38]. Finally, the reduced noise strength  $\xi = \ell/R \propto 1/\sqrt{N}$ , where  $N$  is the total number of surfactants at the droplet interface, connects the the droplet size  $R$  to the molecular length scale  $\ell$ .

### 3 Finite volume method on a sphere

To numerically solve the rescaled dynamic equation (11) for the order parameter field  $\phi$ , we had to decide on an appropriate method. The most widely used numerical methods for solving partial differential equations are the finite difference method (FDM), the finite element method (FEM), and the finite volume method (FVM) [71, 72]. We ruled out FDM due to numerical complications of its algorithm with spherical coordinates. They are most appropriate for the spherical droplet surface but one needs to define an axis within the droplet. The FEM is also very delicate when writing a numerically stable code for our model. This is mainly due to the advective term in eq. (11), which commonly causes difficulties in FEM routines [71]. In contrast, the FVM is especially suited for solving continuity equations. Therefore, it is much more robust for field equations that incorporate advection and we chose it for solving eq. (11) on the droplet surface.

In order to generate a two-dimensional FVM mesh that is as uniform as possible and quasi-isotropic on a sphere, we chose a geodesic grid based on a refined icosahedron [73]. An icosahedron has  $f_0 = 20$  equilateral triangles as faces and  $v_0 = 12$  vertices. In each refinement step, each triangle is partitioned into four equilateral triangles and the three new vertices are projected onto the unit sphere enclosing the icosahedron. Hence, after the  $n$ -th refinement step, the resulting mesh has  $f_n = 4^n f_0$  triangular faces and  $v_n = v_{n-1} + \frac{3}{8} 4^n f_0$  grid points.<sup>1</sup> The ‘‘finite volume’’ then refers to a small volume (in this case an area) surrounding each grid point of the mesh. Thus we have to construct the Voronoi diagram of the triangular mesh. The Voronoi diagram consists of  $v_n$  elements, 12 of

<sup>1</sup> Each face has three edges and every edge belongs to two faces, hence the number of edges is  $e_n = \frac{3}{2} f_n$ . In a refinement step one new grid point is placed on the middle of each edge and  $v_n = v_{n-1} + e_{n-1}$ . Thus,  $v_n = v_{n-1} + \frac{3}{8} 4^n f_0$ , with  $v_1 = 42$ ,  $v_2 = 162$ ,  $v_3 = 642$ ,  $v_4 = 2562$ .

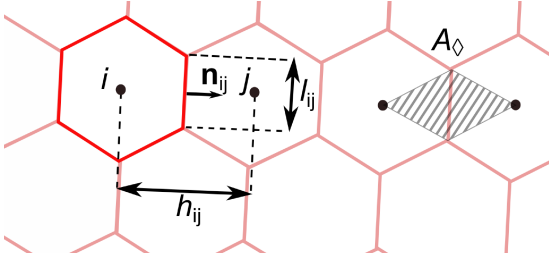


**Fig. 1.** Finite volume element  $i$  with neighboring element  $j$ . The relevant lengths and normal vector are sketched.

which are pentagons associated with the vertices of the original icosahedron while the rest are hexagons. Unless otherwise noted we use a Voronoi mesh with  $v_3 = 642$  FVM elements. The geodesic icosahedral grid is a standard grid in geophysical fluid dynamics. A comprehensive review on numerical methods in geophysical fluid dynamics can be found in [74].

In the following we will outline how we convert the diffusion-advection-reaction equation (11) to a set of ordinary differential equations for a vector  $\underline{\phi}$  comprising the values  $\phi_i$  of the order parameter field at the center points of all FVM elements. FVM was developed for treating current densities in a continuity equation and we illustrate the procedure for the diffusion term of eq. (11). We start by integrating over element  $i$  with area  $A_i$  and use the divergence theorem, where  $\mathbf{n}_i$  is the outward normal at the element boundary:

$$\iint_{A_i} \nabla_s \cdot \mathbf{j}_D \, dA = \int_{\partial A_i} \mathbf{j}_D \cdot \mathbf{n}_i \, dS = \sum_{j=1}^N \mathbf{j}_D \cdot \mathbf{n}_{ij} l_{ij} \quad (14a)$$

$$= - \sum_{j=1}^N D(\phi_i, \phi_j) \frac{\phi_j - \phi_i}{h_{ij}} l_{ij} = \underline{\underline{D}}^i \underline{\phi}. \quad (14b)$$

In the last term of eq. (14a), the line integral is converted into a sum over the  $N$  straight element boundaries of length  $l_{ij}$  and  $\mathbf{n}_{ij}$  is the normal vector at the corresponding boundary. Figure 1 illustrates the relevant quantities. In the second line the directional derivative  $\mathbf{n}_{ij} \cdot \nabla_s \phi$  resulting from  $\mathbf{j}_D$  in eq. (2) is approximated by a difference quotient. The prefactor in  $\mathbf{j}_D$ , which we abbreviated by  $D(\phi_i, \phi_j)$  in eq. (14b), also contains  $\phi$ . It is interpolated at the boundary between elements  $i$  and  $j$  by means of the central differencing scheme as  $(\phi_i + \phi_j)/2$ . Finally, we write the whole term as the product of local diffusion matrix  $\underline{\underline{D}}^i$  and vector  $\underline{\phi}$ . After applying this technique to all elements, the matrices  $\underline{\underline{D}}^i$  are combined into one matrix  $\underline{\underline{D}}$  for the whole mesh.

The same procedure is carried out for the advective term in eq. (11) but discretizing  $\mathbf{j}_A = M\phi\mathbf{u}|_R$  needs more care. While  $\mathbf{u}|_R$  is directly calculated at the boundary between elements  $i$  and  $j$ , the order parameter  $\phi$  is treated differently. If the local Peclet number  $Pe = h_{ij} M|\mathbf{u}|_R|/D(\phi_i, \phi_j) \gg 10^{-3}$ . Figure 2(a) shows the droplet swimming speed  $v_D$  as a function of elapsed time.

oriented flow, *i.e.*  $\mathbf{u}|_R \cdot \mathbf{n}_{ij} > 0$ , one uses the element order parameter  $\phi_i$ , while for inward flow, *i.e.*  $\mathbf{u}|_R \cdot \mathbf{n}_{ij} < 0$ , one uses the order parameter of the neighboring element  $\phi_j$ . In the case  $Pe < 2$ ,  $\phi$  is interpolated by the central difference  $(\phi_i + \phi_j)/2$ .

Finally, the linear terms in  $\phi$  and its time derivative are simply approximated by  $\phi_i$  and  $\dot{\phi}_i$ . In the end, we are able to write the discretized eq. (11) as a matrix equation for the vector  $\underline{\phi}$ :

$$\underline{\underline{M}} \dot{\underline{\phi}} = \underline{\underline{D}} \underline{\phi} - \underline{\underline{M}} \underline{\underline{A}} \underline{\phi} - \kappa \underline{\underline{M}} (\underline{\phi} - \underline{\phi}_{\text{eq}}) + 2 \cdot 12^{1/4} \xi \underline{z}, \quad (15)$$

where the diagonal matrix  $\underline{\underline{M}}$  carries the areas of the elements, and with diffusion matrix  $\underline{\underline{D}}$ , advection matrix  $\underline{\underline{A}}$ , and element noise vector  $\underline{z}$ , which describes typical Gaussian white noise with zero mean and variance one,

$$\langle \underline{z}(t) \rangle = \underline{0}, \quad (16a)$$

$$\langle \underline{z}(t) \otimes \underline{z}(t') \rangle = \underline{\underline{1}} \delta(t - t'). \quad (16b)$$

In appendix C we derive eq. (16b) by integrating eq. (12) over two FVM elements  $i$  and  $j$ . Finally, the set of stochastic differential equations are integrated in time by a standard Runge-Kutta scheme.

In the following we present results obtained with the described numerical scheme.

## 4 Dynamics towards the swimming state

This section focuses on the dynamics of the active emulsion droplet from an initial resting state with swimming speed  $v_D = 0$  to a stable swimming state with swimming speed  $v_D > 0$ . After a comparison with the axisymmetric model of the droplet from our previous work [38], where we also did not include thermal fluctuations, we investigate the coarsening dynamics of the order parameter  $\phi$  at the droplet interface while reaching the swimming state.

### 4.1 Swimming speed $v_D$

In order to test the simulation method, we start our analysis with a set of parameters, for which we found a swimming state in the inherent axisymmetric model [38]. They are given by Marangoni number  $M = 3$ , reduced reaction rate  $\kappa = 0.1$ , and equilibrium order parameter value  $\phi_{\text{eq}} = 0.5$ . We keep these values fixed throughout the following unless otherwise noted. The initial condition for solving eq. (15) is an order parameter field that fluctuates around  $\phi_{\text{eq}}$ :  $\phi(\theta, \varphi) = \phi_{\text{eq}} + \delta\phi(\theta, \varphi)$ . The small fluctuations  $\delta\phi(\theta, \varphi) \ll 1$  are realized by random numbers drawn from the normal distribution  $\mathcal{N}(\phi_{\text{eq}}, \alpha^2)$  with mean  $\phi_{\text{eq}}$  and variance  $\alpha^2 = 10^{-5}$  and added at the grid points of the simulation mesh. Furthermore we set the noise strength to  $2 \cdot 12^{1/4}$ . Figure 2(a) shows the droplet swimming speed  $v_D$  as a function of elapsed time.

First of all, we notice the good agreement with the corresponding graph of  $v_D^{\text{axi}}$  of the axisymmetric system of

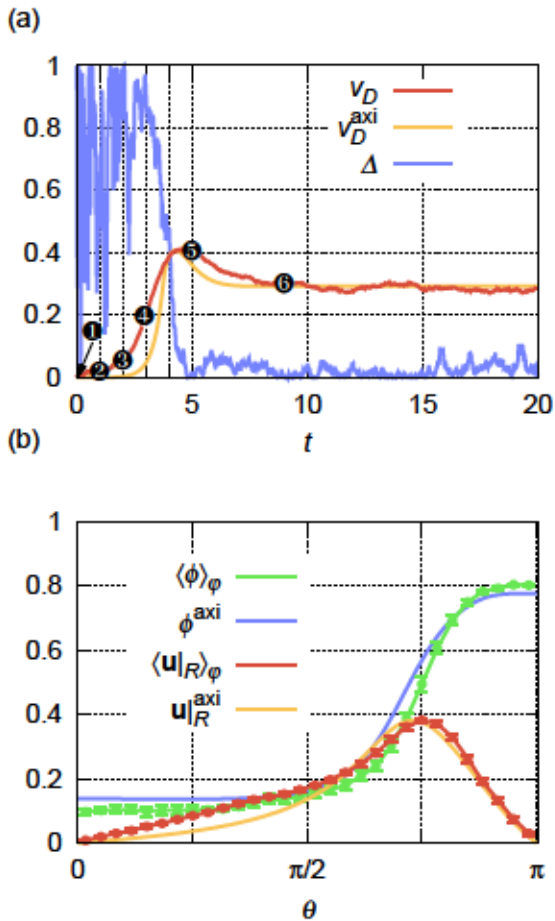


**Fig. 2.** (a) Droplet swimming speed  $v_D(t)$  of an active droplet from a simulation with  $v_4 = 2562$  FVM elements. Order parameter profiles  $\phi$  at the time steps marked with numbers are given in fig. 4(a). For comparison, we plot  $v_D^{\text{axi}}$  of the axisymmetric model taken from fig. 2 (a) of ref. [38] but on a different scale. We also show biaxiality parameter  $\Delta$  of the order parameter field defined in eq. (18). (b) Order parameter profile  $\langle \phi \rangle_\varphi$  and velocity field  $\langle \mathbf{u}|_R \rangle_\varphi$  at  $t = 20$ , averaged about the swimming axis  $\mathbf{e}$  as indicated by  $\langle \dots \rangle_\varphi$  and defined in appendix D. The front of the droplet corresponds to the polar angle  $\theta = 0$ . For comparison, we plot  $\phi^{\text{axi}}$  and  $\mathbf{u}|_R^{\text{axi}}$  from the axisymmetric model taken from fig. 1 of ref. [38]. Note that the Marangoni flow  $\mathbf{u}|_R$  is directed along the gradients of  $\phi$  and surface tension  $\sigma$ .

ref. [38], which we also plot in fig. 2(a). The same applies to the order parameter profile  $\phi$  and the surface velocity field  $\mathbf{u}|_R$  of the swimming state, when averaged about the swimming axis  $\mathbf{e}$ , see fig. 2(b). Thus, the full three-dimensional description presented in this work is consistent with the axisymmetric model of ref. [38]. The same is true for the squirmer parameter  $\beta$  from eq. (28), for which we find  $\beta \approx -1.2$  for  $M = 3$ . This is fairly close to the value of the axisymmetric model ( $\beta \approx -0.8$ ) and confirms that the swimming active droplet is a pusher.

We stress that the Marangoni number  $M$  is the crucial parameter in our model, as it determines whether the

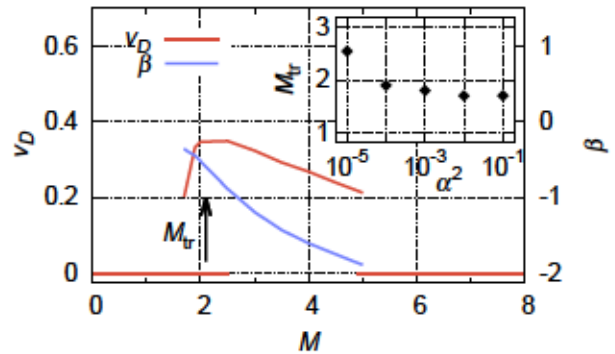


**Fig. 3.** Droplet swimming speed  $v_D$  and squirmer parameter  $\beta$  plotted versus Marangoni number  $M$  for zero thermal noise  $\xi = 0$ . At the transition Marangoni number  $M_{tr}$ ,  $v_D$  jumps to a non-zero value indicating a subcritical bifurcation. Inset:  $M_{tr}$  versus noise strength  $\alpha^2$ , with which the initially uniform order parameter profile is disturbed. The swimming regime terminates at an upper bifurcation, see also ref. [38].

droplet rests or swims. For small  $M$ , the homogeneous state  $\phi = \phi_{eq}$  is stable, *i.e.*, any disturbance  $\delta\phi$  of the initially uniform  $\phi$  is damped by the diffusion and reaction terms of eq. (11). As a result, the droplet rests. The transition to the swimming state occurs at increasing Marangoni number  $M$  via a subcritical bifurcation as illustrated in fig. 3, which shows swimming speed  $v_D$  and squirmer parameter  $\beta$  plotted versus  $M$ . We use here a system without thermal noise, *i.e.*,  $\xi = 0$ , in order to monitor the complete transition region of the subcritical bifurcation. At a transition value  $M_{tr}$  the advective term of eq. (11) overcomes the damping terms. The homogeneous state becomes unstable and the droplet starts to swim with a finite swimming speed  $v_D$ . As usual for a subcritical bifurcation, the transition to the swimming state takes place in a finite interval of  $M$ . There, the transition Marangoni number  $M_{tr}$  depends on the initial disturbance strength  $\alpha^2$  of the uniform order parameter profile. The inset of fig. 3 confirms this statement. Next, we will discuss the biaxial evolution and the coarsening dynamics of the order parameter field, which we could not study in the axisymmetric description.

#### 4.2 Transient biaxial dynamics

The good agreement of the rotationally averaged order parameter profile  $\langle \phi \rangle_\varphi$  and the axisymmetric  $\phi^{\text{axi}}$  from our earlier work, both plotted in fig. 2 (b), suggests that in the steady swimming state, the full three-dimensional solution is also nearly axisymmetric about the swimming axis  $\mathbf{e}$ . However, in non-steady state we expect  $\phi$  to deviate from axisymmetry, which we quantify by introducing an appropriate measure for the biaxiality of the order parameter field  $\phi$ . In analogy to characterizing the orientational order of liquid crystals, we define for the order parameter profile the traceless quadrupolar tensor [75]

$$\mathbf{Q} = \iint \phi \left( \mathbf{n} \otimes \mathbf{n} - \frac{1}{3} \mathbb{1} \right) d\Omega, \quad (17)$$

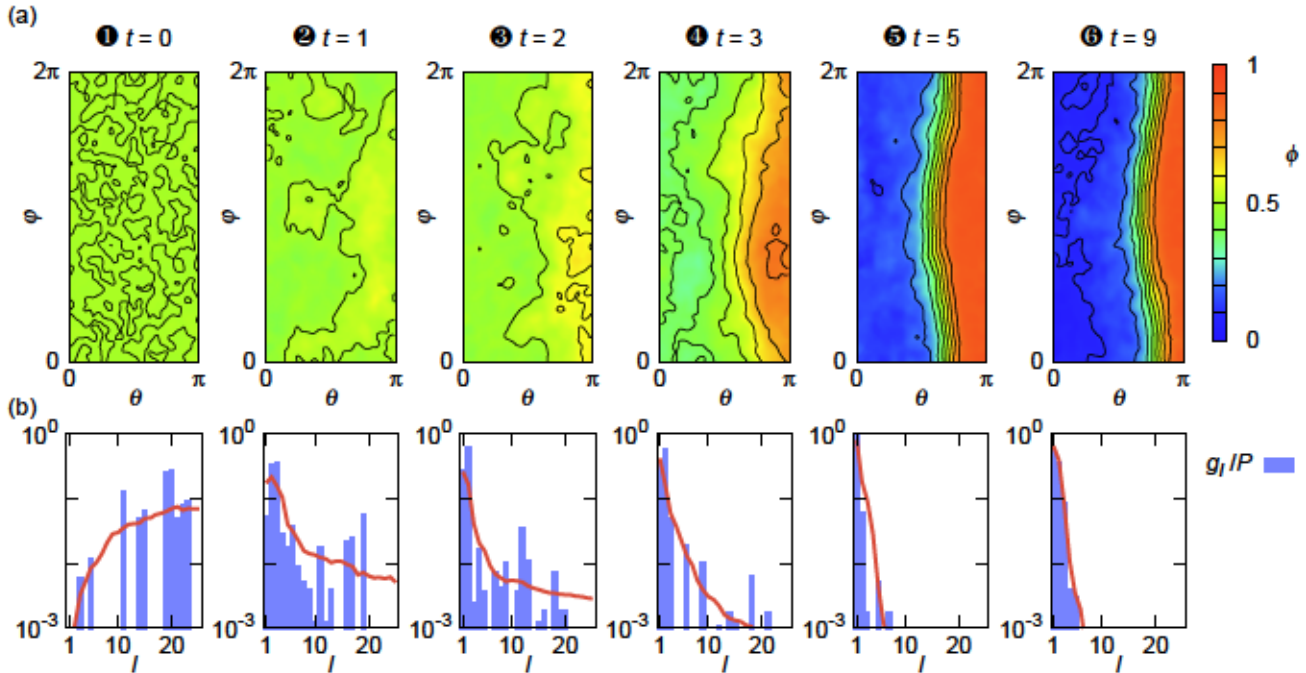


**Fig. 4.** (a) Color-coded order parameter profile  $\phi(\theta, \varphi)$  at various time steps in the coordinate frame of the droplet, where the front of the droplet is located at  $\theta = 0$ . Lines of equal  $\phi$  are drawn. The time snapshots are indicated in fig. 2 (a) in the curve for  $v_D$  (same simulation run). The relevant parameters are:  $M = 3$ ,  $\kappa = 0.1$ ,  $\phi_{\text{eq}} = 0.5$ , and  $\xi = 10^{-3}$ . (b) The bar charts show the normalized polar power spectrum  $g_l/P$  of surface tension  $\sigma$  for the profiles in (a). Lines depict  $g_l/P$  averaged over 500 simulation runs.

with surface normal  $\mathbf{n}$ , unit tensor  $\mathbb{1}$ , and the surface integral is performed over the whole droplet interface. Just as in the case of the moment of inertia tensor, the eigenvalues and eigenvectors of  $\mathbf{Q}$  characterize the symmetries of the order parameter field  $\phi$ . If two eigenvalues of  $\mathbf{Q}$  are equal,  $\phi$  is said to be uniaxial. On the other hand, if all eigenvalues of  $\mathbf{Q}$  are distinct,  $\phi$  is biaxial. Finally, the case of three vanishing eigenvalues, *i.e.*,  $\mathbf{Q} = 0$ , describes an isotropic or uniform order parameter field  $\phi$  or at least with tetrahedral or cubic symmetry. A measure for the degree of biaxiality, which incorporates the three mentioned cases, is given by the biaxiality parameter [76,77]

$$\Delta = 1 - 6 \frac{(\text{tr} \mathbf{Q}^3)^2}{(\text{tr} \mathbf{Q}^2)^3}. \quad (18)$$

If the order parameter field  $\phi$  is axisymmetric or isotropic,  $\Delta = 0$ , while with increasing biaxiality  $\Delta$  approaches 1.

In fig. 2 (a), we plot  $\Delta$  as a function of time. At the initial time  $t = 0$ , the order parameter profile is roughly uniform with  $\Delta \approx 0$  (not visible). As the droplet speeds up, the biaxiality parameter  $\Delta$  fluctuates strongly between 0 and 1. Starting at  $t \approx 3$ ,  $\Delta$  sharply decreases towards zero before the swimming speed becomes maximal. Finally, in the steady swimming state,  $\Delta$  is nearly zero but still fluctuates due to the thermal noise in the order parameter profile  $\phi$ , which we indicate by the error bars in fig. 2 (b). Hence, during the speed up of the droplet, the order parameter field  $\phi$  clearly is not axisymmetric.

### 4.3 Coarsening dynamics

The period of strong biaxiality goes in hand with the coarsening dynamics of the order parameter profile towards steady state. Figure 4(a) shows the order parameter profile  $\phi(\theta, \varphi)$  at various time steps for the same simulation run as in fig. 2. Shortly after the simulation starts with the nearly uniform initial condition, small islands or domains with  $\phi > \phi_{\text{eq}}$  and  $\phi < \phi_{\text{eq}}$  emerge, which rapidly grow until  $t \approx 1$ , where the droplet hardly moves, see fig. 2 (a). Then the coarsening or demixing process is slowed down. The domains coalesce on larger scales and the droplet speeds up significantly. Since the droplet interface area is finite, the domains coalesce at some point to one large region which covers about half of the interface. From then on the droplet interface is covered by only two regions with  $\phi < \phi_{\text{eq}}$  and  $\phi > \phi_{\text{eq}}$ , while the droplet has reached its top speed [compare  $v_D(t \approx 5)$  in fig. 2(a)]. Finally, the domain wall between the two regions moves to its final position while the droplet speed  $v_D$  slows down to its stationary value, which it reaches at  $t \approx 9$ .

Note that depending on the final position of the domain wall separating the two regions, the droplet is either a pusher or a puller. If the domain wall with increasing  $\phi$  is situated in the southern hemisphere ( $\pi/2 < \theta < \pi$ ), the droplet is a pusher. If it is located in the northern hemisphere ( $0 < \theta < \pi/2$ ), a puller is realized. In our simulations the droplet is always a pusher. However, the squirmer parameter  $\beta$  varies in the range  $-2 < \beta < 0$  depending on

Marangoni number  $M$  [see fig. 3] and equilibrium order parameter  $\phi_{\text{eq}}$ . This is in agreement with earlier observations in ref. [38]. The timeframe  $t > 9$ , where the swimming speed fluctuates around its steady-state value, will be covered in sect. 5.

To quantify further the spatial structure of the order parameter profile during coarsening, we examine the angular power spectrum  $|s_l^m|^2$  of the surface tension. It is related to  $\phi$  in eq. (9). Using the orthonormality relation of spherical harmonics  $Y_l^m(\theta, \varphi)$ , given in appendix A, one can compute the total power  $P$  of the surface tension  $\sigma$ :

$$P = \iint \sigma^2 d\Omega = \sum_{l=1}^{\infty} g_l = \sum_{l=1}^{\infty} \sum_{m=-l}^l |s_l^m|^2.$$

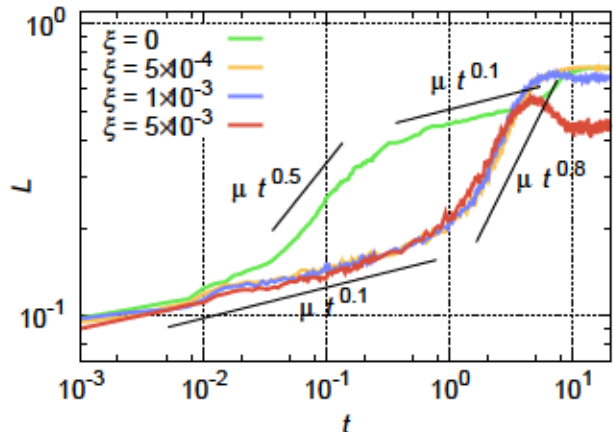
Here, the polar power spectrum  $g_l$  characterizes the variation of the surface tension and thus the order parameter field  $\phi$  along the polar angle  $\theta$ . In particular,  $g_l$  for small  $l$  quantifies the large-angle variations of  $\sigma$ . Note that  $g_1$  is directly related to the swimming speed  $v_D$  calculated from eq. (8) in the polar coefficients  $s_1^m$ . Using  $s_1^{-1} = -s_1^1$ , we find  $g_1 = 3\pi[(2 + 3v)v_D]^2$ .

Figure 4(b) depicts the polar power spectrum  $g_l$  normalized by the total power  $P$  at the same time steps of the coarsening dynamics discussed before in Fig. 4(a). We also show an ensemble average of  $g_l/P$ . At the initial time  $t = 0$ , the spectrum of  $g_l$  is solely characterized by frequencies or polar contributions of the noisy initial condition  $\phi(t = 0) = \phi_{\text{eq}} + \delta\phi$ . Thus, the maximum frequency or polar number  $l$  of the spectrum at  $t = 0$  is set by the level of refinement of the simulation mesh. During the initial period of fast coarsening until  $t = 1$ , the polar power spectrum shifts from high to low frequencies indicating the increase of domain sizes. Then the higher frequencies vanish more and more from the spectrum, as the phases associated with  $\phi < \phi_{\text{eq}}$  and  $\phi > \phi_{\text{eq}}$  separate. Eventually, the spectrum  $g_l$  strongly peaks at  $l = 1$  while the remaining coefficients become insignificant in comparison. Finally, from  $t = 5$  to  $t = 9$ , the first coefficient  $g_1$  of the angular power spectrum decreases again while the second and third coefficients  $g_2$  and  $g_3$  rise. This confirms that in the final stage the droplet slows down its velocity  $v_D$  and tunes its squirmer parameter  $\beta$  by shifting the domain wall further away from the equator.

In order to quantify further the temporal evolution of the coarsening dynamics, we will now investigate the average domain size as a function of time. We define the mean linear size of a phase domain by

$$L = \sqrt{\frac{\langle v_n^+ \rangle}{v_n}}.$$

Here,  $\langle v_n^+ \rangle$  denotes the averaged number of grid points in a connected region, where  $\phi$  is larger than  $\phi_{\text{eq}}$ , and  $v_n$  is the total number of grid points. Thus, the domain size lies within the range  $\sqrt{1/v_n} \leq L \leq 1$ , and  $L(t)$  should increase during the coarsening dynamics towards the steady swimming state. The fluctuations  $\delta\phi$  of the initial profile are normal distributed with zero mean such that at



**Fig. 5.** Mean domain size  $L$  averaged over 200 simulation runs plotted versus reduced time in units of  $\tau_D$  for different noise strengths  $\xi$ . A domain is defined by a compact region with  $\phi > \phi_{\text{eq}}$ . Same parameters as in fig. 4 are used.

$t = 0$  half of the grid points have  $\phi > \phi_{\text{eq}}$ . They cannot all be isolated but rather belong to small connected regions with  $L \approx \sqrt{5/v_n}$ , where we extracted the factor  $\sqrt{5}$  from our simulations at  $t = 0$ . Furthermore, we expect the maximum length to be around  $L \approx \sqrt{1/2}$ . So, in our simulations  $L(t)$  lies in the interval  $\sqrt{5/v_n} \leq L \leq \sqrt{1/2}$ . Figure 5 shows  $L(t)$  averaged over 200 simulation runs for different noise strengths  $\xi$ . The other parameters are the same as before. We clearly see a separation of time scales of the coarsening dynamics for both cases, with and without noise. At early times, we find in both cases a power law behavior  $L(t) \propto t^{0.1}$ . Without noise, coarsening quickly speeds up at a rate  $L(t) \propto t^{1/2}$  and then slows down again to  $L(t) \propto t^{0.1}$ . In contrast, thermal fluctuations in the order parameter profile hinder early coarsening and the mean domain size continues to grow slowly with  $L(t) \propto t^{0.1}$  over several decades and then crosses over to a fast final coarsening with rate  $L(t) \propto t^{0.8}$ . The crossover time is only determined by the diffusion time  $\tau_D$  and does not depend on noise strength  $\xi$ . Interestingly, a similar observation to the second case has been made for coarsening in the dynamical model H, where the Cahn-Hilliard equation couples to fluid flow at low-Reynolds number via an advection term. A slow coarsening rate  $L(t) \propto t^{1/3}$  in a diffusive regime at short times is followed by an advection driven regime with  $L(t) \propto t$  at later times [62, 78–80]. Although we cannot simply reformulate our model as an advective Cahn-Hilliard equation, since the phase separation in our case is driven by the interfacial flow  $\mathbf{u}|_R$  itself, we observe similar coarsening regimes as in model H, when we include some noise.

## 5 Dynamics of the swimming state

We now consider the time regime  $t > 9$ , where the droplet moves in its steady swimming state. However, as can be observed in fig. 2 (a), the droplet speed  $v_D(t > 9)$  in the

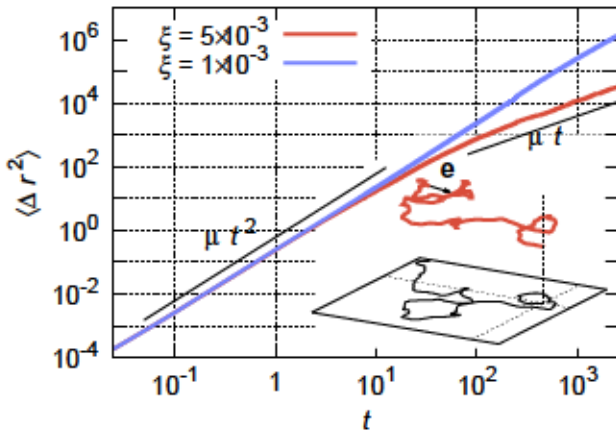


**Fig. 6.** Mean square displacement of the swimming active droplet for different noise strengths  $\xi$ . At  $t = 0$  the droplet is already in the swimming state. Inset: A typical trajectory  $\mathbf{r}(t)$  of an active droplet subject to noise with strength  $\xi = 5 \cdot 10^{-3}$ . The trajectory is reminiscent of an active particle with constant speed and rotationally diffusing orientation vector  $\mathbf{e}(t)$ .

swimming state strongly fluctuates since we have added a thermal noise term to the diffusion-advection-reaction equation (11) for the order parameter field  $\phi$ . These fluctuations also randomly change the swimming direction  $\mathbf{e}$  as the inset of fig. 6 illustrates, where we show an exemplary swimming trajectory  $\mathbf{r}(t) = \mathbf{r}(0) + \int_0^t dt' v_D(t') \mathbf{e}(t')$ . Therefore, we expect the droplet to perform active Brownian motion or a persistent random walk. In a droplet with axisymmetric profile the swimming direction is perpendicular to the domain wall separating both phases. When the order-parameter profile fluctuates, we also expect the domain wall to fluctuate and thereby the swimming direction  $\mathbf{e}$ . There are no other reasons to change the orientation of  $\mathbf{e}$ . In ref. [43] we showed that a spherical emulsion droplet with Marangoni flow at its surface does not experience a frictional torque, which could also change the swimming direction. But this also means that fluctuating flow fields in the surrounding fluid cannot generate a stochastic torque acting on the droplet.

### 5.1 Active Brownian motion of the droplet

To characterize the active Brownian motion of the droplet, we first discuss the mean squared displacement (MSD)  $\langle \Delta r^2 \rangle = \langle [\mathbf{r}(t) - \mathbf{r}(0)]^2 \rangle$ , where we average over an ensemble of trajectories. Here, the droplet is already in the swimming state at  $t = 0$ , thus the MSD does not include the droplet's acceleration towards the steady swimming state as discussed in sect. 4. Figure 6 shows the MSD for a droplet with noise strength  $\xi = 5 \cdot 10^{-3}$ . At early times, the droplet moves ballistically since the MSD grows as  $\langle \Delta r^2 \rangle \propto t^2$ , while between  $t = 10$  and  $t = 100$  it crosses over to diffusive motion with  $\langle \Delta r^2 \rangle \propto t$ . This motion persists as  $t \rightarrow \infty$ . As expected, in the absence of noise,  $\xi = 0$ , we always observe ballistic motion  $\langle \Delta r^2 \rangle \propto t^2$  (not

shown). The MSD for  $\xi = 10^{-3}$  in fig. 6 does not cross over to diffusion in the plotted time range. In the following, we will discuss the influence of the noise strength  $\xi$  on the Brownian motion in more detail but we will first introduce what has become the standard model of an active Brownian particle [15, 81, 11, 12].

If we assume the droplet speed  $v_D$  and orientation vector  $\mathbf{e}$  to be independent random variables, we can factorize the MSD as

$$\langle \Delta r^2 \rangle = \int_0^t dt' \int_0^t dt'' \langle v_D(t') v_D(t'') \rangle \langle \mathbf{e}(t') \cdot \mathbf{e}(t'') \rangle.$$

For active Brownian particles without any aligning field the swimming direction diffuses freely on the unit sphere, which one describes by the rotational diffusion equation  $\partial_t p(\mathbf{e}, t) = D_r \nabla_s^2 p(\mathbf{e}, t)$ . Thus the orientational correlation function decays as [82, 83]

$$\langle \mathbf{e}(0) \cdot \mathbf{e}(t) \rangle = e^{-t/\tau_r}. \quad (19)$$

Here, the rotational correlation time  $\tau_r = 1/(2D_r)$  is the characteristic time it takes the droplet to “forget” about the initial orientation  $\mathbf{e}(0)$ . Hence, for times  $t < \tau_r$  the droplet swims roughly in the direction of  $\mathbf{e}(0)$ , while at later times  $t > \tau_r$  the orientation becomes randomized.

Under the assumption of a constant swimming speed, i.e.  $\langle v_D(t') v_D(t'') \rangle = (v_D)^2$ , one finds for the MSD

$$\langle \Delta r^2 \rangle = 2(v_D \tau_r)^2 \left( \frac{t}{\tau_r} - 1 + e^{-t/\tau_r} \right). \quad (20)$$

Expression (20) confirms the findings of fig. 6: Ballistic motion  $\langle \Delta r^2 \rangle = (v_D t)^2$  with velocity  $v_D$  at  $t \ll \tau_r$  and diffusive motion with

$$\langle \Delta r^2 \rangle = 6D_{\text{eff}} t \quad \text{and} \quad D_{\text{eff}} = (v_D)^2 \tau_r / 3 \quad (21)$$

for  $t \gg \tau_r$ . Here,  $D_{\text{eff}}$  is the effective translational diffusion constant. It neglects any contribution from thermal translational motion, which is o.k. for sufficiently large  $v_D$ .

Indeed, for the active droplet the rotational correlation function  $\langle \mathbf{e}(0) \cdot \mathbf{e}(t) \rangle$  decays exponentially as demonstrated in fig. 7 for different noise strengths and by fits to eq. (19). The rotational correlation time  $\tau_r$ , which acts as fitting parameter, is shown in the inset for various values of noise strength  $\xi$ . For  $\xi = 5 \cdot 10^{-3}$ , we find  $\tau_r \approx 30$ , which is in agreement with the cross-over region from ballistic to diffusive motion in the MSD curve of fig. 6. Furthermore, from the asymptotic behavior at  $t \ll \tau_r$  and  $t \gg \tau_r$  of the MSD in fig. 6, we find  $v_D \approx 0.3$  and  $D_{\text{eff}} \approx 1$ , respectively. This gives the rotational correlation time  $\tau_r = 3D_{\text{eff}}/(v_D)^2 \approx 33$ , which is close to the value determined from the orientational correlations. Thus  $D_{\text{eff}}$  and  $\tau_r$  comprise the same information about the droplet trajectory  $\mathbf{r}(t)$ . However, the measurement of  $\tau_r$  in experiments or simulations can be done on much shorter time scales than  $D_{\text{eff}}$ .

We do not know published experimental data for trajectories of active droplets in an unbounded fluid. However, fig. 1 of ref. [1] shows a trajectory of an active droplet confined between two glass plates. One can estimate

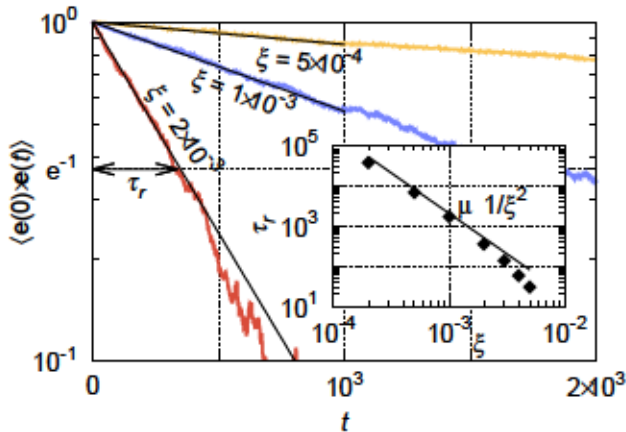


**Fig. 7.** Rotational correlation function of the active droplet and fits to  $e^{-t/\tau_r}$  for different values of noise strength  $\xi$ . At the rotational correlation time  $\tau_r$ , one has  $\langle \mathbf{e}(0) \cdot \mathbf{e}(\tau_r) \rangle = e^{-1}$ , as illustrated for the case  $\xi = 2 \cdot 10^{-3}$ . Inset:  $\tau_r$  plotted versus noise strength  $\xi$  and a fit to  $\xi^{-2}$ .

the rotational correlation time  $\tau_r$  to be on the order of 100s. To compare this value with our model, we recapitulate the noise strength  $\xi = \ell/R$ , which connects surfactant head size  $\ell$  with droplet radius  $R$ , see sect. 2.3. If we assume,  $\xi \approx 10^{-4} \dots 10^{-3}$ , we find from fig. 7 a rotational correlation time  $\tau_r \approx 10^4$  given in units of diffusion time  $\tau_D = R^2/D$  with interfacial diffusion constant  $D$ . Typical values for  $D$  are on the order of  $10^{-5} \text{cm}^2/\text{s}$  [84]. Thus, for a droplet with  $R$  on the order of  $10 \mu\text{m}$ , one finds  $\tau_D \approx 0.1\text{s}$  and the rotational correlation time  $\tau_r \approx 10^3\text{s}$ .

This is only a factor 10 larger than the estimated value of 100s from ref. [1]. Given some uncertainties in our estimate such a difference can be expected. Nevertheless, two causes for the discrepancy are thinkable. First and foremost, our model droplet is allowed to move freely in the bulk fluid, while the real droplet of ref. [1] is confined between two plates, which limits the degrees of freedom and thus alters  $\tau_r$ . Secondly, active emulsion droplets are usually immersed in a surfactant laden fluid well above the critical micelle concentration. Hence, the surfactants from the bulk adsorb in form of micelles. This leads to local disturbances in the surfactant mixture at the front of the swimming droplet, and hence to an additional randomization of the droplet trajectory. We recently modeled the adsorption of micelles explicitly in a different system [43].

## 5.2 How fluctuations randomize the droplet direction

Now, we develop a theory how the noise strength  $\xi$  influences the rotational diffusion of the droplet direction. By increasing  $\xi$  in the diffusion-advection-reaction equation (11), the order parameter profile  $\phi$  is subject to stronger fluctuations. In particular, these fluctuations affect shape and orientation of the domain wall separating the two regions with  $\phi < \phi_{\text{eq}}$  and  $\phi > \phi_{\text{eq}}$  from each other. The surface flow field is largest in this domain wall and thereby

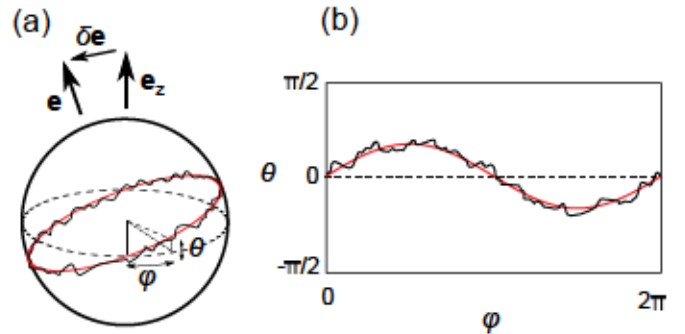


**Fig. 8.** Illustration of a reorienting droplet. (a) The black curve around the droplet interface shows the noisy phase boundary denoted in the coordinate system  $(\theta, \varphi)$  of the droplet without noise. The red curve shows the first mode of a Fourier expansion, see text. (b) Flat representation in the said coordinate system  $(\theta, \varphi)$ .

the orientation of the wall on the droplet interface determines the droplet swimming vector  $\mathbf{e}$ . Thus, increasing noise strength  $\xi$  results in stronger fluctuations of  $\mathbf{e}$  and ultimately a more pronounced rotational diffusion. The inset of fig. 7 confirms this scenario for the rotational correlation time  $\tau_r$ . Interestingly, for noise strengths up to  $\xi \approx 3 \cdot 10^{-3}$ , one fits the data quite well by  $\tau_r \propto 1/\xi^2$ . For the active emulsion droplet it can be explained by applying perturbation theory to the thermal fluctuations of the order parameter profile around its steady profile.

As mentioned before, small fluctuations of the domain wall result in random changes of the droplet direction. Figure 8 shows an exaggerated illustration of the situation. Plot (a) illustrates a tilt in the orientation of the domain wall generated by the sinusoidal variation of the polar angle  $\theta$  along the azimuthal angle  $\varphi$ . In general, fluctuations of the domain wall can be decomposed into Fourier modes,  $\theta = \sum_m a_m \sin[m(\varphi - \varphi_{0m})]$ . Only the first mode,  $m = 1$ , of this expansion determines the change in orientation,  $\delta\mathbf{e}$ , as illustrated in fig. 8 (a). All higher modes cannot change the swimming direction since the effects of the resulting surface flow field on  $\mathbf{e}$  cancel each other.

We now apply perturbation theory to the fluctuating order parameter profile, which determines the surface tension profile and thereby the swimming direction according to eq. (8). We consider a droplet, which initially swims in  $z$ -direction and changes its direction in  $x$  and/or  $y$ -direction, hence  $\mathbf{e} = \mathbf{e}_z + \delta\mathbf{e}$ . We write down a perturbation ansatz for the surface tension profile,  $\sigma = \sigma_0 + \delta\sigma$ , with the unperturbed axisymmetric part  $\sigma_0 = \sum_{l=1}^{\infty} s_l^0 Y_l^0$  and the perturbation  $\delta\sigma = s_1^1 Y_1^1 + s_1^{-1} Y_1^{-1}$ , where we only include the coefficients  $s_1^{\pm 1}$ , which are responsible for changes  $\delta\mathbf{e}$ , as one recognizes from eq. (8). By linearizing the equation of state (9) around  $\phi_{\text{eq}}$ , one can connect the coefficients  $s_l^m$  of  $\sigma$  directly to the expansion coefficients of the order parameter field  $\phi$ . Writing  $\phi = \phi_0 + \delta\phi$ , where  $\phi_0$  describes the unperturbed steady-state field and  $\delta\phi$  its fluctuations, we find  $\phi_0 = a\sigma_0$  and  $\delta\phi = a\delta\sigma$ , where the factor  $a$  is given in appendix E. Similarly, one decomposes  $\mathbf{j}_D$  and  $\mathbf{u}|_R$  into their steady-state fields and a fluctuating small

perturbation (see appendix E). This allows us to derive from the field equation (11) of the order parameter, the dynamic equation linear in the fluctuating perturbations:

$$\partial_t \delta\phi = -\nabla_s \cdot [\delta\mathbf{j}_D + M(\delta\phi\mathbf{u}_0 + \phi_0\delta\mathbf{u})] - \kappa\delta\phi + \xi\zeta. \quad (22)$$

From our study of the coarsening dynamics we know that the first and second term on the right-hand side describe a relaxation towards steady state on times  $t < 10$ . The rotational diffusion of the droplet direction occurs on time scales much larger and can only be due to the noise term. Extracting from Eq. (22) the coefficients  $s_1^{\pm 1}$  relevant for  $\delta\mathbf{e}$ , we obtain

$$\partial_t s_1^{\pm 1} \simeq \frac{\xi}{a} \zeta_1^{\pm 1}. \quad (23)$$

A more thorough derivation of Eq. (23) is presented in appendix F. We have decomposed noise  $\zeta$  into its multipole moments,  $\zeta = \sum_{l,m} \zeta_l^m Y_l^m$ . Projecting the variance of eq. (12) onto the relevant spherical harmonics, we obtain the fluctuation-dissipation theorem

$$\langle \zeta_l^m(t) \bar{\zeta}_{l'}^{m'}(t') \rangle = 2l(l+1)\delta(t-t')\delta_{l,l'}\delta_{m,m'}. \quad (24)$$

Assuming a constant speed  $v_D$  during the reorientation of the droplet, we use eq. (23) in eq. (13b) for the droplet velocity vector to formulate the stochastic equation for rotations of the direction vector  $\mathbf{e}$ :

$$\partial_t \mathbf{e} = \frac{\xi}{\sqrt{6\pi}v_D(2+3\nu)a} \delta\boldsymbol{\zeta}, \quad (25)$$

where we introduced the rotational noise vector

$$\delta\boldsymbol{\zeta} = \begin{pmatrix} \zeta_1^1 - \zeta_1^{-1} \\ i(\zeta_1^1 + \zeta_1^{-1}) \\ 0 \end{pmatrix}.$$

By comparing eq. (25) with the Langevin equation for the Brownian motion of a particle's orientation  $\mathbf{e}$  due to rotational noise  $\boldsymbol{\eta}_r$ :  $\partial_t \mathbf{e} = \sqrt{2D_r} \boldsymbol{\eta}_r \times \mathbf{e}$  [85], we identify  $\delta\boldsymbol{\zeta} = \boldsymbol{\eta}_r \times \mathbf{e}$  and

$$\frac{\xi}{\sqrt{6\pi}v_D(2+3\nu)a} = \sqrt{2D_r}. \quad (26)$$

Hence, the rotational correlation time  $\tau_r = 1/(2D_r)$  scales as  $\tau_r \propto 1/\xi^2$  with noise strength  $\xi$ . This confirms the fit in the inset of fig. 7. Thus, beyond the time scale, the order parameter profile needs to reach its steady state, the dynamics of the swimming active emulsion droplet is equivalent to the dynamics of an active Brownian particle with constant swimming velocity and rotationally diffusing orientation vector  $\mathbf{e}$ .

## 6 Conclusions

In this paper we considered an active emulsion droplet, which is driven by solutocapillary Marangoni flow at its interface [1]. A diffusion-advection-reaction equation for

the surfactant mixture at the droplet interface, which we formulated in ref. [38], is used together with the analytic solution of the Stokes equation [43]. By omitting the axisymmetric constraint and including thermal noise into the description of the surfactant mixture, we generalized the model of ref. [38] to a full three-dimensional system and thereby were able to focus on new aspects.

First, we explored the dynamics from a uniform, but slightly perturbed surfactant mixture to the uniaxial steady swimming state, where the two surfactant types are phase-separated. In between the initial and the swimming state, the surfactant mixture is not axisymmetric, which we verified by introducing and evaluating a biaxiality measure. We then investigated in detail the coarsening dynamics towards the swimming state by means of the polar power spectrum of the surface tension  $\sigma$  as well as the average domain size of the surfactant mixture. The coarsening proceeds in two steps. An initially slow growth of domain size is followed by a nearly ballistic regime, which is reminiscent to coarsening in the dynamic model H [62].

Second, we studied the dynamics of the squirming droplet. Due to the included thermal noise, the surfactant composition fluctuates and thereby the droplet constantly changes its swimming direction performing a persistent random walk. Thus, the swimming dynamics of the squirming droplet is a typical example of an active Brownian particle. The persistence of the droplet trajectory depends on the noise strength  $\xi$ . It is characterized by the rotational correlation time, for which we find the scaling law  $\tau_r \propto \xi^{-2}$ . In fact, we are able to explain this scaling by applying perturbation theory to the diffusion-advection-reaction equation for the mixture order parameter. Thus we can link the dynamics of the surfactants at the molecular level to the dynamics of the droplet as a whole.

Exploring and understanding the swimming mechanisms of both biological and artificial microswimmers is one of the challenges in the field. Here, we demonstrated that this task involves new and fascinating physics. Having gained deeper insights into these mechanisms can help to further improve the design of artificial microswimmers and tailor them for specific needs such as cargo transport.

We acknowledge financial support by the Deutsche Forschungsgemeinschaft in the framework of the collaborative research center SFB 910, project B4 and the research training group GRK 1558.

## A Spherical harmonics

Throughout this paper we use the following definition of spherical harmonics:

$$Y_l^m(\theta, \varphi) = \sqrt{\frac{2l+1}{4\pi} \frac{(l-m)!}{(l+m)!}} P_l^m(\cos\theta) e^{im\varphi},$$

with associated Legendre polynomials  $P_l^m$  of degree  $l$ , order  $m$ , and with orthonormality:

$$\iint Y_l^m \bar{Y}_{l'}^{m'} d\Omega = \delta_{l,l'} \delta_{m,m'},$$

where  $\overline{Y}_l^m$  denotes the complex conjugate of  $Y_l^m$ .

The spherical harmonics fulfill the following helpful relations:

$$\iint Y_l^0 Y_1^m \overline{Y}_1^{m'} d\Omega = \frac{-1}{\sqrt{20\pi}} \delta_{l,2} \delta_{m,m'} , \quad (27a)$$

$$\iint \nabla_s Y_l^0 \cdot \nabla_s Y_1^m \overline{Y}_1^{m'} d\Omega = \frac{-3}{\sqrt{20\pi}} \delta_{l,2} \delta_{m,m'} , \quad (27b)$$

where  $\nabla_s$  is the directional gradient defined in sect. 2.1 and evaluated at  $r = 1$ .

## B Squirmer parameter

The squirmer parameter for a droplet swimming in an arbitrary direction is given by [43]:

$$\beta = -\sqrt{\frac{27}{5}} \frac{\tilde{s}_2^0}{|\tilde{s}_1^0|} , \quad (28a)$$

$$\tilde{s}_1^0 = \sqrt{(s_1^0)^2 - 2s_1^1 s_1^{-1}} , \quad (28b)$$

$$\tilde{s}_2^0 = \left( \sqrt{6} [s_2^2 (s_1^{-1})^2 + s_2^{-2} (s_1^1)^2] - \sqrt{12} s_1^0 [s_2^1 s_1^{-1} + s_2^{-1} s_1^1] + 2s_2^0 [(s_1^0)^2 + s_1^1 s_1^{-1}] \right) / [2(s_1^0)^2 - 4s_1^1 s_1^{-1}] , \quad (28c)$$

with coefficients  $s_l^m$  from eq. (7). By setting  $m = 0$ , this reduces to the case of an axisymmetric droplet swimming along the  $z$ -direction.

## C Element noise vector

Here, we discretize the thermal noise  $\zeta$  in eq. (11) and obtain the element noise vector  $\underline{z}$  with component  $z_i$  for the FVM element  $i$ . We define the correlation function between  $z_i$  and  $z_j$  by integrating eq. (12) over element areas  $A_i$  and  $A_j$ :

$$\langle z_i(t) z_j(t') \rangle \equiv \iint_{A_i} dA_i \iint_{A_j} dA_j \langle \zeta(\mathbf{r}_i, t) \zeta(\mathbf{r}_j, t') \rangle \quad (29a)$$

$$= 2 \int_{\partial A_i} dS_i \mathbf{n}_i \cdot \int_{\partial A_j} dS_j \mathbf{n}_j \delta(\mathbf{r}_i - \mathbf{r}_j) \delta(t - t') \quad (29b)$$

$$= 2 \sum_q l_{iq} \sum_p l_{jp} \delta_{q,p} \mathbf{n}_{iq} \cdot \mathbf{n}_{jp} \delta(t - t') . \quad (29c)$$

In eq. (29b) we used the divergence theorem and in eq. (29c) we converted the line integrals into sums over the element boundaries. Furthermore, we discretized  $\delta(\mathbf{r}_i - \mathbf{r}_j)$  by partitioning the surface into rhombi of area  $A_\diamond$  (see fig. 1) and defined

$$\delta_{q,p} = \begin{cases} 1/A_\diamond & \text{for } q = p , \\ 0 & \text{for } q \neq p , \end{cases}$$

where  $q$  and  $p$  are the indices of the respective boundaries of elements  $i$  and  $j$ . Three cases have to be considered. First, if the elements  $i$  and  $j$  are neither identical nor neighbors,  $\delta_{q,p}$  vanishes in eq. (29c) for all  $q$  and  $p$ . Second, for  $i = j$ ,  $\delta_{q,p} = 1/A_\diamond$  and  $\mathbf{n}_{iq} \cdot \mathbf{n}_{jp} = 1$  for all  $q$  and  $p$ . Finally, for neighboring elements there is one common boundary, where  $\delta_{q,p} = 1/A_\diamond$  and  $\mathbf{n}_{iq} \cdot \mathbf{n}_{jp} = -1$ . Thus, one finds:

$$\langle \underline{z}(t) \otimes \underline{z}(t') \rangle = \frac{2Nl^2}{A_\diamond} \left( \underline{\underline{1}} - \frac{1}{N} \underline{\underline{Q}} \right) \delta(t - t') , \quad (30)$$

where  $N$  is the number of element boundaries. Here,  $Q_{ij} = 1$  if elements  $i$  and  $j$  are neighbors and zero otherwise. Note that in eq. (30), we assumed the same edge length  $l$  and number of boundaries  $N$  for all elements. This is reasonable for a refined icosahedron with 642 FVM elements, as discussed in sect. 3. The form of eq. (30) acknowledges the conservation law for the noise [86]. However, in simulations we did not observe any effect of the next-neighbor correlations and therefore simplified the noise to the expression (16b) in the main text. Furthermore, we take  $N = 6$  and  $A_\diamond = \sqrt{3/4} l^2$ , since our grid is mostly hexagonal, which explains the prefactor  $\sqrt{2Nl^2/A_\diamond} = 2 \cdot 12^{1/4}$  in eq. (15), when we redefine the noise vector by the following replacement,  $\underline{z} \rightarrow 2 \cdot 12^{1/4} \underline{\underline{z}}$ .

## D Average over droplet interface

The average

$$\langle f \rangle_\varphi = \frac{1}{2\pi} \int f(\theta, \varphi) d\varphi ,$$

is taken over the azimuthal angle  $\varphi$  in the coordinate frame whose  $z$ -axis is directed along the swimming direction  $\mathbf{e}$ . Here, the front of the moving droplet is at  $\theta = 0$ .

## E Perturbation ansatz

The zero and first-order contributions of  $\phi = \phi_0 + \delta\phi$ ,  $\mathbf{j}_D = \mathbf{j}_{D,0} + \delta\mathbf{j}_D$ , and  $\mathbf{u}|_R = \mathbf{u}_0 + \delta\mathbf{u}$  are given by:

$$\phi_0 = a \sum_{l=1}^{\infty} s_l^0 Y_l^0 , \quad (31a)$$

$$\delta\phi = a (s_1^1 Y_1^1 + s_1^{-1} Y_1^{-1}) , \quad (31b)$$

$$\mathbf{j}_{D,0} = -b \nabla_s \phi_0 , \quad (31c)$$

$$\delta\mathbf{j}_D = -b \nabla_s \delta\phi , \quad (31d)$$

$$\mathbf{u}_0 = c s_1^0 \nabla_s Y_1^0 + \sum_{l=2}^{\infty} \frac{s_l^0}{2l+1} \nabla_s Y_l^0 , \quad (31e)$$

$$\delta\mathbf{u} = c (s_1^1 \nabla_s Y_1^1 + s_1^{-1} \nabla_s Y_1^{-1}) , \quad (31f)$$

with parameters

$$a = \frac{4(b_1 - b_2)}{2(b_1 - b_2) + \phi_{\text{eq}}(b_1 + b_2)} \approx 1.14, \quad (32a)$$

$$b = (1 - \phi_{\text{eq}}^2)^{-1} - \frac{1}{2}(b_1 + b_2 - b_{12}) \approx 1.11, \quad (32b)$$

$$c = (1 + \nu)/(2 + 3\nu) \approx 0.49. \quad (32c)$$

Here we used the values of sect. 2.3 for  $b_1, b_2, b_{12}, \phi_{\text{eq}}$  and  $\nu$ .

## F Dynamic equation for $s_1^{\pm 1}$

To derive a dynamic equation for the expansion coefficients  $s_1^{\pm 1}$ , we project the dynamic equation (22) for the perturbation  $\delta\phi$  onto the spherical harmonics  $Y_1^{\pm 1}$  [see also eq. (31b)]. Employing the orthonormality relation of the spherical harmonics and using eqs. (27), we ultimately obtain

$$\partial_t s_1^{\pm 1} = s_1^{\pm 1} \left[ -2b - \left( \frac{3}{5} - c \right) \frac{M}{\sqrt{20\pi}} s_2^0 - \kappa \right] + \frac{\xi}{a} \zeta_1^{\pm 1} \quad (33)$$

with noise components  $\zeta_l^m$  defined in eq. (24). Due to the nonlinear advection term  $M\phi\mathbf{u}|_R$  in eq. (11), the coefficients  $s_1^{\pm 1}$  couple to  $s_2^0$ . The term in square brackets on the right-hand side describes a relaxational dynamics for  $s_1^{\pm 1}$ . In particular, for the parameters chosen we find the swimming droplet to be a pusher. Thus, according to eq. (10) the coefficient  $s_2^0 > 0$  and the term in square brackets is always negative. On time scales larger than the relaxation time, we can ignore the relaxational dynamics and the time dependence of the order parameter perturbation is solely determined by the thermal noise term, which confirms relation (23).

Note that in the dynamic equation for  $s_l^0$  equivalent to eq. (33), the advective term  $\propto M$  is always positive and triggers for  $l = 1$  and for sufficiently large  $M$  the onset of forward propulsion of the droplet (see fig. 3 and ref. [38]).

## References

1. S. Thutupalli, R. Seemann, S. Herminghaus, *New J. Phys.* **13**, 073021 (2011)
2. A. Najafi, R. Golestanian, *Phys. Rev. E* **69**, 062901 (2004)
3. R. Dreyfus, J. Baudry, M.L. Roper, M. Fermigier, H.A. Stone, J. Bibette, *Nature* **437**, 862 (2005)
4. E. Gauger, H. Stark, *Phys. Rev. E* **74**, 021907 (2006)
5. E. Lauga, T.R. Powers, *Rep. Prog. Phys.* **72**, 096601 (2009)
6. J. Elgeti, R.G. Winkler, G. Gompper, *Rep. Prog. Phys.* **78**, 056601 (2015)
7. T. Fenchel, *Protist* **152**, 329 (2001), ISSN 1434-4610
8. T. Qiu, T.C. Lee, A.G. Mark, K.I. Morozov, R. Münster, O. Mierka, S. Turek, A.M. Leshansky, P. Fischer, *Nat. Commun.* **5** (2014)
9. D. Alizadehrad, T. Krüger, M. Engstler, H. Stark, *PLoS Comput. Biol.* **11**, e1003967 (2015)
10. C.C. Maass, C. Krüger, S. Herminghaus, C. Bahr, *Annu. Rev. Condens. Matter* **7** (2016)
11. M. Enculescu, H. Stark, *Phys. Rev. Lett.* **107**, 058301 (2011)
12. P. Romanczuk, M. Bär, W. Ebeling, B. Lindner, L. Schimansky-Geier, *Eur. Phys. J.-Spec. Top.* **202**, 1 (2012)
13. A. Zöttl, H. Stark, *Phys. Rev. Lett.* **108**, 218104 (2012)
14. S. Michelin, E. Lauga, D. Bartolo, *Phys. Fluids* **25**, 061701 (2013)
15. J.R. Howse, R.A. Jones, A.J. Ryan, T. Gough, R. Vafabakhsh, R. Golestanian, *Phys. Rev. Lett.* **99**, 048102 (2007)
16. V. Zaburdaev, S. Uppaluri, T. Pfohl, M. Engstler, R. Friedrich, H. Stark, *Phys. Rev. Lett.* **106**, 208103 (2011)
17. M. Theves, J. Taktikos, V. Zaburdaev, H. Stark, C. Beta, *Biophys. J.* **105**, 1915 (2013)
18. F. Kümmel, B. ten Hagen, R. Wittkowski, I. Buttinoni, R. Eichhorn, G. Volpe, H. Löwen, C. Bechinger, *Phys. Rev. Lett.* **110**, 198302 (2013)
19. G. Volpe, I. Buttinoni, D. Vogt, H.J. Kummerer, C. Bechinger, *Soft Matter* **7**, 8810 (2011)
20. K. Drescher, J. Dunkel, L.H. Cisneros, S. Ganguly, R.E. Goldstein, *Proc. Natl. Acad. Sci. U. S. A.* **108**, 10940 (2011)
21. T. Majmudar, E.E. Keaveny, J. Zhang, M.J. Shelley, J. R. Soc. Interface **9**, 1809 (2012)
22. K. Schaar, A. Zöttl, H. Stark, *Phys. Rev. Lett.* **115**, 038101 (2015)
23. M.C. Marchetti, J.F. Joanny, S. Ramaswamy, T.B. Liverpool, J. Prost, M. Rao, R.A. Simha, *Rev. Mod. Phys.* **85**, 1143 (2013)
24. T. Ishikawa, T.J. Pedley, *Phys. Rev. Lett.* **100**, 088103 (2008)
25. A.A. Evans, T. Ishikawa, T. Yamaguchi, E. Lauga, *Phys. Fluids* **23**, 111702 (2011)
26. J. Dunkel, S. Heidenreich, K. Drescher, H.H. Wensink, M. Bär, R.E. Goldstein, *Phys. Rev. Lett.* **110**, 228102 (2013)
27. F. Alarcón, I. Pagonabarraga, *J. Mol. Liq.* **185**, 56 (2013)
28. A. Zöttl, H. Stark, *Phys. Rev. Lett.* **112**, 118101 (2014)
29. M. Hennes, K. Wolff, H. Stark, *Phys. Rev. Lett.* **112**, 238104 (2014)
30. O. Pohl, H. Stark, *Phys. Rev. Lett.* **112**, 238303 (2014)
31. A. Zöttl, H. Stark, to be published in *J. Phys.: Condens. Matter*, arXiv preprint arXiv:1601.06643 (2016)
32. A. Walther, A.H. Müller, *Soft Matter* **4**, 663 (2008)
33. T. Bickel, A. Majee, A. Würger, *Phys. Rev. E* **88**, 012301 (2013)
34. R. Golestanian, T.B. Liverpool, A. Ajdari, *Phys. Rev. Lett.* **94**, 220801 (2005)
35. W.F. Paxton, A. Sen, T.E. Mallouk, *Chem. Eur. J.* **11**, 6462 (2005)
36. J.L. Moran, J.D. Posner, *J. Fluid. Mech.* **680**, 31 (2011)
37. I. Buttinoni, G. Volpe, F. Kümmel, G. Volpe, C. Bechinger, *J. Phys.: Condens. Matter* **24**, 284129 (2012)
38. M. Schmitt, H. Stark, *Europhys. Lett.* **101**, 44008 (2013)
39. M.J. Lighthill, *Commun. Pur. Appl. Math.* **5**, 109 (1952)
40. J.R. Blake, *J. Fluid. Mech.* **46**, 199 (1971)
41. M.T. Downton, H. Stark, *J. Phys.: Condens. Matter* **21**, 204101 (2009)

42. O. Pak, E. Lauga, *J. Eng. Math.* **88**, 1 (2014), ISSN 0022-0833
43. M. Schmitt, H. Stark, *Phys. Fluids* **28**, 012106 (2016)
44. M.M. Hanczyc, T. Toyota, T. Ikegami, N. Packard, T. Sugawara, *J. Am. Chem. Soc.* **129**, 9386 (2007)
45. T. Toyota, N. Maru, M.M. Hanczyc, T. Ikegami, T. Sugawara, *J. Am. Chem. Soc.* **131**, 5012 (2009)
46. H. Kitahata, N. Yoshinaga, K.H. Nagai, Y. Sumino, *Phys. Rev. E* **84**, 015101 (2011)
47. T. Banno, R. Kuroha, T. Toyota, *Langmuir* **28**, 1190 (2012)
48. T. Ban, T. Yamagami, H. Nakata, Y. Okano, *Langmuir* **29**, 2554 (2013)
49. S. Herminghaus, C.C. Maass, C. Krüger, S. Thutupalli, L. Goehring, C. Bahr, *Soft Matter* **10**, 7008 (2014)
50. Z. Izri, M.N. van der Linden, S. Michelin, O. Dauchot, *Phys. Rev. Lett.* **113**, 248302 (2014)
51. Y.J. Chen, Y. Nagamine, K. Yoshikawa, *Phys. Rev. E* **80**, 016303 (2009)
52. O. Bliznyuk, H.P. Jansen, E.S. Kooij, H.J.W. Zandvliet, B. Poelsema, *Langmuir* **27**, 11238 (2011)
53. A.Y. Rednikov, Y.S. Ryazantsev, M.G. Velarde, *J. Non-Equil. Thermody.* **19**, 95 (1994)
54. A.Y. Rednikov, Y.S. Ryazantsev, M.G. Velarde, *Phys. Fluids* **6**, 451 (1994)
55. M.G. Velarde, A.Y. Rednikov, Y.S. Ryazantsev, *J. Phys.: Condens. Matter* **8**, 9233 (1996)
56. M.G. Velarde, *Phil. Trans. R. Soc. Lond. A* **356**, 829 (1998)
57. N. Yoshinaga, K.H. Nagai, Y. Sumino, H. Kitahata, *Phys. Rev. E* **86**, 016108 (2012)
58. E. Tjhung, D. Marenduzzo, M.E. Cates, *Proc. Natl. Acad. Sci. U. S. A.* **109**, 12381 (2012)
59. N. Yoshinaga, *Phys. Rev. E* **89**, 012913 (2014)
60. S. Yabunaka, T. Ohta, N. Yoshinaga, *J. Chem. Phys.* **136**, 074904 (2012)
61. K. Furtado, C.M. Pooley, J.M. Yeomans, *Phys. Rev. E* **78**, 046308 (2008)
62. A. Bray, *Phil. Trans. R. Soc. Lond. A* **361**, 781 (2003)
63. V.A. Nepomniashchii, M.G. Velarde, P. Colinet, *Interfacial phenomena and convection*, 1st edn. (Chapman & Hall / CRC, 2002)
64. R.C. Desai, R. Kapral, *Dynamics of Self-Organized and Self-Assembled Structures* (Cambridge University Press, 2009)
65. S. Chandrasekhar, *Hydrodynamic and hydromagnetic stability* (Oxford Univ. Press, 1961)
66. H.A. Stone, A.D. Samuel, *Phys. Rev. Lett.* **77**, 4102 (1996)
67. J. Bławdziewicz, P. Vlahovska, M. Loewenberg, *Physica A* **276**, 50 (2000)
68. J.A. Hanna, P.M. Vlahovska, *Phys. Fluids* **22**, 013102 (2010)
69. J.T. Schwalbe, F.R. Phelan Jr, P.M. Vlahovska, S.D. Hudson, *Soft Matter* **7**, 7797 (2011)
70. O.S. Pak, J. Feng, H.A. Stone, *J. Fluid. Mech.* **753**, 535 (2014)
71. J.H. Ferziger, M. Perić, *Computational methods for fluid dynamics*, Vol. 3 (Springer Berlin, 1996)
72. R. Eymard, T. Gallouët, R. Herbin, *Handbook of Numerical Analysis*, Vol. 7 (2000)
73. J.R. Baumgardner, P.O. Frederickson, *SIAM J. Numer. Anal.* **22**, 1107 (1985)
74. J.A. Pudykiewicz, *J. Comput. Phys.* **213**, 358 (2006)
75. N.J. Mottram, C.J. Newton, arXiv preprint arXiv:1409.3542 (2014)
76. L. Longa, H.R. Trebin, *Phys. Rev. A* **42**, 3453 (1990)
77. P. Kaiser, W. Wiese, S. Hess, *J. Non-Equil. Thermody.* **17**, 153 (1992)
78. A.J. Bray, *Adv. Phys.* **51**, 481 (2002)
79. Y. Brenier, F. Otto, C. Seis, *SIAM J. Math. Anal.* **43**, 114 (2011)
80. D.S. Felix Otto, Christian Seis, *Commun. Math. Sci.* **11**, 441 (2013)
81. V. Lobaskin, D. Lobaskin, I. Kulić, *Eur. Phys. J.-Spec. Top.* **157**, 149 (2008)
82. P.S. Lovely, F. Dahlquist, *J. Theor. Biol.* **50**, 477 (1975)
83. M. Doi, S. Edwards, *The Theory of Polymer Dynamics* (Oxford University Press, 1986)
84. S. Dukhin, G. Kretzschmar, R. Miller, *Dynamics of Adsorption at Liquid Interfaces: Theory, Experiment, Application*, Studies in Interface Science (Elsevier Science, 1995), ISBN 9780080530611
85. J. Dhont, *An Introduction to Dynamics of Colloids* (Elsevier, 1996)
86. K.A. Hawick, D.P. Playne, *International Journal of Computer Aided Engineering and Technology* **2**, 78 (2010)



## 5 Conclusion and Outlook

Active matter is a collection of active agents, which rely on a constant supply of energy to move or generate mechanical forces. A typical biological example is a suspension of bacteria, where the individual bacteria cells are the active agents. The hydrodynamics of swimming bacteria takes place in the low Reynolds number regime, where hydrodynamic turbulence is absent. This eases the theoretical and numerical treatment to a great extent and allows to rigorously study the fundamental physics of their collective motion.

It is therefore of great interest to design well-controllable synthetic active agents in the low Reynolds number regime. A possible candidate is the active emulsion droplet. In contrast to Janus colloids, active emulsion droplets are “soft” and thereby resemble living cells. Furthermore, emulsion droplets have already been studied extensively in the past decade in the context of microfluidics. Most prominently, labs-on-a-chip can combine several digital fluidic operations such as transport, mixing, and sorting of droplets on a single chip.

In a first step, we build the theoretical groundwork by deriving a model for active emulsion droplets. The interface of an emulsion droplet is characterized by a concentration of one or several surfactant species. By carefully including all relevant physical processes, we gain a diffusion-advection-reaction equation for the surfactant density at the interface. Here, the advection part of the equation is coupled to the flow field at the interface. Thus, in order to close the equation, we also need to solve the Stokes equation to derive the flow field at the interface. The model of an active emulsion droplet, which we obtain in the end, is quite general and can be applied to many different setups. We do this by specializing our model droplet and numerically solving the underlying field equation for the droplet interface. The results are evaluated by employing standard tools of statistical physics.

In the first model, we study an axisymmetric bromine enriched water droplet in oil. This setup has been realized experimentally by Thutupalli *et al.* in Ref. [8]. The droplet interface is covered with surfactants, which react with the dissolved bromine and as a result increase the surface tension of the interface. Hence, the “bromination” reaction locally increases the surface tension, which induces Marangoni flow, *i.e.*, flow in direction of increasing surface tension. This flow advects surfactants and thereby further enhances the gradients in surface tension, which ultimately breaks the isotropic symmetry and leads to stationary swimming of the droplet. We confirm these experimental results by numerically solving our diffusion-advection-reaction equation. In addition, we identify further patterns of motion. We find that the droplet stops after an initial motion or that it oscillates back and forth. The latter also resembles recent experimental results [15, 16].

Due to the axisymmetric constraint, the droplet of our first model can only move along a straight line. However, in real systems the finite temperature at the droplet interface leads to fluctuations in the surfactant mixture, which in turn randomize the swimming direction  $\mathbf{e}$ . This is analyzed in a second model, where we omit the axisymmetric constraint and include thermal noise in the diffusion-advection-reaction for the droplet interface. We find, both in numerical solutions and in a perturbation analysis that the amplitude  $\xi$  of the thermal noise is connected to the rotational correlation time  $\tau_r$  of the swimming path via  $\tau_r \propto 1/\xi^2$ . The full three-dimensional treatment of the interface also allows to shed light on the demixing process or phase separation of the two types of surfactants (pristine and brominated) at the interface during the non-steady speed up of the droplet. We quantify the coarsening dynamics of the phase-separating surfactants by means of the growth rate of domain size. Two steps exist: An initially slow growth of domain size followed by a nearly ballistic regime. Furthermore, we study the deviation from axisymmetry during the non-steady speed up by introducing an appropriate measure for the biaxiality of the surfactant mixture. Here we find that the droplet is clearly not axisymmetric during the speed up of the droplet.

In a second model we present a way to spontaneously break the droplet symmetry without resorting to a chemical reaction. We assume an initially surfactant free emulsion droplet in a micelle enriched bulk phase. When a micelle adsorbs at the droplet interface, it spreads due to the Marangoni effect. This spreading also leads to a finite motion of the droplet in direction of the adsorption site. The corresponding outer flow field, however, preferentially advects other micelles towards the existing adsorption site. Hence, this mechanism can spontaneously break the isotropic symmetry of the droplet and lead to directed motion. We find parameter regimes in which the droplet either performs a random walk or directed motion.

As an outlook, we want to mention possible extensions of the presented models that we consider to be of interest. A straightforward extension is the combination of both models, *i.e.*, to implement the bromination droplet with explicitly modeled micelle adsorption. As a matter of fact, it has been shown that micelles are crucial in many active droplet systems [133, 132]. It would be interesting to see the effect of an explicitly modeled micelle adsorption on the rotational correlation time  $\tau_r$ . Furthermore, active droplets are usually confined between two plates in experiments to ease the observation. However, our model droplet is allowed to move freely in the bulk fluid. One could overcome this discrepancy by including appropriate boundary conditions in the Stokes equation for the flow field around the droplet. Lastly, as mentioned before, active droplets resemble active agents. Therefore a thorough study of the collective motion of active emulsion droplets is a worthwhile endeavor. In fact, experiments have shown that active droplets tend to swim in swarms [16]. However, all computer simulations of the collective motion of spherical microswimmers so far, assumed a fixed surface velocity field of the swimmer, *i.e.*, they implement the squirmer model [28, 29]. This could be extended to active droplets, where the surface velocity field is not a fixed boundary condition but rather depends dynamically on obstacles and neighboring droplets.

An alternative way to activate an emulsion droplet is to partially illuminate it with light. If the droplet is covered with light-switchable surfactants, one locally generates a

spot of different surface tension, which induces Marangoni flow and with that propulsion of the droplet. Since such a droplet is also covered by two types of surfactants, we can employ a similar model as before. In numerical solutions we find that the emulsion droplet can be pushed with UV light or pulled with blue light, which resembles recent experiments done with droplets on interfaces [20]. Furthermore, depending on the relaxation rate of the surfactant towards the surfactant in bulk, the droplet shows a plethora of trajectories, including a damped oscillation about the beam axis, oscillation into the beam axis, and a motion out of the beam followed by a complete stop. We also dwell on the dependence of the trajectories on the droplet and bulk fluids. In particular, we distinguish between strongly absorbing and transparent droplets.

A thinkable extension of our model is the combination of two perpendicular light beams which intersect at the position of the droplet. By slowly changing the intersection point of the two beams one could move the emulsion droplet to an arbitrary position in a bulk medium. Another generalization that might be worthwhile is the addition of external flows. Here, one could control the position of droplets in microchannel Poiseuille flow by shining light onto the channel from one side. Similar systems have recently been studied theoretically in the context of control theory of inertial flow [139, 140].

## 6 Bibliography

- [1] S. Ramaswamy, “The mechanics and statistics of active matter,” *Annu. Rev. Condens. Matter*, vol. 1, pp. 323–345, 2010.
- [2] E. Schrödinger, *What is life?* University Press, 1967.
- [3] M. C. Marchetti, “Active matter: Spontaneous flows and self-propelled drops,” *Nature*, vol. 491, no. 7424, pp. 340–341, 2012.
- [4] T. Sanchez, D. T. Chen, S. J. DeCamp, M. Heymann, and Z. Dogic, “Spontaneous motion in hierarchically assembled active matter,” *Nature*, vol. 491, no. 7424, pp. 431–434, 2012.
- [5] E. Tjhung, D. Marenduzzo, and M. E. Cates, “Spontaneous symmetry breaking in active droplets provides a generic route to motility,” *Proc. Natl. Acad. Sci. U. S. A.*, vol. 109, pp. 12381–12386, 2012.
- [6] C. C. Maass, C. Krüger, S. Herminghaus, and C. Bahr, “Swimming droplets,” *Annu. Rev. Condens. Matter*, vol. 7, no. 1, 2016.
- [7] A. Walther and A. H. Müller, “Janus particles,” *Soft Matter*, vol. 4, pp. 663–668, 2008.
- [8] S. Thutupalli, R. Seemann, and S. Herminghaus, “Swarming behavior of simple model squirmers,” *New J. Phys.*, vol. 13, p. 073021, 2011.
- [9] S.-Y. Teh, R. Lin, L.-H. Hung, and A. P. Lee, “Droplet microfluidics,” *Lab Chip*, vol. 8, pp. 198–220, 2008.
- [10] N. Nam-Trung, *Droplet Microreactor*. Springer US, 2008.
- [11] I. Lagzi, “Chemical robotics—chemotactic drug carriers,” *Open Med.*, vol. 8, no. 4, pp. 377–382, 2013.
- [12] M. M. Hanczyc, “Droplets: Unconventional protocell model with life-like dynamics and room to grow,” *Life*, vol. 4, no. 4, pp. 1038–1049, 2014.
- [13] V. A. Nepomniashchii, M. G. Velarde, and P. Colinet, *Interfacial phenomena and convection*. Chapman & Hall / CRC, 1 ed., 2002.
- [14] E. Lauga and T. R. Powers, “The hydrodynamics of swimming microorganisms,” *Rep. Prog. Phys.*, vol. 72, p. 096601, 2009.

- [15] H. Kitahata, N. Yoshinaga, K. H. Nagai, and Y. Sumino, “Spontaneous motion of a droplet coupled with a chemical wave,” *Phys. Rev. E*, vol. 84, p. 015101, 2011.
- [16] S. Thutupalli and S. Herminghaus, “Tuning active emulsion dynamics via surfactants and topology,” *Eur. Phys. J. E*, vol. 36, no. 8, pp. 1–10, 2013.
- [17] M. Schmitt and H. Stark, “Swimming active droplet: A theoretical analysis,” *Europhys. Lett.*, vol. 101, p. 44008, 2013.
- [18] M. Schmitt and H. Stark, “Active brownian motion of emulsion droplets: Coarsening dynamics at the interface and rotational diffusion,” *Submitted to Eur. Phys. J. E*, 2016.
- [19] M. Schmitt and H. Stark, “Marangoni flow at droplet interfaces: Three-dimensional solution and applications,” *Phys. Fluids*, vol. 28, p. 012106, 2016.
- [20] A. Diguët, R.-M. Guillermic, N. Magome, A. Saint-Jalmes, Y. Chen, K. Yoshikawa, and D. Baigl, “Photomanipulation of a droplet by the chromocapillary effect,” *Angew. Chem. Int. Edit.*, vol. 121, no. 49, pp. 9445–9448, 2009.
- [21] J. Dunkel, S. Heidenreich, K. Drescher, H. H. Wensink, M. Bär, and R. E. Goldstein, “Fluid dynamics of bacterial turbulence,” *Phys. Rev. Lett.*, vol. 110, no. 22, p. 228102, 2013.
- [22] E. M. Purcell, “Life at low reynolds number,” *Am. J. Phys.*, vol. 45, no. 1, pp. 3–11, 1977.
- [23] G. Subramanian and P. R. Nott, “The fluid dynamics of swimming microorganisms and cells,” *J. Indian Inst. Sci.*, vol. 91, no. 3, pp. 283–314, 2012.
- [24] J. Elgeti, R. G. Winkler, and G. Gompper, “Physics of microswimmers—single particle motion and collective behavior: a review,” *Rep. Prog. Phys.*, vol. 78, no. 5, p. 056601, 2015.
- [25] M. J. Lighthill, “On the squirming motion of nearly spherical deformable bodies through liquids at very small reynolds numbers,” *Commun. Pur. Appl. Math.*, vol. 5, pp. 109–118, 1952.
- [26] J. R. Blake, “A spherical envelope approach to ciliary propulsion,” *J. Fluid. Mech.*, vol. 46, pp. 199–208, 1971.
- [27] M. T. Downton and H. Stark, “Simulation of a model microswimmer,” *J. Phys.: Condens. Matter*, vol. 21, p. 204101, 2009.
- [28] A. A. Evans, T. Ishikawa, T. Yamaguchi, and E. Lauga, “Orientational order in concentrated suspensions of spherical microswimmers,” *Phys. Fluids*, vol. 23, p. 111702, 2011.

- [29] A. Zöttl and H. Stark, “Hydrodynamics determines collective motion and phase behavior of active colloids in quasi-two-dimensional confinement,” *Phys. Rev. Lett.*, vol. 112, p. 118101, 2014.
- [30] O. Pak and E. Lauga, “Generalized squirming motion of a sphere,” *J. Eng. Math.*, vol. 88, pp. 1–28, 2014.
- [31] G. Batchelor, “The stress system in a suspension of force-free particles,” *J. Fluid. Mech.*, vol. 41, no. 03, pp. 545–570, 1970.
- [32] T. Ishikawa, M. P. Simmonds, and T. J. Pedley, “Hydrodynamic interaction of two swimming model micro-organisms,” *J. Fluid. Mech.*, vol. 568, no. 1, pp. 119–160, 2006.
- [33] “Biodidac: A bank of digital resources for teaching biology.” <http://biodidac.bio.uottawa.ca/>.
- [34] T. Fenchel, “How dinoflagellates swim,” *Protist*, vol. 152, no. 4, pp. 329 – 338, 2001.
- [35] I. Llopis and I. Pagonabarraga, “Hydrodynamic interactions in squirmer motion: Swimming with a neighbour and close to a wall,” *J. Non-Newton. Fluid.*, vol. 165, no. 17, pp. 946–952, 2010.
- [36] Y. Hatwalne, S. Ramaswamy, M. Rao, and R. A. Simha, “Rheology of active-particle suspensions,” *Phys. Rev. Lett.*, vol. 92, no. 11, p. 118101, 2004.
- [37] B. M. Haines, A. Sokolov, I. S. Aranson, L. Berlyand, and D. A. Karpeev, “Three-dimensional model for the effective viscosity of bacterial suspensions,” *Phys. Rev. E*, vol. 80, p. 041922, 2009.
- [38] M. Moradi and A. Najafi, “Rheological properties of a dilute suspension of self-propelled particles,” *Europhys. Lett.*, vol. 109, no. 2, p. 24001, 2015.
- [39] T. Bickel, A. Majee, and A. Würger, “Flow pattern in the vicinity of self-propelling hot janus particles,” *Phys. Rev. E*, vol. 88, p. 012301, 2013.
- [40] R. Golestanian, T. B. Liverpool, and A. Ajdari, “Propulsion of a molecular machine by asymmetric distribution of reaction products,” *Phys. Rev. Lett.*, vol. 94, p. 220801, 2005.
- [41] W. F. Paxton, A. Sen, and T. E. Mallouk, “Motility of catalytic nanoparticles through self-generated forces,” *Chem. Eur. J.*, vol. 11, pp. 6462–6470, 2005.
- [42] J. L. Moran and J. D. Posner, “Electrokinetic locomotion due to reaction-induced charge auto-electrophoresis,” *J. Fluid. Mech.*, vol. 680, pp. 31–66, 2011.
- [43] I. Buttinoni, G. Volpe, F. Kümmel, G. Volpe, and C. Bechinger, “Active brownian motion tunable by light,” *J. Phys.: Condens. Matter*, vol. 24, p. 284129, 2012.

- [44] T. C. Adhyapak and H. Stark, “Zipping and entanglement in flagellar bundle of *E. coli* : Role of motile cell body,” *Phys. Rev. E*, vol. 92, p. 052701, 2015.
- [45] S. B. Babu and H. Stark, “Modeling the locomotion of the african trypanosome using multi-particle collision dynamics,” *New J. Phys.*, vol. 14, no. 8, p. 085012, 2012.
- [46] D. Alizadehrad, T. Krüger, M. Engstler, and H. Stark, “Simulating the complex cell design of trypanosoma brucei and its motility,” *PLoS Comput. Biol.*, vol. 11, p. e1003967, 2015.
- [47] E. Frey and K. Kroy, “Brownian motion: a paradigm of soft matter and biological physics,” *Ann. Phys.*, vol. 14, no. 1-3, pp. 20–50, 2005.
- [48] J. Dhont, *An Introduction to Dynamics of Colloids*. Elsevier, 1996.
- [49] J. R. Howse, R. A. Jones, A. J. Ryan, T. Gough, R. Vafabakhsh, and R. Golestanian, “Self-motile colloidal particles: from directed propulsion to random walk,” *Phys. Rev. Lett.*, vol. 99, p. 048102, 2007.
- [50] V. Lobaskin, D. Lobaskin, and I. Kulić, “Brownian dynamics of a microswimmer,” *Eur. Phys. J.-Spec. Top.*, vol. 157, pp. 149–156, 2008.
- [51] B. ten Hagen, S. van Teeffelen, and H. Löwen, “Brownian motion of a self-propelled particle,” *J. Phys.: Condens. Matter*, vol. 23, no. 19, p. 194119, 2011.
- [52] P. S. Lovely and F. Dahlquist, “Statistical measures of bacterial motility and chemotaxis,” *J. Theor. Biol.*, vol. 50, pp. 477–496, 1975.
- [53] M. Doi and S. Edwards, *The Theory of Polymer Dynamics*. Oxford University Press, 1986.
- [54] P. Romanczuk, M. Bär, W. Ebeling, B. Lindner, and L. Schimansky-Geier, “Active brownian particles,” *Eur. Phys. J.-Spec. Top.*, vol. 202, pp. 1–162, 2012.
- [55] M. Enculescu and H. Stark, “Active colloidal suspensions exhibit polar order under gravity,” *Phys. Rev. Lett.*, vol. 107, p. 058301, 2011.
- [56] F. Peruani and L. G. Morelli, “Self-propelled particles with fluctuating speed and direction of motion in two dimensions,” *Phys. Rev. Lett.*, vol. 99, p. 010602, 2007.
- [57] E. Bormashenko, Y. Bormashenko, and G. Oleg, “On the nature of the friction between nonstick droplets and solid substrates,” *Langmuir*, vol. 26, no. 15, pp. 12479–12482, 2010.
- [58] A. Yarin, “Drop impact dynamics: splashing, spreading, receding, bouncing,” *Annu. Rev. Fluid Mech.*, vol. 38, pp. 159–192, 2006.
- [59] A. Cassie and S. Baxter, “Wettability of porous surfaces,” *T. Faraday Soc.*, vol. 40, pp. 546–551, 1944.

- [60] K. Kawasaki, "Study of wettability of polymers by sliding of water drop," *J. Colloid Sci.*, vol. 15, no. 5, pp. 402–407, 1960.
- [61] K. Ichimura, S.-K. Oh, and M. Nakagawa, "Light-driven motion of liquids on a photoresponsive surface," *Science*, vol. 288, no. 5471, pp. 1624–1626, 2000.
- [62] F. D. Dos Santos and T. Ondarçuhu, "Free-running droplets," *Phys. Rev. Lett.*, vol. 75, pp. 2972–2975, 1995.
- [63] Y.-J. Chen, Y. Nagamine, and K. Yoshikawa, "Self-propelled motion of a droplet induced by marangoni-driven spreading," *Phys. Rev. E*, vol. 80, p. 016303, 2009.
- [64] M. D. Levan and J. Newman, "The effect of surfactant on the terminal and interfacial velocities of a bubble or drop," *AIChE Journal*, vol. 22, pp. 695–701, 1976.
- [65] K. V. Beard and C. Chuang, "A new model for the equilibrium shape of raindrops," *J. Atmos. Sci.*, vol. 44, no. 11, pp. 1509–1524, 1987.
- [66] Y. Pawar and K. J. Stebe, "Marangoni effects on drop deformation in an extensional flow: The role of surfactant physical chemistry. i. insoluble surfactants," *Phys. Fluids*, vol. 8, no. 7, pp. 1738–1751, 1996.
- [67] F. Blanchette, "Simulation of mixing within drops due to surface tension variations," *Phys. Rev. Lett.*, vol. 105, no. 7, p. 074501, 2010.
- [68] G. Katsikis, J. S. Cybulski, and M. Prakash, "Synchronous universal droplet logic and control," *Nat Phys*, 2015.
- [69] C. V. Kulkarni, W. Wachter, G. Iglesias-Salto, S. Engelskirchen, and S. Ahualli, "Monoolein: a magic lipid?," *Phys. Chem. Chem. Phys.*, vol. 13, no. 8, pp. 3004–3021, 2011.
- [70] N. T. Southall, K. A. Dill, and A. Haymet, "A view of the hydrophobic effect," *J. Phys. Chem. B*, vol. 106, no. 3, pp. 521–533, 2002.
- [71] S. Glathe and D. Schermer, "Wasser, wäsche, umwelt: Alles sauber?," *Chem. unserer Zeit*, vol. 37, no. 5, pp. 336–346, 2003.
- [72] P. Atkins and J. de Paula, *Atkins' Physical Chemistry*. OUP Oxford, 2010.
- [73] I. Roberts and G. E. Kimball, "The halogenation of ethylenes," *J. Am. Chem. Soc.*, vol. 59, no. 5, pp. 947–948, 1937.
- [74] O. Karthaus, M. Shimomura, M. Hioki, R. Tahara, and H. Nakamura, "Reversible photomorphism in surface monolayers," *J. Am. Chem. Soc.*, vol. 118, no. 38, pp. 9174–9175, 1996.

- [75] J. Y. Shin and N. L. Abbott, “Using light to control dynamic surface tensions of aqueous solutions of water soluble surfactants,” *Langmuir*, vol. 15, no. 13, pp. 4404–4410, 1999.
- [76] J. Eastoe and A. Vesperinas, “Self-assembly of light-sensitive surfactants,” *Soft Matter*, vol. 1, pp. 338–347, 2005.
- [77] E. Chevallier, A. Mamane, H. A. Stone, C. Tribet, F. Lequeux, and C. Monteux, “Pumping-out photo-surfactants from an air-water interface using light,” *Soft Matter*, vol. 7, pp. 7866–7874, 2011.
- [78] Y. Zhao and T. Ikeda, *Smart light-responsive materials: azobenzene-containing polymers and liquid crystals*. John Wiley & Sons, 2009.
- [79] T. Hayashita, T. Kurosawa, T. Miyata, K. Tanaka, and M. Igawa, “Effect of structural variation within cationic azo-surfactant upon photoresponsive function in aqueous solution,” *Colloid Polym. Sci.*, vol. 272, no. 12, pp. 1611–1619, 1994.
- [80] A. Diguët, H. Li, N. Queyriaux, Y. Chen, and D. Baigl, “Photoreversible fragmentation of a liquid interface for micro-droplet generation by light actuation,” *Lab Chip*, vol. 11, no. 16, pp. 2666–2669, 2011.
- [81] A. Venancio-Marques, F. Barbaud, and D. Baigl, “Microfluidic mixing triggered by an external led illumination,” *J. Am. Chem. Soc.*, vol. 135, no. 8, pp. 3218–3223, 2013.
- [82] A. Venancio-Marques and D. Baigl, “Digital optofluidics: Led-gated transport and fusion of microliter-sized organic droplets for chemical synthesis,” *Langmuir*, vol. 30, no. 15, pp. 4207–4212, 2014.
- [83] D. Baigl, “Photo-actuation of liquids for light-driven microfluidics: state of the art and perspectives,” *Lab Chip*, vol. 12, no. 19, pp. 3637–3653, 2012.
- [84] M. Ichikawa, F. Takabatake, K. Miura, T. Iwaki, N. Magome, and K. Yoshikawa, “Controlling negative and positive photothermal migration of centimeter-sized droplets,” *Phys. Rev. E*, vol. 88, no. 1, p. 012403, 2013.
- [85] U. Thiele, A. J. Archer, and M. Plapp, “Thermodynamically consistent description of the hydrodynamics of free surfaces covered by insoluble surfactants of high concentration,” *Phys. Fluids*, vol. 24, no. 10, p. 102107, 2012.
- [86] S. Dukhin, G. Kretzschmar, and R. Miller, *Dynamics of Adsorption at Liquid Interfaces: Theory, Experiment, Application*. Studies in Interface Science, Elsevier Science, 1995.
- [87] S. Sadhal, P. Ayyaswamy, and J. Chung, *Transport Phenomena with Drops and Bubbles*. Mechanical Engineering Series, Springer, 1996.

- [88] R. C. Desai and R. Kapral, *Dynamics of Self-Organized and Self-Assembled Structures*. Cambridge University Press, 2009.
- [89] K. A. Hawick and D. P. Playne, “Modelling, simulating and visualising the cahn-hilliard-cook field equation,” *International Journal of Computer Aided Engineering and Technology*, vol. 2, no. 1, pp. 78–93, 2010.
- [90] J. Thomson, “On certain curious motions observable at the surfaces of wine and other alcoholic liquors,” *Philos. Mag.*, vol. 10, no. 67, pp. 330–333, 1855.
- [91] J. Fournier and A. Cazabat, “Tears of wine,” *Europhys. Lett.*, vol. 20, no. 6, p. 517, 1992.
- [92] C. Marangoni, *Sull’ espansione delle gocce liquide*. PhD thesis, University of Pavia, 1865.
- [93] J. W. Gibbs, “On the equilibrium of heterogeneous substances,” *Trans. Connect. Acad. Arts Sci.*, vol. 3, 1876.
- [94] M. Roché, Z. Li, I. M. Griffiths, S. Le Roux, I. Cantat, A. Saint-Jalmes, and H. A. Stone, “Marangoni flow of soluble amphiphiles,” *Phys. Rev. Lett.*, vol. 112, no. 20, p. 208302, 2014.
- [95] J. Berg, *An Introduction to Interfaces & Colloids: The Bridge to Nanoscience*. World Scientific, 2010.
- [96] S. Phongikaroon, R. Hoffmaster, K. P. Judd, G. B. Smith, and R. A. Handler, “Effect of temperature on the surface tension of soluble and insoluble surfactants of hydrodynamical importance,” *J. Chem. Eng. Data*, vol. 50, no. 5, pp. 1602–1607, 2005.
- [97] L. Napolitano, “Plane marangoni-poiseuille flow of two immiscible fluids,” *Acta Astronaut.*, vol. 7, pp. 461 – 478, 1980.
- [98] Z. Mao, P. Lu, G. Zhang, and C. Yang, “Numerical simulation of the marangoni effect with interphase mass transfer between two planar liquid layers,” *Chinese J. Chem. Eng.*, vol. 16, pp. 161 – 170, 2008.
- [99] X.-Y. You, L.-D. Zhang, and J.-R. Zheng, “Marangoni instability of immiscible liquid–liquid stratified flow with a planar interface in the presence of interfacial mass transfer,” *J. Taiwan Inst. Chem. E.*, vol. 45, pp. 772 – 779, 2014.
- [100] J. Hadamard, “Mouvement permanent lent d’une sphere liquide et visqueuse dans un liquide visqueux,” *CR Acad. Sci.*, vol. 152, pp. 1735–1738, 1911.
- [101] W. Rybczynski, “Über die fortschreitende bewegung einer flüssigen kugel in einem zähen medium,” *Bull. Acad. Sci. Cracovie Ser. A*, vol. 1, pp. 40–46, 1911.
- [102] V. G. Levich, *Physicochemical Hydrodynamics*. Prentice-Hall, 1962.

- [103] M. D. Levan, “Motion of a droplet with a newtonian interface,” *J. Colloid Interface Sci.*, vol. 83, no. 1, pp. 11–17, 1981.
- [104] J. Bławdziewicz, P. Vlahovska, and M. Loewenberg, “Rheology of a dilute emulsion of surfactant-covered spherical drops,” *Physica A*, vol. 276, pp. 50–85, 2000.
- [105] J. A. Hanna and P. M. Vlahovska, “Surfactant-induced migration of a spherical drop in stokes flow,” *Phys. Fluids*, vol. 22, p. 013102, 2010.
- [106] J. T. Schwalbe, F. R. Phelan Jr, P. M. Vlahovska, and S. D. Hudson, “Interfacial effects on droplet dynamics in poiseuille flow,” *Soft Matter*, vol. 7, pp. 7797–7804, 2011.
- [107] H. A. Stone and A. D. Samuel, “Propulsion of microorganisms by surface distortions,” *Phys. Rev. Lett.*, vol. 77, p. 4102, 1996.
- [108] C. Sternling and L. Scriven, “Interfacial turbulence: hydrodynamic instability and the marangoni effect,” *AIChE Journal*, vol. 5, no. 4, pp. 514–523, 1959.
- [109] T. S. Sørensen, M. Hennenberg, A. Steinchen, and A. Sanfeld, “Chemical and hydrodynamical analysis of stability of a spherical interface,” *J. Colloid Interface Sci.*, vol. 56, no. 2, pp. 191–205, 1976.
- [110] T. Sørensen and M. Hennenberg, “Instability of a spherical drop with surface chemical reactions and transfer of surfactants,” in *Dynamics and Instability of Fluid Interfaces* (T. Sørensen, ed.), vol. 105 of *Lecture Notes in Physics*, pp. 276–315, Springer Berlin Heidelberg, 1979.
- [111] Y. S. Ryazantsev, “Thermocapillary motion of a reacting droplet in a chemically active medium,” *Fluid Dyn.*, vol. 20, no. 3, pp. 491–495, 1985.
- [112] A. Golovin, Y. P. Gupalo, and Y. S. Ryazantsev, “Chemothermocapillary effect for the motion of a drop in a liquid,” in *Soviet Physics Doklady*, vol. 31, p. 700, 1986.
- [113] Y. K. Bratukhin, “Thermocapillary drift of a droplet of viscous liquid,” *Fluid Dyn.*, vol. 10, no. 5, pp. 833–837, 1975.
- [114] A. Golovin and Y. S. Ryazantsev, “Drift of a reacting droplet due to the concentration capillary effect,” *Fluid Dyn.*, vol. 25, no. 3, pp. 370–378, 1990.
- [115] Y. S. Ryazantsev, A. Rednikov, and M. Velarde, “Solutocapillary motion of chemically reacting drop in microgravity,” in *Graz International Astronautical Federation Congress*, vol. 1, 1993.
- [116] A. Y. Rednikov, V. N. Kurdyumov, Y. S. Ryazantsev, and M. G. Velarde, “The role of time-varying gravity on the motion of a drop induced by marangoni instability,” *Phys. Fluids*, vol. 7, no. 11, pp. 2670–2678, 1995.

- [117] A. Y. Rednikov, Y. S. Ryazantsev, and M. G. Velarde, “Drop motion with surfactant transfer in a homogeneous surrounding,” *Phys. Fluids*, vol. 6, pp. 451–468, 1994.
- [118] A. Y. Rednikov, Y. S. Ryazantsev, and M. G. Velarde, “Drop motion with surfactant transfer in an inhomogeneous medium,” *Int. J. Heat Mass Tran.*, vol. 37, pp. 361–374, 1994.
- [119] A. Y. Rednikov, Y. S. Ryazantsev, and M. G. Velarde, “Active drops and drop motions due to nonequilibrium phenomena,” *J. Non-Equil. Thermody.*, vol. 19, pp. 95–113, 1994.
- [120] A. Y. Rednikov, Y. S. Ryazantsev, and M. G. Velarde, “On the development of translational subcritical marangoni instability for a drop with uniform internal heat generation,” *J. Colloid Interface Sci.*, vol. 164, pp. 168 – 180, 1994.
- [121] M. G. Velarde, A. Y. Rednikov, and Y. S. Ryazantsev, “Drop motions and interfacial instability,” *J. Phys.: Condens. Matter*, vol. 8, p. 9233, 1996.
- [122] Y. Sumino, N. Magome, T. Hamada, and K. Yoshikawa, “Self-running droplet: Emergence of regular motion from nonequilibrium noise,” *Phys. Rev. Lett.*, vol. 94, no. 6, p. 068301, 2005.
- [123] K. Nagai, Y. Sumino, H. Kitahata, and K. Yoshikawa, “Mode selection in the spontaneous motion of an alcohol droplet,” *Phys. Rev. E*, vol. 71, no. 6, p. 065301, 2005.
- [124] M. M. Hanczyc, T. Toyota, T. Ikegami, N. Packard, and T. Sugawara, “Fatty acid chemistry at the oil-water interface: self-propelled oil droplets,” *J. Am. Chem. Soc.*, vol. 129, pp. 9386–91, 2007.
- [125] T. Toyota, N. Maru, M. M. Hanczyc, T. Ikegami, and T. Sugawara, “Self-propelled oil droplets consuming “fuel” surfactant,” *J. Am. Chem. Soc.*, vol. 131, pp. 5012–5013, 2009.
- [126] N. Yoshinaga, K. H. Nagai, Y. Sumino, and H. Kitahata, “Drift instability in the motion of a fluid droplet with a chemically reactive surface driven by marangoni flow,” *Phys. Rev. E*, vol. 86, p. 016108, 2012.
- [127] S. Yabunaka, T. Ohta, and N. Yoshinaga, “Self-propelled motion of a fluid droplet under chemical reaction,” *J. Chem. Phys.*, vol. 136, p. 074904, 2012.
- [128] T. Ban, T. Yamagami, H. Nakata, and Y. Okano, “pH-dependent motion of self-propelled droplets due to marangoni effect at neutral pH,” *Langmuir*, vol. 29, pp. 2554–2561, 2013.
- [129] K. H. Nagai, F. Takabatake, Y. Sumino, H. Kitahata, M. Ichikawa, and N. Yoshinaga, “Rotational motion of a droplet induced by interfacial tension,” *Phys. Rev. E*, vol. 87, p. 013009, 2013.

- [130] S. Michelin, E. Lauga, and D. Bartolo, “Spontaneous autophoretic motion of isotropic particles,” *Phys. Fluids*, vol. 25, no. 6, p. 061701, 2013.
- [131] N. Yoshinaga, “Spontaneous motion and deformation of a self-propelled droplet,” *Phys. Rev. E*, vol. 89, p. 012913, 2014.
- [132] Z. Izri, M. N. van der Linden, S. Michelin, and O. Dauchot, “Self-propulsion of pure water droplets by spontaneous marangoni-stress-driven motion,” *Phys. Rev. Lett.*, vol. 113, p. 248302, 2014.
- [133] S. Herminghaus, C. C. Maass, C. Krüger, S. Thutupalli, L. Goehring, and C. Bahr, “Interfacial mechanisms in active emulsions,” *Soft Matter*, vol. 10, pp. 7008–7022, 2014.
- [134] Banno and T. Taro Toyota, “Design of reactive surfactants that control the locomotion mode of cell-sized oil droplets,” *Current Phys. Chem.*, vol. 5, no. 1, 2014.
- [135] C. A. Whitfield, D. Marenduzzo, R. Voituriez, and R. J. Hawkins, “Active polar fluid flow in finite droplets,” *Eur. Phys. J. E*, vol. 37, p. 8, 2014.
- [136] S. Shklyaev, “Janus droplet as a catalytic micromotor,” *Europhys. Lett.*, vol. 110, no. 5, p. 54002, 2015.
- [137] D. Zwicker, R. Seyboldt, C. A. Weber, A. A. Hyman, and F. Jülicher, “Growth and Division of Active Droplets: A Model for Protocells,” *ArXiv e-print 1603.01571*, 2016.
- [138] A. J. Bray, “Theory of phase-ordering kinetics,” *Adv. Phys.*, vol. 51, pp. 481–587, 2002.
- [139] C. Prohm, F. Tröltzsch, and H. Stark, “Optimal control of particle separation in inertial microfluidics,” *Eur. Phys. J. E*, vol. 36, pp. 1–13, 2013.
- [140] C. Prohm and H. Stark, “Feedback control of inertial microfluidics using axial control forces,” *Lab Chip*, vol. 14, pp. 2115–2123, 2014.

# Danksagung

Hiermit möchte ich allen danken, die am Zustandekommen dieser Arbeit beteiligt waren.

Zuallererst danke ich Herrn Prof. Holger Stark für die Stellung der Aufgabe und die geduldige Betreuung über viele Jahre hinweg. Weiterhin danke ich Herrn Prof. Uwe Thiele für die Begutachtung dieser Arbeit und Prof. Martin Schoen für die Leitung des Promotionsausschusses.

Mein Dank gilt auch allen Mitarbeitern der Arbeitsgruppe von Prof. Holger Stark. Besonders hervorheben möchte ich die vielen wissenschaftlichen Diskussionen mit Reinhard Vogel, Andreas Zöttl, Sebastian Reddig und Katrin Wolff. Ich danke weiterhin Stefan Fruhner für das Bereitstellen der Meshview Software.

Schließlich danke ich Shashi Thutupalli, dessen Experimente mit schwimmenden Tropfen den Grundstein für diese Arbeit bildeten.

## Zusammenfassung in deutscher Sprache

Angestoßen durch neue Erkenntnisse auf dem Gebiet der kollektiven Dynamik im Nichtgleichgewicht, sowie der Mikrofluidik in sogenannten Chiplabors, erleben aktive Emulsionstropfen derzeit eine Renaissance in der Physik der weichen Materie. *Aktive* Emulsionstropfen zeichnen sich dadurch aus, dass sie sich ohne externe Kräfte bewegen. Der Ursprung dieser Bewegung ist eine inhomogene Oberflächenspannung auf der Grenzfläche des Tropfens. Oberflächenspannung basiert auf den molekularen Anziehungskräften zwischen Flüssigkeitsmolekülen an der Grenzfläche. Folglich wird die Flüssigkeit auf beiden Seiten der Grenzfläche des Tropfens in Richtung steigender Oberflächenspannung gezogen. Diesen Effekt nennt man Marangoni-Effekt. Das daraus resultierende Geschwindigkeitsfeld um den Tropfen induziert die Bewegung des Tropfens.

Eine einfache Möglichkeit den Marangoni-Effekt zu nutzen um einen Tropfen in Bewegung zu setzen, basiert auf der Adsorption kugelförmiger Aggregate aus Tensiden, sogenannter Mizellen. Tenside sind grenzflächenaktive Moleküle, die die Oberflächenspannung einer Grenzfläche verringern. Wenn eine Mizelle an einen Tropfen adsorbiert, verringert sich lokal die Oberflächenspannung, was zu einem Marangoni-Fluss weg von der Adsorptionsstelle führt. Das induzierte Geschwindigkeitsfeld um den Tropfen bewegt den Tropfen in Richtung der Adsorptionsstelle und sorgt für einen verstärkten Fluss zur Tropfenoberfläche auf der Vorderseite des Tropfens. In dieser Arbeit erklären wir wie dieser einfache Mechanismus zu gerichteter Bewegung des Tropfens führen kann.

Alternativ kann man die molekulare Struktur, und damit die Oberflächenspannung, von Tensiden mittels einer chemischen Reaktion mit Brom ändern. Ein mit Brom angereicherter Tropfen, dessen Grenzfläche mit Tensiden belegt ist, kann so eine spontane Symmetriebrechung erfahren, die zu gerichteter Bewegung führt. Auch wenn diese Bewegung gerichtet ist, so zeichnet sie sich doch durch eine auf großen Längenskalen zufällige Richtungsänderung des Tropfens aus. Dieses Verhalten lässt sich zurückführen auf das thermische Rauschen des Tensidfilms auf der Tropfenoberfläche. Diese Arbeit entwickelt ein Modell für den Tensidfilm auf der Tropfenoberfläche und erklärt sowohl die spontane Vorwärtsbewegung als auch die erratische Richtungsänderung des Tropfens.

Im Gegensatz zur Änderung der Oberflächenspannung mittels einer chemischen Reaktion, welche relativ unkontrolliert abläuft, lässt sich die Oberflächenspannung auch sehr präzise mit Hilfe von Licht modulieren. Dabei nutzt man den *cis-trans* Isomorphismus spezieller Tenside aus. Diese ändern ihre Struktur und Oberflächenspannung wenn man sie mit Licht einer bestimmten Wellenlänge beleuchtet. So kann man lokal auf der Tropfenoberfläche die Oberflächenspannung verringern oder erhöhen und ein Marangoni-Flussfeld generieren. In Simulationen solcher Tropfen finden wir eine Vielzahl von Bewegungsmustern, angefangen von gerichteter Bewegung in Richtung des Lichtstrahls, bis hin zu gedämpften und stabilen Oszillationen um den Lichtstrahl.